

NORTHWESTERN UNIVERSITY

Understanding and Controlling Reaction Pathways for Synthesis of Oxynitride Materials

A DISSERTATION

SUBMITTED TO THE GRADUATE SCHOOL
IN PARTIAL FULFILLMENT OF THE REQUIREMENTS

for the degree

DOCTOR OF PHILOSOPHY

Field of Materials Science and Engineering

By

Elise A. Goldfine

EVANSTON, ILLINOIS

June 2023

© Copyright by Elise A. Goldfine, 2023

All Rights Reserved

Abstract

Understanding Reaction Pathways for Bulk and Thin Film Synthesis of Oxynitride Materials

Elise A. Goldfine

Heteroanionic materials are a class of materials of interest for their unique and tunable electronic, ionic, thermal, and optical properties, which are distinct from their homoanionic counterparts due to their multi-anionic nature. Oxynitrides, a type of heteroanionic material, are useful catalysts due to the effect of mixing oxygen and nitrogen atoms on their bandgap and catalytic binding energy. Oxynitride materials have been relatively underutilized because of the difficulty in synthesizing them. In this work, in situ x-ray diffraction is used to study the ammonolysis reaction for the synthesis of bulk oxynitride materials. Two promising catalytic oxynitride materials are studied in depth: MoON and TaON. Once the reaction mechanisms are elucidated, methods for controlling the syntheses to produce materials with desirable properties are explored. Additionally, methods for the thin film growth of targeted oxynitride materials predicted by computational discovery are explored.

Chapter 1 provides an in depth look at the ammonolysis of MoO₃ to form MoON by combined in situ XRD and TEM. The reaction pathway, roles of reaction intermediates, and crystallographic relationships among the phases are mapped. Building off the understanding of the ammonolysis reaction gleaned in Chapter 1, Chapter 2 explores the use of alternate precursors to bypass a critical intermediate phase and thus produce the target oxynitride phase at low temperature with high surface area and Chapter 3 details the use of alternate heating conditions to produce the target phase with ultra-low oxygen content. In Chapter 4, the in situ

synthesis technique is applied to the ammonolysis of Ta_2O_5 to synthesize TaON, and several key insights into the reaction are determined. Chapter 5 details three methods investigated for the growth of MoON and TaON thin films, including (1) PLD of oxide films with post-deposition ammonolysis, (2) N-plasma assisted PLD, and (3) reactive sputtering. The thesis concludes with a summary of and outlook on the progress towards the goal of synthesis-on-demand of oxynitrides.

Acknowledgements

I would like to use this opportunity to express my gratitude to those who supported, helped, and mentored me during my graduate studies. First I would like to thank my advisors, Professors Michael Bedzyk and Sossina Haile for their guidance and for helping me to become a better scientist and to hone my scientific communication skills. I would also like to thank Professors Christopher Wolverton and Mercouri Kanatzidis for serving on my thesis committee and for the guidance they supplied to my project in that role.

I want to acknowledge all the collaborators I worked with along the way and all the members of the Bedzyk and Haile research groups. A special thanks to the members of the HAM subgroup, Shobhit Pandey, Jill Wenderott, Dylan Bardgett, and Arthur Shih. Their teamwork and support were invaluable to the completion of my work. I would also like to thank Carlos Torres for his many discussions on thin film growth and x-ray diffraction and for accompanying me on one monster of a beamtime, Roger Reinertsen, the best office mate I could have asked for, without whom I surely would not have composed or sent any emails, Joey McCourt for being my own personal IT guy, and David Garcia for always being ready to get pie.

I would like to thank the wonderful staff and managers of the facilities at which I worked. A special thanks to Bruce Buchholz for imparting some of his PLD artistry to me and to Jerry Carsello for never saying no to the crazy things I set up in the X-ray lab.

I would also like to thank my friends and family for keeping me sane along the way: My first year study buddies, Tom Schmitt, James Male, Tyler Gish, and Louis Wang. Jennie Glerum, whose friendship at Northwestern and beyond made my time here so much more enjoyable. Rachael Van Pelt, the adventures we went on during her time in Illinois were a highlight of my

stay in the Midwest. And of course, to my sisters, Cari and Mara Goldfine, for innumerable phone calls and sister dates, and to my parents for always supporting me.

List Of Abbreviations

BET	Brunauer-Emmett-Teller surface area analysis
CA	Chronoamperogram
CIF	Crystallographic information file
DFT	Density functional theory
DI	Deionized
FReS	Forward recoil spectrometry
GSAS II	General Structure Analysis System II
HAM	Heteroanionic material
HER	Hydrogen evolution reaction
HRXRD	High-resolution x-ray diffraction
ICSD	Inorganic Crystal Structure Database
LSAT	$(\text{LaAlO}_3)_{0.3}-(\text{SrAl}_{0.5}\text{Ta}_{0.5}\text{O}_3)_{0.7}$
LSV	Linear sweep voltammogram
MIT	Metal-insulator transition
NUANCE	Northwestern University Atomic and Nanoscale Characterization Experimental Center
NUFAB	Northwestern University Micro/Nano Fabrication Facility
ORR	Oxygen reduction reaction
PLD	Pulsed laser deposition
PXRD	Powder x-ray diffraction
RBS	Rutherford backscattering spectrometry
REACT	Reactor Engineering and Catalyst Core Testing
RHE	Reversible hydrogen electrode
SCCM	Standard cubic centimeter per minute
SEM	Scanning electron microscopy
SIMS	Secondary ion mass spectrometry
STO	Strontium titanate, SrTiO_3
TCU	Temperature control unit
TEM	Transmission electron microscopy
TGA	Thermogravimetric analysis
XPS	X-ray photoelectron spectroscopy
XRD	X-ray diffraction
XRR	X-ray reflectivity
YSZ	Yttria-stabilized zirconia

Table of Contents

Abstract	3
Acknowledgements	5
List Of Abbreviations	7
Table of Contents	8
List of Figures	10
List of Tables	20
Chapter 1: Introduction	23
1.1 Molybdenum oxynitride.....	25
1.2 Tantalum oxynitride.....	27
Chapter 2: Experimental Methods	29
2.1 <i>In situ</i> synthesis and phase mapping	29
2.2 Thin film growth	29
2.3 Characterization	30
Chapter 3: In situ phase mapping of the Mo-O-N system	32
3.1 Methods	35
3.1.1 Materials	35
3.1.2 Powder X-ray Diffraction.....	36
3.1.3 Transmission Electron Microscopy	39
3.2 Results and Discussion	40
3.2.1 Macroscopic Reaction Pathway.....	40
3.2.2 Morphological and Crystallographic Relationships: MoO ₃ and γ -MoO _x N _y	49
3.2.3 Microscopic Reaction Pathway	52
3.2.4 Structure Evolution	65
3.3 Summary and Conclusions	68
Chapter 4: Low temperature synthesis of high surface area γ-Mo₂N	76
4.1 Synthesis of precursors and conventional “γ-Mo₂N”	78
4.2 Ammonolysis reaction pathways	83
4.3 Chemical and physical features of γ-Mo_{1-e}(N_xO_y)H_z products	87
4.4 Electrochemical characterization	94
4.5 Methods	97
4.6 Conclusions	101
4.7 Chapter 4 Supplemental Information	102
4.7.1 Synthesis of H _x MoO ₃ phases.....	102
4.7.2 Synthesis of H ₂ MoO ₅	103
4.7.3 Panoramic and conventional synthesis of γ -Mo _{1-(N_xO_y)H_z.....}	104
4.7.4 Discussion of the ammonolysis of H _x MoO _{3-l} (x \approx 0.3).....	105
Chapter 5: Synthesis of oxygen-free Mo₂N	107

	9
5.1 Introduction	107
5.2 Methods	109
5.3 Discussion.....	112
5.4 Conclusions	120
Chapter 6: In situ phase space mapping of the Ta-O-N system	121
6.1 In situ studies of the synthesis of TaON via ammonolysis	121
6.2 Ex situ synthesis of γ-TaON	128
Chapter 7: PLD growth of Ta- and Mo- oxynitride films	132
7.1 Growth of rutile tantalum oxynitride	132
7.1.1 Growth Method 1: Tantalum oxide PLD with post-deposition ammonolysis	133
7.1.2 Growth method 2: N-plasma assisted PLD of TaON	145
7.1.3 Growth method 3: Reactive sputtering of TaON.....	148
7.2 Growth of monoclinic molybdenum oxynitride	150
7.2.1 Growth method 1: Molybdenum oxide PLD with post-deposition ammonolysis	152
7.2.2 Growth method 2: N-plasma assisted PLD of MoON films.....	160
7.2.3 Growth method 3: Reactive sputtering of MoON films.....	162
Chapter 8: Outlook and Summary	166
Funding Acknowledgements.....	168
Appendix: User Manual for In Situ XRD on the Smartlab 9kW Gen 3 at the J. B. Cohen X-ray Diffraction Facility	169
References	187

List of Figures

- Figure 3.1:** Rietveld refinements of the powder x-ray diffraction of the MoO_3 and MoO_2 precursors used in the ammonolysis studies. **36**
- Figure 3.2:** Heating profiles used for (a) ex situ ammonolysis with a quench at 400°C , (b) ex situ ammonolysis with a quench at 500°C , (c) standard in situ ammonolysis of MoO_3 , (d) extended in situ ammonolysis of MoO_3 , (e) in situ ammonolysis of MoO_2 , and (f) in situ ammonolysis with a hold and quench at 390°C **38**
- Figure 3.3:** Diffraction patterns collected at (a) 275°C , (b) 380°C , (c) 405°C , (d) 600°C , (e) 690°C , and (f) 800°C during the in situ ammonolysis of MoO_3 . The overall reaction pathway displaying the phases present at each selected temperature is located below the diffraction patterns. **40**
- Figure 3.4:** Phase fraction as a function of temperature for the in situ ammonolysis of (a) MoO_3 using the standard heating profile, (b) MoO_3 using the extended heating profile, and (c) MoO_2 **42**
- Figure 3.5:** Contour maps of the diffraction data compiled into the phase fraction maps in Figure 3.2 for (a) MoO_3 using the standard heating profile, (b) MoO_3 using the extended heating profile, and (c) MoO_2 **42**
- Figure 3.6:** g- MoO_xN_y product of (a) MoO_3 using the standard heating profile, (b) MoO_3 using the extended heating profile, and (c) MoO_2 . The superstructure peaks of the $Pm\bar{3}m$ g^2 -variant are indicated with arrows in (a). **44**

- Figure 3.7:** Rietveld refinements of the PXRD of samples quenched during the standard ammonolysis of MoO_3 at (a) 400°C , containing 57% $\text{H}_x\text{MoO}_3\text{-I}$ and 43% MoO_2 , and (b) 500°C , containing 53% MoO_2 and 47% $\text{g-MoO}_x\text{N}_y$ 47
- Figure 3.8:** TEM EDX of particles of $\text{H}_x\text{MoO}_3\text{-I}$ and MoO_2 from the sample quenched at 400°C , showing negligible N signal in particles of either phase. 48
- Figure 3.9:** Morphology of MoO_3 Particle 1 at the (a) initial and (b) final stage during the ammonolysis. The scale bar is 100 nm. The inserted images are corresponding SAED patterns. The scale bar is 5 $1/\text{nm}$ 50
- Figure 3.10:** Simulated SAED patterns of MoO_3 along (a) [010] and (b) [211] zone axes, MoO_2 along (c) [112] and (d) [102] zone axes and MoO_xN_y along (e) [010] and (f) [231] zone axes. 51
- Figure 3.11:** Morphology structure changes of MoO_3 Particle 2 during heating under ammonia gas. (a1-h1) TEM images and (a2-h2) SAED patterns of the region of interest at (a-h) 25°C , 250°C , 350°C , 450°C , 475°C , 500°C , 600°C , and 650°C 53
- Figure 3.12:** Morphology of MoO_3 Particle 2 at the (a) initial and (b) final stage during the ammonolysis. The scale bar is 100 nm. The inserted images are corresponding SAED patterns showing the MoO_3 single crystallite along [010] zone axis became cubic phase along [010] zone axis after the reaction. The scale bar is 5 $1/\text{nm}$ 54
- Figure 3.13:** Radially accumulated intensity of SAED patterns at different temperatures showing the evolution of structure. Extra peaks were observed starting from 250°C to 450°C , as indicated by the purple box. From 350°C to 450°C , the spots at halfway are significantly weaker, as indicated by the red dashed arrows. At 475°C , MoO_2 phase shows up with obvious peaks as indicated by the red solid arrows. Both patterns at 600°C and 650°C can

be indexed with a cubic structure, but the intensity of spots at halfway (marked by black dashed arrows) are obviously stronger at 650 °C..... 54

Figure 3.14: Phase transition from MoO₃ to Bronze H_xMoO₃-I. SAED patterns at (a) 25 °C and (b) 250 °C along [010] zone axis. (c) Overlaid simulated SAED patterns of MoO₃ (Purple) and Bronze (Pink). Structure schematic of (d) MoO₃ and (d) Bronze H_xMoO₃-I, where Mo, O and H atoms are represented by purple, red and pink balls. 56

Figure 3.15: The orientation relationship between the intermediate phase MoO₂ with the initial and the final phases. (a1-c1) TEM images and (a2-c2) SAED patterns of Particle 3 at (a-c) 25°C, 475°C and 800°C..... 59

Figure 3.16: Phase transition from MoO₂ to g-MoO_xN_y. (a) Typical TEM image of a crystal quenched from 500°C. (b) EDS mapping shows the distribution of Mo, O and N. (c) TEM image and (d) SAED pattern from area A, indicating a phase of MoO₂. (e) TEM image and (f) SAED pattern from area B, indicating a phase of g-MoO_xN_y. (g) experimental and (h) simulated SAED pattern from area C, indicating a mixture of both phases. 61

Figure 3.17: (a) TEM image of quenched sample containing a mixture of MoO₂ and g-MoO_xN_y. (b) High-magnified TEM image of the region marked by box in (a). (c) On focus TEM image and (c) slightly underfocused image of g-MoO_xN_y showing a random mosaic of small domains on the platelet. This type of image contrast is caused by density variations in the specimen and is commonly encountered in porous solids..... 62

Figure 3.18: EELS of g-MoO_xN_y synthesized at 700 °C (red) and 800 °C (black)..... 64

Figure 3.19: Stereogram showing the relationships between the reciprocal lattices of MoO₃ (purple), MoO₂ (red) and Cubic MoO_xN_y (blue). The $(\bar{1}\bar{1}\bar{1})$ of MoO₃ is parallel to the (020) of MoO₂. The (100) and $(\bar{1}\bar{1}0)$ and $(00\bar{1})$ and $(1\bar{1}\bar{1})$, which were observed in Particle 1, and

the $(\bar{2}01)$ and $(\bar{1}11)$, which were observed in Particle 2, were all consistent with the orientation relationship. 65

Figure 3.20: Schematic of the structure evolution: (a) layered MoO_3 precursor along the $[1\bar{0}\bar{1}]$ direction showing the $[\text{MoO}_3]$ sheets built upon distorted edge-and corner-sharing $[\text{MoO}_6]$ octahedra. The layers are stacked along the b axis. (b) Bronze H_xMoO_3 $[1\bar{0}\bar{1}]$ direction showing intercalated hydrogen atoms bonded with oxygen atoms and off-center interlayer oxygens. (c) After CS MoO_3 loses oxygen atoms and the polyhedra shear from corner sharing to edge sharing to form a more compact transition structure. (d) The rutile-like structure of MoO_2 formed from reorientation of the polyhedra in the transition structure. (e) Cubic $\text{g-MoO}_x\text{N}_y$ produced by reconstruction of the MoO_2 polyhedra - at a lower temperature (upper) and with ordered site occupancy at a higher temperature (lower). 66

Figure 4.1: (a) Images of as synthesized precursor powders, (b) XRD patterns of the precursors with reflections for the known phases: H_xMoO_3 -phase I sg. $Cmcm$ ($x \approx 0.3$),⁹³ H_xMoO_3 -phase III sg. $C2/m$ ($x \approx 1.7$),⁹⁷ and H_2MoO_5 sg. $P2_1/n$.¹¹⁶ 80

Figure 4.2: XRD and Rietveld refinement results for the precursor materials: (a) H_xMoO_3 -I, (b) H_xMoO_3 -III, and (c) H_2MoO_5 81

Figure 4.3: X-ray photoelectron emission spectra about the Mo 3d region of the precursors used in this study and of MoO_2 . In the case of the reduced materials, MoO_2 and H_xMoO_3 bronzes, two doublets are evident, with the peak at ~ 233.5 eV being a component of both. The doublet at the more oxidized energy values reflects surface oxidation of these materials. 81

- Figure 4.4:** (a) XRD patterns and (b,c) SEM images of the (b) A700-MoO₃ and (c) A800-MoO₃ products. Dashed lines on the XRD plot indicate the reflections of the Pm3m space group of both materials. 82
- Figure 4.5:** (a) In situ PXRD contour plots, (b) selected cut XRD scans, and (c) phase fraction as a function of temperature for the ammonolysis of H_xMoO₃-phase I. Colored lines on the contour plots (a) correspond to selected XRD scans (b). White dashed lines on contour plots (a) represent phases present during reactions. Observed phases during the reaction are indicated by arrows on the phase fraction plot (c). 83
- Figure 4.6:** (a) In situ PXRD contour plots, (b) selected cut XRD scans, and (c) phase fraction as a function of temperature for the ammonolysis of H_xMoO₃-phase III. Colored lines on the contour plots (a) correspond to selected XRD scans (b). White dashed lines on contour plots (a) represent phases present during reactions. Observed phases during the reaction are indicated by arrows on the phase fraction plot (c). 84
- Figure 4.7:** (a) In situ PXRD contour plots, (b) selected cut XRD scans, and (c) phase fraction as a function of temperature for the ammonolysis of H₂MoO₅. Colored lines on the contour plots (a) correspond to selected XRD scans (b). White dashed lines on contour plots (a) represent phases present during reactions. Observed phases during the reaction are indicated by arrows on the phase fraction plot (c). 85
- Figure 4.8:** SEM images (a,b) pre and (c,d) post ammonolysis of (a,c) H_xMoO₃-III and (b,d) H₂MoO₅. A550-H-bronze displays a morphology in (c) that is similar to that of the precursor in (a), whereas A400-peroxo displays a morphology in (d) that is smaller and blocky compared to the precursor in (b). 87

- Figure 4.9:** (a) XRD patterns of A400-peroxo and A550-H-bronze, (b) thermogravimetric analysis (TGA) of A400-peroxo and A550-H-bronze with dashed reference lines indicating the expected mass losses for compositions MoN and Mo₂N, and the measured mass losses for A400-peroxo and A550-H-bronze (c) x-ray photoelectron spectroscopy (XPS) of the four γ -Mo_{1-x}(N_xO_y)H_z materials: A550-H-bronze, A400-peroxo, A700-MoO₃, and A800-MoO₃. XPS data for the A700-MoO₃, and A800-MoO₃ are taken from our previous work.⁴⁷ **87**
- Figure 4.10:** Comparison of the XRD of the five batches of (a) A550-H-bronze and (b) A400-peroxo used for ex situ characterization. **89**
- Figure 4.11:** Nitrogen adsorption-desorption, pore size distribution, and cumulative pore volume plots for (a)-(c) A550-H-bronze, (d)-(f) A400-peroxo, (g)-(i) A700-MoO₃, and (j)-(l) A800-MoO₃. **90**
- Figure 4.12:** Survey of high surface area γ with surface area compared to the synthesis temperature of the material. Results for the typical ammonolysis reaction temperature range of 650-800 °C are indicated by a dashed box. **92**
- Figure 4.13:** (a) LSVs for A550-H-bronze show increased activity over the course of electrochemical measurement. Error bars represent noise at each stable current, largely due to bubble formation. (b) “Activated” anodic LSVs for each sample, compared with electrodes with commercial Pt/C and carbon black. (c) Tafel plot of each sample from initial cathodic LSV (dashed) and “activated” anodic LSV (solid), with colors corresponding to samples as denoted in the legend of (b). **94**
- Figure 4.14:** XPS of the Mo 3d region of the A550-H-bronze sample before and after stabilizing at -0.8V vs. RHE in chronoamperometry (CA). **97**

- Figure 4.15:** Heating protocols used for the preparation of $\gamma\text{-Mo}_{1-x}(\text{N}_x\text{O}_y)\text{H}_z$ from the indicated precursors using (a) an Anton Paar XRK 900 reactor chamber in conjunction with the collection of diffraction patterns, and (b) a horizontal tube furnace..... **98**
- Figure 5.1:** XRD of samples synthesized by ammonolysis of MoO_3 at temperatures of 700°C , 800°C , and 900°C , with oxygen contents of 14%, 4%, and 0.3%, respectively..... **108**
- Figure 5.2:** Heating profile for the in situ ammonolysis of MoO_3 at 900°C **110**
- Figure 5.3:** Diffraction patterns collected at 350°C , 380°C , 640°C , 740°C , 870°C , 900°C , 850°C , and 25°C during the in situ ammonolysis of MoO_3 . The overall reaction pathway displaying the phases present at each selected temperature is shown below the diffraction patterns..... **112**
- Figure 5.4:** Phase fractions as a function of temperature for the ammonolysis of MoO_3 at 900°C as extracted from the in situ synthesis. **114**
- Figure 5.5:** Images of the MoO_3 precursor and A900 product of the in situ ammonolysis reaction show significant densification after the reaction. **114**
- Figure 5.6:** Lattice constant of A900 as a function of temperature during the ammonolysis reaction shows anion loss from 540°C to 780°C during heating and anion gain from 840°C to 600°C during cooling..... **116**
- Figure 5.7:** TGA mass loss profile for the complete reduction of A900 showing sharp mass loss beginning at 700°C and resulting in anion loss of 8.98%..... **117**
- Figure 5.8:** In situ XRD of the complete reduction of A700 and A800 under 7% H_2 (balance He). (a) Ratio of the intensities of the (200) and (111) peaks in A800 and A700 materials. In principle, the $I(200)/I(111)$ intensity ratio serves as a measure of the global cation:anion ratio⁴. Here, preferential orientation has not been completely eliminated despite spinning the

sample, and thus the intensity ratio cannot be interpreted quantitatively. (b)

Lattice constant of A700 and A800 materials. Under these conditions, both materials are fully transformed to Mo at 780°C. The onset of apparent cell contraction at $\approx 450^\circ\text{C}$ is taken to be indicative of bulk changes in composition. This coincides with a slight decline in the intensity ratio of the (200) to (111) peaks shown in a. **118**

Figure 6.1: Rietveld refinement of the sample produced by in situ ammonolysis of Ta_2O_5 using dry ammonia and a holding time of 24 hours shows the product to be a mixture of β -, γ -, and δ - TaON, and Ta_3N_5 **123**

Figure 6.2: a) Flow rate and b) temperature calibrations for the XRK 900 in situ furnace. **126**

Figure 6.3: Phase fractions as a function of temperature for a representative dry ammonolysis in situ reaction (03262021). The reaction shows the phase progression to be $\text{Ta}_2\text{O}_5 \rightarrow \gamma\text{-TaON} \rightarrow \beta\text{-TaON} \rightarrow \text{Ta}_3\text{N}_5 \rightarrow \text{TaN}$ during the reaction. **128**

Figure 6.4: Rietveld refinement of a sample produced by in situ ammonolysis of Ta_2O_5 using dry ammonia and a holding time of 24 hours on 10072021 shows the product to be phase pure γ -TaON. **129**

Figure 7.1: (a) HRXRD of epitaxial (101) $\text{Ta}_{0.8}\text{O}_2$ on (012) Al_2O_3 and (b) comparison of HRXRD of single crystal orthorhombic Ta_2O_5 and rutile $\text{Ta}_{0.8}\text{O}_2$ **137**

Figure 7.2: Crystal structure of (101) oriented rutile $\text{Ta}_{0.8}\text{O}_2$ on r-sapphire. **138**

Figure 7.3: Pre-ammonolysis (a) specular XRD, (c) XRR, (e) in-plane diffraction, and post ammonolysis (a) specular XRD, (c) XRR, (e) in-plane diffraction indicates no change in crystal structure following the ammonolysis treatment. **140**

Figure 7.4: XPS of (a) the Ta4f and (b) the O1s spectra of the as deposited $\text{Ta}_{0.8}\text{O}_2$ film and (c) the Ta4f, (d) O1s, (e) N1s spectra of the film after ammonolysis. The N1s spectra overlaps

with the Ta 4p and appears as the sharp peak to the right in the spectrum. A

comparison of the Ta4f spectra pre- and post-ammonolysis is shown in (f). 141

Figure 7.5: (a) After dry ammonolysis using a flow of 50 sccm anhydrous NH_3 the $\text{Ta}_{0.8}\text{O}_2$ film turned red, a color indicative of Ta_3N_5 , (b) after wet ammonolysis using a flow of 50 sccm NH_3 and 20 sccm $\text{Ar}/\text{H}_2\text{O}$ the $\text{Ta}_{0.8}\text{O}_2$ film turned yellow, a color indicative of TaON. ... 143

Figure 7.6: (a) GIXRD and XPS of the (b) Ta4f, (c) N1s (overlapping with Ta4p), and (d) O1s from a polycrystalline film produced by N-plasma assisted PLD of Ta_2O_5 147

Figure 7.7: XPS of the (a) Ta4f, (b) N1s (overlapping with the Ta4p), and (c) O1s spectra for the TaON film produced by reactive sputtering. GIXRD of (d) the as deposited film shows the film to be amorphous and (e) after annealing at 1200°C the film became polycrystalline. 149

Figure 7.8: Crystal structures and single crystal diffraction patterns oriented with the (200) direction up of (a) MoO_2 , (b) $\alpha\text{-MoON}$, and (c) $\beta\text{-MoON}$. The $\beta\text{-MoON}$ phase has the same structure as MoO_2 with half the oxygen atoms replaced with nitrogen. 152

Figure 7.9: (a) Specular XRD, (b) in-plane XRD, (c) Mo3d XPS spectrum, and (d) O1s spectrum for the as deposited MoO_2 film. 154

Figure 7.10: Crystal structure of (200) oriented MoO_2 on c-sapphire. 155

Figure 7.11: XPS of the MoON film produced by ammonolysis of MoO_2 using a flow rate of 100 sccm NH_3 and 35 sccm $\text{Ar}/\text{H}_2\text{O}$ at a temperature of 500°C for 16 hours: (a) Mo3d, (b) N1s (overlapping with Mo3p), (c) O1s, and (d) comparison of Mo3d spectra pre- and post-ammonolysis. 158

Figure 7.12: Specular XRD (a), (b) and rocking curves (c), (d) of the MoO_2 film pre- and post-ammonolysis. 159

- Figure 7.13:** FReS measurement of the MoON film produced by ammonolysis of PLD grown MoO₂ in comparison to a mica reference sample containing 9.5% H shows the film to contain ~1% H after the ammonolysis procedure. **160**
- Figure 7.14:** (a) Specular XRD of a representative film grown by N-plasma assisted PLD of an MoO₃ target shows a poorly crystallized film with large polycrystalline contribution. XPS of the (b) Mo3d, (c) O1s, and (d) N1s (overlapping with Mo3p) spectra. No N1s signal is seen in the N1s/Mo3p range. **162**
- Figure 7.15:** (a) Specular XRD, (b) XRR showing a 11 nm film with 1 nm surface layer, XPS of (c) the Mo3d, (d) N1s (overlapping with Mo3p), and (e) O1s spectra for the MoON film grown by reactive sputtering. **164**
- Figure 7.16:** Low temperature conductivity of MoON film grown by reactive sputtering. **165**

List of Tables

- Table 3.1:** Summary of crystallographic properties from the Rietveld refinements at 275°C. The number in parentheses reflects the uncertainty in the final digit(s) of the parameter value. Atomic coordinates were fixed to the values given in the cited references..... **71**
- Table 3.2:** Summary of crystallographic properties from the Rietveld refinements at 380°C. The number in parentheses reflects the uncertainty in the final digit(s) of the parameter value. Atomic coordinates were fixed to the values given in the cited references..... **72**
- Table 3.3:** Summary of crystallographic properties from the Rietveld refinements at 405°C. The number in parentheses reflects the uncertainty in the final digit(s) of the parameter value. Atomic coordinates were fixed to the values given in the cited references..... **73**
- Table 3.4:** Summary of crystallographic properties from the Rietveld refinements at 600°C. The number in parentheses reflects the uncertainty in the final digit(s) of the parameter value. Atomic coordinates were fixed to the values given in the cited references..... **73**
- Table 3.5:** Summary of crystallographic properties from the Rietveld refinements at 690°C. The number in parentheses reflects the uncertainty in the final digit(s) of the parameter value. Atomic coordinates were fixed to the values given in the cited references..... **74**
- Table 3.6:** Summary of crystallographic properties from the Rietveld refinements at 800°C. The number in parentheses reflects the uncertainty in the final digit(s) of the parameter value. Atomic coordinates were fixed to the values given in the cited references..... **75**
- Table 4.1:** Comparison of crystallographic properties, specific surface area, and composition of cubic $\gamma\text{-Mo}_{1-c}(\text{N}_x\text{O}_y)\text{H}_z$ samples produced from varying precursors and synthesis temperatures. The number in parentheses reflects the uncertainty in the final digit(s) of the

parameter value. Diffraction analysis and BET measurements of A700-MoO ₃ and A800-MoO ₃ are from the present work.	93
Table 4.2: HER activity metrics, reported as averages, for γ -Mo _{1-c} (N _x O _y)H _z materials from initial cathodic sweep and from anodic sweep following activation (CA at -0.8 V vs. RHE).	95
Table 4.3: Summary of crystallographic properties from the Rietveld refinements of the precursors H _x MoO ₃ -phase I, H _x MoO ₃ -phase III, and H ₂ MoO ₅ . The number in parentheses reflects the uncertainty in the final digit(s) of the parameter value. Atomic coordinates were fixed to the values given in the cited references.	103
Table 5.1: Sample composition as determined by combined TGA and combustion analysis. ..	119
Table 5.2: Density and surface area of A900. The density as determined by pycnometry is compared to the expected densities of molybdenum nitrides with the stoichiometries Mo ₂ N and MoN.	120
Table 6.1: Conditions and synthesis results for the in situ ammonolysis of Ta ₂ O ₅ using dry NH ₃ . Unless otherwise noted the synthesis was performed at 850°C using a ramp rate of 5°C/min from room temperature to 850°C.	124
Table 6.2: Ammonia dissociation levels for various set point temperatures and flow rates in the in situ furnace.	126
Table 6.3: Conditions and synthesis results for the ex situ ammonolysis of Ta ₂ O ₅ using dry NH ₃ . Unless otherwise noted the synthesis was performed at 850°C using a ramp rate of 5°C/min from room temperature to 850°C.	130
Table 7.1: PLD growth parameters for attempted growth of tantalum oxide films from a Ta ₂ O ₅ target. Unless otherwise noted, substrates were r-sapphire. Successful single crystal growths	

of rutile TaO_x are marked in bold. Marked in italics is the growth that resulted in

single crystal orthorhombic Ta₂O₅..... 136

Table 7.2: Ammonolysis recipes and corresponding results for the nitridation of TaO_x single crystal films deposited by PLD..... 142

Table 7.3: PLD growth parameters for attempted growth of TaON films by N-plasma assisted PLD. A Ta₂O₅ target, r-sapphire substrates, and target-substrate separation of 100mm were used for all depositions. 146

Table 7.4: Ammonolysis recipes and corresponding results for the nitridation of MoO₂ single crystal films deposited by PLD..... 157

Table 7.5: PLD growth parameters for attempted growth of MoON films by N-plasma assisted PLD. A MoO₃ target and c-sapphire substrates were used for all depositions. 161

Table 7.6: Deposition parameters for attempted growth of MoON films by reactive sputtering. A Mo target, c-sapphire substrates, substrate temperature of 400°C, and 20 minute equilibration and pump down time upon reaching the target temperature were used for all depositions. All films were cooled in base pressure unless otherwise noted..... 163

Chapter 1: Introduction

Heteroanionic materials (HAMs) are materials containing multiple anionic species in a single phase. Owing to varying atomic radii, electronegativities, and charges, the utilization of two or more anionic species leads to materials with excellent tunability of their physical, chemical, and electronic properties that exhibit unique, and potentially superior, properties to those of traditional single anion compounds.^{1,2} Furthermore, the variety of heteroanionic combinations, such as oxide-fluoride, oxide-sulfide, and oxide-nitride, provides a vast landscape of potential research. In comparison to other classes of materials, they are relatively unexplored, as evidenced by the 51,856 oxide entries in the Inorganic Crystal Structure Database (ICSD) and only 612 oxynitride entries.¹ This relative lack of exploration leaves room for significant materials synthesis and discovery in the field of HAMs.

Owing to their relatively undiscovered nature, a key step towards enabling the more widespread use of HAMs is an understanding of how to make them. This entails both a better understanding of the reaction mechanisms in current techniques used to synthesize HAMs, as well as the creation of new methods for broadening the scope of the types of heteroanionic materials that are synthetically realizable. This work aims to study not just the properties but also the science of synthesis of these types of materials. The study of the science of synthesis was approached from two ways: (1) the use of in situ synthesis techniques to study the mechanism of a common synthesis method, the ammonolysis reaction, and (2) the use of thin film growth and epitaxial stabilization as a method for producing new types of heteroanionic materials.

In this work, the synthesis science approach was applied to oxynitrides, materials containing both oxygen and nitrogen anions. These types of HAM are of interest for their

catalytic properties.³ In contrast to transition metal oxides, where the bandgap is defined by the empty orbitals of the metal and the oxygen 2p orbitals, oxynitrides have hybridized N and O 2p orbitals, which lowers the valence band and allows modulation of the band gap.⁴ Additionally, the interaction of both oxygen and nitrogen anions with the cation can influence the catalytic binding energy,^{5,6} giving the oxynitride different and potentially tunable activity in comparison to the oxide or nitride materials.

The synthesis of oxynitride materials can be challenging, especially in achieving control of the composition and structure. Balancing the incorporation of two types of anions can often lead to the formation of mixed phase or nonstoichiometric materials. There are many synthesis methods for making oxynitrides and nitrides – molybdenum nitrides for example have been synthesized by methods including high temperature direct nitridation of Mo metal,^{7,8} carbothermal reduction-nitridation,^{9,10} direct-arc discharge,¹¹ autoclave reduction-nitridation,^{12,13} sol-gel based self-propagation reaction,¹⁴ metathesis reaction of MoCl₅ with Ca₃N₃,¹⁵ thermolysis of organo-Mo complexes,^{16,17} and urea glass based synthesis.^{18,19} However, the most common bulk synthesis method for making oxynitrides for catalytic applications is the ammonolysis reaction, in which anhydrous ammonia gas is flowed over oxide precursors at elevated temperatures, as it is scalable and known to produce high surface area materials.²⁰⁻²⁵

In this thesis the reaction mechanism of the ammonolysis reaction as applied to two oxynitride materials – MoON and TaON – is studied by in situ x-ray diffraction. Both MoON and TaON are useful catalysts for which understanding and control of their synthesis mechanisms could better enable their use for catalytic applications. The understanding gained from the in situ studies is then used to manipulate the synthesis parameters to produce materials with desirable properties to better enable the utilization of these HAMs. Additionally, thin film

growth methods are explored for the synthesis of new, not previously realized phases of these materials. The work establishes methods for understanding the reaction mechanisms in the synthesis of these heteroanionic materials, as well as methods for characterizing the resulting oxynitride products, and explores methods for the growth of new phases of oxynitride materials in order to expand the range of heteroanionic materials that can be achieved.

1.1 Molybdenum oxynitride

Molybdenum nitrides, and in particular the cubic γ -phase, typically represented with stoichiometry Mo_2N , have garnered substantial interest from the (electro)catalytic community for use in various applications, including ammonia synthesis, ammonia decomposition, hydrodenitrogenation, acetylene dehydrogenation, hydrogen electrochemical evolution, and oxygen electrochemical reduction.^{5,6,33–42,18,43,26–32} Molybdenum oxynitrides are often misclassified as nitrides due to the difficulties in differentiating and quantifying bulk oxygen and nitrogen.^{5,44} Further complicating the compositional determination of these materials, molybdenum nitrides and oxynitrides are often nonstoichiometric with compounds of the form $\text{Mo}_{1-x}\text{N}_x$ predicted to be stable over a large compositional range ($0.2 < x < 0.7$).⁴⁵ Molybdenum “nitrides” have been experimentally realized in three crystalline phases: the γ -phase, a non-stoichiometric rock salt cubic phase (sg: Fm-3m) with composition $\text{Mo}_2\text{N}_{1\pm x}$, the β -phase, a low temperature tetragonal variant of the γ -phase (sg: I4₁/amd), and the δ -phase, a stoichiometric hexagonal phase with composition MoN (sg: P6₃mc).⁴⁶ These nitride phases may actually contain relatively high amounts of oxygen, especially if synthesized from an oxygen-containing precursor. Recent studies in our group have shown that while it is common to assign stoichiometry Mo_2N to the γ -phase, the material obtained from a typical ammonolysis reaction

performed at 700 to 800 °C is more appropriately described as $\gamma\text{-Mo}_{1-c}(\text{N}_x\text{O}_y)\text{H}_z$.⁴⁷

Specifically, the resulting γ phase has high concentrations not only of oxygen, as recognized in several earlier studies,^{22,33} but also of hydrogen, the latter presumably originating from the NH_3 reactant. Furthermore, and unexpectedly, the product nitride has vacancies on the cation rather than anion sites. Accordingly, the γ phase is hereafter recognized in this work to encompass a broad range of chemistries. For consistency with prior literature, it is also denoted here as “ $\gamma\text{-Mo}_2\text{N}$ ”.

A common route for preparing “ $\gamma\text{-Mo}_2\text{N}$ ”, and indeed a broad range of nitrides and oxynitrides, is by the ammonolysis reaction – in which a solid state precursor, typically MoO_3 in the case of molybdenum nitrides, is reacted with ammonia at elevated temperatures.^{48,49} For the Mo-O-N system, this ammonolysis process routinely produces a phase-pure product with specific surface area in the range of 50-200 m^2/g .^{21,25,30–32,42,43} Multiple reaction pathways have been proposed for the synthesis of MoO_xN_y phases from MoO_3 , most proceeding through the formation of reduced oxide MoO_2 and hydrogen molybdenum bronze intermediates to form a mixture of $\gamma\text{-Mo}_2\text{N}$ and MoN products, although some also claim the formation of an oxynitride intermediate as well.^{20,21,23,25,34,50,51} The precursor and intermediates, along with reaction conditions, affect the final composition and phase of the product oxynitride. Elucidating the complex reaction pathway for these materials is crucial to targeting active phases, specifically the γ -phase, for catalysis. A better understanding of this pathway is key to understanding both how to produce the different phases of molybdenum nitride, and how the reaction conditions influence the composition and structure of the final product; and thus establishing methods for tuning the final properties of the product phase.

Beyond the known phases of molybdenum nitrides and oxynitrides, the never-before-

synthesized monoclinic MoON phase is also of interest, as it is predicted by first principles DFT calculations to have a metal-insulator transition (MIT) similar to VO_2 .⁵² This material is a prime example of a heteroanionic material in which incorporation of the two types of anions induces properties not present in the homoanionic counterparts; it is the combined interaction of the oxygen and nitrogen anions that puts the Mo cation in the correct electronic state to display the transition.

1.2 Tantalum oxynitride

The tunable bandgap of oxynitrides is beneficial for developing photoactive catalysts for electrolysis, where the bandgap must span the redox potentials of hydrogen and oxygen while remaining small enough to allow absorption of visible light.^{3,53–56} Transition metal oxides are often used for water splitting due to their relative ease of synthesis and stability against the oxidative potentials used in these applications. However, the large bandgap of transition metal oxides makes them unsuitable for photocatalysis, as they cannot absorb a large portion of the solar light spectrum. In contrast, the bandgaps of oxynitrides can be significantly smaller than those of their oxide counterparts due to the higher energy of nitrogen 2p orbitals, thereby allowing them to absorb in the visible region.^{54,55} Tantalum oxynitride, in particular, has been well studied due to the ideal placement of its bandgap in relation to the hydrogen and oxygen redox potentials and its subsequent promise for photocatalytic water splitting.^{4,57–64}

TaON has been experimentally realized in three crystalline phases: the stable β -phase with a monoclinic baddeleyite structure (sg: $P2_1/c$),^{65,66} and the metastable γ -phase (sg: $C2/m$),^{67–69} and δ -phase (sg: $I4_1/amd$).^{69,70} $\text{Ta}_3\text{O}_6\text{N}$ has also been synthesized in the Nb_2TiO_7 structure type.⁷¹ A hexagonal α -phase was reported, but later falsified by DFT calculations.⁷² Like

molybdenum oxynitrides, bulk TaON is commonly synthesized through ammonolysis.^{59,61,67,70,73–77} Ammonolysis typically results in the formation of the stable β -TaON phase, or mixtures containing the β -, γ -, and δ - phases, as well as tantalum nitrides. Isolating the less stable γ - and δ - phases is challenging and because of this, definitive studies of the properties of different TaON phases, specifically their catalytic activity, are lacking. A better understanding of the reaction mechanism could enable more controlled synthesis in order to isolate the different TaON phases.

In addition to the experimentally realized phases, several metastable phases have been predicted by first principle DFT calculations. Bredow et al. reported the relative stability of several TaON phases, with the baddeleyite (β) structure at the lowest energy, followed by the anatase (δ), rutile, and fluorite structures, respectively.⁷⁸ The baddeleyite and anatase phases have been realized experimentally, while the rutile and fluorite phases have not. The rutile phase, however, is only slightly less stable than the anatase phase, making it a potentially synthesizable target. The use of epitaxial stabilization to grow the metastable rutile TaON phase, and thereby expand the achievable phases of oxynitride materials, was explored in this work.

Chapter 2: Experimental Methods

A brief overview of the methods used in this thesis is given below. Detailed experimental procedures are given in the corresponding chapters.

2.1 *In situ* synthesis and phase mapping

In-situ x-ray diffraction (XRD) was used to panoramically observe and map the reaction pathways for the synthesis of oxynitride materials by ammonolysis. In situ XRD measurements were performed in the J. B. Cohen X-Ray Diffraction Facility on a 9kW Cu rotating anode Rigaku Smartlab XE with a D/TEX Ultra 250 1D silicon strip detector using an Anton Paar XRK 900 reactor chamber. In this method, the precursor oxide was loaded into the reactor chamber and ammonia gas was flowed over the sample. Diffraction measurements were collected as the sample was heated and reacted with the NH_3 . In this way, the appearance and disappearance of precursor, intermediate, and final products was observed, and the phase fractions, lattice constants, and crystallite size were tracked as a function of temperature and reaction time.

2.2 Thin film growth

Pulsed laser deposition (PLD) was used to grow oxide and oxynitride thin films. PLD was performed in the Pulsed Laser Deposition Facility at Northwestern University using a PVD nanoPLD 1000 chamber with a 248 nm KrF excimer laser. In this technique, a high energy pulsed laser is used to ablate the material from a target. The plasma plume of ablated material is then deposited on a substrate to grow a thin film. This method can be used to grow epitaxial

single crystal thin films, with the composition of the films controlled by the target material and gas atmosphere in the chamber during deposition, along with other deposition parameters such as the laser power and substrate temperature.

Reactive sputtering was also used to grow oxynitride thin films. Sputtering was performed in the Northwestern University Micro/Nano Fabrication Facility (NUFAB) using an AJA Orion sputter system. In this method cation atoms are sputtered from a metal target and anion atoms are supplied from a gas stream at the substrate that is activated by the plasma from the target. This method can also be used to grow epitaxial single crystal thin films, with the composition of the films controlled by the target material, flow of reactive gases supplied, and power applied to the target.

2.3 Characterization

X-ray reflectivity (XRR), high-resolution x-ray diffraction (HRXRD), in-plane and off-specular diffraction measurements, and pole figure measurements were used to characterize the phases and structures of the thin films. These measurements were also performed in the J. B. Cohen X-Ray Diffraction Facility, typically on a 9kW Cu rotating anode Rigaku Smartlab with a 0D detector. XRR measurements were used to determine the film thickness, roughness, and density, while the diffraction measurements were used to determine film phase, crystal structure, and orientation.

XPS measurements were used to measure the composition of thin film samples. These measurements were done in the Northwestern University Atomic and Nanoscale Characterization

Experimental (NUANCE) Facility. XPS measurements were taken on a Thermo Scientific ESCALAB 250Xi with a monochromatic Al K α source. An electron flood gun was used to minimize surface charging. All peaks were calibrated to the C 1s peak at 284.8 eV. Analysis was carried out using the Avantage software and peak areas were corrected for the relative sensitivity factors and inelastic mean free paths of the photoelectrons.

The composition of bulk samples was determined using a combination of thermogravimetric analysis (TGA) and combustion analysis. TGA measurements were performed using a Netzsch STA F3 and were used to determine the Mo content (mass %) upon complete reduction under hydrogen. Microchemical combustion analysis was performed at Midwest Microlab, to determine the nitrogen and hydrogen mass percentages. Once the Mo and N content of the sample was determined, the remaining mass was attributed to oxygen.

Brunauer–Emmett–Teller (BET) measurements were used to characterize the surface area and pore characteristics of the oxynitride samples. BET measurements were performed at the Reactor Engineering and Catalyst Core Testing (REACT) Facility using nitrogen physisorption isotherms measured at liquid nitrogen temperature on a Micromeritics 3Flex instrument.

Chapter 3: In situ phase mapping of the Mo-O-N system

The work in this chapter is manuscript in preparation titled *Elucidating the reaction pathway for the ammonolysis of MoO₃ via in situ powder X-ray diffraction and transmission electron microscopy* (Elise A. Goldfine, Chi Zhang, Kun He, Jill K. Wenderott, Shobhit A. Pandey, Roberto dos Reis, Jiahong Shen, Chris Wolverton, Michael J. Bedzyk, Kenneth R. Peoppelmeier, Sossina M. Haile, and Vinayak P. Dravid).

Molybdenum nitrides are notable for their tunable mechanical, electronic, thermal, and magnetic properties. Of particular interest here is their use as catalysts spanning a range of reactions, from ammonia synthesis and acetylene hydrogenation to hydrogen evolution and oxygen reduction.^{18,25,37–39,41,42,79–82,26–32,36} While there are many routes to the synthesis of molybdenum nitride powders, including for example, direct nitridation of Mo metal and exotic processes such as thermolysis of organo-Mo complexes, the most common method for producing high surface area materials of this class is via ammonolysis of MoO₃,^{20–25,33} specifically, orthorhombic α -MoO₃ (sp. gr. *Pbnm*⁸³). In such reactions, anhydrous ammonia gas is flowed over oxide precursors at elevated temperatures. The product of ammonolysis of MoO₃ is often described to be γ -Mo₂N, a material with the rock salt structure type (space group *Fm* $\bar{3}$ *m*) and 50% occupancy on the anion sites. In a recent study we showed that the material produced from such a reaction using typical conditions is in fact best described as Mo_{1-x}O_xN_yH_z, meaning that γ -phase molybdenum nitride can retain residual oxygen (as noted in some prior literature), it can incorporate hydrogen, it hosts cation vacancies which may or may not be accompanied by anion

vacancies, and the cation and anion species are ordered so as to lower the space group symmetry from $Fm\bar{3}m$ to $Pm\bar{3}m$.^{5,47} We furthermore established the occurrence of two variants of this phase with slightly differing chemistries and crystallographic features. Ordering of cation vacancies enables detection of the $Pm\bar{3}m$ symmetry by X-ray and electron diffraction in the nearly oxygen-free γ'' variant, whereas neutron methods are required to observe the $Pm\bar{3}m$ symmetry in the oxygen-rich γ' variant. Hereafter we designate the material simply as γ - MoO_xN_y (and products in the literature as “ γ - Mo_2N ”), recognizing the wide chemical space of the phase and its inclusion of the γ' and γ'' variants.

The high surface area of γ - Mo_2N resulting from ammonolysis of α - MoO_3 has been attributed to the topotactic nature of the reaction.²⁵ The specific volume association with Mo is lower in the nitride product than the oxide precursor. Hence, topotactic transformation of a crystal of MoO_3 to γ - Mo_2N along with a retention of macroscopic dimensions generates nanometric pores and the observed high surface area. While the drive to create high surface area γ - Mo_2N has motivated extensive studies to reveal the reaction pathway, the details of the transformation remain unclear. Uncertainty remains in part because slight variations in synthesis parameters (e.g., reaction gas space velocity, temperature, and heating rate) can influence the pathway, as reflected in influences on the nature of the product.^{21,22,25,47,51} Moreover, definitive in situ studies are lacking. Nevertheless, there is broad agreement in the literature^{7,20,22,23,34,50} that the reaction proceeds through one or more reduced intermediates, with two specific compounds having been observed: H_xMoO_3 ($0.23 < x < 0.40$), also known as phase-I bronze, and MoO_2 . Choi et al. have demonstrated that low heating rates favor the pathway $\text{MoO}_3 \rightarrow \text{H}_x\text{MoO}_3 \rightarrow \gamma$ -

Mo₂N”, whereas high heating rates favor the pathway MoO₃ → MoO₂ → “γ-Mo₂N”.²²

Several authors have argued that the topotactic transformation, which generates the crystallographic relationship {100}Mo₂N || {010}MoO₃,^{21,25,51} is only possible via the H_xMoO₃ pathway. Furthermore, where MoO₂ is encountered as an intermediate (or directly employed as precursor),⁸⁴ extremely high temperatures are required to induce its nitridation. The low reactivity of MoO₂ has even earned it the title of spectator,²⁵ rather than participant, in the ammonolysis reaction. In agreement with this characterization, several authors have shown that when reaction conditions are tailored to channel the reaction through H_xMoO₃, achieved through control of the heating profile, high surface area products can be obtained.^{21,22,24,28,32,85}

Beyond considerations of the ammonolysis of MoO₃ to produce molybdenum nitrides, there has been fundamental interest in the pathway by which MoO₃ is reduced to MoO₂. Significantly, this reaction has been shown by several authors to proceed topotactically.⁸⁶⁻⁸⁸ Bertrand has reported the structural relationships (010)MoO₃ || (20 $\bar{1}$)MoO₂ upon reduction of MoO₃ both in H₂ and under electron beam irradiation in vacuum with a preservation of the crystal morphology.⁸⁶ Dufour has observed three other possible crystallographic orientations of MoO₂ nuclei under H₂ parallel to (010)MoO₃: (210)MoO₂, (100)MoO₂, or (41 $\bar{1}$)MoO₂, the first of which has also been observed by Chen under electron beam irradiation.^{86,88} Given the topotactic relationship between MoO₃ and MoO₂ and between MoO₃ and “γ-Mo₂N”, the apparent absence of a topotactic relationship between MoO₂ and “γ-Mo₂N” is surprising.

In this study, we employ both in situ and ex situ methods to elucidate the transformation pathway from MoO₃ to γ-MoO_xN_y upon high temperature exposure to flow of ammonia. Using

powder X-ray diffraction (PXRD) we obtain a panoramic overview of the phase transitions,⁸⁹⁻⁹¹ whereas using transmission electron microscopy (TEM) we observe the morphological, crystallographic, and chemical relationships between the phases encountered during the reaction. We find that H_xMoO_3 -I ($x \approx 0.3$) and MoO_2 form as nano-sized intermediates during ammonolysis of MoO_3 , with small amounts of hexagonal δ - MoN occurring as a transient secondary product, depending on reaction conditions. Ultimately, nano-sized, single-crystalline-like cubic γ - MoO_xN_y appears as the phase pure product. Notably, both H_xMoO_3 -I and MoO_2 intermediates are found to participate in the topotactic transformation of MoO_3 to γ - MoO_xN_y . The mechanistic understanding achieved by monitoring the reaction pathway lays the foundation for rational design of more material- and energy-efficient synthesis strategies of γ - MoO_xN_y in particular, while demonstrating the value of in situ studies of gas-solid reactions in general.

3.1 Methods

3.1.1 Materials

The precursors α - MoO_3 (99.9995% metals basis, Alfa Aesar) and MoO_2 (99% metals basis, Alfa Aesar) were used as received after confirmation of phase purity by powder X-ray diffraction (Figure 3.1). In situ ammonolysis studies of the MoO_3 precursor were performed as described below. Ex situ studies were carried out on reaction intermediates obtained from interrupting the ammonolysis reaction as implemented in a conventional horizontal tube furnace at the selected temperatures of 400 and 500 °C. Approximately 100 mg of the oxide precursor was placed in a quartz boat within the furnace hot zone, exposed to ammonia flow (100 sccm NH_3 , Airgas, anhydrous), and subjected to the heating profiles presented in Figure S2a and S2b.

Upon reaching the target reaction temperature, the samples were immediately quenched to room temperature while still under ammonia flow. Measurement of the ammonia dissociation behavior indicated that the 100 sccm flow rate was sufficiently high to deliver fully undissociated NH_3 to the oxide sample.⁹² The Brunauer–Emmett–Teller (BET) specific surface area of selected samples was characterized by nitrogen physisorption isotherms measured at liquid nitrogen temperature using a Micromeritics 3Flex instrument. Data were analyzed using the MicroActiv software package.

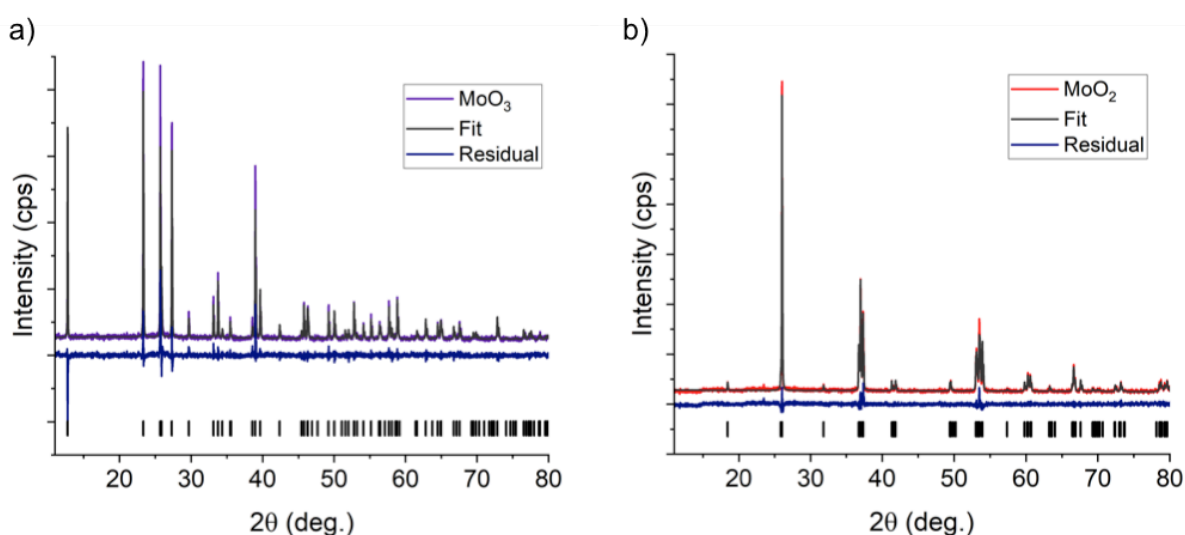


Figure 3.1: Rietveld refinements of the powder x-ray diffraction of the MoO_3 and MoO_2 precursors used in the ammonolysis studies.

3.1.2 Powder X-ray Diffraction

In situ x-ray diffraction studies were performed using an Anton Paar XRK 900 reactor chamber mounted onto a 9 kW Cu rotating anode Rigaku Smartlab equipped with a D/TEX Ultra 250 1D silicon strip detector with a Ni filter to remove $\text{K}\beta$ radiation. Measurements were taken in $\theta/2\theta$ geometry over the 2θ range 9° – 82° with a scan speed of 50° $2\theta/\text{min}$ to minimize dwell time at each temperature. Approximately 100 mg of the oxide precursor was placed inside the

reactor chamber at ambient temperature, purged with N₂ (Airgas, 99.999%), and subjected to a flow of 100 sccm of NH₃ (Airgas, anhydrous). While the gas flow rate was identical to that used in the ex situ experiments, evaluation of the ammonia dissociation in the Anton Paar reactor suggested a greater level of decomposition of NH₃ into H₂ and N₂, than the former.⁹² Thus, comparisons are made to understand overall trends, without an expectation of exact correspondence. Diffraction patterns were collected on both heating to and cooling from the upper reaction temperature of 800 °C, at which the samples were held for 3 h. The sample was equilibrated for 2 minutes at each data acquisition temperature before collecting the diffraction pattern. The thermal profiles are detailed in Figure 3.2. The heating profile applied to MoO₃ included a relatively low heating rate in the intermediate temperature regime (350 – 500 °C, 1 °C/min between XRD pattern acquisitions) in accord with typical ammonolysis reactions targeting high surface area from this precursor (standard heating profile). Several authors maintain that slow heating in this temperature range facilitates bronze formation, which as noted, is believed to be essential for the topotactic pathway. To directly study this possibility, a second reaction in which a 1 h hold at 400 °C was included was pursued (extended heating profile). In situ synthesis was also performed to produce targeted intermediates for further study, as discussed below.

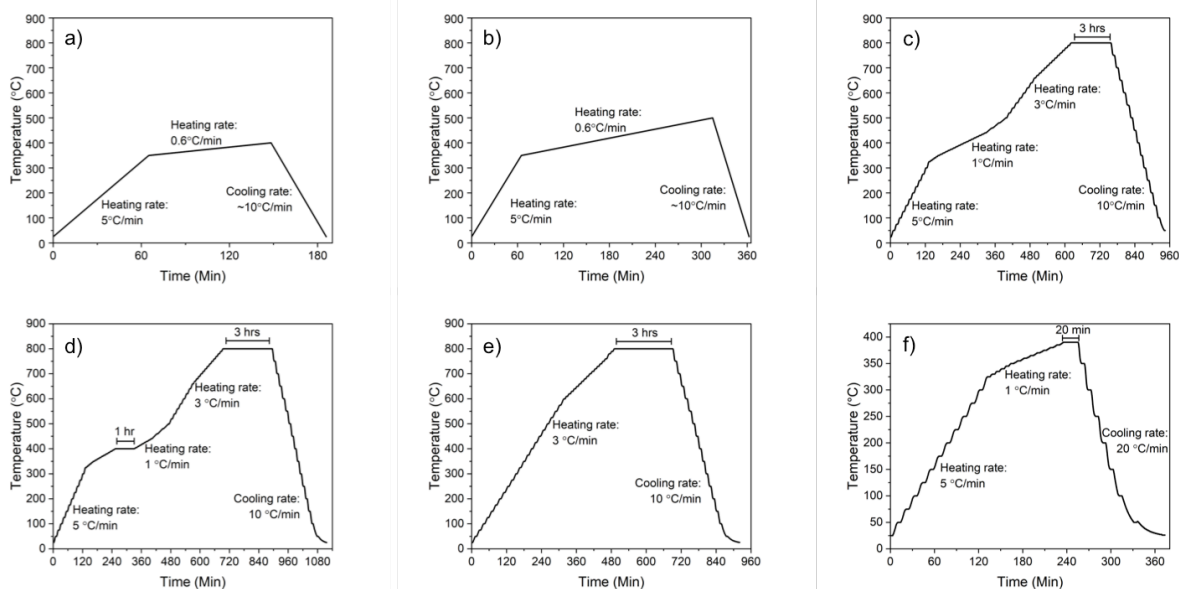


Figure 3.2: Heating profiles used for (a) ex situ ammonolysis with a quench at 400°C, (b) ex situ ammonolysis with a quench at 500°C, (c) standard in situ ammonolysis of MoO₃, (d) extended in situ ammonolysis of MoO₃, (e) in situ ammonolysis of MoO₂, and (f) in situ ammonolysis with a hold and quench at 390°C.

Ex situ XRD data of furnace-prepared samples were collected using a 3kW Cu rotating anode Rigaku Smartlab diffractometer equipped with a Rigaku HyPix3000 X-ray detector operated in 1D mode with a Ni filter to remove K β radiation.

Analysis of the XRD data was performed using GSAS II using CIFs taken from ICSD (MoO₃,⁸³ H_{0.3}MoO₃-I,⁹³ MoO₂,⁹⁴ γ -MoO_xN_y,³⁰ and δ -MoN⁹⁵) for the initial model.⁹⁶ Phase fraction, lattice parameters, and crystallite size were allowed to vary in each Rietveld refinement and spherical harmonic preferred orientation corrections were applied. Atomic positions and thermal displacements were not refined. Chebyshev polynomials with 4-6 terms were used to model the background. The standard reference material LaB₆ was used to determine instrument broadening and these instrument parameters were applied to all patterns.

3.1.3 Transmission Electron Microscopy

The in-situ electron microscopy experiment was carried out using an aberration-corrected JEOL ARM 200CF incorporated with the commercially available atmosphere TEM holder (Protochips Atmosphere gas system). The microscope was operated at 200 kV. Before assembling, the gas cell components were plasma treated for 2 minutes to remove contaminants and render the surface hydrophilic. The top and bottom chips containing the electron beam transparent silicon nitride membrane windows were used to sandwich and isolate the gas environment from the high vacuum column of the microscope. After the two chips were assembled, the spacing was controlled to be around 5 μm . The gas flow and pressure were controlled by the Protochips atmosphere gas system. To minimize concentration gradients in the packed bed, a high ratio of NH_3 flow rate to the amount of powder was maintained. The gas lines were cleaned three times using ultrahigh purity (UHP) Ar gas by pump/purge process prior to reaction. During measurement, a mixture of 10% NH_3 (Airgas, anhydrous) + 90% Ar (Airgas, 99.999%) gas was used. The gas was supplied at 1 sccm with 760 Torr pressure and the sample stage heated at 5° C/min between analysis temperatures, up to a maximum of 800 °C. Differences in NH_3 supply rate to the reacting solid again imply that similarities in trends rather than absolute correspondences between the experiment types are expected. TEM images and selected area electron diffraction patterns (SAED) patterns were collected at various temperatures after allowing the system to equilibrate at each temperature for 1 minute. The sample was exposed to the electron beam only when collecting images and diffraction patterns with an exposure time of 1.0 s, and no changes resulting from the electron beam exposure were detected. Beam induced reduction of MoO_3 is reported to occur at higher electron beam intensity than used here. All in situ results reported here were collected in a single experimental study,

implying all particles were exposed to identical conditions. Ex situ TEM images and SAED patterns were collected using the same aberration-corrected JEOL ARM 200CF microscope again at 200 kV.

3.2 Results and Discussion

3.2.1 Macroscopic Reaction Pathway

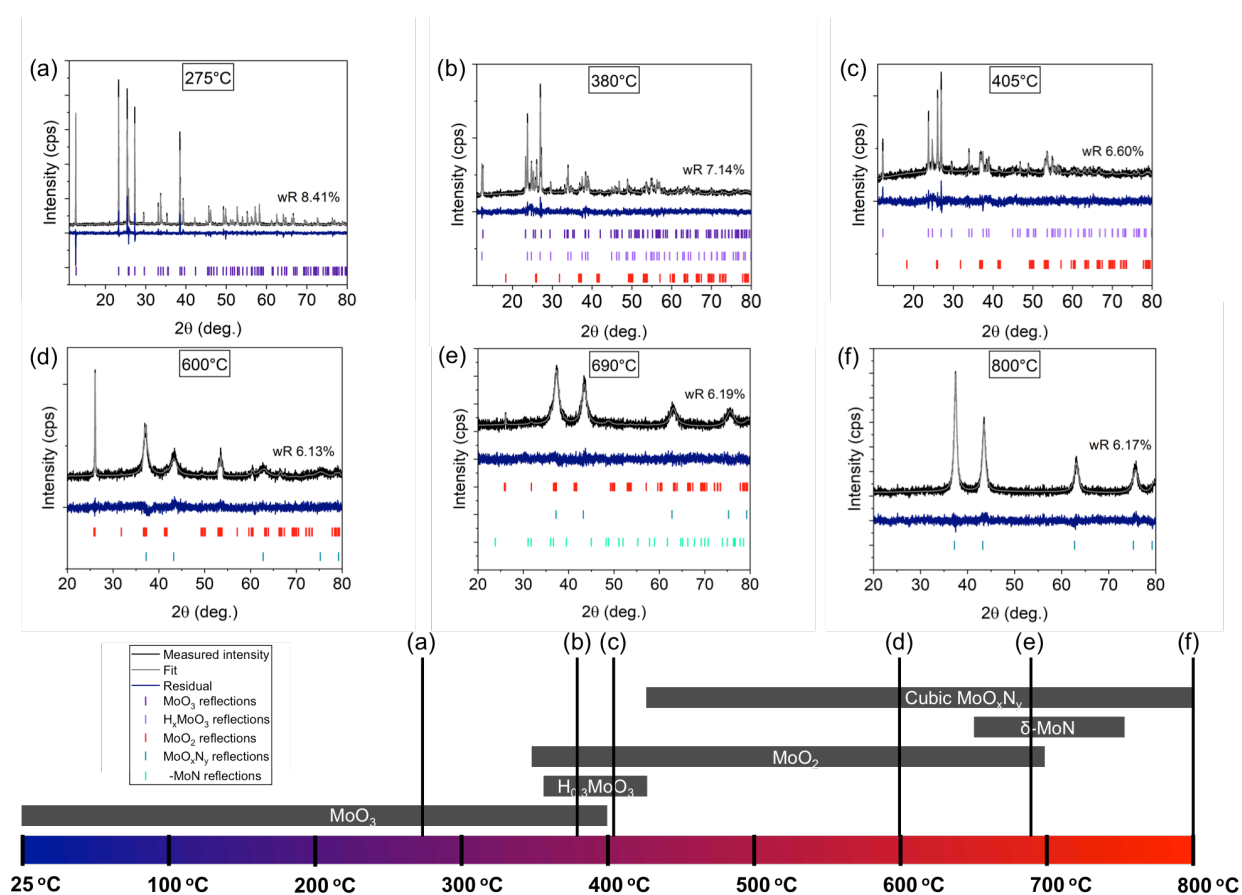


Figure 3.3: Diffraction patterns collected at (a) 275°C, (b) 380°C, (c) 405°C, (d) 600°C, (e) 690°C, and (f) 800°C during the in situ ammonolysis of MoO_3 . The overall reaction pathway displaying the phases present at each selected temperature is located below the diffraction patterns.

Shown in Figure 3.3 are diffraction patterns at select temperatures for in situ ammonolysis of MoO_3 under the standard heating profile, whereas Figure 3.4 contains a

compilation of the results for both heating profiles and for both precursors (MoO_3 and MoO_2) in the form of phase fraction as a function of temperature. Contour maps of the diffraction data are presented in Figure 3.5. In the case of MoO_3 , the experiments revealed the near-simultaneous appearance at 300 – 340°C of the two phases identified in the literature to be the primary reaction intermediates: monoclinic reduced oxide, MoO_2 , with space group $P2_1/c$ ⁹⁴ and an orthorhombic hydrogen molybdenum bronze, $\text{H}_x\text{MoO}_3\text{-I}$ where $x \approx 0.3$, with space group $Cmcm$ ⁹³. Although MoO_3 and the three known H_xMoO_3 phases are structurally similar, the emergence of the $\text{H}_x\text{MoO}_3\text{-I}$ bronze was established by growth of its (020) and (110) peaks at 12.3° and 23.7° 2θ , respectively, which distinguish it from the trioxide and the bronzes with higher hydrogen content.^{93,97,98}

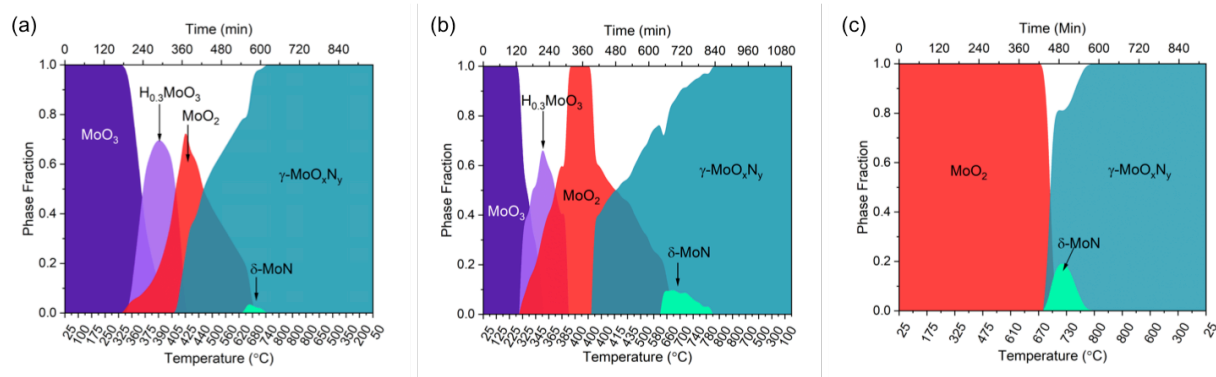


Figure 3.4: Phase fraction as a function of temperature for the in situ ammonolysis of (a) MoO_3 using the standard heating profile, (b) MoO_3 using the extended heating profile, and (c) MoO_2 .

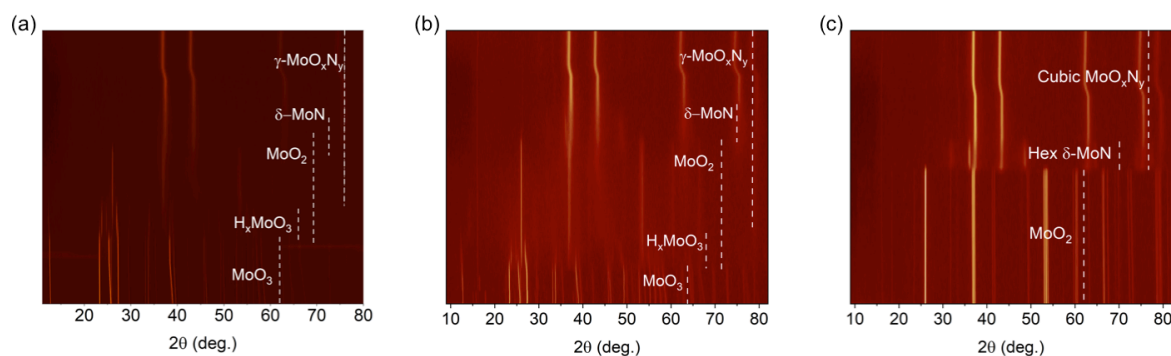


Figure 3.5: Contour maps of the diffraction data compiled into the phase fraction maps in Figure 3.2 for (a) MoO_3 using the standard heating profile, (b) MoO_3 using the extended heating profile, and (c) MoO_2 .

The short-lived H_xMoO_3 -I intermediate formed from MoO_3 was fully consumed by 395 – 435°C; its maximal phase fraction occurred at 335°C under the standard heating profile and at 395°C under the extended profile. The MoO_2 , in contrast, remained a component in the system in both experiments to almost 700°C. Furthermore, the diffraction peaks of this phase were substantially sharper than those of the bronze and the eventual product cubic phase. The persistence of the dioxide is consistent with several prior studies that have shown that complete transformation of this phase by ammonolysis to “ $\gamma\text{-Mo}_2\text{N}$ ” requires temperatures of at least 650 °C.^{20,23,25,34,84} The sharpness of the MoO_2 peaks indicates a high level of crystallinity in this

phase, implying relatively large crystalline domains (0.2-0.4 μm) that are free of large concentrations of defects.

Under the standard heating profile, the $\gamma\text{-MoO}_x\text{N}_y$ phase³⁹ first appeared at 420 °C, becoming the dominant phase at 500 °C; under the extended heating profile this phase appeared during the 400 °C hold, and became the dominant phase at the relatively low temperature of 420 °C. In both experiments, a small amount of a third intermediate phase, the diffraction pattern of which could be matched to that of $\delta\text{-MoN}$ with space group $P6_3mc$,⁹⁵ appeared at a temperature of 640 – 660 °C. Its emergence nearly coincided with the disappearance of MoO_2 . The minor hexagonal and dominant cubic phases co-existed until a temperature of 740 °C under the standard heating profile, and to 790°C under the extended profile, beyond which only cubic $\gamma\text{-MoO}_x\text{N}_y$ remained. At the conclusion of the experiments, the γ'' variant of $\gamma\text{-MoO}_x\text{N}_y$ was detected, with peaks of mixed hkl parity (mixed odd and even indices) showing clear non-zero intensity, consistent with space group $Pm\bar{3}m$ rather than $Fm\bar{3}m$, Figure 3.6. Furthermore, the peaks were broad, indicative of a small crystalline domain size; specifically, 14.6(1) nm was found from Rietveld refinement of the final pattern from the standard heating profile, a value typical of materials produced by ammonolysis of commercial MoO_3 at 800 °C.⁹⁹

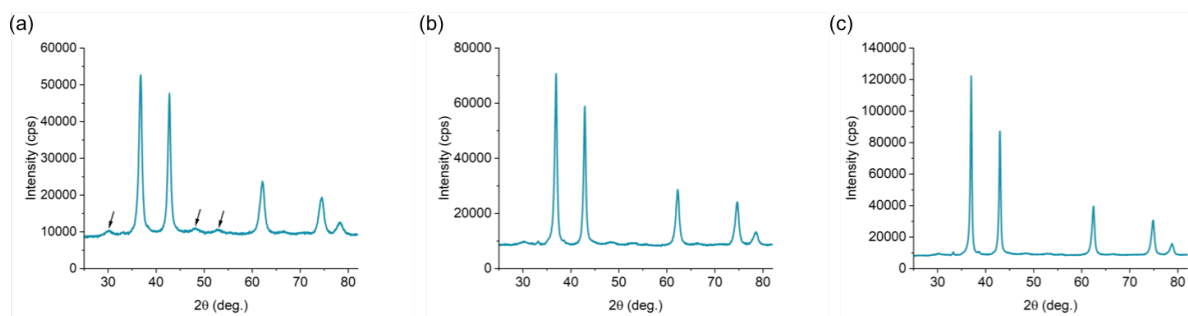


Figure 3.6: γ - MoO_xN_y product of (a) MoO_3 using the standard heating profile, (b) MoO_3 using the extended heating profile, and (c) MoO_2 . The superstructure peaks of the $Pm\bar{3}m$ γ '-variant are indicated with arrows in (a).

Prior to the 400 °C hold in the extended heating profile experiment, the results of the two studies were similar, as would be expected. Differences in the reaction onset temperatures (from MoO_3 to intermediates) and the preponderance profiles of the H_xMoO_3 -I and MoO_2 intermediates during heating to 400 °C are likely due to slight differences in gas flow conditions or initial particle size. In the case of the extended heating profile experiment (Figure 3.2e), complete transformation of the material to MoO_2 occurred immediately upon reaching 400 °C. Formation of γ - MoO_xN_y was then detected after approximately 40 minutes at 400 °C, demonstrating the surprising (partial) transformation of MoO_2 to the desired product at low temperature. Several authors report that intermediate temperature ammonolysis of MoO_3 favors H_xMoO_3 -I formation (justifying literature recipes which apply slow initial heating rates),^{22,24} but no evidence of that was observed here. Despite the emergence of γ - MoO_xN_y at low temperature in the extended heating profile experiment, complete transformation to this phase was delayed compared to the standard heating profile. Here, the competing δ - MoN phase, which grew to be a somewhat larger component of the system along the reaction pathway, was retained as a secondary phase to 780 °C. Irrespective of this delay in attaining phase purity, the results show

conclusively that, contrary to widely held views, MoO_2 can be fully converted to γ - MoO_xN_y by ammonolysis. Furthermore, the competition between the H_xMoO_3 -I and MoO_2 intermediates at low temperatures (in the range from 250 to 400 °C) appears subtle and thus sensitive to small variations in reaction conditions. These slight variations in pathway at low temperature appear to have only small impact on the final product of high temperature (800 °C) ammonolysis of MoO_3 . In both cases, the product is γ '- MoO_xN_y with the extended heating profile resulting in a slightly increased crystalline domain size of 20.1(2) nm, as compared to 14.6(1) nm from the standard heating profile (Figure 3.6).

Ammonolysis of MoO_2 supplied as a precursor (instead of that appearing as an intermediate), Figure 3.4c, occurred by a substantially simpler reaction pathway than ammonolysis of MoO_3 . From the dioxide, the phases γ - MoO_xN_y and δ -MoN appeared simultaneously at 690 °C with the cubic phase being dominant. This low reactivity immediately indicates a difference between the commercial MoO_2 and that obtained as a reaction intermediate. The hexagonal phase disappeared from ammonolysis of the commercial MoO_2 by 800 °C, beyond which only the cubic phase was present (crystalline domain size 31.5(3) nm). Notably, H_xMoO_3 -I did not appear as an intermediate. Elsewhere, we have examined the ammonolysis of phase pure H_xMoO_3 -I⁹⁹ and observed the formation of MoO_2 (but no δ -MoN) as a reaction intermediate. Of further significance is the larger crystalline domain size of the γ - MoO_xN_y obtained by ammonolysis of commercial MoO_2 than ammonolysis of MoO_3 (31.5(3) nm vs 14.6(1) nm, Figure 3.6), despite the appearance of MoO_2 as an intermediate phase in the latter reaction pathway. The difference in final outcome again indicates a difference in the physico-chemical features of the MoO_2 obtained as an intermediate and those of the commercial MoO_2 precursor.

Leveraging the observations of transient phase formation, phase-pure, intermediate MoO_2 was produced for further analysis by application of a prolonged low-temperature hold during in situ ammonolysis. Specifically, after first following the standard heating profile, the sample was maintained at $390\text{ }^\circ\text{C}$ until only MoO_2 was observed in the diffraction pattern (~ 20 minutes) and then quenched to room temperature while still under ammonia flow (heating profile detailed in Figure 3.2f). While the XRD domain size was found to be $65.8(2)$ nm, the BET surface area of this material was found to be $26\text{ m}^2/\text{g}$, far larger than the $1\text{-}2\text{ m}^2/\text{g}$ of the precursor MoO_3 . This high surface area is undoubtedly a significant factor in the higher reactivity of intermediate MoO_2 than the commercial material, which has a surface area of $2\text{ m}^2/\text{g}$, for the formation of the nitride-bearing product. The result, and specifically the combination of high specific surface area with relatively large domain size, further suggests that some, but not all, of the topotactic densification that produces high surface area $\gamma\text{-MoO}_x\text{N}_y$ (with typical surface area of 110 to $170\text{ m}^2/\text{g}^{99}$) and large internal porosity may already occur in the MoO_2 intermediate.

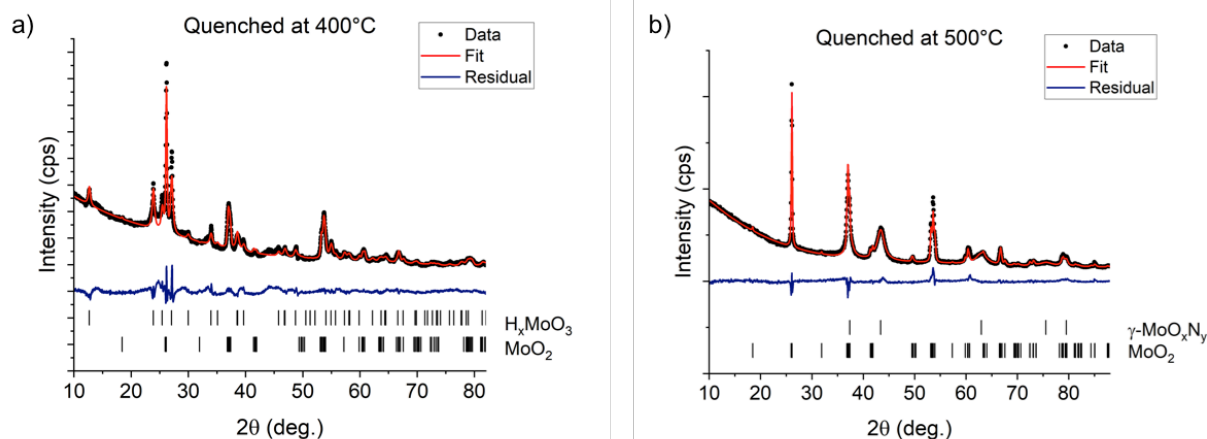


Figure 3.7: Rietveld refinements of the PXRD of samples quenched during the standard ammonolysis of MoO_3 at (a) $400^\circ C$, containing 57% H_xMoO_3 -I and 43% MoO_2 , and (b) $500^\circ C$, containing 53% MoO_2 and 47% $\gamma-MoO_xN_y$.

Further insight was gained from the quenched materials prepared in the tube furnace. Ex situ XRD analysis, Figure 3.7, revealed the sample quenched from $400^\circ C$ to be a mixture of 57% H_xMoO_3 -I and 43% MoO_2 with domain sizes of 27.2(8) nm and 136(6) nm, respectively. This is in general agreement with the in situ studies, in which either a mixture of these two phases or MoO_2 alone was observed at $400^\circ C$. In combination, the in situ and ex situ studies suggest that formation of the bronze is kinetically facile at $400^\circ C$, but that the dioxide is thermodynamically favored. Chemical composition studies by TEM EDX mapping of particles of H_xMoO_3 -I and MoO_2 revealed negligible N signal in either phase (Figure 3.8). The material quenched from $500^\circ C$ was observed to be a mixture of 53% MoO_2 and 47% $\gamma-MoO_xN_y$ phases with domain sizes of 88(3) nm and 5.8(1) nm, respectively, Figure 3.7. The phase assemblage is entirely consistent with the results of the in situ studies, despite a higher overall heating rate in the ex situ experiment and differences in the gas dissociation properties, indicating these factors have only a small impact on the reaction outcome at $500^\circ C$. As discussed below, TEM EDX

mapping revealed the presence of N in particles identified crystallographically as γ - MoO_xN_y in this quenched material.

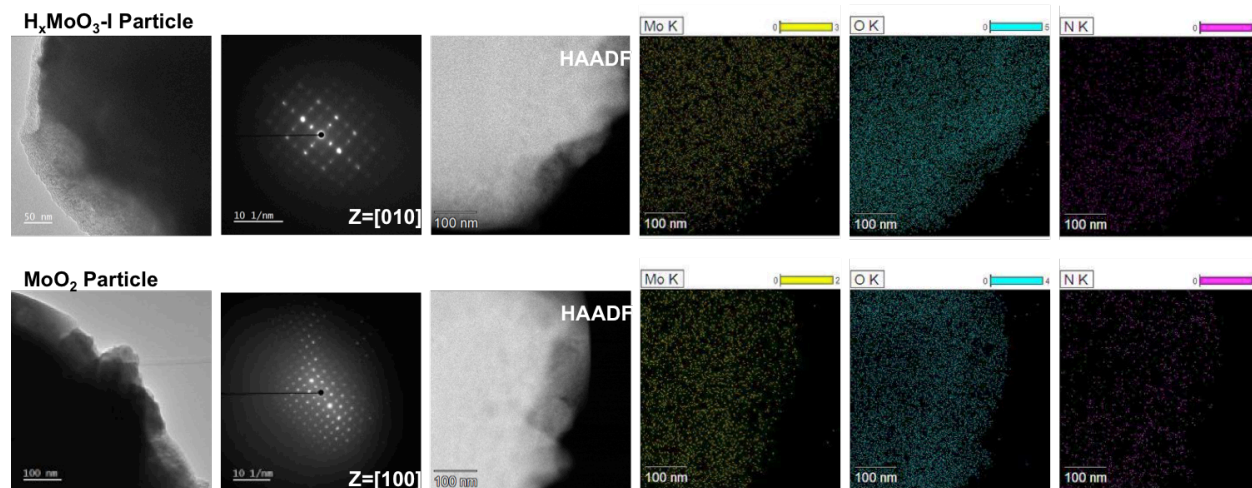


Figure 3.8: TEM EDX of particles of $\text{H}_x\text{MoO}_3\text{-I}$ and MoO_2 from the sample quenched at 400°C , showing negligible N signal in particles of either phase.

Significant conclusions can be drawn about the reaction pathway from the overall phase evolution. First, although MoO_2 requires high temperature for its conversion, ammonolysis of this phase produces γ - MoO_xN_y . Second, the near simultaneous appearance of the MoO_2 and $\text{H}_x\text{MoO}_3\text{-I}$ intermediates implies both are formed directly from the MoO_3 precursor. Furthermore, although the reaction with NH_3 produces these intermediates, nitrogen incorporation into these phases appears negligible. Third, because the amount of MoO_2 increased after the MoO_3 precursor had completely reacted, MoO_2 must be formed from the $\text{H}_x\text{MoO}_3\text{-I}$ intermediate as well as from MoO_3 . This conclusion is supported by the prior observation that even when phase-pure $\text{H}_x\text{MoO}_3\text{-I}$ serves as the precursor, MoO_2 is not avoided.⁹⁹ Furthermore, while the reaction of in situ generated $\text{H}_x\text{MoO}_3\text{-I}$ is not exactly identical to that of $\text{H}_x\text{MoO}_3\text{-I}$ used as a precursor, the results indicate non-reciprocal characteristics of $\text{H}_x\text{MoO}_3\text{-I}$ and MoO_2 as reactants in the formation of γ - MoO_xN_y ($\text{H}_x\text{MoO}_3\text{-I}$ passes through MoO_2 , but not vice versa).

Fourth, although direct transformation from H_xMoO_3 to $\gamma-MoO_xN_y$ cannot be entirely ruled out by these and even the previous experiments, no evidence for such a pathway appears. Indeed, under no conditions was a two-phase mixture of only H_xMoO_3 to $\gamma-MoO_xN_y$ observed, arguing against direct transformation of the bronze to the γ phase. Fifth, there appears to be a correlation between the magnitude of MoO_2 that appears along the reaction pathway and the maximum phase fraction of $\delta-MoN$. It is unclear at this point whether the correlation, which may potentially relate to the undesirability of MoO_2 as an intermediate, extends beyond these three experiments. Notably, both $\delta-MoN$ and MoO_2 eventually transform to $\gamma-MoO_xN_y$; the dioxide is completely consumed in all cases by 660 - 690 °C, whereas the hexagonal phase requires particularly high temperatures for its transformation to the γ phase.

3.2.2 Morphological and Crystallographic Relationships: MoO_3 and $\gamma-MoO_xN_y$

Shown in Figure 3.9 are the crystal morphologies of a representative MoO_3 crystallite **Particle 1** imaged at 25 °C and its ammonolysis product imaged at 800 °C, both under the flow of ammonia. The MoO_3 crystal is oriented at the initiation of the experiment along the [010] zone axis (see the inset in Figure 3.9a). Due to weak Van der Waals force between the double layers parallel to (010) plane, MoO_3 can easily cleave along (010) and hence for a TEM sample prepared by the crushing method, a plate-like habit of MoO_3 with [010] as the normal direction is common. The space-group-forbidden (100) and (001) reflections appear in the pattern because of double diffraction.^{88,100} At the completion of the reaction, the macroscopic shape of the crystal was found to be unchanged. The SAED pattern was found to be square, reflective of cubic $\gamma-MoO_xN_y$ (see the inset in Figure 3.9b). The non-zero intensity of ($h0l$) peaks with $h + l = 2n + 1$

is indicative of space group $Pm\bar{3}m$ rather than $Fm\bar{3}m$ and thus the formation of the γ''

phase. A notable characteristic of the particle is its high level of porosity in combination with its single-crystalline nature. The latter was determined from the identical nature of SAED patterns collected at various positions across the porous particle. While these features of the ammonolysis of MoO_3 have been reported in the previous literature, the example captured here is particularly striking.

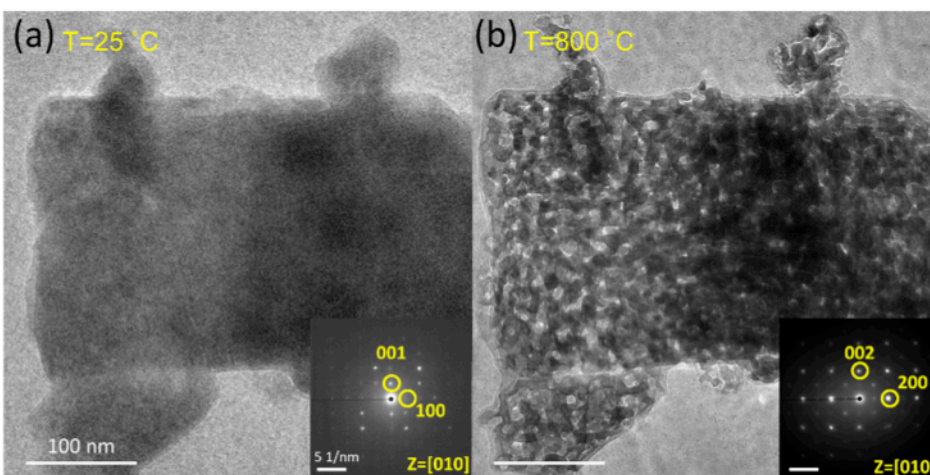


Figure 3.9: Morphology of MoO_3 Particle 1 at the (a) initial and (b) final stage during the ammonolysis. The scale bar is 100 nm. The inserted images are corresponding SAED patterns. The scale bar is 5 $1/\text{nm}$.

Beyond the morphological features, comparison of the crystallographic orientation of the reactant and product phases reveals the relationship $[010]\gamma\text{-MoO}_x\text{N}_y \parallel [010]\text{MoO}_3$, a result that is also consistent with the prior literature. A second MoO_3 particle (**Particle 2**) with similar initial orientation in the beam showed nearly identical behavior both in terms of crystallographic orientation and morphology. The transformation of this particle is discussed in detail below. Examination of a third MoO_3 particle (**Particle 3**) with a different orientation relative to the electron beam revealed $[231]\gamma\text{-MoO}_x\text{N}_y \parallel [211]\text{MoO}_3$, with the macroscopic crystal morphology

similarly retained and a similar, high level of porosity evident in the product phase.

The behavior of this particle is also described further below. The simulated SAED patterns used for establishing these relationships are presented in Figure 3.10.

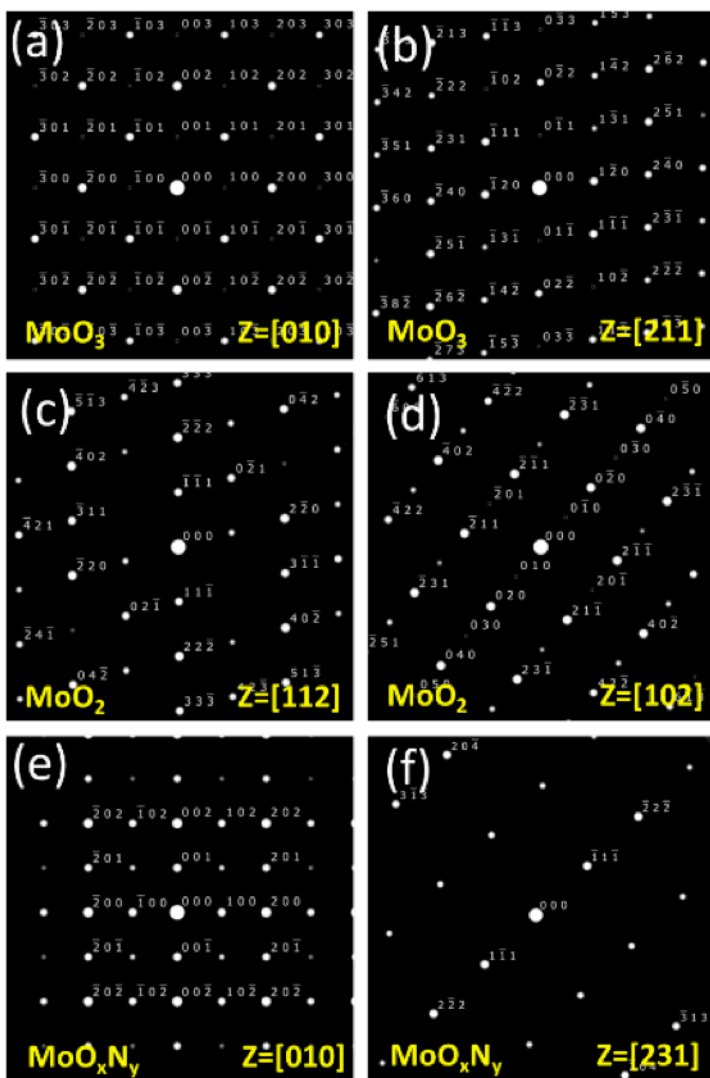


Figure 3.10: Simulated SAED patterns of MoO_3 along (a) $[010]$ and (b) $[211]$ zone axes, MoO_2 along (c) $[112]$ and (d) $[102]$ zone axes and MoO_xN_y along (e) $[010]$ and (f) $[231]$ zone axes.

3.2.3 Microscopic Reaction Pathway

The evolution of MoO₃ crystallite **Particle 2**, initially closely aligned to the [010] zone axis, is presented in Figure 3.11 (large area image shown in Figure 3.12). The corresponding radial intensity profiles, obtained by accumulating the SAED patterns, are presented in Figure 3.13. In broad terms, the MoO₃ crystal (Figure 3.11a) transformed to highly defective bronze H_xMoO₃-I at 250-450°C (Figure 3.11b-d), then to a mixture of γ'-MoO_xN and MoO₂ at 475°C (Figure 3.11e), then to γ'-MoO_xN_y at 600°C (Figure 3.11g), and finally to γ''-MoO_xN_y at 650°C (Figure 3.11h). Significantly, the MoO₂ phase was observed as an intermediate phase in each of the two crystals (**Particle 2** and **Particle 3**) that were tracked. Thus, in agreement with the XRD results, the TEM studies reveal that H_xMoO₃-I does not circumvent MoO₂ as a reaction intermediate, whereas MoO₂ can and does transform directly to γ'-MoO_xN_y. Whether, as suggested by the XRD experiments, MoO₃ can directly transform to MoO₂ under NH₃ (without first passing through the bronze phase) is not resolved by the TEM experiments which are inherently limited to investigation of many orders of magnitude fewer crystals than the macroscopic XRD experiments. Furthermore, slight differences in the XRD and TEM pathways are to be expected given the differences in gas flow dynamics and the action of the electron beam. A particular example of this are the conditions of coexistence of H_xMoO₃-I and MoO₂. While coexistence of these two phases was clearly observed in the XRD studies (Figure 3.3c) and in the material quenched from 400 °C (Figure 3.7), the in situ TEM studies instead suggested coexistence of H_xMoO₃-I and a defective oxide (Figure 3.11b-c) which served as a precursor to MoO₂. Despite such differences, global characteristics are reasonably considered to be similar between the two studies.

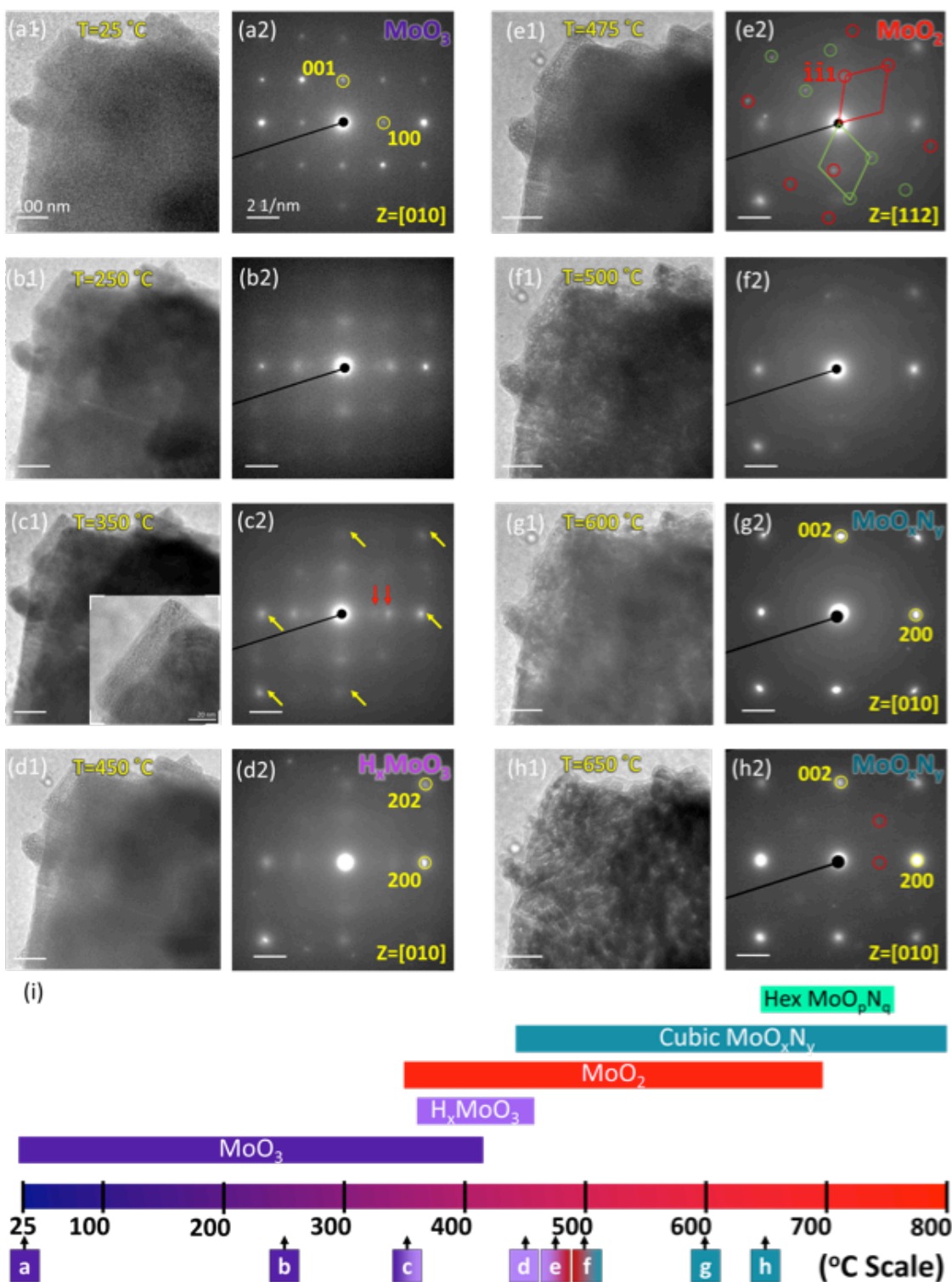


Figure 3.11: Morphology structure changes of MoO_3 Particle 2 during heating under ammonia gas. (a1-h1) TEM images and (a2-h2) SAED patterns of the region of interest at (a-h) 25°C , 250°C , 350°C , 450°C , 475°C , 500°C , 600°C , and 650°C .

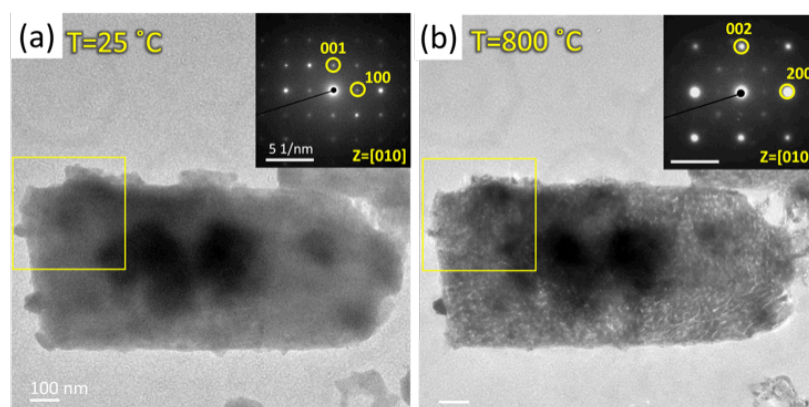


Figure 3.12: Morphology of MoO₃ Particle 2 at the (a) initial and (b) final stage during the ammonolysis. The scale bar is 100 nm. The inserted images are corresponding SAED patterns showing the MoO₃ single crystallite along [010] zone axis became cubic phase along [010] zone axis after the reaction. The scale bar is 5 1/nm.

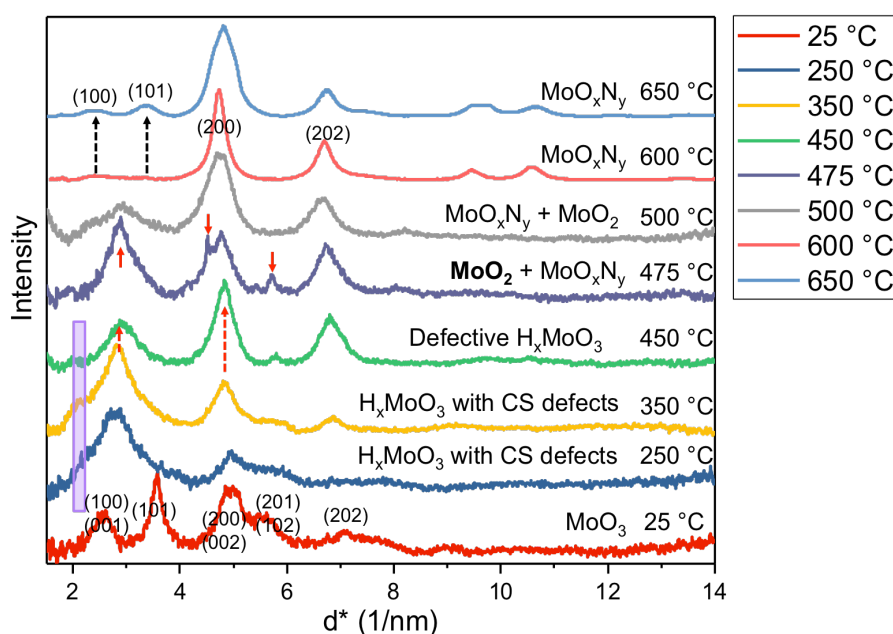


Figure 3.13: Radially accumulated intensity of SAED patterns at different temperatures showing the evolution of structure. Extra peaks were observed starting from 250 °C to 450 °C, as indicated by the purple box. From 350 °C to 450 °C, the spots at halfway are significantly weaker, as indicated by the red dashed arrows. At 475 °C, MoO₂ phase shows up with obvious peaks as indicated by the red solid arrows. Both patterns at 600 °C and 650 °C can be indexed with a cubic structure, but the intensity of spots at halfway (marked by black dashed arrows) are obviously stronger at 650 °C.

With the general reaction sequence established, the morphological and crystallographic changes observed with each of the transformation steps are described in full detail below. The discussion is supplemented using results from the MoO₃ particle (**Particle 3**) with initial orientation along the [211] zone axis and identical sequence of transformations.

3.2.3.1 Transformation Transformation from MoO₃ to Bronze H_xMoO₃-I: 25 to 450 °C

As reflected in the results obtained from **Particle 2** (Figure 3.11), the reaction of MoO₃ to form bronze H_xMoO₃-I is marked by a significant broadening of the diffraction peaks at 250 °C without any change in crystal morphology or porosity, (Figure 3.11b). Accompanying this broadening are distinct changes in the radial intensity profile (Figure 3.13). At 250 °C only the (100) and (200) peaks have significant intensity, whereas the previously intense (101) peak is virtually absent. Furthermore, the (001) peaks shift to larger position in reciprocal space, while also acquiring satellite peaks at smaller d^* . We attribute the changes in peak positions and intensities to the incipient formation of H_xMoO₃-I. The unit cell of the bronze structure of is contracted along a relative to MoO₃, and the (101) peak is forbidden due to the glide plane symmetry and is absent even under double diffraction. In this step, the H₂ formed from the dissociation of NH₃ enters the MoO₃ structure and produces the H_xMoO₃ phase by a topotactic reaction, Figure 3.14.^{24,28,51,98} Proton incorporation in some, but not all, regions of the crystal and a concomitant disruption to the long-range order can explain the peak broadening. The formation of oxygen vacancies may also contribute to the peak broadening. The MoO₃ phase appears to be completely consumed by 250 °C, a somewhat lower reaction temperature than observed by in situ PXRD (Figure 3.4).

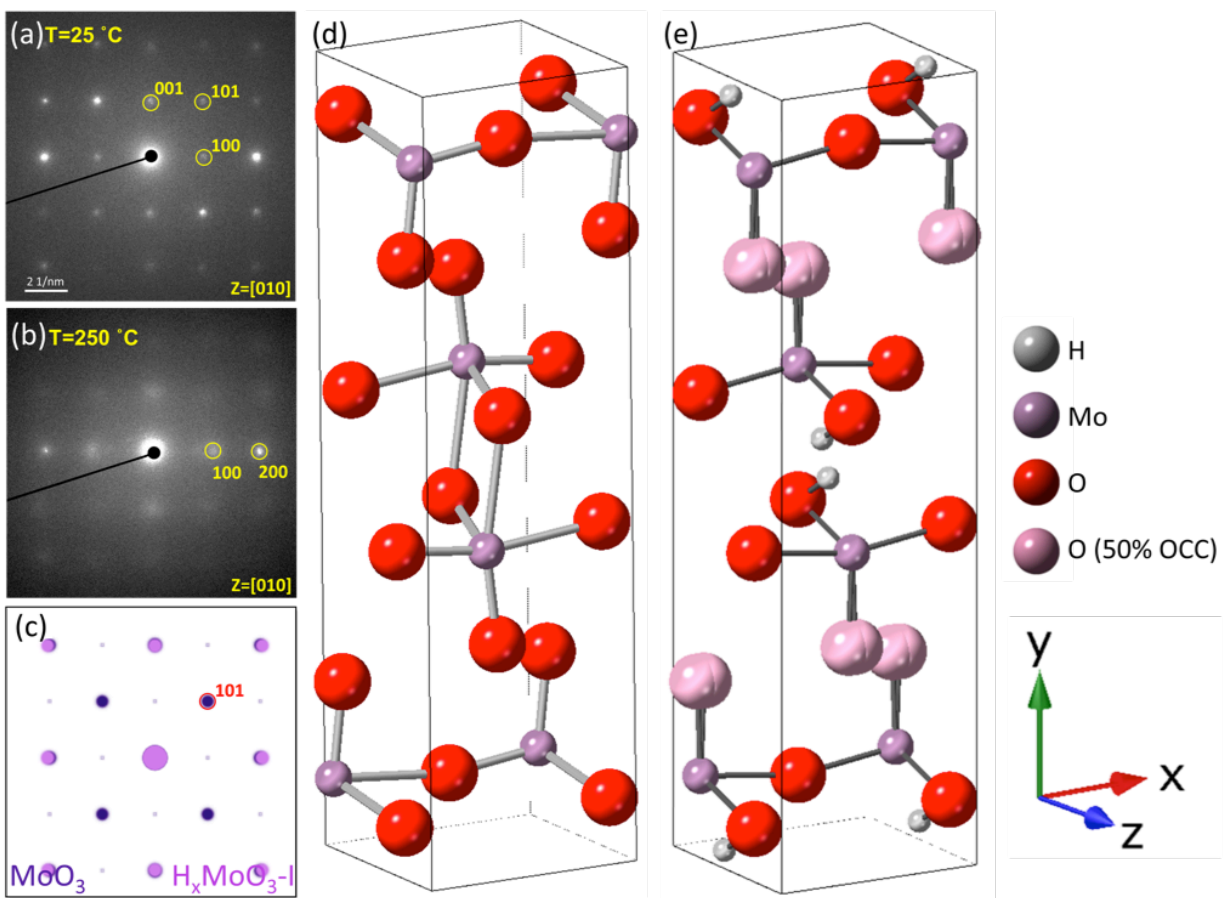


Figure 3.14: Phase transition from MoO₃ to Bronze H_xMoO₃-I. SAED patterns at (a) 25 °C and (b) 250 °C along [010] zone axis. (c) Overlaid simulated SAED patterns of MoO₃ (Purple) and Bronze (Pink). Structure schematic of (d) MoO₃ and (d) Bronze H_xMoO₃-I, where Mo, O and H atoms are represented by purple, red and pink balls.

Between 250 and 350 °C (Figure 3.11c), pores emerge at the surface of the crystal. Simultaneously, the SAED collected at 350 °C shows slight differences in the distribution of intensities from that collected at 250 °C, with the intensities of the second order diffraction spots (i.e., $h = 2n$, $l = 2n$, marked by yellow arrows in Figure 3.11c2) increasing somewhat relative to the first order spots. Furthermore, additional diffraction spots and peak splitting appear at 350 °C, as marked by red arrows in the SAED (Figure 3.11c2). This new intensity is also evident

in the radial intensity profile (Figure 3.13) as a peak at $\sim 2 \text{ nm}^{-1}$. These changes are attributed to the loss of oxygen from the structure, accommodated by the formation of pores and crystallographic shear (CS) defects. Crystallographic shear, which is often revealed by peak splitting in diffraction patterns, is a common occurrence in the reduction of transition metal oxides, serving as an alternative to oxygen vacancy formation.¹⁰¹⁻¹⁰³ In MoO_3 , CS occurs by $[\text{MoO}_6]$ octahedra shearing from corner to edge sharing as oxygen is lost.¹⁰⁰ As edge-sharing octahedra are not a feature of either MoO_3 or $\text{H}_x\text{MoO}_3\text{-I}$, the regions in which CS defects occur can be considered precursors of the MoO_2 phase.

With continued heating to $450 \text{ }^\circ\text{C}$, the intensities of the second order diffraction spots further increase, whereas those of the first order spots decrease (Figure 3.11d2). At this temperature, the crystal appears to be fully $\text{H}_x\text{MoO}_3\text{-I}$, but with defects as evidenced by the breadth of the diffraction peaks and the occurrence of diffraction intensity at $\sim 2 \text{ nm}^{-1}$ and 6.5 nm^{-1} (Figure 3.13). Accompanying this crystallographic change is a very slight increase in porosity between 350 and $450 \text{ }^\circ\text{C}$.

3.2.3.2 Emergence of MoO_2 : $475 \text{ }^\circ\text{C}$

At $475 \text{ }^\circ\text{C}$, sharp peaks emerge in the radial intensity profile at $d^* = 4.61 \text{ nm}^{-1}$ and 5.80 nm^{-1} , while the relatively broad peak at $d^* = 2.9 \text{ nm}^{-1}$ gains substantial intensity (Figure 3.13). Consistent with the observations in the XRD study (Figure 3.3), these changes reflect the appearance of well-crystallized MoO_2 and the growth of the $(0\bar{2}1)$, $(2\bar{2}\bar{2})$, and $(\bar{1}10)$ peaks of this phase. These changes coincide with the loss of diffraction intensity associated with the CS defect at $\sim 2 \text{ nm}^{-1}$, suggesting edge-sharing octahedra are no longer defects but rather the basis of the extended structure at this temperature, as expected for the transformation to MoO_2 . Porosity

slightly increases between 450 and 475 °C, (Figure 3.11d1 vs. Figure 3.11e1) consistent with the relatively high surface area of the single-phase intermediate MoO₂ obtained from the targeted in situ synthesis of that material (26 m²/g). The remaining peaks in the radial intensity profile at 475 °C (Figure 3.13) are attributed to the (200) and (202) peaks of γ-MoO_xN_y.

In the SAED, Figure 3.11e2, two variants of MoO₂ are evident, both of which can be indexed with MoO₂ along the [112] zone axis. Because MoO₂ has nearly identical diffraction patterns along the [112], $\bar{1}11$, and [211] directions (due to the similarity of the polyhedral stacking along these directions), the latter two directions cannot be ruled out as possible zone axis orientations on the basis of Figure 3.11e2 alone. These alternative relationships have been suggested in the prior literature (based on studies of beam-induced⁸⁷ and thermal reduction⁸⁸ of MoO₃). Unambiguous assignment of the crystallographic relationship between MoO₂ and MoO₃ was made possible here by consideration of the features of **Particle 3**, Figure 3.15, in which the initial MoO₃ particle is aligned along the [211] zone axis (Figure 3.15a). At 475 °C the resulting MoO₂ is oriented along [102] (Figure 3.15b). From these images it is evident that the $\bar{1}\bar{1}\bar{3}1$ plane in MoO₃ is preserved in the transition and becomes the (020) plane of MoO₂, and that $\bar{1}11$ of MoO₃ is parallel to $\bar{2}01$ of MoO₂. The simulated SAEDs assuming these relationships match the experimental patterns for the two phases in both particles 2 and 3 (Figure 3.10), justifying the interpretation that the [010] zone axis of MoO₃ becomes the [112] zone axis of MoO₂. In the case of Particle 3, the second MoO₂ variant is not aligned with a zone axis along the beam direction and hence only one variant is observed. The relationship reported by Bertrand et al.,⁸⁶ of $[010]_{\text{MoO}_3} \parallel [100]_{\text{MoO}_2}$ has not been observed here. Regardless of the specific orientational relationship, the increase in porosity from MoO₃ to MoO₂ is consistent with a topotactic

transformation. Furthermore, consistent with the in situ XRD result (Figure 3.4), the bronze phase, which is completely consumed at 475 °C, is not an immediate precursor of γ - MoO_xN_y .

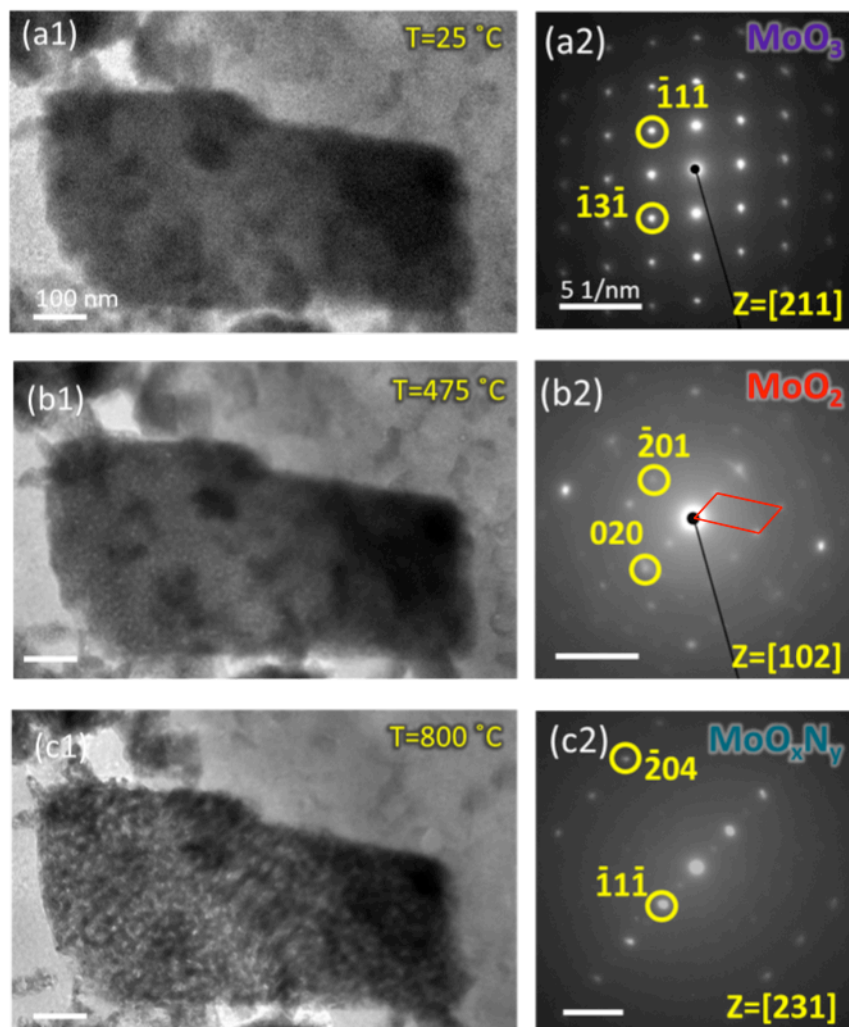


Figure 3.15: The orientation relationship between the intermediate phase MoO_2 with the initial and the final phases. (a1-c1) TEM images and (a2-c2) SAED patterns of Particle 3 at (a-c) 25°C, 475°C and 800°C.

The crystallographic relationship between MoO_2 and γ - MoO_xN_y , implied but not directly evaluated from the in situ studies, was fully confirmed from TEM examination of the sample

quenched from 500°C. As noted, above, this material consisted of a mixture of the dioxide and oxynitride phases (Figure 3.7b). The representative image in Figure 3.16a shows a small particle, outlined in yellow, adjoining a larger, darker particle. As evident from the EDS map, Figure 3.16b, the large particle presents a strong signal from N in addition to Mo and O, and the SAED pattern in this area matches well to that of γ -MoO_xN_y aligned along the [010] zone axis, Figure 3.16f. The SAED pattern of the small particle, Figure 3.16d, matches well to that of MoO₂ aligned along the [112] zone axis. The N signal from this region is relatively weak and plausibly originates from the underlying γ -MoO_xN_y rather than the small particle itself. The SAED pattern obtained from a region encompassing both phases is shown in Figure 3.16g and is represented schematically in Figure 3.16h. As already implied from the SAED patterns of the isolated particles, this pattern reveals the [010] zone axis of γ -MoO_xN_y to be aligned with the [112] zone axis of MoO₂. The high degree of porosity within single crystallites of the cubic γ -MoO_xN_y phase was confirmed by additional imaging studies (Figure 3.17).

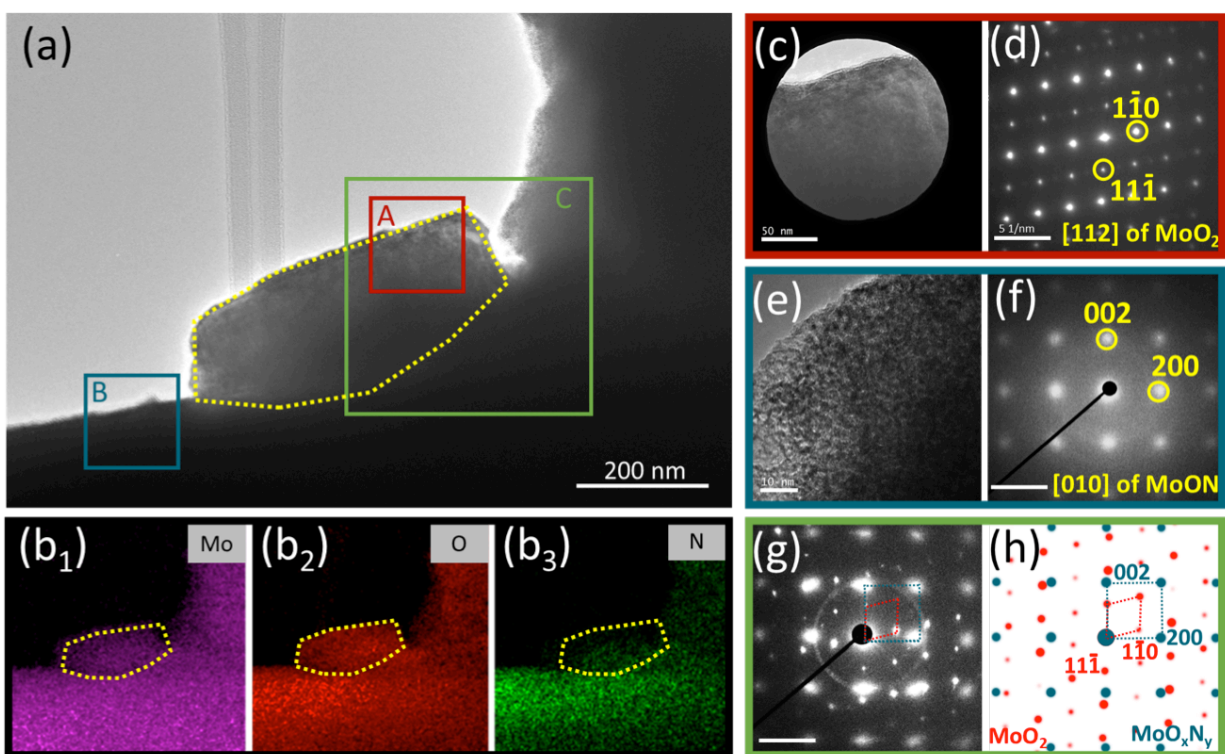


Figure 3.16: Phase transition from MoO₂ to γ -MoO_xN_y. (a) Typical TEM image of a crystal quenched from 500°C. (b) EDS mapping shows the distribution of Mo, O and N. (c) TEM image and (d) SAED pattern from area A, indicating a phase of MoO₂. (e) TEM image and (f) SAED pattern from area B, indicating a phase of γ -MoO_xN_y. (g) experimental and (h) simulated SAED pattern from area C, indicating a mixture of both phases.

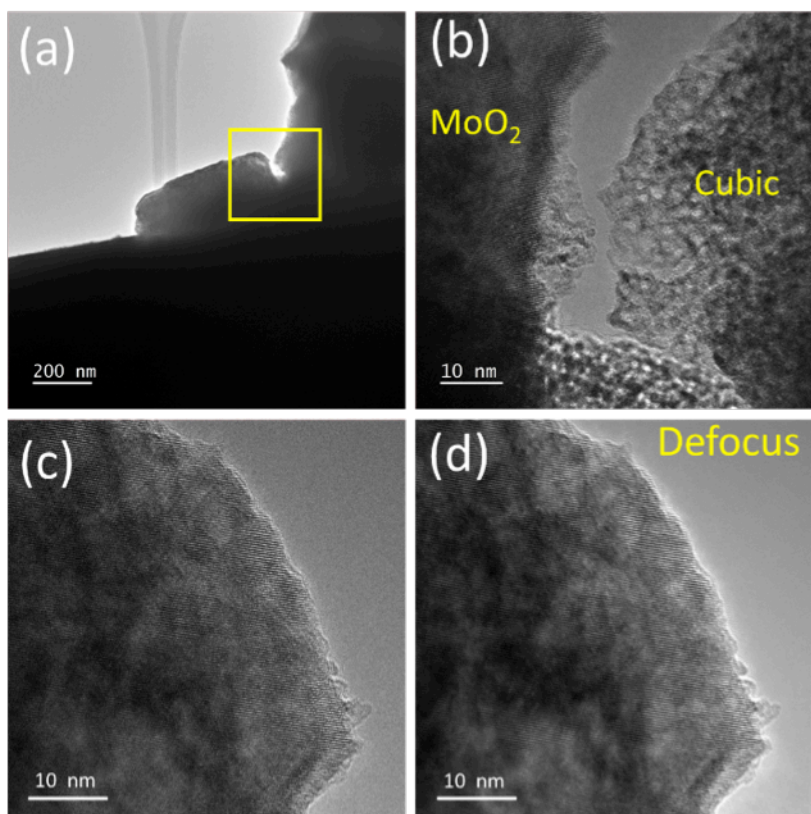


Figure 3.17: (a) TEM image of quenched sample containing a mixture of MoO_2 and $\gamma\text{-MoO}_x\text{N}_y$. (b) High-magnified TEM image of the region marked by box in (a). (c) On focus TEM image and (c) slightly underfocused image of $\gamma\text{-MoO}_x\text{N}_y$ showing a random mosaic of small domains on the platelet. This type of image contrast is caused by density variations in the specimen and is commonly encountered in porous solids.

3.2.3.3 Transformation to Single-Phase $\gamma''\text{-MoO}_x\text{N}_y$: 475 to 650 °C

Upon heating to 500 °C, the diffraction spots due to MoO_2 largely disappear (compare Figure 3.11e2 and 3.11f2), and the radial intensity profile is dominated by diffraction from cubic $\gamma\text{-MoO}_x\text{N}_y$ (Figure 3.13). Thus, the dioxide is rather short-lived as a reaction intermediate in the in situ TEM studies, a contrast to the in situ XRD studies. Between 500°C (Figure 3.11f) and 600°C (Figure 3.11g) the diffraction spots due to $\gamma\text{-MoO}_x\text{N}_y$ sharpened, and the intensity distribution of the spots became more symmetric. The latter results because of closer alignment

of the low index zone axis of the γ -MoO_xN_y crystal with the incident beam. The absence of hkl peaks of mixed parity [e.g., (100) and (101)] in the SAED indicates the phase to be the γ' variant. At 650 °C, new spots marked by red circles appeared in the diffraction pattern (Figure 3.11h), features which are also evident as new peaks in the radial intensity profile Figure 3.13. This reflects a crystallographic transformation to γ'' -MoO_xN_y as a result of high temperature loss of anions and changes of site occupancies. Both the γ' and γ'' phases crystallize in space group $Pm\bar{3}m$, with anion ordering detectable by neutron diffraction. Additional ordering of cation vacancies accompanies high temperature loss of anions in γ'' -MoO_xN_y, rendering the $Pm\bar{3}m$ symmetry of this phase detectable by electron and X-ray diffraction.²⁷ The reduction of Mo in γ'' -MoO_xN_y relative to that in γ' -MoO_xN_y, also discussed previously, is confirmed here from ex situ EELS analysis of the two phases (Figure 3.18). Our previous ex situ studies revealed the γ' and γ'' phases to form from ammonolysis performed at temperatures of 700 and 800 °C, respectively. Again, while precise temperature correspondence between the various synthesis experiments cannot be expected, the present results confirm that γ'' is favored at higher synthesis temperatures.

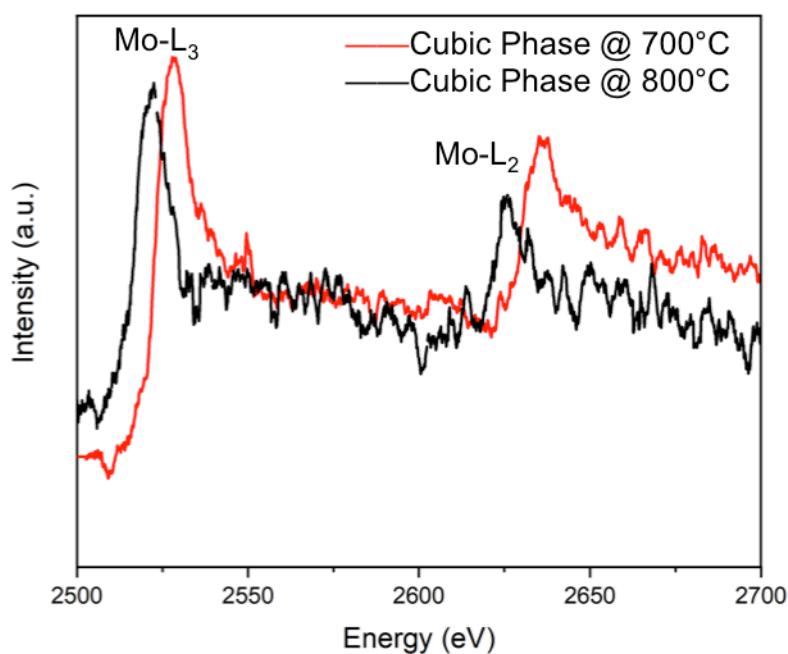


Figure 3.18: EELS of γ -MoO_xN_y synthesized at 700 °C (red) and 800 °C (black).

Concomitant with the crystallographic transformation from MoO₂ to γ -MoO_xN_y, the material undergoes a substantial increase in porosity. Furthermore, while pores are largely restricted to the surfaces of the particles at lower temperatures, at 500 °C and greater, pores emerge at the inner part of the crystal (Figure 3.11f1-4h1) and the overall porosity increases with increasing temperature, consistent with a higher specific surface area of γ -MoO_xN_y than MoO₂. The TEM domain size of ~ 15 nm observed at 800 °C, Figure 3.9, is entirely consistent with the 14.6(1) nm domain size determined by Rietveld refinement (Figure 3.6) of material prepared at this temperature.

3.2.4 Structure Evolution

The combined in-situ and ex-situ TEM data discussed above demonstrate that the phase transitions in the ammonolysis reaction of MoO_3 to form $\gamma\text{-MoO}_x\text{N}_y$ are topotactic at all stages of the reaction. Though there are subtle changes in symmetry upon transformation of MoO_3 to $\text{H}_x\text{MoO}_3\text{-I}$, these two phases can be grossly considered isostructural and the well-established relationship between them is not discussed here. From the orientation relationships of all the observed particles, the overall 3-dimensional orientation relationship among precursor, intermediates, and final products can be summarized as:

$$[010]_{\text{MoO}_3} \parallel [112]_{\text{MoO}_2} \parallel [010]_{\text{MoO}_x\text{N}_y}$$

$$[211]_{\text{MoO}_3} \parallel [102]_{\text{MoO}_2} \parallel [231]_{\text{MoO}_x\text{N}_y}$$

$$(\bar{1}\bar{3}\bar{1})_{\text{MoO}_3} \parallel (\bar{1}\bar{3}\bar{1})_{\text{H}_x\text{MoO}_3} \parallel (020)_{\text{MoO}_2} \parallel (\bar{1}\bar{1}\bar{1})_{\text{MoO}_x\text{N}_y}$$

$$(\bar{1}11)_{\text{MoO}_3} \parallel (\bar{1}11)_{\text{H}_x\text{MoO}_3} \parallel (\bar{2}01)_{\text{MoO}_2} \parallel (\bar{4}14)_{\text{MoO}_x\text{N}_y}$$

The orientation relationship between the MoO_3 , MoO_2 and $\gamma\text{-MoO}_x\text{N}_y$ phases are summarized in the pole figure (Figure 3.19).

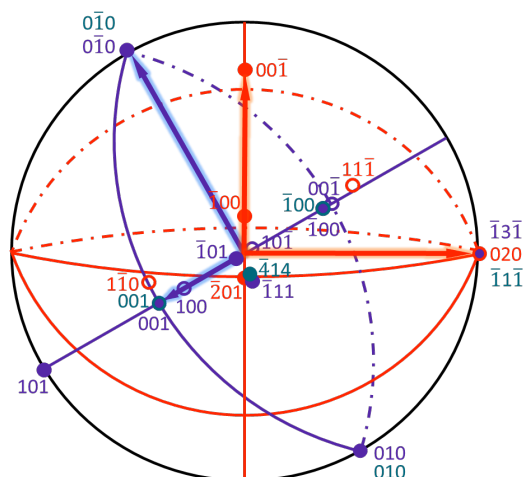


Figure 3.19: Stereogram showing the relationships between the reciprocal lattices of MoO_3 (purple), MoO_2 (red) and Cubic MoO_xN_y (blue). The $(\bar{1}\bar{3}\bar{1})$ of MoO_3 is parallel to the (020) of MoO_2 . The (100) and $(\bar{1}\bar{1}0)$ and $(00\bar{1})$ and $(1\bar{1}\bar{1})$, which were observed in Particle 1, and the

$(\bar{2}01)$ and $(\bar{1}11)$, which were observed in Particle 2, were all consistent with the orientation relationship.

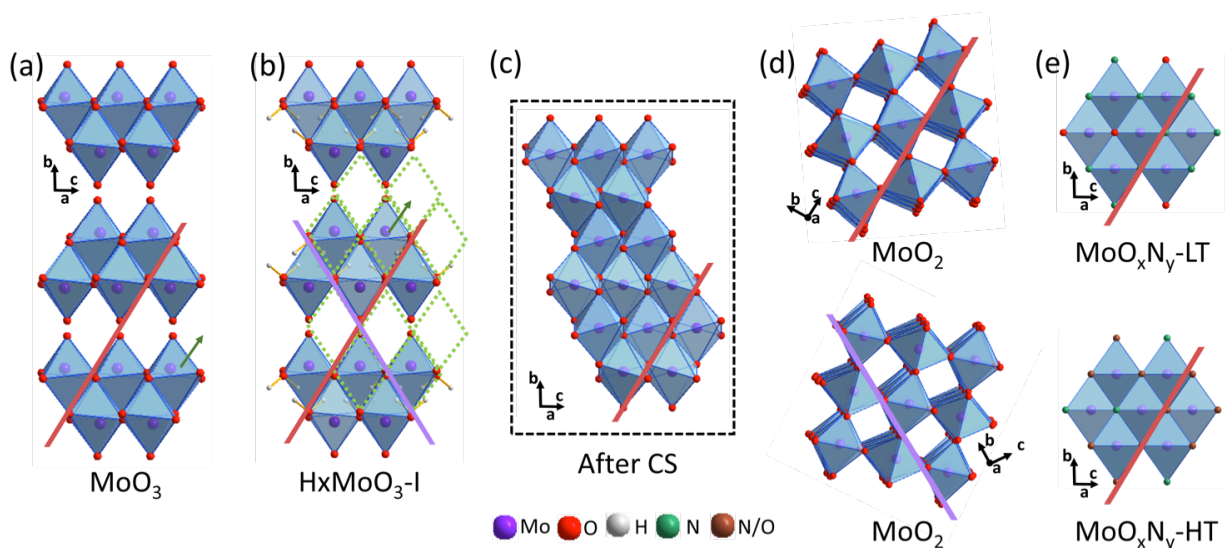


Figure 3.20: Schematic of the structure evolution: (a) layered MoO₃ precursor along the $[1\bar{0}1]$ direction showing the $[\text{MoO}_3]$ sheets built upon distorted edge- and corner-sharing $[\text{MoO}_6]$ octahedra. The layers are stacked along the b axis. (b) Bronze H_xMoO₃ $[1\bar{0}1]$ direction showing intercalated hydrogen atoms bonded with oxygen atoms and off-center interlayer oxygens. (c) After CS MoO₃ loses oxygen atoms and the polyhedra shear from corner sharing to edge sharing to form a more compact transition structure. (d) The rutile-like structure of MoO₂ formed from reorientation of the polyhedra in the transition structure. (e) Cubic γ -MoO_xN_y produced by reconstruction of the MoO₂ polyhedra - at a lower temperature (upper) and with ordered site occupancy at a higher temperature (lower).

Based on the orientation relationship observed from in-situ TEM, we propose the following process for the structure evolution: (1) The reaction begins with the MoO₃ precursor built of double-layers of $[\text{MoO}_6]$ edge- and corner-sharing octahedra (Figure 3.20a). (2) During ammonolysis, hydrogen atoms from NH₃ incorporate into MoO₃ in intra-layer sites and form the bronze H_xMoO₃ (Figure 3.20b). (3) At higher temperature, oxygen vacancies form in the structure as the oxygen atoms between the weakly bonded double layers are lost. The hydrogen intercalation in the structure may assist in the formation of these vacancies as it further attenuates the Van der Waals bonding between the layers.⁹⁸ The accumulation of oxygen vacancies in these

layers causes some corner sharing polyhedra to shear and become edge sharing.

Consequently, through the CS process the double layers collapse along the direction marked by the green arrows in Figure 3.20b. Were the entire structure to undergo CS uniformly, this would result in the formation of an anatase-like structure as all the polyhedra shear to become edge sharing and the Mo:O ratio changes from 1:3 to 1:2 through oxygen loss (Figure 3.20c). With an energy of 0.27 eV/atom above the convex hull (as calculated on OQMD),^{104,105} this is not a stable structure, and it was not observed as an intermediate during the in situ reaction. Nevertheless, there is evidence it formed locally as subsequent areas of the material underwent transition and is useful in formulating an understanding of the reaction process. (4) The phase transition to MoO₂ occurs from the locally sheared transition regions by the change in orientation and in interatomic distances of the [MoO₆] octahedra, as shown in Figure 3.20d. During this transition, the {131} planes of MoO₃ become the {020} planes of MoO₂, as marked by the red planes in Figure 3.20. Although not directly observed here, this type of transition between an anatase-like structure and rutile-like structure has been observed in titanium dioxide with the same inherited planes as in this reaction carried through the transformation.¹⁰⁶⁻¹⁰⁹ Because of the multiple possible shear directions, there are several possible variants of MoO₂ that can form, such as the two shown in Figure 3.20d. As a result, we observed two sets of diffraction patterns from MoO₂ in Figure 3.11e2, which is consistent with twinning of MoO₂ that has also been observed in previous studies.⁸⁸ (5) Finally, the structure changes to cubic with the reconstruction of octahedra (Figure 3.20e). With continued increase in temperature, changes of site occupancy result in ordering of cation and anion species within the cubic structure (Figure 3.20e, lower). In this transition the {020} planes of MoO₂ are inherited and become the {111} planes of γ -MoO_xN_y. Thus, the overall phase transition from MoO₃ through H_xMoO₃ and MoO₂

to γ - MoO_xN_y is topotactic with the $\{131\}$ planes of MoO_3 and $\text{H}_{0.3}\text{MoO}_3$ becoming the $\{020\}$ planes of MoO_2 , and finally the $\{111\}$ planes of the γ - MoO_xN_y product.

3.3 Summary and Conclusions

In this work, the ammonolysis of MoO_3 is investigated via in situ powder X-ray diffraction and in situ transmission electron microscopy. The PXRD shows the macroscopic reaction pathway to consist of the conversion of the MoO_3 precursor to two intermediates, MoO_2 and $\text{H}_x\text{MoO}_3\text{-I}$, at 350°C and 355°C respectively. The $\text{H}_x\text{MoO}_3\text{-I}$ phase was short-lived, fully reacting by 425°C , while the MoO_2 was not fully consumed until 700°C . A transient intermediate identified as δ - MoN was present from 660 - 750°C . The γ - MoO_xN_y first appeared at 420°C and became the sole phase at 750°C when the last of the intermediates was consumed. Two alternate reactions were observed by PXRD to investigate the role of MoO_2 in the ammonolysis reaction: (1) ammonolysis of MoO_3 in which a 1 hour hold at 400°C was introduced, and (2) ammonolysis of MoO_2 as a precursor. In the first reaction, the $\text{H}_x\text{MoO}_3\text{-I}$ intermediate was consumed during the hold at 400°C , leaving only MoO_2 present before the conversion to γ - MoO_xN_y . In the second reaction, the MoO_2 precursor produced γ - MoO_xN_y with δ - MoN as an intermediate. Combined, these reactions show MoO_2 to be a key intermediate in the reaction pathway of the ammonolysis of MoO_3 to produce γ - MoO_xN_y . The in situ TEM showed that the single-crystalline powder MoO_3 produced pseudomorphous single-crystalline powder cubic γ - MoO_xN_y through the formation of the bronze followed by the formation of MoO_2 . This topological transition has the crystallographic relationships $[211]_{\text{MoO}_3} \parallel [211]_{\text{H}_x\text{MoO}_3} \parallel [102]_{\text{MoO}_2} \parallel [231]_{\text{MoO}_x\text{N}_y}$. At the early stage of the reaction, hydrogen atoms from NH_3 incorporate into

MoO₃ and form bronze H_xMoO₃. At higher temperature, oxygen vacancies form because of the weak Van der Waals force double layers, causing some corner sharing polyhedra to shear and become edge sharing. As a result, the double layers collapse and transit to MoO₂. Finally, the structure changes to γ-MoO_xN_y with the reconstruction of octahedra. During the transition, the {131} planes of MoO₃ are inherited and become {020} planes of MoO₂ and finally become {111} planes of γ-MoO_xN_y.

3.4 Chapter 3 Supplementary Information

3.4.1 Methods

Powder X-ray Analysis

Phase fraction and reaction completeness was verified with laboratory powder X-ray diffraction patterns (PXRD) collected over a 2θ range of 20-70° on a Rigaku IV (Ultima) X-ray diffractometer under ambient conditions.

Reactions beginning with MoO₃ precursor: ~0.25 g MoO₃ was placed inside the reactor chamber at ambient temperature, purged with N₂ (Airgas, 99.999%), and subjected to a flow of 100 sccm of NH₃ (Airgas, anhydrous). The material was then treated according to the following thermal profile: heat to 350 °C (5°C/min, no hold), heat to 500°C (1 °C/min, no hold), heat to 800 °C (3°C/min, 3 h hold), and cool to ambient temperature (10°C/min) while still under ammonia flow. XRD measurements were taken every 25°C from room temperature to 325°C, every 5°C from 325°C to 440°C, every 20°C from 440°C to 660°C, every 10°C from 660°C to 800°C, every 10 minutes for the first 30 minutes of the hold at 800°C and every 30 minutes for the remainder of the hold, and every 50°C during cooling. The chamber was purged with N₂ for 30 minutes before exposing sample to air for removal.

Reactions beginning with MoO₂ precursors: ~0.25 g MoO₂ was placed inside the reactor chamber at ambient temperature, purged with N₂ (Airgas, 99.999%), and subjected to a flow of 100 sccm of NH₃ (Airgas, anhydrous). The material was then subjected to the following thermal profile: heat to 350 °C (5°C/min, no hold), heat to 500°C (1 °C/min, no hold), heat to either 700 °C (3°C/min, 3 hr hold), and cool to ambient temperature (10°C/min) while still under ammonia flow. The chamber was purged with N₂ for 30 minutes before exposing sample to air. XRD measurements were taken every 25°C from room temperature to 500°C, every 10°C from 500°C to 700°C, every 10 minutes for the first 30 minutes of the hold at 800°C and every 30 minutes for the remainder of the hold, and every 50°C during cooling.

Electron energy loss spectroscopy (EELS)

Powder products were grounded to a finer powder, sonicated in ethanol, and dropped on ultrathin carbon-coated Cu grids. Conventional transmission electron microscopy (CTEM) images and selected area electron diffraction (SAED) patterns were obtained using a JEOL Grand ARM 300F operated at 300 kV.

Scanning transmission electron microscopy (STEM) and STEM/Electron energy loss spectroscopy (EELS) were acquired at 200 kV using a Cs-corrected JEOL ARM 200CF equipped with Quantum Dual EELS system. Core- and Low-loss EELS were collected using an entrance aperture of 5 mm and energy dispersion of 0.25 eV/channel, which resulted in a 1.5 eV energy resolution. The convergence angle was set to be 20.6mrad and probe size of ~2Å. STEM/EELS datasets were collected using Gatan Microscopy Suite® (GMS). The simultaneous acquisitions from multiple channels were synchronized using Digiscan® system. Final EELS spectra were obtained by averaging the signal across different areas within the sample. Data

analysis was performed with GMS and Origin®. For EELS analysis, core-loss spectra of were aligned using simultaneously acquired low-loss spectrum followed by background subtraction then was performed on both spectra using a power law AE^{-r} in the pre-edge energy window 180-220 eV. The multiple scattering was then removed by Fourier-ratio deconvolution following methods described by Egerton.

This microscope was equipped with a cold field emission gun, dual solid-state detectors (SSDs) and Gatan image filter (GIF) Quantum® system. The camera of GIF system has been updated with a direct counting K2 camera. The convergence angle of the high angle annular dark field (HAADF) and electron energy loss spectrum (EELS) acquisition is 30 mrad. The collection angle of the HAADF imaging and EELS data were 90-370 mrad and <90 mrad respectively.

3.4.2 Macroscopic Reaction Pathway

Table 3.1: Summary of crystallographic properties from the Rietveld refinements at 275°C. The number in parentheses reflects the uncertainty in the final digit(s) of the parameter value. Atomic coordinates were fixed to the values given in the cited references.

MoO ₃	
Phase Fraction	1
Space Group	<i>Pbnm</i>
a	3.97278(5)
b	14.0283(2)
c	3.69518(5)
β (deg.)	90
Reference Structure	

Crystallite size (μm)	1.3(2)
Texture index	1.73
wR	8.41%

Table 3.2: Summary of crystallographic properties from the Rietveld refinements at 380°C. The number in parentheses reflects the uncertainty in the final digit(s) of the parameter value. Atomic coordinates were fixed to the values given in the cited references.

	MoO ₃	H _x MoO ₃	MoO ₂
Phase Fraction	0.258(8)	0.578(7)	0.163(3)
Space Group	<i>Pbnm</i>	<i>Cmcm</i>	<i>P2₁/c</i>
a	3.968(3)	3.8835(2)	5.65(1)
b	14.141(6)	14.4003(6)	4.8474(8)
c	3.746(3)	3.7265(2)	5.63(1)
β (deg.)	90	90	120.90(2)
Reference Structure			
Crystallite size (μm)	0.0159(8)	0.144(3)	0.147(8)
Texture index	1.674(7)	1.100(6)	1.127(6)
wR			7.14%

Table 3.3: Summary of crystallographic properties from the Rietveld refinements at 405°C. The number in parentheses reflects the uncertainty in the final digit(s) of the parameter value. Atomic coordinates were fixed to the values given in the cited references.

	H _x MoO ₃	MoO ₂
Phase Fraction	0.55(2)	0.45(2)
Space Group	<i>Cmcm</i>	<i>P2₁/c</i>
a	3.8828(3)	5.64(1)
b	14.422(1)	4.8570(9)
c	3.7269(3)	5.63(1)
β (deg.)	90	120.94(2)
Reference Structure		
Crystallite size (μm)	0.092(2)	0.085(3)
Texture index	1.227(3)	3.474(6)
wR		6.60%

Table 3.4: Summary of crystallographic properties from the Rietveld refinements at 600°C. The number in parentheses reflects the uncertainty in the final digit(s) of the parameter value. Atomic coordinates were fixed to the values given in the cited references.

	MoO ₂	MoO _x N _y
Phase Fraction	0.297(4)	0.702(4)
Space Group	<i>P2₁/c</i>	<i>Pm3m</i>
a	5.641(7)	4.1848(9)

b	4.8589(6)	
c	5.638(8)	
β (deg.)	120.95(1)	90
Reference Structure		
Crystallite size (μm)	0.116(4)	0.0060(1)
Texture index	1.012(7)	1.032(4)
wR		6.13%

Table 3.5: Summary of crystallographic properties from the Rietveld refinements at 690°C. The number in parentheses reflects the uncertainty in the final digit(s) of the parameter value. Atomic coordinates were fixed to the values given in the cited references.

	MoO ₂	MoO _x N _y	MoN
Phase Fraction	0.025(2)	0.931(6)	0.044(6)
Space Group	<i>P2₁/c</i>	<i>Pm3m</i>	<i>P6₃mc</i>
a	5.32(6)	4.159(8)	5.73(3)
b	4.666(5)		
c	5.78(8)		5.59(2)
β (deg.)	120.7(1)	90	90
Reference Structure			
Crystallite size (μm)	0.10(2)	0.0076(1)	0.0060(1)
Texture index	1	1.031(3)	1
wR			6.19%

Table 3.6: Summary of crystallographic properties from the Rietveld refinements at 800°C. The number in parentheses reflects the uncertainty in the final digit(s) of the parameter value. Atomic coordinates were fixed to the values given in the cited references.

MoO _x N _y	
Phase Fraction	1
Space Group	<i>Pm3m</i>
a	4.1726(2)
b	
c	
β (deg.)	90
Reference Structure	
Crystallite size (μm)	0.0145(1)
Texture index	1.035(3)
wR	6.17%

Chapter 4: Low temperature synthesis of high surface area γ -Mo₂N

The work in this chapter is published in *Inorganic Chemistry* as *Molybdenum Oxide Precursors that Promote the Low-Temperature Formation of High-Surface-Area Cubic Molybdenum (Oxy)nitride* (Elise A. Goldfine, Jill K. Wenderott, Matthew E. Sweers, Shobhit Pandey, Linsey C. Seitz, Michael J. Bedzyk, and Sossina M. Haile).⁹⁹

In light of the importance of surface area for (electro)catalytic applications, substantial effort has been directed to revealing the ammonolysis conditions which favor high surface area in the synthesis of γ -Mo_{1-e}(N_xO_y)H_z.^{20,21,23,25,110} Following the initial studies of Volpe and Boudart,²⁵ several authors have associated high surface area in the γ phase with a topotactic transformation from MoO₃, in which the final and precursor phases bear the relationship $\{100\}\gamma \parallel \{010\}\text{MoO}_3$.^{32,51,85} While there is some disagreement in the literature on the detailed reaction pathway from precursor to product (which can depend on the specifics of the gas flow rate, the heating rate, and the gas flow dynamics in the reaction chamber), Choi et al.²² have argued that transformation via a hydrogen molybdenum bronze intermediate (H_xMoO₃, $x \leq 0.34$) is essential to the topotactic transition and realization of high surface area. These authors have further argued that the formation of this intermediate is favored at low heating rates and high gas flow rates. Transformation via the MoO₂ intermediate, favored at high heating rates and low gas flow rates, is believed to yield lower surface area γ due to an apparent absence of a topotactic pathway from the dioxide. Furthermore, as revealed by both ex situ^{20,25} and in situ³⁴ powder X-ray diffraction (PXRD) studies, as well as thermal analysis under flow of ammonia,^{23,84} MoO₂ does not fully nitride until temperatures at or even well above 650 °C. It can thus be anticipated that synthesis

pathways that minimize or eliminate MoO_2 as an intermediate have the potential to yield high surface area γ phase at reduced reaction temperatures (below $650\text{ }^\circ\text{C}$).

Accordingly, we pursue here high surface area $\gamma\text{-Mo}_{1-c}(\text{N}_x\text{O}_y)\text{H}_z$ by ammonolysis of atypical precursors, specifically, two hydrogen molybdenum bronze compounds, H_xMoO_3 , with distinct structures, and the peroxy molybdate H_2MoO_5 ($\text{MoO}_2(\text{O}_2)\text{H}_2\text{O}$). Three H_xMoO_3 bronze phases have been described in the literature, each corresponding to a distinct range of hydrogen content and with slight differences in structure, though all can be described as derivatives of MoO_3 with intercalated protons: phase I, $x = 0.25\text{-}0.4$; phase II, $x = 0.85\text{-}1.04$; and phase III, $x = 1.55\text{-}1.72$. Previous ammonolysis studies of bronzes ($x = 0.04, 0.13, 0.31, \text{ and } 0.80$) by Jagers et al.²³ indicated that these precursors indeed circumvent the dioxide. However, the resulting specific surface areas were only moderate for the final reaction temperature of $725\text{ }^\circ\text{C}$, between 58 and $66\text{ m}^2/\text{g}$, in those cases where γ was obtained as a phase pure product. The results also revealed a slightly increasing surface area with increasing hydrogen content. Here we employ a phase I bronze ($x \approx 0.3$) and a phase III bronze ($x \approx 1.7$), where studies of the first material enable comparisons to the earlier work and those of the second, previously unexplored material, provide the potential for enhanced surface area as a result of its large hydrogen content. Ammonolysis of the peroxy molybdate, H_2MoO_5 , has been reported by Panda and Kaskel.²⁰ These authors were able to obtain phase-pure γ from this precursor with an impressive specific surface area of $124\text{ m}^2/\text{g}$ following reaction at $650\text{ }^\circ\text{C}$, in comparison to the $105\text{ m}^2/\text{g}$ obtained under similar conditions using MoO_3 as the precursor. Synthesis from the peroxy molybdate hydrate, $\text{H}_2\text{MoO}_5\cdot\text{H}_2\text{O}$, resulted in an even higher specific surface area ($158\text{ m}^2/\text{g}$); however, the product was contaminated with a small amount of MoO_2 . These promising results motivate the present investigation.

Here we employ in situ x-ray powder diffraction (XRD) studies to follow the reaction of the candidate precursors as they transform to $\gamma\text{-Mo}_{1-e}(\text{N}_x\text{O}_y)\text{H}_z$ under flow of ammonia. Contradicting the work of Jagers et al.,²³ we find that the $\text{H}_x\text{MoO}_3\text{-I}$ bronze transforms, in part, to MoO_2 . The dioxide is retained as a component in the phase mixture until 700 °C, at which temperature phase pure $\gamma\text{-Mo}_{1-e}(\text{N}_x\text{O}_y)\text{H}_z$ forms as the final product. In contrast to $\text{H}_x\text{MoO}_3\text{-I}$, both $\text{H}_x\text{MoO}_3\text{-III}$ and H_2MoO_5 follow reaction pathways that bypass MoO_2 . These precursors yield phase-pure and exceptionally high surface-area γ at remarkably low reaction temperatures, well below the previously reported temperature of 650 °C – 480 °C in the case of $\text{H}_x\text{MoO}_3\text{-III}$ and 380 °C for H_2MoO_5 , with surface areas of 206 m²/g and 152 m²/g, respectively. We then evaluate these high surface area products, as well as conventional γ -phase materials prepared by high-temperature ammonolysis of the typical MoO_3 precursor,⁴⁷ as catalysts for the hydrogen evolution reaction (HER).

4.1 Synthesis of precursors and conventional “ $\gamma\text{-Mo}_2\text{N}$ ”

The bronze precursors were prepared by the reduction of MoO_3 by hydrogen liberated from reaction between Zn metal and HCl, following the method described by Glemser et al.^{111–114} The synthesis of H_2MoO_5 was performed by oxidation of MoO_3 using H_2O_2 solution.^{20,115} Complete procedural details for all syntheses are provided in the Supporting Information. Phase formation was confirmed by XRD measurements, Figure 4.1b, and by the colors of the resulting materials, Figure 4.1a: the $\text{H}_x\text{MoO}_3\text{-I}$ was a metallic dark blue, the $\text{H}_x\text{MoO}_3\text{-III}$ a lustrous, dark maroon, and the H_2MoO_5 a bright yellow. The crystal structures were referenced to reported phases in the Inorganic Crystal Structure Database (ICSD, $\text{H}_x\text{MoO}_3\text{-I}$ sg. *Cmcm*,⁹³ $\text{H}_x\text{MoO}_3\text{-III}$ sg. *C2/m*,⁹⁷ and H_2MoO_5 sg. *P2₁/n*¹¹⁶). The hydrogen contents in the bronze materials were not

directly measured. They are approximated as $x = 0.3$ and 1.7 , respectively, on the basis of the diffraction analyses and reported structure changes with hydrogen concentration.^{93,97} Rietveld refinement results and the structures of these phases are presented in Figure 4.2 and Table 4.3. The X-ray photoelectron (XP) spectra about the Mo 3d edge for all precursors (H_2MoO_5 , MoO_3 , $\text{H}_x\text{MoO}_3\text{-I}$, $\text{H}_x\text{MoO}_3\text{-III}$, and for completeness, MoO_2) are presented in Figure 4.3.

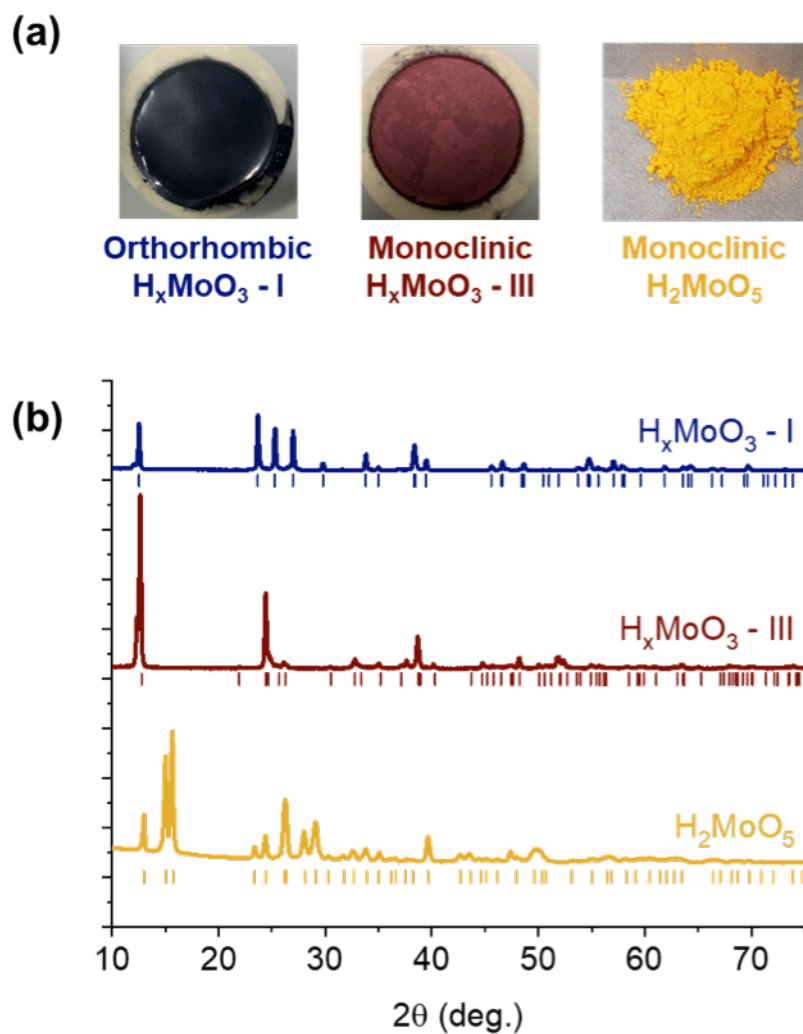


Figure 4.1: (a) Images of as synthesized precursor powders, (b) XRD patterns of the precursors with reflections for the known phases: H_xMoO_3 -phase I sg. $Cmcm$ ($x \approx 0.3$),⁹³ H_xMoO_3 -phase III sg. $C2/m$ ($x \approx 1.7$),⁹⁷ and H_2MoO_5 sg. $P2_1/n$.¹¹⁶

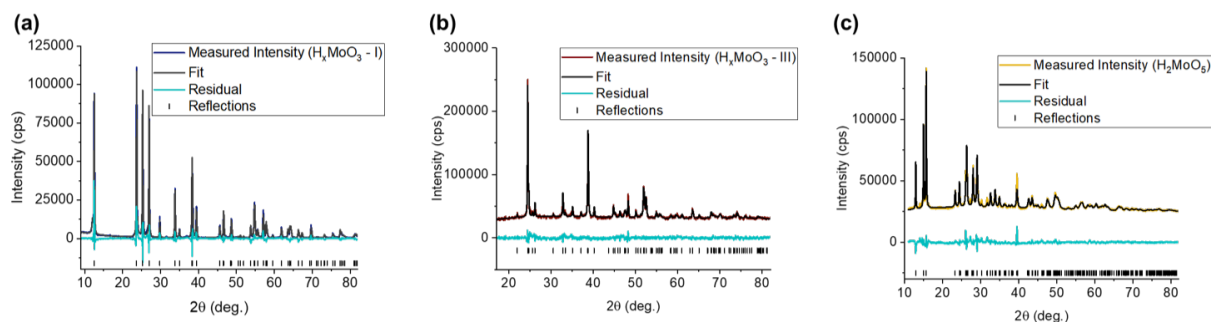


Figure 4.2: XRD and Rietveld refinement results for the precursor materials: (a) H_xMoO₃-I, (b) H_xMoO₃-III, and (c) H₂MoO₅.

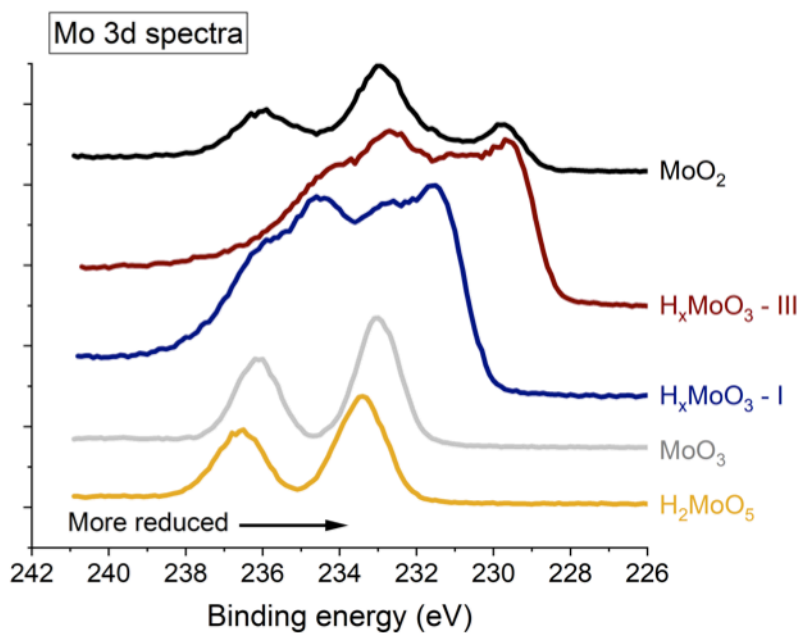


Figure 4.3: X-ray photoelectron emission spectra about the Mo 3d region of the precursors used in this study and of MoO₂. In the case of the reduced materials, MoO₂ and H_xMoO₃ bronzes, two doublets are evident, with the peak at ~ 233.5 eV being a component of both. The doublet at the more oxidized energy values reflects surface oxidation of these materials.

Conventional “ γ -Mo₂N” (recognized here to be described by the complete stoichiometry γ -Mo_{1-e}(N_xO_y)H_z was prepared by ammonolysis of MoO₃ (Supplementary Information)). Using final reaction temperatures of 700 and 800 °C, two types of γ -Mo_{1-e}(N_xO_y)H_z were obtained, hereafter denoted A700-MoO₃ and A800-MoO₃, respectively. As noted elsewhere,⁴⁷ both

materials crystallize in the space group $Pm\bar{3}m$ (in contrast to the conventionally accepted $Fm\bar{3}m$ space group for this phase). In the latter case ($A800-MoO_3$) the loss of translational symmetry characteristic of the $Fm\bar{3}m$ space group can be readily detected by X-ray (or electron) diffraction (Figure 4.4) because it involves vacancy ordering on cation sites, along with N and O ordering on anion sites. In $A700-MoO_3$, N and O ordering and the occurrence of the $Pm\bar{3}m$ space group, which is difficult to observe by X-ray and electron methods, can be detected by neutron diffraction. Thus, these two forms of “ $\gamma-Mo_2N$ ” have slightly different stoichiometries, cell parameters, and specific surface areas,⁴⁷ factors which can be anticipated to influence catalytic function.

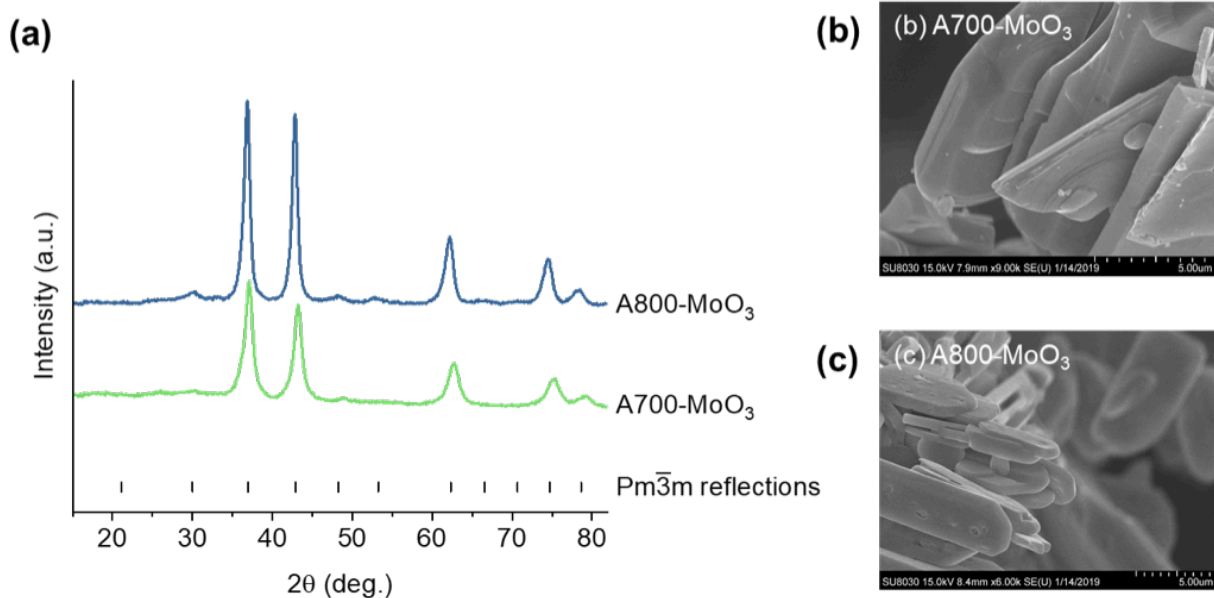
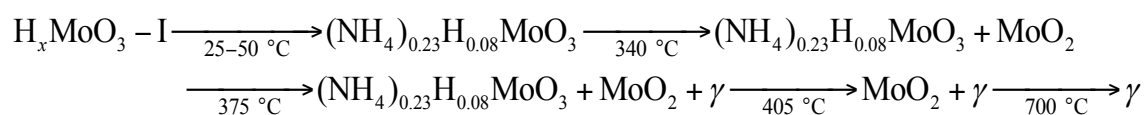


Figure 4.4: (a) XRD patterns and (b,c) SEM images of the (b) $A700-MoO_3$ and (c) $A800-MoO_3$ products. Dashed lines on the XRD plot indicate the reflections of the $Pm\bar{3}m$ space group of both materials.

4.2 Ammonolysis reaction pathways

Shown in Figure 4.5 are the results of the in situ diffraction study of the ammonolysis of H_xMoO_3 -I. Almost immediately upon introduction of ammonia, the precursor reacts to form the intermediate $(NH_4)_{0.23}H_{0.08}MoO_3$, an ammonium hydrogen molybdenum oxide bronze of known crystal structure,¹¹⁷ with MoO_2 appearing at higher temperatures. The overall reaction can be described according to:



The retention of MoO_2 to 700 °C confirms the earlier literature that transformation of the dioxide to “ γ - Mo_2N ” requires high reaction temperatures.^{20,23,25,34,84} Because ammonolysis of H_xMoO_3 -I does not appear to readily provide a synthesis route to the γ phase that circumvents MoO_2 formation, it was not pursued further (additional discussion of the reaction pathway from this bronze is presented in the Supplementary Information).

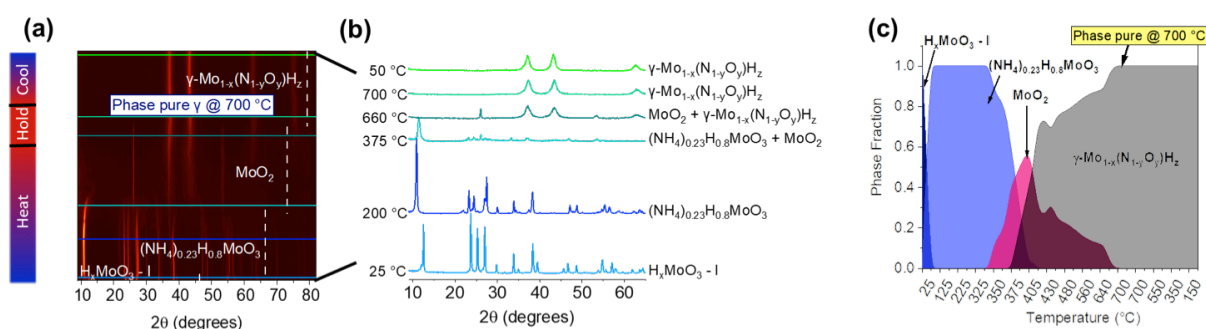


Figure 4.5: (a) In situ PXRD contour plots, (b) selected cut XRD scans, and (c) phase fraction as a function of temperature for the ammonolysis of H_xMoO_3 -phase I. Colored lines on the contour plots (a) correspond to selected XRD scans (b). White dashed lines on contour plots (a) represent phases present during reactions. Observed phases during the reaction are indicated by arrows on the phase fraction plot (c).

The phase evolution trajectories of ammonolysis of H_xMoO_3 -III and H_2MoO_5 are presented, respectively, in Figure 4.6 and Figure 4.7. Significantly, in both cases, the undesired intermediate MoO_2 was avoided. Furthermore, the γ phase appeared at exceptionally low temperatures. From H_xMoO_3 -III γ became the sole phase at 480 °C, whereas from H_2MoO_5 γ was the sole phase at just 380 °C. Thus, precursors and pathways that avoid the MoO_2 intermediate indeed appear to be essential for obtaining $\gamma-Mo_{1-x}(N_xO_y)H_z$ at reduced temperatures.

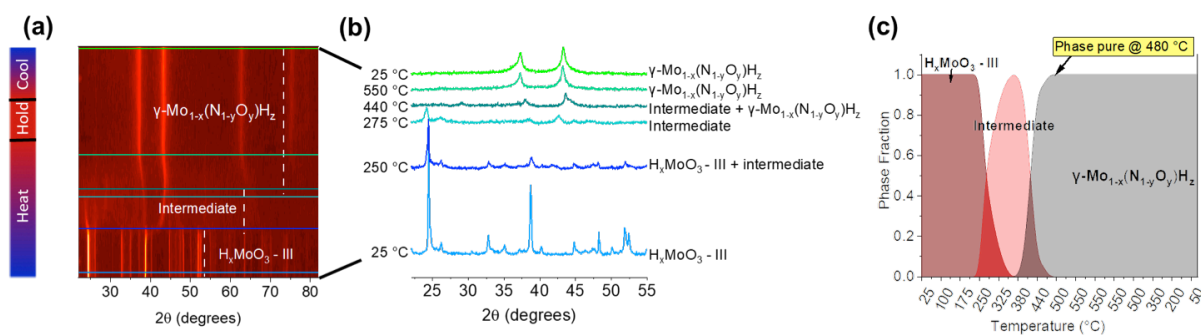


Figure 4.6: (a) In situ PXRD contour plots, (b) selected cut XRD scans, and (c) phase fraction as a function of temperature for the ammonolysis of H_xMoO_3 -phase III. Colored lines on the contour plots (a) correspond to selected XRD scans (b). White dashed lines on contour plots (a) represent phases present during reactions. Observed phases during the reaction are indicated by arrows on the phase fraction plot (c).

Despite the global similarities, the phase evolution pathways from the H_xMoO_3 -III and H_2MoO_5 precursors were markedly different. In the case of H_xMoO_3 -phase III (Figure 4.6), the reaction proceeds according to:



Specifically, the sample remained single-phase H_xMoO_3 -III until 250 °C, beyond which (at 275 °C) a crystalline intermediate appeared and coexisted with H_xMoO_3 -III until 350 °C. Between 360 °C and 380 °C, only this intermediate phase was detected. At 400 °C, the targeted

γ -phase appeared, following which the intermediate was gradually consumed. The conversion to γ was complete at 480 °C. Upon annealing at 550 °C the peaks due to γ - $\text{Mo}_{1-x}(\text{N}_x\text{O}_y)\text{H}_z$ sharpened, indicating an increase in crystallinity and crystallite size. The intermediate could not be indexed to any known phase in the ICSD, but the peaks match most closely to $(\text{NH}_4)_2\text{MoO}_4$ (s.g. $C2/m$).¹¹⁸ This intermediate, as discussed below, was identified clearly in the reaction starting with H_2MoO_5 . The γ - $\text{Mo}_{1-x}(\text{N}_x\text{O}_y)\text{H}_z$ product obtained by ammonolysis of H_xMoO_3 -III at 550 °C is hereafter denoted A550-H-bronze.

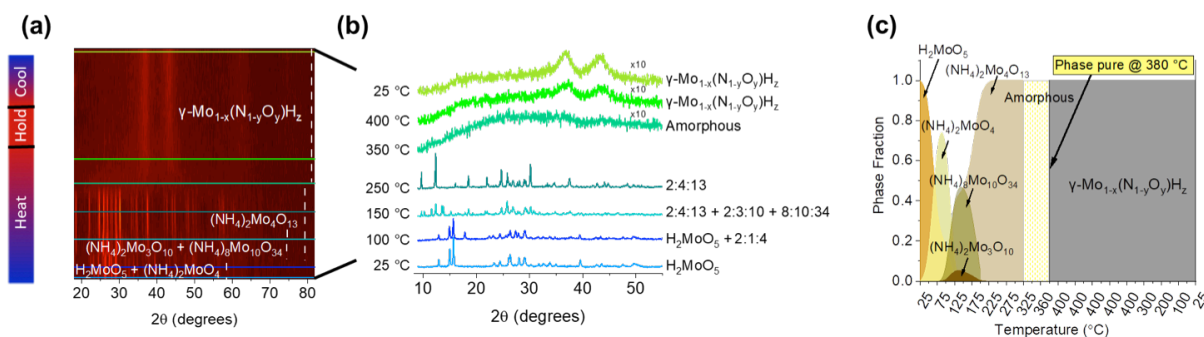
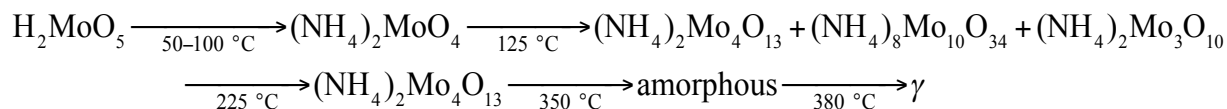


Figure 4.7: (a) In situ PXRD contour plots, (b) selected cut XRD scans, and (c) phase fraction as a function of temperature for the ammonolysis of H_2MoO_5 . Colored lines on the contour plots (a) correspond to selected XRD scans (b). White dashed lines on contour plots (a) represent phases present during reactions. Observed phases during the reaction are indicated by arrows on the phase fraction plot (c).

Ammonolysis proceeded via a more complex pathway when H_2MoO_5 was the precursor (Figure 4.7). The transformation can be generally described according to:



Much like the reaction from H_xMoO_3 -III, the H_2MoO_5 almost immediately incorporated NH_3 (and in this case lost oxygen) to form the ammonium bearing compound, diammonium molybdate, $(\text{NH}_4)_2\text{MoO}_4$.¹¹⁸ Gradual loss of ammonia from this phase upon further heating

generated various other ammonium bearing compounds over the temperature range 125 to 350 °C.^{119–121} At 350 °C a fully amorphous phase formed, which then crystallized to yield the γ phase at an extremely low temperature of 380 °C. Despite a 3 hour anneal at 400 °C, the sample remained less crystallized than A550-H-bronze, likely due to the lower reaction temperature. The γ - $\text{Mo}_{1-e}(\text{N}_x\text{O}_y)\text{H}_z$ product obtained by ammonolysis of H_2MoO_5 at 400 °C is hereafter denoted A400-peroxo.

These reaction pathways suggest an important role for ammonium bearing intermediates for achieving γ - $\text{Mo}_{1-e}(\text{N}_x\text{O}_y)\text{H}_z$ at reduced temperature. In the case of H_xMoO_3 -I, the relevant intermediate has an ammonium:Mo ratio of just 0.23:1, whereas in the cases of H_xMoO_3 -III and H_2MoO_5 , the ratio is much larger, ranging from 0.5:1 to as much as 2:1. We speculate that bulk incorporation of large concentrations of N in the phases along the reaction pathway, despite being in the form of $(\text{NH}_4)^+$ groups, facilitates low temperature formation of γ - $\text{Mo}_{1-e}(\text{N}_x\text{O}_y)\text{H}_z$. Significantly, Jagers et al. have reported that ammonolysis of $(\text{NH}_4)_2\text{MoO}_4$ and of $(\text{NH}_4)_8\text{Mo}_7\text{O}_{24}\cdot 4\text{H}_2\text{O}$ each yields rock-salt type molybdenum oxynitride at temperatures of just 325 °C and 450 °C, respectively, along reaction pathways that ultimately produce hexagonal MoN or a mixture of hexagonal MoN and “ γ - Mo_2N ”, respectively, at 625 °C.²³ While those authors considered the oxynitride to be a distinct phase from Mo_2N , we recognize $\text{MoO}_x\text{N}_{1-x}$, γ - $\text{Mo}_{1-e}(\text{N}_x\text{O}_y)\text{H}_z$, and γ - Mo_2N to all be part of the same phase space. Overall, use of highly nitrogen-enriched oxide precursors thus emerges as a potential strategy for reduced temperature synthesis of γ - $\text{Mo}_{1-e}(\text{N}_x\text{O}_y)\text{H}_z$. Separately, it is noted that while Panda and Kaskel have previously concluded that ammonolysis of H_2MoO_5 likely avoids MoO_2 as an intermediate, these authors have not provided further information regarding the reaction pathway.²⁰

4.3 Chemical and physical features of $\gamma\text{-Mo}_{1-c}(\text{N}_x\text{O}_y)\text{H}_z$ products

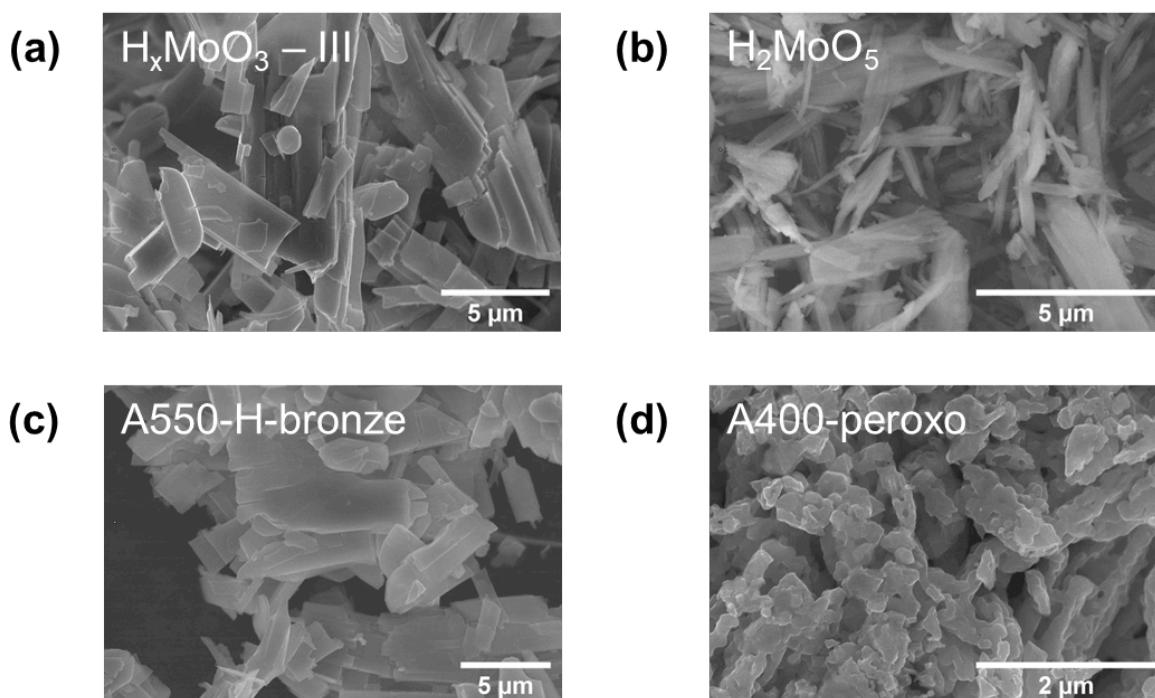


Figure 4.8: SEM images (a,b) pre and (c,d) post ammonolysis of (a,c) $\text{H}_x\text{MoO}_3\text{-III}$ and (b,d) H_2MoO_5 . A550-H-bronze displays a morphology in (c) that is similar to that of the precursor in (a), whereas A400-peroxo displays a morphology in (d) that is smaller and blocky compared to the precursor in (b).

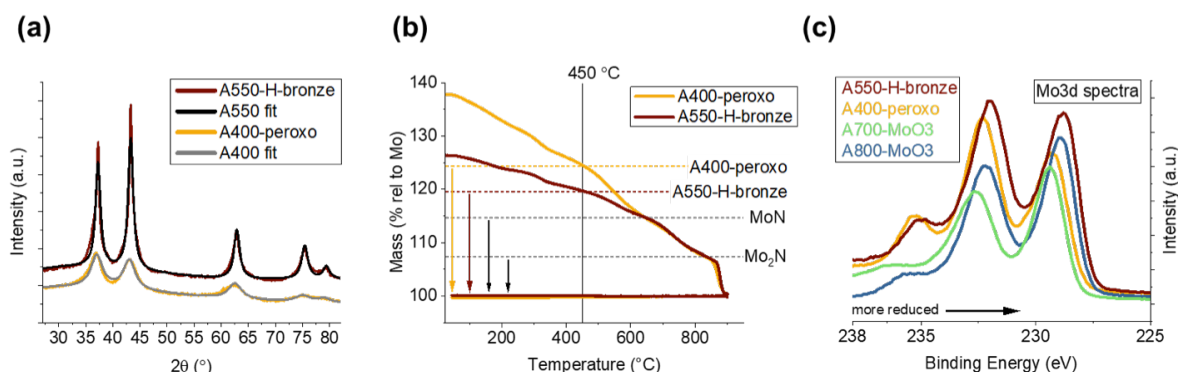


Figure 4.9: (a) XRD patterns of A400-peroxo and A550-H-bronze, (b) thermogravimetric analysis (TGA) of A400-peroxo and A550-H-bronze with dashed reference lines indicating the expected mass losses for compositions MoN and Mo_2N , and the measured mass losses for A400-peroxo and A550-H-bronze (c) x-ray photoelectron spectroscopy (XPS) of the four $\gamma\text{-Mo}_{1-c}(\text{N}_x\text{O}_y)\text{H}_z$ materials: A550-H-bronze, A400-peroxo, A700-MoO₃, and A800-MoO₃. XPS data for the A700-MoO₃, and A800-MoO₃ are taken from our previous work.⁴⁷

The morphological, crystallographic, and chemical features of the γ phase materials obtained from low temperature ammonolysis using the H_xMoO_3 -III and H_2MoO_5 precursors are summarized in Figure 4.8 and Figure 4.9, and their properties are compared in Table 4.1 to those of typical “ γ - Mo_2N ” materials obtained from high temperature ammonolysis of MoO_3 .⁴⁷ For A400-peroxo and A550-H-bronze, the crystallographic results reflect average values over 5 distinct in situ synthesis experiments, for which essentially identical reaction trajectories and final products (Figure 4.10) were observed. Consistent with the avoidance of the MoO_2 phase and the low reaction temperatures, both the A400-peroxo and A550-H-bronze materials have exceptionally high specific surface areas, 152 and 206 m^2/g , respectively, exceeding all other reports of passivated “ γ - Mo_2N ” that could be found in the literature, Figure 4.12. Notably, despite the higher synthesis temperature required for the formation of A550-H-bronze, this material has a higher surface area than A400-peroxo. A comparison of the powder morphologies, before and after ammonolysis (Figure 4.8), reveals that the morphology of the H_xMoO_3 -III precursor is largely retained in the γ product, whereas significant changes are evident when H_2MoO_5 serves as the precursor. This observation suggests that the H_xMoO_3 -III \rightarrow γ - $Mo_{1-e}(N_xO_y)H_z$ transformation is topotactic in nature, similar to that proposed for the formation of high surface area γ - $Mo_{1-e}(N_xO_y)H_z$ from MoO_3 ,^{22,25} whereas the transformation from H_2MoO_5 is not. The occurrence of an amorphous intermediate upon ammonolysis of the peroxo precursor, Figure 4.7, indeed precludes a topotactic process. The product of this amorphous intermediate remains poorly crystalline after the hold at 400 °C, with an effective crystallite size, 3.5(2) nm, smaller than that of A550-H-bronze, despite the lower specific surface area. Analysis of the porosity of the four γ - $Mo_{1-e}(N_xO_y)H_z$ materials shows them to all have similar total pore volumes

of around $0.1 \text{ cm}^3/\text{g}$, with the A400-peroxo having a slightly lower cumulative pore volume of $0.07 \text{ cm}^3/\text{g}$, perhaps due to the lack of a topotactic transformation in the synthesis of that material (Figure 4.11). Despite their overall similar cumulative pore volumes, the two higher temperature materials, A700-MoO₃ and A800-MoO₃, have lower surface areas. Although the total pore volume is the same, A700-MoO₃ and A800-MoO₃ have a higher number of larger pores, with only 67% and 24% of the pore volume due to pores less than 5 nm, respectively. Nearly all the porosity in the A550-H-bronze and A400-peroxo samples, 96% in each case, derives from pores less than 5 nm. This suggests that the nanopores less than 5 nm are the largest contributor to surface area in these materials.

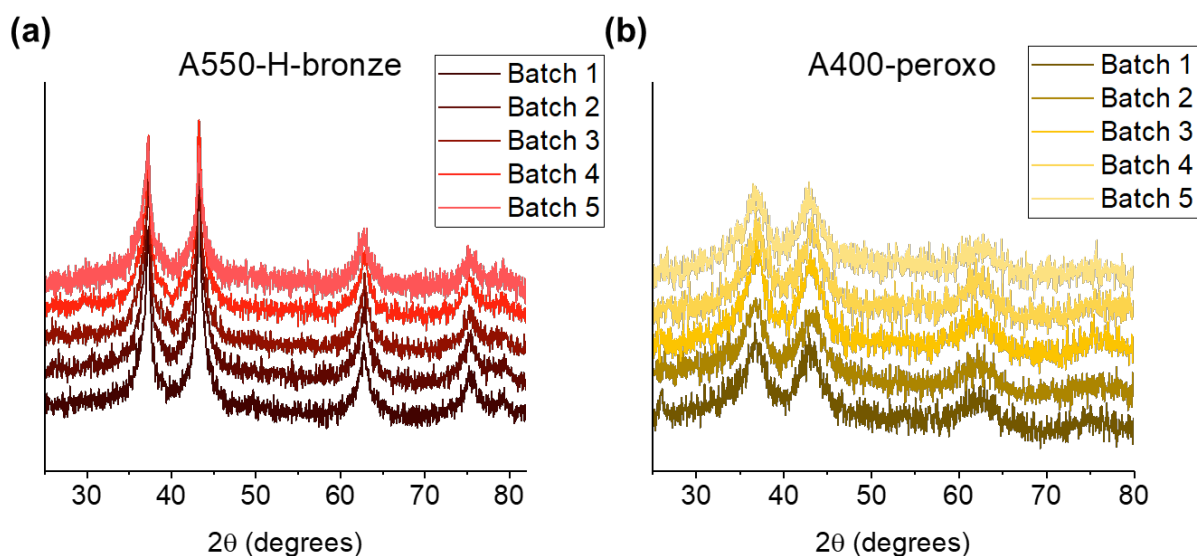


Figure 4.10: Comparison of the XRD of the five batches of (a) A550-H-bronze and (b) A400-peroxo used for ex situ characterization.

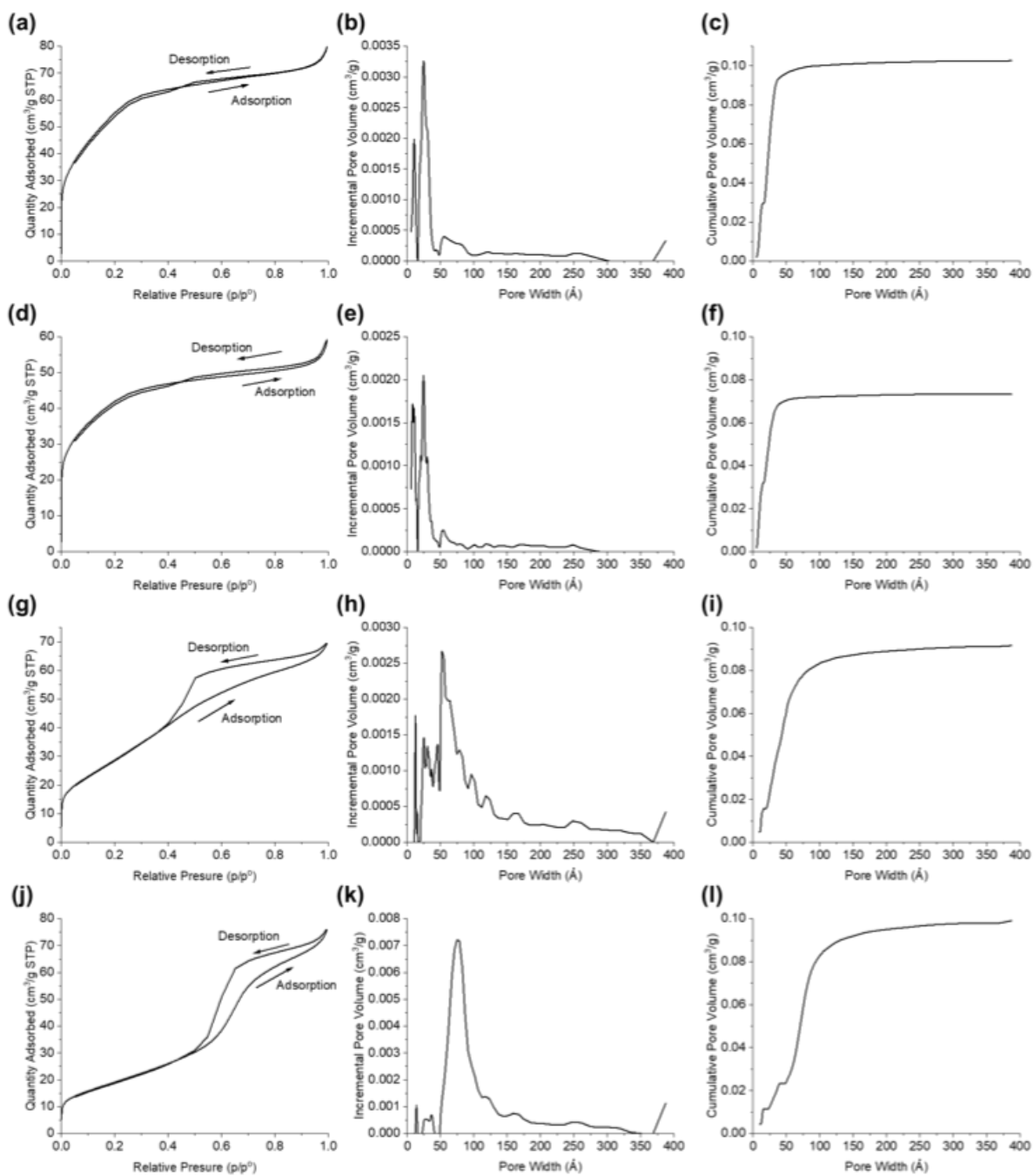


Figure 4.11: Nitrogen adsorption-desorption, pore size distribution, and cumulative pore volume plots for (a)-(c) A550-H-bronze, (d)-(f) A400-peroxo, (g)-(i) A700-MoO₃, and (j)-(l) A800-MoO₃.

The combination of phase formation temperature and specific surface area obtained here for phase pure “ γ -Mo₂N” in the A550-H-bronze and A400-peroxo materials is unique, as evident from the comparison to literature reports provided in Figure 4.12. The only work with specific surface area exceeding the $S_{\text{BET}} = 206 \text{ m}^2/\text{g}$ of A550-H-bronze is that of Volpe and Boudart, who reported a specific surface area of 220-225 m^2/g , but this was prior to passivation.²⁵ As noted, high surface area in “ γ -Mo₂N” has been associated with a topotactic transformation from the precursor phase. When the macroscopic crystallite dimensions are unchanged, the decrease in Mo specific volume from precursor to product is accommodated by the formation of nanoscale porosity and hence high surface area. The literature²² suggests that such a transformation is possible from both MoO₃ and H_xMoO₃ (which each involve a decrease in Mo molar volume of $\sim 65\%$), but not MoO₂ (where the corresponding decrease in volume is 44%). Why these precursors follow different pathways remains unclear. Here we find that H₂MoO₅, which has a decrease of Mo molar volume of 81% from precursor to product due to the high O:Mo molar ratio in the precursor, does not support a topotactic pathway. Nevertheless, this precursor yields a product with specific surface area and nanoporosity rivaling that of materials produced from MoO₃.

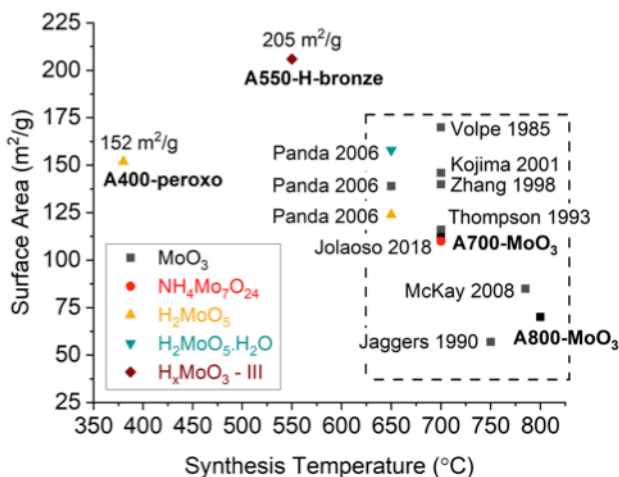


Figure 4.12: Survey of high surface area γ with surface area compared to the synthesis temperature of the material. Results for the typical ammonolysis reaction temperature range of 650-800 °C are indicated by a dashed box.

Beyond the morphological differences, the four γ phases also show chemical differences. When reduced under hydrogen, the thermogravimetric mass-loss profiles (Figure 4.9b) of A400-peroxo and A550-H-bronze indicate a significant portion of the sample mass is due to species other than Mo and establish that these materials, similar to A700-MoO₃ and A800-MoO₃, cannot be described by the stoichiometry Mo₂N. That is, the final product from complete reduction has too little mass for the initial material to correspond to a composition of Mo₂N. This is particularly true of A400-peroxo, which undergoes a mass loss amounting to 38% of the Mo mass over the course of the reduction. For both materials, a portion of the low temperature mass loss is undoubtedly due to desorption of surface species rather than release of volatile species from the bulk. In our earlier study of A700-MoO₃ and A800-MoO₃ materials we showed that bulk loss of anion species from γ -Mo_{1-e}(N_xO_y)H_z initiated at a temperature of 450 to 550 °C.⁴⁷ Based on those studies (carried out under similar conditions to the present work), we take 450 °C

as the approximate temperature at which bulk loss commences from the A400-peroxo and A550-H-bronze materials as well. Assigning the bulk mass loss to equal parts of N and O yields estimates for the bulk atomic ratios of anion to molybdenum species in the respective products of 1.5 and 1.3, implying stoichiometries of $\text{Mo}_{0.67}(\text{ON})$ and $\text{Mo}_{0.77}(\text{ON})$, respectively. Thus, these materials are anion rich, suggesting the presence of cation, rather than anion, vacancies in their structures. High nitrogen contents are also indicated by the combustion analysis (Table 4.1), which further indicates non-trivial hydrogen contents. Along with the compositional differences, the XPS measurements (Figure 4.9c) reveal a variation in Mo oxidation state amongst the product phases (Table 4.1). The spectra show a small peak at higher binding energy (~ 236 eV), particularly evident in A550-H-bronze and A400-peroxo, that is indicative of the presence of a molybdenum oxide on the surface due to passivation and exposure of the materials to air. The main doublet is attributed to the Mo within the bulk of the materials and shows that the oxidation state varies rather substantially across the products, underscoring our previous finding that “ $\gamma\text{-Mo}_2\text{N}$ ” can adopt a range of chemistries.

Table 4.1: Comparison of crystallographic properties, specific surface area, and composition of cubic $\gamma\text{-Mo}_{1-c}(\text{N}_x\text{O}_y)\text{H}_z$ samples produced from varying precursors and synthesis temperatures. The number in parentheses reflects the uncertainty in the final digit(s) of the parameter value. Diffraction analysis and BET measurements of A700-MoO₃ and A800-MoO₃ are from the present work.

	A550-H-bronze	A400-peroxo	A700-MoO ₃	A800-MoO ₃
Precursor	H _x MoO ₃ -III	H ₂ MoO ₅	MoO ₃	MoO ₃
Lattice Parameter (Å)	4.1792(8)	4.190(6)	4.1700(5)	4.2124(3)
Crystallite Size (nm)	8.1(8)	3.5(2)	8.7(1)	13.1(2)
XPS Mo binding energy (eV)	228.8	229.2	229.3 ⁴⁷	228.9 ⁴⁷

BET specific surface area (m ² /g)	206(1)	151.7(5)	111.9(8)	70.3(3)
Cumulative pore volume (cm ³ /g)	0.100	0.073	0.092	0.099
Fraction of pore volume from pores < 5 nm	0.96	0.96	0.67	0.24
Absolute N content, mass % (combustion analysis)	12.0(3)	12.1(3)	11.1(3) ⁴⁷	10.1(3) ⁴⁷
Absolute H content, mass % (combustion analysis)	0.6(3)	0.7(3)	0.8(3) ⁴⁷	0.1(3) ⁴⁷
Atomic anion:Mo (TGA)	≈ 1.3	≈ 1.5	≈ 1.1 ⁴⁷	≈ 0.9 ⁴⁷

4.4 Electrochemical characterization

The activity of the γ -Mo_{1-e}(N_xO_y)H_z materials for the hydrogen evolution reaction (HER) in acidic solution was evaluated in a rotating disk electrode geometry and a 3-electrode cell. Linear sweep voltammograms (LSVs) were recorded between 0.1 and -0.8 V vs. reversible hydrogen electrode (RHE) at 5 mV/s in both the cathodic and anodic directions. To differentiate steady state activity from transient current, chronoamperograms (CAs) were recorded at increasingly cathodic 50 mV intervals until current stabilized or for a maximum of 30 minutes.

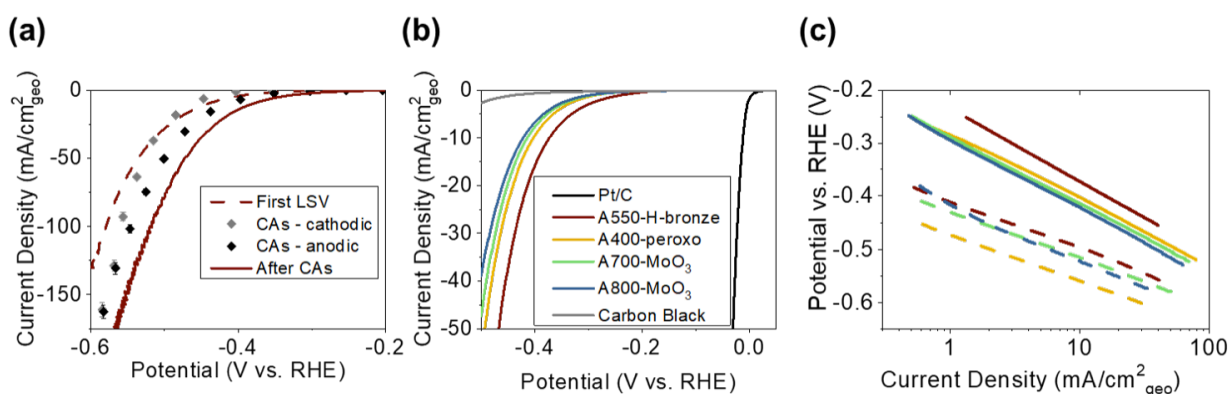


Figure 4.13: (a) LSVs for A550-H-bronze show increased activity over the course of electrochemical measurement. Error bars represent noise at each stable current, largely due to bubble formation. (b) “Activated” anodic LSVs for each sample, compared with electrodes with commercial Pt/C and carbon black. (c) Tafel plot of each sample from initial cathodic LSV

(dashed) and “activated” anodic LSV (solid), with colors corresponding to samples as denoted in the legend of (b).

The initial LSVs of the four distinct $\gamma\text{-Mo}_{1-e}(\text{N}_x\text{O}_y)\text{H}_z$ materials were broadly similar, Table 4.2, with surprisingly little sensitivity to specific surface area. Moreover, the activities of each increased over the course of the measurement, suggesting a transformation at reductive potentials, particularly upon exposure to potential around or more cathodic than -0.5 V vs. RHE. In the initial condition, all the materials revealed relatively low activity for HER. The average overpotentials (measured at $10 \text{ mA/cm}^2_{\text{geo}}$) ranged from 519 to 585 mV (Table 4.2), respectively, as compared to literature values of 350 – 450 mV for “ $\gamma\text{-Mo}_2\text{N}$ ”.^{18,35} However, the Tafel slopes of $\sim 80 \text{ mV/decade}$ were lower than those reported in literature, which range from 100-138 mV/decade, indicative of a more favorable reaction pathway. Initial geometric current densities at -0.4 V vs. RHE (a potential at which bias-induced transformation was avoided) fell between -0.44 and -0.58 mA/cm^2 .

Table 4.2: HER activity metrics, reported as averages, for $\gamma\text{-Mo}_{1-e}(\text{N}_x\text{O}_y)\text{H}_z$ materials from initial cathodic sweep and from anodic sweep following activation (CA at -0.8 V vs. RHE).

Material	Overpotential @ $10 \text{ mA/cm}^2_{\text{geo}}$ (mV)		Current @ -0.4 V vs. RHE ($\text{mA/cm}^2_{\text{geo}}$)		j_0 ($\mu\text{A/cm}^2$)		Tafel slope (mV/decade)	
	initial	activated	initial	activated	initial	activated	initial	activated
A400-peroxo	85	402	0.44	-9.49	0.002	5.9	75	125
A550-H-bronze	519	373	0.53	-15.96	0.014	18.7	85	137
A700-MoO ₃	18	414	-0.47	-7.68	0.010	5.8	86	128
A800-MoO ₃	27	421	-0.58	-6.73	0.038	5.5	92	130

The influence of prolonged exposure to reductive potentials is evident from the representative CA holds of A550-H-bronze at various potential intervals, presented as data points reflecting the stable current for each potential hold (Figure 4.13a); the activity is lower for the cathodic-stepped potential holds than for the subsequent anodic-stepped holds. Accordingly, an “activated” version of each material was also characterized using anodic LSVs after holding the materials at -0.8 V vs RHE until the current stabilized (Figure 4.13b). This activation procedure induced dramatic changes in both the Tafel slope and the exchange current density (Figure 4.13c, Table 4.2) and resulted in activities comparable to the literature values.^{18,35}

The nature of the changes that resulted from exposure to cathodic potential were examined by ex situ XPS measurements. The XPS of the Mo 3d region for A550-H-bronze, the material with the largest change in electrochemical behavior upon activation, reveals both decreased intensity of the high binding-energy peak that corresponds to high oxidation states, and a peak shift toward lower binding-energy for activated samples compared to as-deposited samples (Figure 4.14). While further studies are required to definitively assign the enhanced activity to the changes in Mo oxidation state, we suggest that electrochemical reduction of Mo and in particular removal of surface oxygen may be responsible for the very large increase in activity in $\gamma\text{-Mo}_{1-x}(\text{N}_x\text{O}_y)\text{H}_z$ materials upon activation. Significantly, after activation, the activity, as reflected in the magnitude of the geometric current at -0.4 V, trends with specific surface area (Table 4.2). Thus, in the as-synthesized (and passivated) state, surface oxidation of the A550-H-bronze and A400-peroxo materials (Figure 4.9c) may have blocked access to sites. The bulk Mo oxidation state may also play a role, as it has been shown that HER activity of “ $\gamma\text{-Mo}_2\text{N}$ ” varies with bulk Mo:O:N composition, with more reduced materials of lower O content and higher N content having the highest activity.^{5,30}

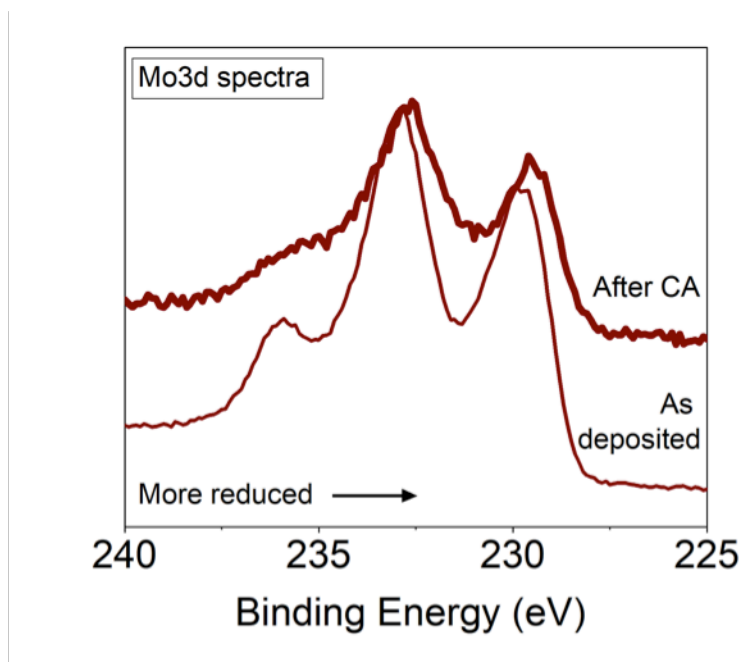


Figure 4.14: XPS of the Mo 3d region of the A550-H-bronze sample before and after stabilizing at -0.8V vs. RHE in chronoamperometry (CA).

4.5 Methods

Ex situ powder X-ray diffraction (PXRD) patterns were collected on either a Rigaku Ultima IV or Rigaku Smartlab diffractometer using Cu $K\alpha$ radiation. Diffraction patterns were collected in $\theta/2\theta$ geometry over the angular range 9° - 82° 2θ with a scan speed of 5° $2\theta/\text{min}$. In situ PXRD experiments were performed using an Anton Paar XRK 900 reactor chamber mounted on a 9kW Cu rotating anode Rigaku Smartlab diffractometer equipped with a D/TEX Ultra 250 1D silicon strip X-ray detector and Ni filter to remove $K\beta$ radiation. Diffraction patterns were collected in $\theta/2\theta$ geometry over the angular range 9° - 82° 2θ with a scan speed of 50° $2\theta/\text{min}$ to minimize dwell time at each temperature. The precursor amount was set at 0.25 g and the gas flow fixed at 100 sccm of ammonia (Airgas, anhydrous) after first purging the

system with N_2 . Presented in Figure 4.15a are the heating profiles corresponding to each precursor synthesis pathway shown in Figure 4.5-4.7. The materials were held at the final reaction temperature for 3 h and then cooled stepwise to 25 °C (10 °C/min between 50 °C steps) while still under ammonia flow. The reproducibility of the synthesis is indicated by the series of unique sample diffraction patterns shown in Figure 4.10. Due to their pyrophoric nature, all samples were passivated before removal from the reaction chamber using a flow of 100 sccm of 1% O_2 /bal. Ar (Airgas) for 1 hour. All A550-H-bronze and A400-peroxo samples of γ - $Mo_{1-e}(N_xO_y)H_z$ used in subsequent studies were synthesized in this manner. The A700- MoO_3 and A800- MoO_3 , in contrast, were synthesized in a conventional tube furnace using the heating profiles shown in Figure 4.15b. In this case, the Ar purge at ambient temperature before sample removal provided sufficient oxygen for surface passivation.

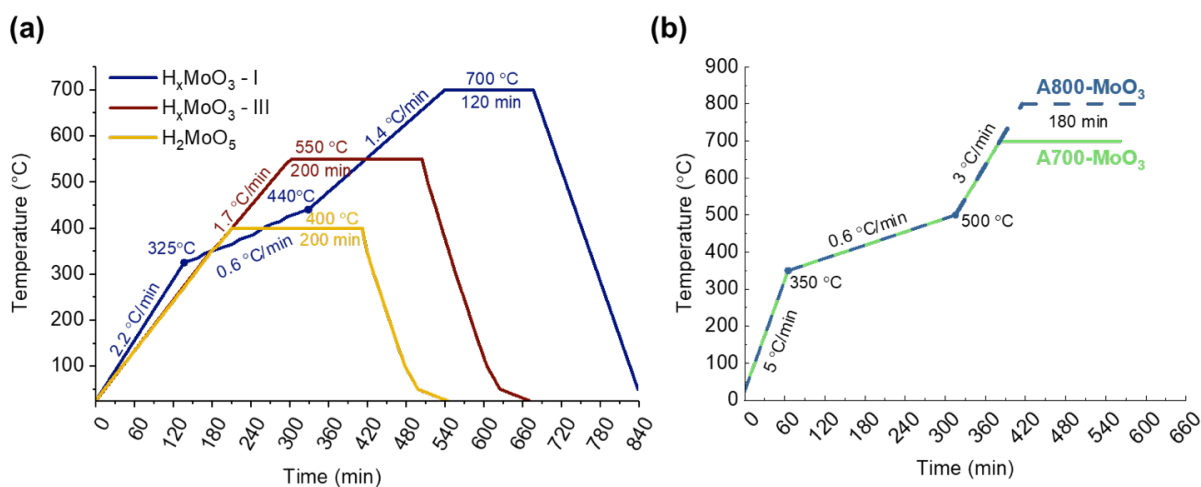


Figure 4.15: Heating protocols used for the preparation of γ - $Mo_{1-e}(N_xO_y)H_z$ from the indicated precursors using (a) an Anton Paar XRK 900 reactor chamber in conjunction with the collection of diffraction patterns, and (b) a horizontal tube furnace.

Analysis of the XRD data was performed using GSAS II.⁹⁶ Phase fraction, lattice parameters, and crystallite size were allowed to vary in each Rietveld refinement and spherical harmonic preferred orientation corrections were applied. Atomic positions and thermal

displacements were not refined. Chebyshev polynomials with 4-6 terms were used to model the background. The standard reference material LaB₆ was used to determine instrument broadening and these instrument parameters were applied to all patterns.

Sample morphology was studied by scanning electron microscopy (SEM) in secondary electron imaging mode using a Hitachi SU8030 equipped with a cold field-emission source operating at 15 kV and 10 μ A. X-ray photoelectron (XPS) spectroscopy was performed using a Thermo Scientific ESCALAB 250Xi instrument equipped with an aluminum anode (Al K α =1486.6 eV) source and an electron flood gun. Samples were prepared by placing powder on copper tape. Charging effects were corrected by referencing the adventitious carbon C1s binding energy at 284.8 eV. Brunauer–Emmett–Teller (BET) surface areas were determined from nitrogen physisorption isotherms measured at liquid nitrogen temperature using a Micromeritics 3Flex instrument. Data were analyzed using the MicroActiv software package.

Chemical analyses of final oxynitride products were performed using a combination of thermogravimetric analysis (TGA) and combustion analysis. TGA measurements (Netzsch STA F3) were used to determine the Mo content (mass %) upon complete reduction under 3 % H₂ (balance Ar) at 900 °C (2 °C/min, 3 h hold). 50 mg to 75 mg of ground powder was used in each experiment. Laboratory XRD (not shown) was used to confirm retention of only Mo metal after the complete reduction experiment. Microchemical combustion analysis was performed at Midwest Microlabs, to determine the nitrogen and hydrogen mass percentages. Samples were combusted at 1000 °C under ultra-pure oxygen and the effluent stream was evaluated in doublet measurements. Significant challenges in chemical analysis of these materials by these methods arise from the presence of unknown quantities of surface species (H₂O, O₂, N₂, NH₃), which

contribute to both mass loss and combustion analysis. Furthermore, Mo and N peaks overlap in the XP spectra, limiting the effectiveness of XPS for determining chemical composition.

Catalyst inks were prepared for each sample by combining equal masses of catalyst and carbon black (Vulcan XC 72), approximately 2 mg each, with 800 μL Milli-Q water, 150 μL ethanol, and 50 μL Nafion 117. The carbon black was ground with a mortar and pestle and the inks were sonicated for 30 minutes to ensure dispersion of the solids. Electrodes were prepared by dropcasting 5 μL of ink onto polished glassy carbon disks and left to dry overnight. Resulting catalyst loadings on the glassy carbon disks were 9.5 μg for A400-peroxo and A550-H-bronze, and 10.0 μg for A700-MoO₃ and A800-MoO₃.

Electrochemical measurements were performed via rotating disk electrode (RDE, Pine Research Instrumentation) in N₂-purged 0.5 M H₂SO₄ electrolyte using a 3-electrode cell, with Ag/AgCl (4 M KCl) and a graphite rod as reference and counter electrodes, respectively. Open circuit potential was measured until stable (~5 minutes). Activity was determined via linear sweep voltammograms (LSVs) between 0.1 and -0.8 V vs. reversible hydrogen electrode (RHE) at 5 mV/s in both the cathodic and anodic directions periodically throughout electrochemical testing. Polarization curves were post-corrected for iR drop using series resistance from electrochemical impedance spectroscopy. To differentiate steady state activity from transient current, chronoamperograms (CAs) were recorded at increasingly cathodic 50 mV intervals until current stabilized or for a maximum of 30 minutes. Electrodes with Pt/C control (Alfa Aesar 20% Pt) and carbon black only were measured for comparison. The impact of reductive potential on the electronic state of the catalysts was evaluated ex situ. For this, an A550-H-bronze sample was held at -0.8 V vs. RHE until current became stable (approximately 30-60 min), then

removed from the electrolyte solution while still under applied potential. The electrode was then quickly rinsed with Milli-Q water to remove electrolyte salts, dried, and immediately analyzed with XPS.

4.6 Conclusions

Three atypical precursors: H_xMoO_3 -I, with $x \approx 0.3$, H_xMoO_3 -III, with $x \approx 1.7$, and the peroxy molybdate H_2MoO_5 were evaluated as precursors for the synthesis of γ - $Mo_{1-e}(N_xO_y)H_z$ via ammonolysis, with the aim of producing high surface area γ by avoiding the formation of MoO_2 during the reaction. As revealed by in situ powder XRD, ammonolysis of H_xMoO_3 -phase I did not circumvent the formation of MoO_2 and the resulting γ - $Mo_{1-e}(N_xO_y)H_z$ was not phase pure until 700 °C. In contrast, the synthesis pathways beginning from both H_xMoO_3 -III and H_2MoO_5 circumvented MoO_2 and resulted in the formation of phase pure γ - $Mo_{1-e}(N_xO_y)H_z$ at temperatures lower than any reported in literature: 480 °C for the H_xMoO_3 -III precursor and 380 °C for the H_2MoO_5 precursor. We suggest that ready incorporation of NH_3 into the bulk of these materials facilitates transformation to γ - $Mo_{1-e}(N_xO_y)H_z$ at such low temperatures.

In addition to the low temperature of formation, BET results revealed strikingly high surface areas for the two γ - $Mo_{1-e}(N_xO_y)H_z$ products: 206 m^2/g for the H_xMoO_3 -III-derived material synthesized at 550 °C and 152 m^2/g for the H_2MoO_5 -derived material synthesized at 400 °C. Despite the apparent absence of a topotactic reaction from H_2MoO_5 , the γ - $Mo_{1-e}(N_xO_y)H_z$ generated from the peroxide precursor displayed a specific surface area comparable to the high values typically associated with a topotactic transformation from MoO_3 . This result suggests synthesis temperature, when coupled with the ability of the precursor to incorporate

ammonium at low reaction temperatures, may be more critical than a topotactic relationship between precursor and product in attaining high specific surface area.

Catalytic characterization for HER and comparison with conventional $\gamma\text{-Mo}_{1-e}(\text{N}_x\text{O}_y)\text{H}_z$ materials synthesized by high temperature ammonolysis of MoO_3 showed the materials to have initially low activity, which was drastically improved after exposure to reducing potentials. This behavior is associated with a reduction of the catalyst and the likely removal of surface oxides. After catalyst activation under reductive potentials, the electrochemical activity displayed a trend that followed, albeit weakly, the catalyst specific surface area. Thus, use of alternative precursors for synthesis of $\gamma\text{-Mo}_{1-e}(\text{N}_x\text{O}_y)\text{H}_z$ by ammonolysis yields materials that match or exceed the electrochemical activity of those produced by more traditional methods, while significantly reducing the synthesis temperature. Additionally, by expanding the temperature at which the ammonolysis reaction produces $\gamma\text{-Mo}_{1-e}(\text{N}_x\text{O}_y)\text{H}_z$ to the range $400^\circ\text{C} - 800^\circ\text{C}$, these alternative precursors may offer a route for achieving fine control over the composition and morphology of the final product.

4.7 Chapter 4 Supplemental Information

4.7.1 Synthesis of H_xMoO_3 phases

The H_xMoO_3 precursors were prepared by the reduction of MoO_3 with hydrogen generated in situ from the reaction of Zn metal and HCl, following a procedure described by Glemser et al.¹¹¹⁻¹¹⁴ Specifically, 2 g MoO_3 (Sigma Aldrich, 99.99%) was suspended in 50 ml DI water by stirring for 10 min. To this suspension 10 ml of 12M HCl was slowly added under continued stirring. After an additional 5 min of stirring, the suspension was cooled to 0°C using a dry ice bath and Zn granules (Cerac Specialty Inorganics, 99.9%) were slowly added: 2 g in the

case of H_xMoO_3 -III ($x \approx 1.7$) and 0.3 g in the case of H_xMoO_3 -I ($x \approx 0.3$). To prevent a runaway reaction, no more than ~ 0.2 g of Zn was added at a time, and after each increment the suspension was stirred for 5 min before adding the next. Hydrogen bubbles immediately formed upon introduction of the first increment of Zn. Upon addition of the entire quantity of Zn to the suspension, it was stirred for an additional 15 min. The suspension was held at room temperature for 24 h. The final suspension was filtered and washed with DI water and 1-2M HCl multiple times. The collected powder was dried under vacuum and stored in a glove box. Phase formation was confirmed by X-ray powder diffraction (Figure 4.1).

4.7.2 Synthesis of H_2MoO_5

The synthesis of H_2MoO_5 was performed by oxidation of MoO_3 using aqueous H_2O_2 .^{20,115} 100 ml of 30% wt H_2O_2 solution was heated to 40 °C under constant stirring, to which 2 g MoO_3 (Sigma Aldrich, 99.99%) was slowly added. The solution was further heated to ~ 55 °C and held overnight at this temperature under continued stirring until the suspension changed color from white to light green to clear bright yellow. The water was allowed to evaporate under ambient conditions by storing the open solution for 48 h in a fume hood. The resulting bright yellow powder H_2MoO_5 was collected and further dried in an oven at 80 °C overnight in air. Phase formation was confirmed by X-ray powder diffraction (Figure 4.1).

Table 4.3: Summary of crystallographic properties from the Rietveld refinements of the precursors H_xMoO_3 -phase I, H_xMoO_3 -phase III, and H_2MoO_5 . The number in parentheses reflects the uncertainty in the final digit(s) of the parameter value. Atomic coordinates were fixed to the values given in the cited references.

	H_xMoO_3 -phase I	H_xMoO_3 -phase III	H_2MoO_5

Space group	<i>Cmcm</i>	<i>C2/m</i>	<i>P2₁/n</i>
a	3.8916(2)	13.969(3)	12.088(2)
b	14.0772(6)	3.7707(4)	3.8286(2)
c	3.7374(2)	4.0544(6)	7.376(1)
β (deg.)	90	93.80(1)	77.719(6)
Reference structure	Adams (2000) ⁹³	Brařda (2005) ⁹⁷	Reid (2018) ¹¹⁶
Crystallite size (μm)	0.148(7)	0.20(3)	0.6(2)
Texture index	1.60	2.16	1.21
wR	18.83%	4.71%	3.32%

The phase I bronze is reported to adopt a slight distorted structure in space group *P2₁/b* at ambient temperature. However, the higher temperature *Cmcm* form (expected above 141 °C) was found to give a slightly better fit to the data.

4.7.3 Panoramic and conventional synthesis of $\gamma\text{-Mo}_{1-x}(\text{N}_x\text{O}_y)\text{H}_z$

A comparison of the temperature profiles used in the preparation γ from ammonolysis of the various precursors examined is shown in Figure 4.15. The profiles employed for panoramic syntheses, performed using the precursors $\text{H}_x\text{MoO}_3\text{-I}$, $\text{H}_x\text{MoO}_3\text{-III}$ and H_2MoO_5 with phase evolution tracked in situ by X-ray diffraction, are shown in Figure 4.15a. The reproducibility of the synthesis outcomes is indicated in Figure 4.10. The diffraction patterns of each batch of A550-H-bronze and A400-peroxo used for subsequent characterization were essentially identical. Shown in Figure 4.15b are the profiles for the conventional syntheses performed using MoO_3 as a precursor. This latter procedure was identical to our previous report.⁴⁷ Specifically,

0.25 g of the precursor oxide (Sigma Aldrich MoO₃, 99.99%) was placed in a horizontal tube furnace and exposed to a flow of 100 mL/min (space velocity of 1.65 cm/s) of anhydrous NH₃ (Airgas). The material was then subjected to the following thermal profile: heat at a rate of 5 °C/min from ambient to 350 °C (no hold), heat at rate of 0.6 °C/min to 500 °C (no hold), heat at rate of 3 °C/min to either 700 °C (A700-MoO₃) or 800 °C (A800-MoO₃), hold for 3 h, then furnace cool to ambient temperature while still under ammonia flow. The diffraction patterns of the resulting materials, Figure 4.4a, suggest at first glance that A700-MoO₃ crystallized in space group $Fm\bar{3}m$ and A800-MoO₃ in space group Fm3m and A800-MoO₃ in space group Pm3m. However, both crystallize in space group Pm3m (in contrast to the conventionally accepted Fm3m space group for this phase). In the case of A800-MoO₃, the loss of the translational symmetry characteristic of the Fm3m space group is readily detected by X-ray (or electron) diffraction because it involves vacancy ordering on cation sites, along with N and O ordering on anion sites. In A700-MoO₃, N and O ordering and the occurrence of the Pm3m space group, which is difficult to observe by X-ray and electron methods, has been detected by neutron diffraction.⁴⁷

4.7.4 Discussion of the ammonolysis of H_xMoO₃-I (x ≈ 0.3)

The reaction pathway observed in this work differs from the results reported by Jagers et al., who state that the dioxide is circumvented during ammonolysis of H_xMoO₃ phases I and II. Those authors employed an ammonia flow rate of 150 sccm and for a sample mass of 20-50 mg, in contrast to the 100 sccm flow rate and 250 mg mass employed here. These differences are consistent with an overall higher tendency towards nitridation in the work by Jagers.

It is of some significance that in the present work the dioxide remains in the reaction mixture long after the H_xMoO_3 -phase I is consumed (Figure 4.5). At first glance, this suggests that the ammonium bronze is a necessary precursor to the formation of MoO_2 ; however, the present results do not provide evidence that ammonium bronze phases occur in the ammonolysis of MoO_3 . It is known that H_xMoO_3 ($x \leq 0.34$) phases form during MoO_3 ammonolysis. However, the temperatures at which they appear (≈ 400 °C)^{21,22} are higher than the 25 °C at which the H_xMoO_3 precursor was exposed to ammonia flow in this work. The high temperatures at which hydrogen bronzes form during synthesis might not be compatible with subsequent formation of ammonium bronze phases. That is, one can expect that reaction of the hydrogen bronze with ammonia to form the ammonium bronze becomes increasingly unfavorable with increasing temperature, and accordingly, ammonium bronze phases may not be encountered during ammonolysis of MoO_3 following the high temperature at which the hydrogen bronze phases form.

Chapter 5: Synthesis of oxygen-free Mo₂N

5.1 Introduction

As discussed in the previous chapters, molybdenum nitride catalysts are often synthesized by ammonolysis of molybdenum oxide - the reaction of the oxide with ammonia at high temperatures – as this reaction is known to produce nitrides with high specific surface area.^{20–23,25,110} The product of this reaction is often assigned the composition Mo₂N based on its diffraction pattern, without additional verification of the chemical composition.^{9,20–23,25,50,80,85,122} The diffraction pattern of Mo₂N correspond to a material identified as a face centered cubic rock salt structure of Mo with N occupying half of the octahedral sites.⁴⁸ However, x-ray diffraction is not well suited to distinguishing O and N in a structure owing to their nearly identical scattering factors and thus identification of the materials via x-ray diffraction may cause misidentification of the chemical composition if oxygen and nitrogen are occupying the same site. The wide compositional variation that can be accommodated by the Mo₂N structure without apparent change in the diffraction pattern is evidenced by comparing the diffraction patterns of samples synthesized by ammonolysis of MoO₃ at temperatures of 700°C, 800°C, and 900°C, which have oxygen contents of 14%, 4%, and 0.3% respectively,⁴⁷ and yet can all be fit with the nominal “Mo₂N” structure (Figure 5.1). Chemical analysis of molybdenum nitrides produced by the ammonolysis method has shown that they can have oxygen content as high as 15 atomic %, with the composition dependent on reaction conditions such as the precursor, heating rates, and reaction temperature.^{5,47} Thus chemical composition analysis beyond matching of the structure to

that of Mo_2N is needed in order to truly identify the composition of molybdenum nitrides, especially those synthesized by ammonolysis from oxygen containing precursors. Furthermore, recent work has studied the effect of oxygen in these molybdenum nitrides on their catalytic performance and demonstrated that the varying composition can impact the activity of the materials, highlighting the importance of accurately knowing the composition of these types of materials when deployed for catalytic applications.^{5,6} In this work we present an approach for producing molybdenum nitrides with low oxygen content using the ammonolysis of MoO_3 as the synthesis method: when the ammonolysis reaction temperature is increased to 900°C , the sample is reduced to Mo metal and all anion species are removed. Upon cooling under NH_3 , the sample is nitrated to produce Mo_2N free of bulk oxygen.

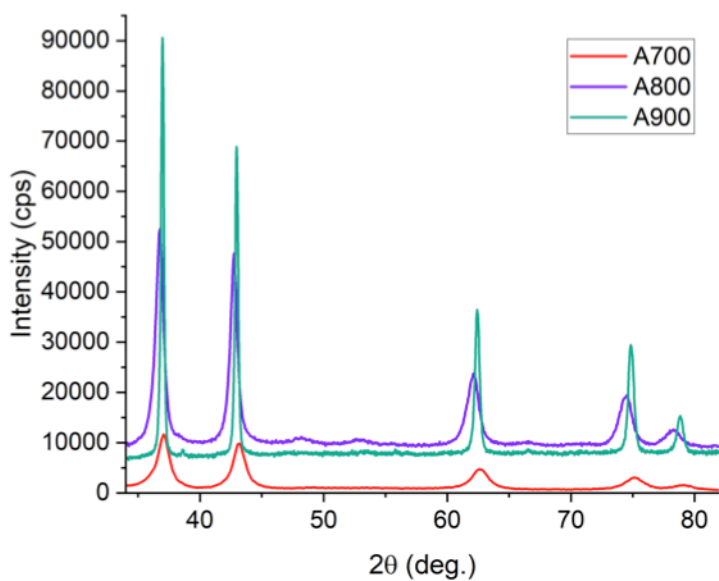


Figure 5.1: XRD of samples synthesized by ammonolysis of MoO_3 at temperatures of 700°C , 800°C , and 900°C , with oxygen contents of 14%, 4%, and 0.3%, respectively.

5.2 Methods

In situ x-ray diffraction studies were performed using an Anton Paar XRK 900 reactor chamber mounted onto a 9 kW Cu rotating anode Rigaku Smartlab equipped with a D/TEX Ultra 250 1D silicon strip detector with a Ni filter to remove $K\beta$ radiation. Measurements were taken in $\theta/2\theta$ geometry over the 2θ range 9° - 82° with a scan speed of 50° $2\theta/\text{min}$ to minimize dwell time at each temperature. Sample spinning was used to minimize the effects of preferential orientation. Approximately 20 mg of the MoO_3 precursor was placed inside the reactor chamber at ambient temperature, purged with N_2 (Airgas, 99.999%), and subjected to a flow of 100 sccm of NH_3 (Airgas, anhydrous). Diffraction patterns were collected at intervals selected to best observe the reaction on both heating to and cooling from the upper reaction temperature of 900°C , at which the samples were held for 4 h. Data were collected at intervals of 50°C from room temperature to 300°C , 5°C from 325°C to 420°C , 20°C from 440°C to 800°C , 10°C from 800°C to 900°C , every 20 minutes during the hold at 900°C , 10°C from 900°C to 750°C during cooling, and 50°C from 750°C to room temperature during cooling. The sample was equilibrated for 2 minutes at each data acquisition temperature before collecting the diffraction pattern. A heating profile of $5^\circ\text{C}/\text{min}$ from room temperature to 350°C , $1^\circ\text{C}/\text{min}$ from 350°C to 500°C , and $3^\circ\text{C}/\text{min}$ from 500°C to 900°C was used. The thermal profiles are detailed in Figure 5.2. The heating profile included a relatively low heating rate in the intermediate temperature regime ($350 - 500^\circ\text{C}$, $1^\circ\text{C}/\text{min}$ between XRD pattern acquisitions) in accord with typical ammonolysis reactions targeting high surface area from this precursor. Analysis of the XRD data was performed using GSAS II using CIFs taken from ICSD (MoO_3 ,²⁸ $\text{H}_{0.3}\text{MoO}_3\text{-I}$,⁴¹ MoO_2 ,⁴² $\gamma\text{-MoO}_x\text{N}_y$,⁷ $\delta\text{-MoN}$,⁴³ and Mo^{123}) for the initial model.⁴⁴ Scale factor, sample displacement, phase fraction, lattice parameters, and crystallite size were allowed to vary in each Rietveld refinement

and spherical harmonic preferred orientation corrections were applied. Atomic positions and thermal displacements were not refined. Chebyshev polynomials with 5 terms were used to model the background. The standard reference material LaB_6 was used to determine instrument broadening and these instrument parameters were applied to all patterns.

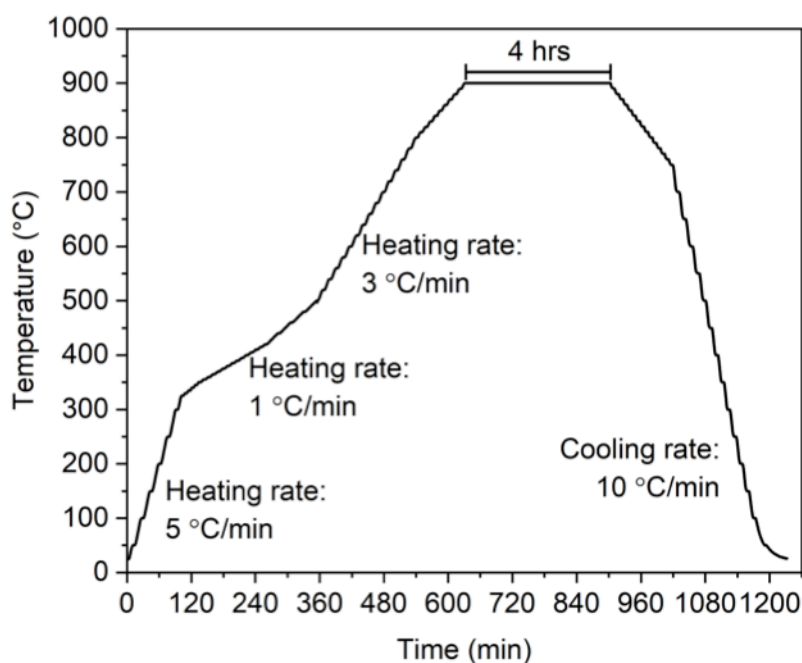


Figure 5.2: Heating profile for the in situ ammonolysis of MoO_3 at 900°C .

The composition of the sample was determined by a combination of TGA and combustion analysis. Four batches of sample produced by in situ synthesis were combined for the chemical and structural characterization and, prior to the chemical analyses, the sample was annealed under Ar at 400°C to remove adsorbed surface species. TGA was used to completely reduce the material and determine the mass percent of Mo in the sample, and thus the anion to cation ratio. Data was collected using a Netzsch STA F3. 50 mg of sample was loaded into a Pt pan, heated under 2% H_2 /balance Ar to 900°C at $2^\circ\text{C}/\text{min}$ and held for 3 hours. XRD was

performed after the complete reduction experiment to confirm the presence of only Mo in the product. The onset of bulk anion loss was determined to be $\sim 400\text{-}500^\circ\text{C}$ by in situ XRD (details below), with mass loss prior to this temperature attributed to the removal of adsorbed surface species, so the Mo mass % was calculated from a bulk sample mass taken to be the mass at 400°C . Determination of the N and H content was by microchemical combustion analysis performed by the commercial service of Midwest Microlab. Duplicate samples were combusted at 990°C in ultrapure oxygen and the effluent gas stream was evaluated for N_2 and H_2O content. Once the Mo and N content of the sample was determined, the remaining mass was attributed to oxygen.

In situ PXRD was used to observe the complete reduction of MoO_3 under H_2 . ~ 0.2 g of molybdenum oxynitride synthesized at 700°C or 800°C was placed inside the reactor chamber at room temperature, purged with N_2 for 30 minutes, and subjected to a flow of 100 mL/min of 7% H_2 /balance He. The material was then subjected to the following thermal profile: heat to 900°C ($2^\circ\text{C}/\text{min}$, 3 hour hold) and cool to room temperature ($10^\circ\text{C}/\text{min}$) while still under gas flow. The chamber was purged with N_2 for 30 minutes before exposing the sample to air. XRD measurements were collected in 20°C intervals during heating, in 10 minute increments for the first 30 minutes and 30 minutes increments for the remainder of the holding time, and in intervals of 100°C during cooling. Diffraction data were analyzed as described above.

BET surface area and the pore size were determined from nitrogen physisorption isotherms measured at liquid nitrogen temperature using a Micromeritics 3Flex instrument and samples ~ 300 mg in mass. Data were analyzed using the MicroActiv software package, which provides quantitative uncertainty estimates for the surface area. The uncertainty in the pore-size determination was taken to be 1 in the final digit obtained from the analysis.

A Micromeritics AccuPyc II 1340 pycnometer was utilized for density determination. ~300 mg of the sample was loaded into an aluminum cap (1 mL), and the volume was determined on the basis of He displacement. The volume of the sample was measured three times, and the standard deviation was recorded along with the average volume. The measured mass (obtained using an analytical balance) was then used for the density calculations. The estimated standard deviation was obtained from the range in values across the three measurements.

5.3 Discussion

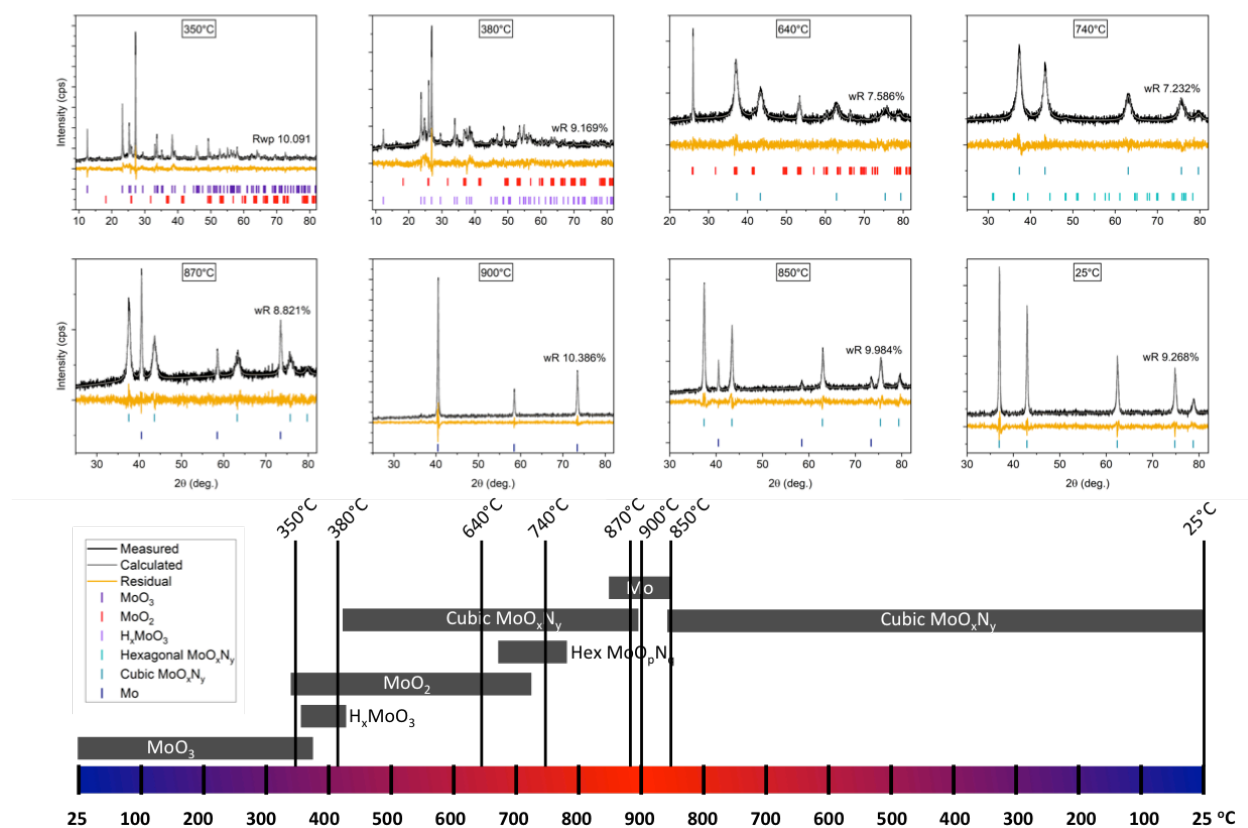


Figure 5.3: Diffraction patterns collected at 350°C, 380°C, 640°C, 740°C, 870°C, 900°C, 850°C, and 25°C during the in situ ammonolysis of MoO_3 . The overall reaction pathway

displaying the phases present at each selected temperature is shown below the diffraction patterns.

The diffraction patterns for select temperatures from the in situ ammonolysis of MoO_3 up to 900°C , as well as the overall reaction pathway, are shown in Figure 5.3. The in situ diffraction showed the appearance of MoO_2 at 335°C , followed by the appearance of H_xMoO_3 at 355°C . Following the formation of the two intermediates, the MoO_3 precursor was consumed by 380°C . The H_xMoO_3 phase was relatively short-lived and was fully consumed by 420°C . The cubic $\gamma\text{-MoO}_x\text{N}_y$ phase first appeared at 410°C and coexisted with the MoO_2 intermediate up to 660°C , at which point the hexagonal MoN phase appeared. As heating continued, both the MoO_2 and MoN were consumed at 720°C and 790°C , respectively. $\gamma\text{-MoO}_x\text{N}_y$ was the sole phase up to 850°C , beyond which it began to be reduced to Mo . The reduction was complete after approximately 10 minutes at 900°C . Following the hold at 900°C , the $\gamma\text{-MoO}_x\text{N}_y$ reappeared during cooling beginning at 870°C and the conversion of Mo to $\gamma\text{-MoO}_x\text{N}_y$ was complete by 840°C . The phase fractions as a function of temperature are presented in Figure 5.4. After the reaction, the sample was a steely gray color and showed significant densification in comparison to the starting precursor (Figure 5.5). The molybdenum oxynitride sample produced by ammonolysis of MoO_3 up to 900°C will hereafter be referred to as A900.

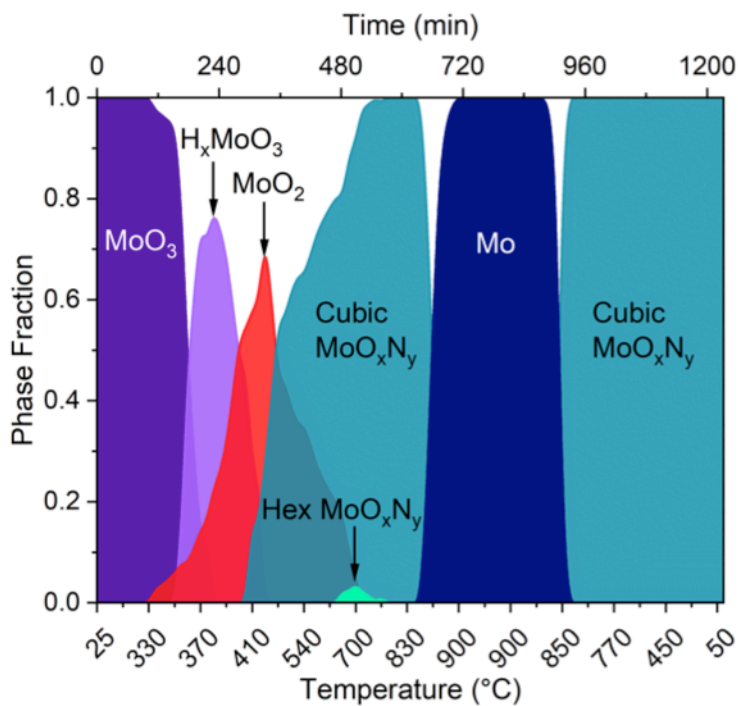
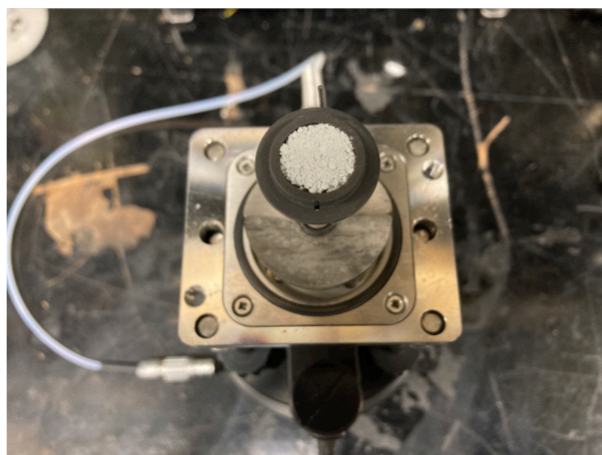


Figure 5.4: Phase fractions as a function of temperature for the ammonolysis of MoO_3 at 900°C as extracted from the in situ synthesis.

Before ammonolysis:



After ammonolysis:



Figure 5.5: Images of the MoO_3 precursor and A900 product of the in situ ammonolysis reaction show significant densification after the reaction.

Anion loss and uptake in the γ -MoO_xN_y phase was readily apparent by tracking the lattice parameter as a function of temperature during the ammonolysis reaction (Figure 5.6). During heating the lattice constant initially showed the expected increase due to thermal expansion; however, between 540°C and 780°C the lattice constant decreased with continued heating. This apparent negative thermal expansion is attributed to the loss of bulk anions from the material resulting in a reduction of the unit cell volume. The same phenomenon was observed during cooling, with the lattice constant increasing between 840°C and 600°C despite the decreasing temperature due to uptake of nitrogen into the lattice, only showing the expected thermal contraction at temperatures below 600°C once the anion incorporation was complete.

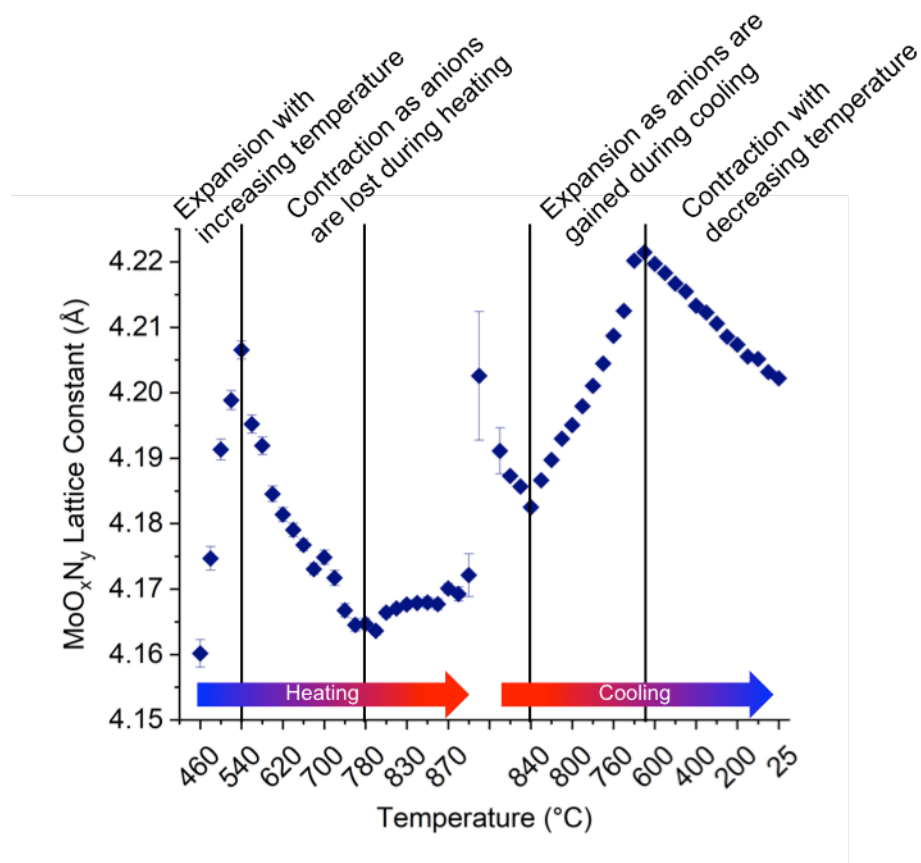


Figure 5.6: Lattice constant of A900 as a function of temperature during the ammonolysis reaction shows anion loss from 540°C to 780°C during heating and anion gain from 840°C to 600°C during cooling.

The TGA profile for the complete reduction of A900 showed nearly no mass loss up to 600°C (Figure 5.7). After this temperature, relatively gradual mass loss occurred until approximately 850°C, at which point a sharp decrease in mass occurred. The onset of bulk mass loss was tracked by in situ XRD of molybdenum oxynitride samples produced at 700°C (A700) and 800°C (A800) under flowing 7% H₂ (balance He). The sample was fully reduced in the flowing hydrogen at 900°C and the lattice constant and ratio of the first two peaks were tracked as a function of temperature. The in situ diffraction experiments under H₂ (Figure 5.8) revealed that changes in the lattice parameter, beyond simple thermal expansion, initiated at ~450°C. On

heating beyond 450°C, cell contraction was observed for both A700 and A800, along with a decline in the I(200)/I(111) peak intensity ratio. The onset of cell contraction was taken to indicate the loss of bulk anions from the sample. Taking bulk mass loss to begin at 450°C, the complete reduction TGA experiment revealed that Mo composed 91.0197% of the bulk sample mass. This falls between the expected values of 93.2 mass % and 87.3 mass % Mo for the ideal stoichiometric compositions of Mo₂N and MoN, respectively.

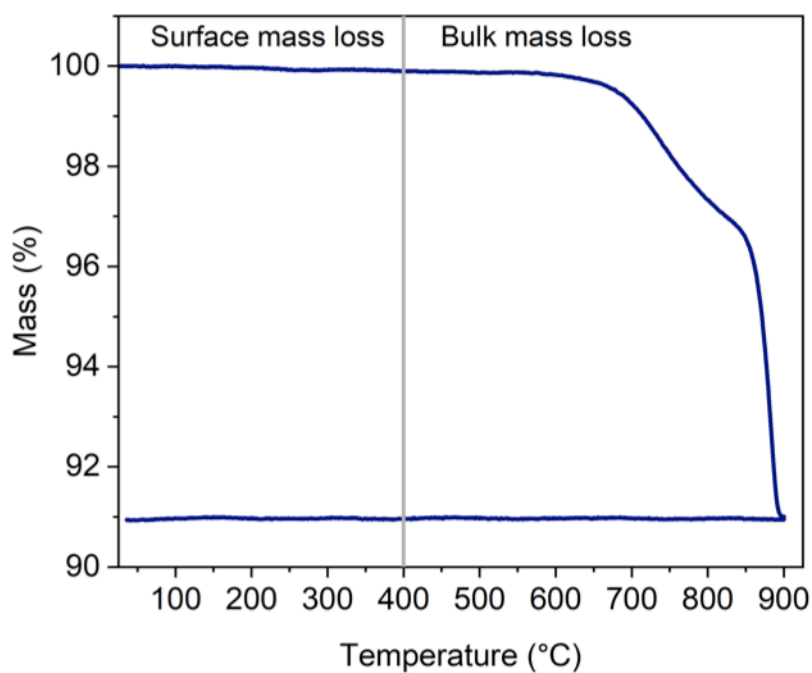


Figure 5.7: TGA mass loss profile for the complete reduction of A900 showing sharp mass loss beginning at 700°C and resulting in anion loss of 8.98%.

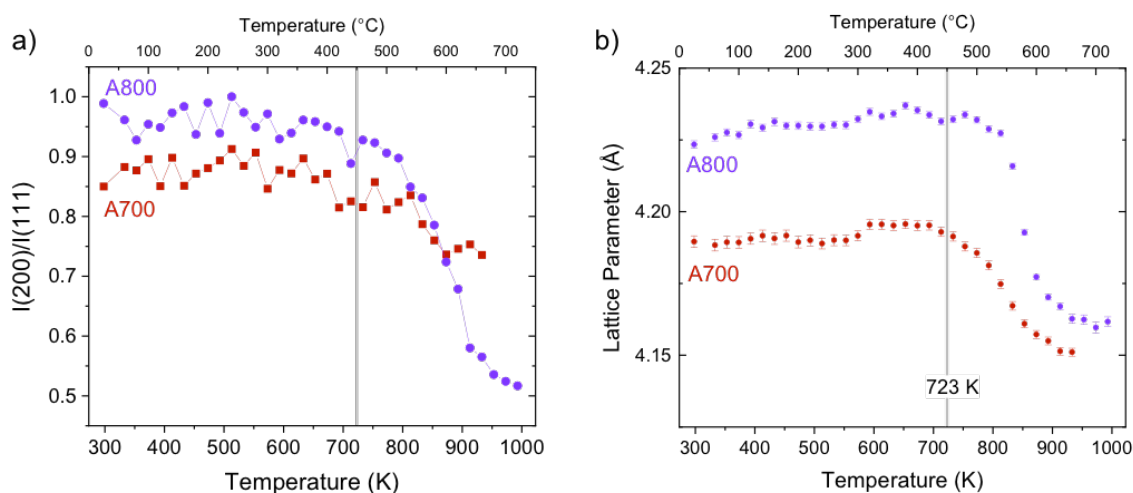


Figure 5.8: In situ XRD of the complete reduction of A700 and A800 under 7% H₂ (balance He). (a) Ratio of the intensities of the (200) and (111) peaks in A800 and A700 materials. In principle, the $I(200)/I(111)$ intensity ratio serves as a measure of the global cation:anion ratio⁴. Here, preferential orientation has not been completely eliminated despite spinning the sample, and thus the intensity ratio cannot be interpreted quantitatively. (b) Lattice constant of A700 and A800 materials. Under these conditions, both materials are fully transformed to Mo at 780°C. The onset of apparent cell contraction at $\approx 450^\circ\text{C}$ is taken to be indicative of bulk changes in composition. This coincides with a slight decline in the intensity ratio of the (200) to (111) peaks shown in a.

The combustion analysis indicated absolute N content in the A900 sample of 8.915 mass % N, as averaged from duplicate measurements (Table 5.1). Although the combustion analysis method is not capable of measuring trace elements, no H was detected within the limits of the measurement. Combined with the Mo mass as determined by the TGA experiment, this yields atomic masses of 59.7% Mo and 40.0% N. The remaining 0.3 atomic % is attributed to O content in the sample. Consistent with the observed bulk Mo mass, the resulting anion/cation ratio of 0.675 falls between the expected ratios of 0.5 and 1 for Mo₂N and MoN, respectively. The overall composition of the A900 sample as determined by the quantitative chemical analysis is Mo₁N_{0.67}O_{0.0043}.

Table 5.1: Sample composition as determined by combined TGA and combustion analysis.

Mo mass % (measured by TGA)	91.0197
N mass % (measured by combustion analysis)	8.915
H mass % (measured by combustion analysis)	0.00
Expected Mo mass % for Mo ₂ N	93.2
Expected Mo mass % for MoN	87.3
Atomic % Mo	59.7
Atomic % N	40.0
Atomic % O	0.3
Atomic anion/cation ratio	0.675
Composition	Mo ₁ N _{0.67} O _{0.0043}

Structural characterization of the A900 sample was conducted using pycnometry and BET (Table 5.2). The density measured by pycnometry was 8.98 g/cm³, slightly lower than the expected densities of 9.46 and 9.2 g/cm³ for Mo₂N and MoN. This result suggests that the sample has closed pores or crystallographic vacancies that are not accessible to the He in the pycnometry measurement. BET revealed a low surface area of 1.9919 ± 0.1122 m²/g and large surface pores, with the majority of the pore volume coming from pores larger than 50Å.

Table 5.2: Density and surface area of A900. The density as determined by pycnometry is compared to the expected densities of molybdenum nitrides with the stoichiometries Mo₂N and MoN.

Measured density	8.985(1) g/cm ³
Expected density for Mo ₂ N	9.46 g/cm ³
Expected density for MoN	9.2 g/cm ³
Surface area	1.9919 ± 0.1122 m ² /g

5.4 Conclusions

Molybdenum nitride with very low oxygen content was produced by the ammonolysis of MoO₃ at 900°C. In situ PXRD showed the complete reduction to Mo when the reaction temperature was increased up to 900°C. Upon cooling in NH₃, N was incorporated into the sample to form molybdenum nitride. Because of the removal of all anions at high temperature, this method produced a nitride of composition Mo₁N_{0.67}O_{0.0043} with nearly no oxygen content. Significant densification was observed during the reaction, and the resulting molybdenum nitride product had a low surface area of 1.99 m²/g. Although the product had low surface area, making it unsuitable for catalytic application, this study provides insight into how to tune the chemical composition and oxygen content of molybdenum oxynitrides produced by ammonolysis.

Chapter 6: In situ phase space mapping of the Ta-O-N system

TaON is a promising photoactive catalyst that can be synthesized by ammonolysis of Ta_2O_5 .^{57,58,127,60–62,68,77,124–126} Three phases of TaON have been experimentally produced - with the β phase being the most common, followed by the γ - and δ - phases - as well as several nitride phases, including Ta_3N_5 , Ta_4N_5 , and TaN. The ammonolysis reaction typically produces mixtures of these phases. Identifying synthesis pathways to isolate the different phases is important for evaluating the catalytic activity of the each phase and the effect of the TaON structure on the activity. Some initial research in our group has suggested that the γ -TaON phase may be more active than the β -phase.⁹²

6.1 In situ studies of the synthesis of TaON via ammonolysis

In order to better understand the ammonolysis reaction of Ta_2O_5 and achieving sufficient control of the synthesis to target specific phases, in situ synthesis, similar to that performed for the Mo-O-N system, was attempted for the Ta-O-N system. This study built on previous ex situ synthesis of TaON done in the group.⁹² It was found that using dry ammonolysis with a flow rate of 40 sccm NH_3 and a 24 hour hold at 850°C produced single phase Ta_3N_5 , while shorter holds under the same conditions produced a mixture of Ta_3N_5 and β -TaON. Wet ammonolysis produced mixtures of TaON phases, without Ta_3N_5 . Of the wet ammonolysis syntheses, gas mixtures with less steam favored the β -TaON phase, with single phase β -TaON produced using a flow of 20 sccm NH_3 and 50 sccm Ar through a water bubbler and a 35 hour hold at 850°C . Lower hold times at the same gas conditions produced mixtures of β -, γ -, and δ -TaON. Gas mixtures with higher steam (20 sccm NH_3 and 80 sccm Ar through a water bubbler) favored the

γ -TaON phase, with a 24 hour hold at 850°C producing up to 67% γ -TaON under these gas conditions. However, the product still contained a mixture of the three TaON phases, and single-phase γ -TaON was not achieved. In order to better understand the effects of reaction conditions on the product phases and the relationships between the different TaON phases, in situ synthesis was utilized to study the reaction.

Interestingly, the in situ reactions did not match with what was seen ex situ. Using dry ammonolysis (100 sccm NH_3 , heat to 850°C at 5°C/min, hold for 24 hours) produced a mixture of TaON phases consisting of 13% β -TaON, 83% γ -TaON, and 4% δ -TaON (Figure 6.1) – as opposed to the 100% Ta_3N_5 expected to form at these conditions according to the ex situ synthesis. A number of slightly varying reaction conditions were explored to try to recreate the Ta_3N_5 synthesis, but the ex situ results were not achieved in the in situ furnace (Table 6.1).

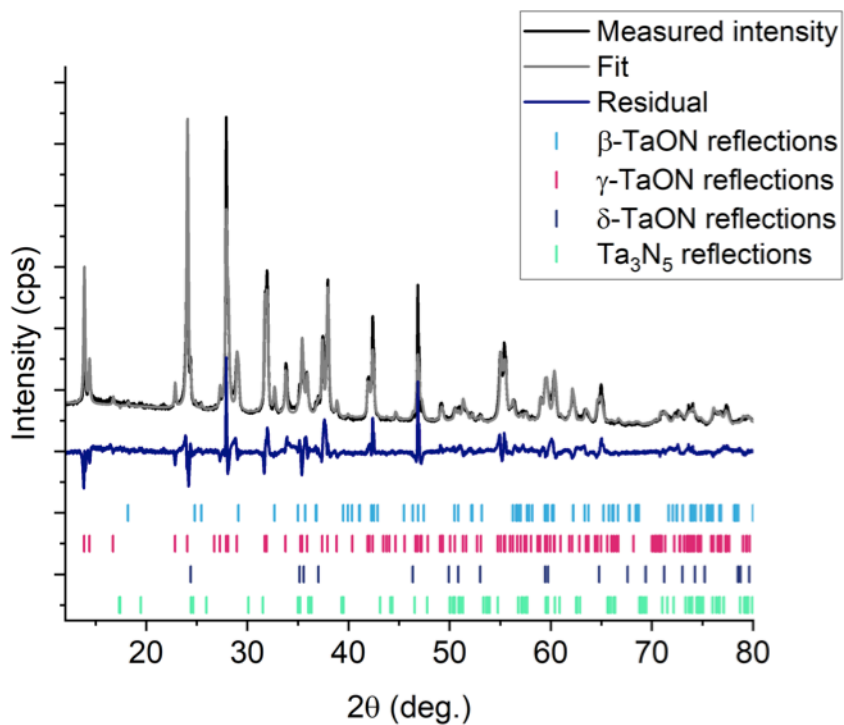


Figure 6.1: Rietveld refinement of the sample produced by in situ ammonolysis of Ta₂O₅ using dry ammonia and a holding time of 24 hours shows the product to be a mixture of β-, γ-, and δ-TaON, and Ta₃N₅.

Table 6.1: Conditions and synthesis results for the in situ ammonolysis of Ta₂O₅ using dry NH₃. Unless otherwise noted the synthesis was performed at 850°C using a ramp rate of 5°C/min from room temperature to 850°C.

Date	Flow Rate (sccm)	Holding Time (hrs)	Product
02092021	100 sccm NH ₃	24	13% β-TaON 83% γ-TaON 4% δ-TaON
03262021	100 sccm NH ₃	36	76% β-TaON 6% γ-TaON 5% Ta ₃ N ₅ 13% TaN
04132021	100 sccm NH ₃	32 at 900°C	Majority β-TaON Minority unknown phase
06092021	100 sccm NH ₃ Anneal Ta ₂ O ₅	24	28% β-TaON 10% γ-TaON 33% Ta ₃ N ₅ 29% TaN
10072021	100 sccm NH ₃	24	100% γ-TaON
10272021	100 sccm NH ₃	24 at 865°C	22% β-TaON 63% γ-TaON 15% δ-TaON
10292021	200 sccm NH ₃	24 at 865°C	Majority β-TaON Minority unknown phase
11092021	500 sccm NH ₃	24 at 865°C	50% β-TaON 23% γ-TaON 6% Ta ₃ N ₅ 21% Ta ₄ N ₅
11112021	100 sccm NH ₃ 500 sccm N ₂	24 at 865°C	14% β-TaON 76% γ-TaON 10% δ-TaON

In order to determine the cause of the discrepancies between the in situ and ex situ reactors, flow rate, temperature, and ammonia dissociation calibrations were performed on the in situ reactor set up (Figure 6.2). The gas flow was calibrated using a Sensodyne Gilibrator. N_2 was used for the calibration since NH_3 could not be used directly in the Gilibrator. A flow rate was set using the flow controller and then the flow was measured using the Gilibrator and converted to the corresponding flow rate for NH_3 using the gas correction factor for thermal-based mass flow of 0.73 for NH_3 . The measured gas flow was found to be minimally different from the set point across a range of flow rates (50 – 500 sccm). The temperature was calibrated by running an external thermocouple through the gas line at the base of the sample holder. The temperature was set by the computer controlled TCU and the corresponding temperature on the thermocouple was read after 15 minutes of equilibration. The temperature was found to be $15^\circ C$ lower than the set point at all temperatures from 500 - $900^\circ C$. Correspondingly, set points of $865^\circ C$ were used after the temperature calibration in order to achieve a furnace temperature of $850^\circ C$. Ammonia dissociation was measured using an ammonia dissociation burette. The exhaust gas from the furnace at varying temperatures and flow rates was flowed into the burette and the dissociation rate was measured (Table 6.2). It was found that the ammonia dissociation rate was much higher in the in situ furnace than the ex situ furnace; for a flow rate of 100 sccm at $850^\circ C$, the ammonia was 90% dissociated in the in situ furnace as opposed to nearly completely undissociated in the ex situ furnace. Since only undissociated ammonia participates in the ammonolysis reaction, this difference in dissociation explains the drastically different reaction outcomes for nominally the same set point values; because the ammonia in the in situ furnace was majority dissociated, the reactions occurred much more slowly than in the ex situ furnace.

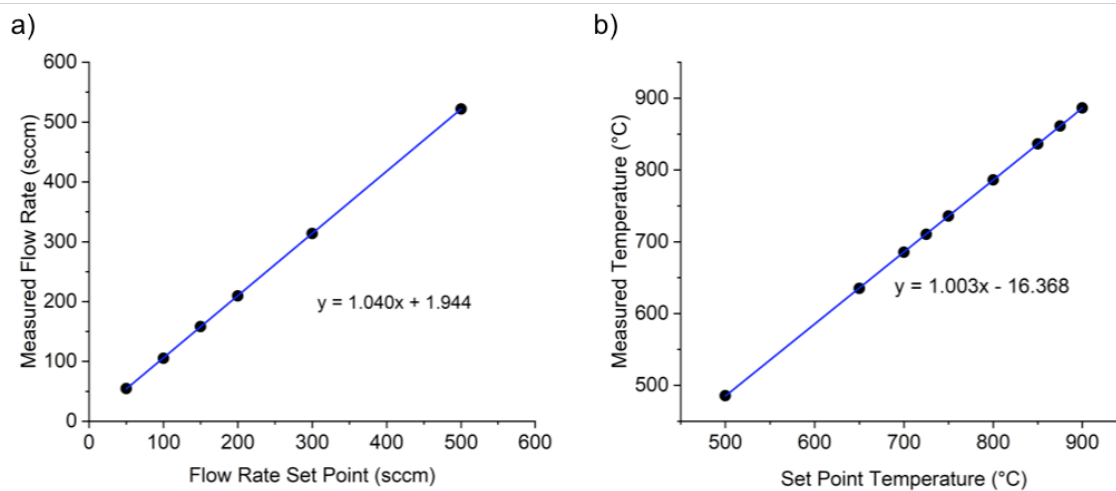


Figure 6.2: a) Flow rate and b) temperature calibrations for the XRK 900 in situ furnace.

Table 6.2: Ammonia dissociation levels for various set point temperatures and flow rates in the in situ furnace.

Temperature (°C)	Set Point (°C)	Flow Rate (sccm)	Dissociation (%)
700	715	100	88
700	715	200	82
700	715	500	58
750	765	100	87
750	765	500	65
800	815	100	89
800	815	500	67
850	865	100	90
850	865	500	69

It can be concluded from the analysis of discrepancies between the ex situ and in situ reactors that the synthesis of TaON is sensitive to the flow rate of ammonia supplied during the reaction. Although the conditions in the in situ reactor were unsuitable for accurately replicating

the ex situ reactions, conclusions about the reaction pathways were nevertheless possible from the in situ data. The phase fractions as a function of temperature from a representative in situ ammonolysis reaction of Ta_2O_5 are shown in Figure 6.3. The in situ diffraction showed the appearance of γ -TaON immediately upon reaching 850°C , followed by the formation of β -TaON after 30 minutes at 850°C . The phase fraction of γ -TaON peaked after 2.5 hours at 850°C , after which point it gradually declined as the amount of β -TaON increased. Ta_3N_5 appeared after 13 hours at 850°C , followed by TaN after 18 hours. The amount of Ta_3N_5 and TaN gradually increased during the remainder of the hold at 850°C , and remained steady during the cooling to room temperature, ultimately resulting in the formation of a product containing a mixture of 76% β -TaON, 6% γ -TaON, 5% Ta_3N_5 , and 13% TaN. From this reaction we see that the γ -TaON phase forms first, followed by β -TaON, and then the nitrides. From this we glean two key pieces of information about the reaction: (1) the oxynitrides appear to form as intermediates on the way to the nitrides, and (2) the γ -phase forms before the β -phase. This suggests that if the reaction is allowed to go to completion, it will result in the formation of tantalum nitrides, and thus controlling the length of the reaction can be used to form oxynitrides without the presence of nitride phases. Additionally, since the γ -phase forms first, it is likely that γ -TaON forms as an intermediate during the synthesis of β -TaON, so if the reaction is sufficiently slow it may favor the formation of the γ -phase.

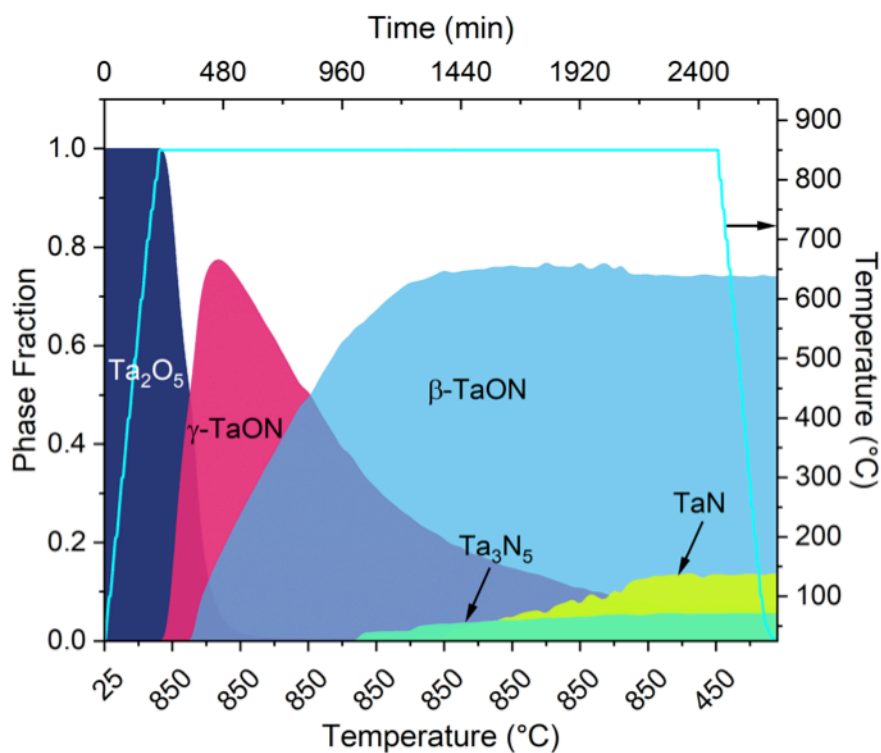


Figure 6.3: Phase fractions as a function of temperature for a representative dry ammonolysis in situ reaction (03262021). The reaction shows the phase progression to be $\text{Ta}_2\text{O}_5 \rightarrow \gamma\text{-TaON} \rightarrow \beta\text{-TaON} \rightarrow \text{Ta}_3\text{N}_5 \rightarrow \text{TaN}$ during the reaction.

6.2 Ex situ synthesis of $\gamma\text{-TaON}$

A majority - or even phase pure $\gamma\text{-TaON}$ (Figure 6.4) - could be produced in the in situ furnace using amounted to essentially a much lower flow rate of NH_3 because of the high degree of dissociation. Since previous attempts to synthesize single phase $\gamma\text{-TaON}$ ex situ had been unsuccessful, attempts to recreate the in situ reaction conditions ex situ were pursued. A series of syntheses using very low flow rates of NH_3 or combinations of NH_3 , N_2 , and H_2 in order to replicate the gas conditions caused by the high degree of NH_3 dissociation were performed in the ex situ furnace (Table 6.3).

In all cases, the syntheses resulted in the formation of a mixture of tantalum oxynitride and nitride phases, with β -TaON as the dominant phase. To further slow the reaction, a quartz wool plug was used to inhibit gas flow through the furnace. A bundle of quartz wool was placed near the end of the tube and several more flow conditions were explored. Although this did reduce the amount of nitride phases formed, none of the conditions resulted in a product with majority γ -TaON.

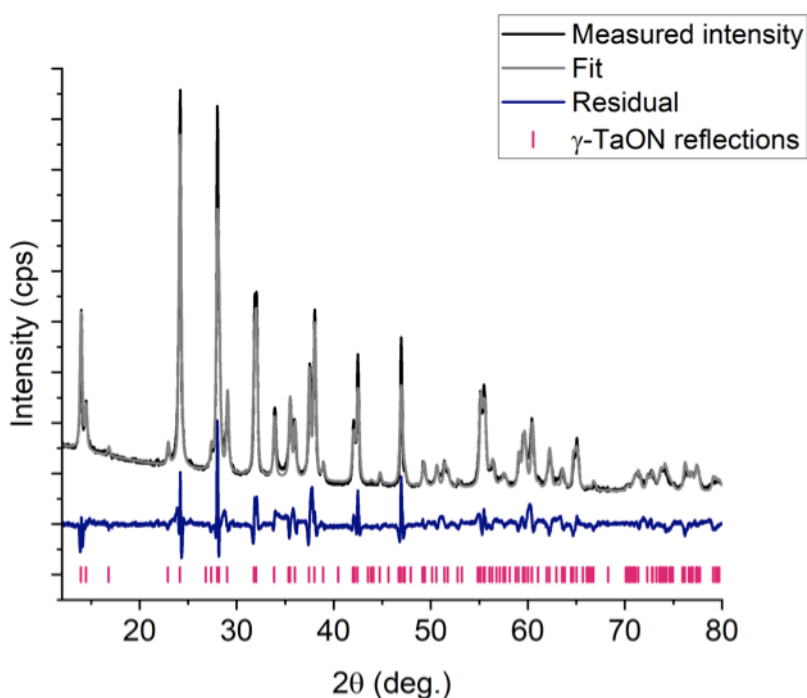


Figure 6.4: Rietveld refinement of a sample produced by in situ ammonolysis of Ta_2O_5 using dry ammonia and a holding time of 24 hours on 10072021 shows the product to be phase pure γ -TaON.

Table 6.3: Conditions and synthesis results for the ex situ ammonolysis of Ta₂O₅ using dry NH₃. Unless otherwise noted the synthesis was performed at 850°C using a ramp rate of 5°C/min from room temperature to 850°C.

Date	Flow Rate (sccm)	Holding Time (hrs)	Product
11/30/2021	50 sccm N ₂ 150 sccm H ₂	24	Ta ₂ O ₅
12/01/2021	14.6 sccm NH ₃ 131 sccm N ₂	24	88% β-TaON 12% Ta ₃ N ₅
12/16/2021	33 sccm N ₂ 66 sccm N ₂	24	Ta ₂ O ₅
12/20/2021	10 sccm NH ₃ 30 sccm N ₂ 60 sccm N ₂	24	Ta ₃ N ₅
2/10/2022	5 sccm NH ₃ 95 sccm N ₂	12	98% β-TaON 2% Ta ₃ N ₅
2/23/2022	5 sccm NH ₃	12	β-TaON
3/2/2022	5 sccm NH ₃	2	Ta ₂ O ₅
12/13/2022	2 sccm NH ₃ Quartz wool obstruction	12	Ta ₂ O ₅
12/19/2022	20 sccm NH ₃ Quartz wool obstruction	12	64% β-TaON 36% Ta ₃ N ₅

1/10/2023	5 sccm NH ₃ Quartz wool obstruction	12	96% β-TaON 3% γ-TaON 1% Ta ₃ N ₅
2/2/2023	5 sccm NH ₃ Quartz wool obstruction	4	95% β-TaON 2% γ-TaON 1% δ-TaON 2% Ta ₂ O ₅
2/15/2023	5 sccm NH ₃ Quartz wool obstruction	6	98% β-TaON 1% γ-TaON 1% Ta ₂ O ₅

Chapter 7: PLD growth of Ta- and Mo- oxynitride films

One of the goals of this thesis is to develop methods for the synthesis of new oxynitride materials. In this chapter thin film growth is explored as a method for achieving that goal. By utilizing epitaxial stabilization – where a film is strained by the epitaxial relationship with the substrate and this strain allows the film to grow as a phase that would not otherwise be stable – metastable phases that are not achievable by bulk synthesis methods can be grown as thin films. If an appropriate substrate is selected as a template, specific targeted phases can be grown. This allows the growth of new, never-before-synthesized oxynitride phases beyond those commonly produced by bulk synthesis and would expand the space of known and synthesizable oxynitrides.

In this chapter, three growth methods were explored to target the growth of metastable MoON and TaON phases: (1) PLD growth of epitaxial single crystal oxide films of the desired structure with post-deposition ammonolysis to incorporate N, (2) N-plasma assisted PLD, and (3) reactive sputtering. XPS and RBS were employed as methods to determine the composition of the films, while XRR, HRXRD, and in-plane, off-specular, and pole figure diffraction measurements were used to characterize the structure of the films.

7.1 Growth of rutile tantalum oxynitride

The lowest energy phase of TaON is the β -phase (sg: $P2_1/c$). Several other metastable phases, including the γ -phase (sg: $C2/m$) and δ -phase (sg: $I4_1/amd$), have been realized experimentally. In addition to the metastable phases that have been synthesized, the relative energy of rutile and fluorite phases have been calculated by DFT. The rutile phase is only ~ 20 kJ/mol higher energy than the anatase δ -phase. Since the δ -phase has been produced and the

rutile phase is only slightly less stable, it is potentially synthesizable and a good target for the use of epitaxial stabilization to further lower the energy. Achieving this phase would provide proof of concept for the use of thin film growth as a method for achieving oxynitride materials with target structures beyond those readily available by bulk synthesis methods, and as such in this chapter, growth of the rutile TaON phase was targeted via epitaxial thin film stabilization.

TaON films have been grown most commonly by sputter deposition, pulsed laser deposition (PLD), and ammonolysis of oxide films.^{74,128–133} While ammonolysis of Ta₂O₅ films resulted in polycrystalline β -TaON,^{128,129} single crystal films of β -TaON have been grown on yttria-stabilized zirconia (YSZ) by RF magnetron sputtering¹³⁴ and single-crystal δ -TaON films have been grown on (LaAlO₃)_{0.3}-(SrAl_{0.5}Ta_{0.5}O₃)_{0.7} (LSAT) by nitrogen plasma assisted PLD, using epitaxial stress from the substrate to stabilize the metastable δ -TaON phase.^{135,136} A similar method was employed for the growth of the rutile TaON phase.

7.1.1 Growth Method 1: Tantalum oxide PLD with post-deposition ammonolysis

Methods

Films of tantalum oxide were grown on α -Al₂O₃ (012) (r-plane sapphire) substrates by PLD. Substrates were annealed for two hours at 1000°C in air and cleaned with isopropanol before deposition. Deposition was performed in a PVD Products nanoPLD 1000 chamber with a 248 nm KrF excimer laser with a 25 ns pulse duration. A target of dense hot-pressed Ta₂O₅ purchased from Kurt J. Lesker Company was used. The deposition was performed at a pressure of 50 mTorr with a flow of 20 sccm O₂ and set point temperature of 1200°C, which corresponds

to a substrate temperature of $\sim 850^{\circ}\text{C}$. The substrate was glued to the holder with silver paste to achieve the highest possible substrate temperature. The film was deposited with 3000 pulses at 5 Hz and 200 mJ with a target-substrate separation of 100 mm.

A parallel beam with a Ge(220) 2-bounce monochromator was used for XRR, HRXRD, and in-plane measurements. 0.114° soller slits on the receiving arm were used to increase resolution for in-plane measurements. 0.5° soller slits on the incident and receiving arms were used for the off-specular and pole figure measurements. XRR, HRXRD, and off-specular measurements were collected in $\theta/2\theta$ geometry and the sample was aligned parallel to the incident beam. In-plane and pole figure measurements were collected in grazing incidence geometry.

Discussion

R-sapphire (Al_2O_3 (012)) was selected as the substrate for the targeted growth of rutile TaON due to the lattice match between the surface cell of the r-face of sapphire and the rutile phase. C-sapphire, Si, and strontium titanate (STO) substrates were also briefly explored, but r-sapphire was found to be the best substrate candidate. PLD depositions of tantalum oxide resulted in the growth of single crystal films of two structure types, rutile $\text{Ta}_{0.8}\text{O}_2$ and orthorhombic Ta_2O_5 . A range of deposition parameters was explored to optimize the conditions for film growth (Table 7.1). Ultimately, the growth of high quality tantalum oxide films was found to depend most strongly on the deposition temperature. The growths that resulted in single crystal films are marked in bold in the Table 7.1. Nearly all depositions done at set point temperatures below 1200°C did not produce single crystal films, with the exception of the 09302020a deposition, where a set point temperature of 1150°C still produced a single crystal

film. In this deposition a high oxygen pressure of 75 mTorr was used, and this may have contributed to a higher substrate temperature even at the lower set point temperature as the gas molecules present when using a high chamber pressure can more effectively conduct heat from the heater blocks to the substrate. Ultimately, extremely high temperatures were needed to produce single crystal tantalum oxide films, with only the maximum set point of 1200°C, corresponding to a substrate temperature of approximately 850°C, sufficient to crystallize the films. This set point could only be achieved when the heater blocks were new or freshly cleaned. Lower temperature depositions, including depositions with older heating blocks operating at 100% power but not able to reach 1200°C, resulted in polycrystalline or amorphous Ta₂O₅ films. Because the necessary deposition temperature was on the edge of the instrument capabilities, difficulties in reproducibly growing consistent films arose and high quality single crystal films were only produced on three occasions. Should the instrument be upgraded in the future to more consistently achieve higher substrate temperatures during the depositions, it may be possible to resolve these issues.

When single crystal growth was achieved, depositions resulted in the growth of either single crystal rutile Ta_{0.8}O₂ films with space group P4₂/mm or orthorhombic Ta₂O₅ films with space group Cmm2 or Cmmm (Figure 7.1b). The rutile Ta_{0.8}O₂ film was of interest as a first step to growth of rutile TaON and, as such, XRR, HRXRD, in-plane diffraction, pole figures, and XPS were used to characterize the film after growth.

Table 7.1: PLD growth parameters for attempted growth of tantalum oxide films from a Ta₂O₅ target. Unless otherwise noted, substrates were r-sapphire. Successful single crystal growths of rutile TaO_x are marked in bold. Marked in italics is the growth that resulted in single crystal orthorhombic Ta₂O₅.

Date	Chamber	Temperature (°C)	Oxygen Pressure (mTorr)	Laser Power (mJ)	Frequency (Hz)	Target-substrate separation	Notes
02112019	nanoPLD	1200	50	200	5	100	c-, r-, Si
05292019	nanoPLD	1000 (650)	50	200	5	75	
06112019	nanoPLD	1050 (700)	50	200	5	75	
07122019	nanoPLD	1200 (850)	50	200	5	100	
08082019	nanoPLD	1170	50	200	5	100	
08292019	nanoPLD	1200	50	200	5	100	Rubicon vs. UW
09132019	nanoPLD	1200	50	200	5	100	
06082020	PLD/MBE	1175	50	200	5	100	
06182020	PLD/MBE	1100	50	200	5	100	
07082020	nanoPLD	1100	50	200	5	100	not glued
07172020	nanoPLD	1120	50	200	5	100	
09042020	nanoPLD	1200	50	200	5	100	
09302020a	nanoPLD	1150	75	200	5	100	polished target
09302020b	nanoPLD	1150	25	200	5	100	low miscut
10012020	nanoPLD	1150	100	200	5	100	
10052020	nanoPLD	1150	50	120	1	100	
<i>04132021</i>	<i>nanoPLD</i>	<i>1200 (895)</i>	<i>50</i>	<i>200</i>	<i>5</i>	<i>100</i>	<i>new target</i>
05062021	nanoPLD	1150 (860)	50	200	5	100	
05192021	nanoPLD	1150 (850)	50	200	5	60	
06222021	nanoPLD	1140	50	130	5	100	
07142021	nanoPLD	1130 (805)	10	200	5	100	

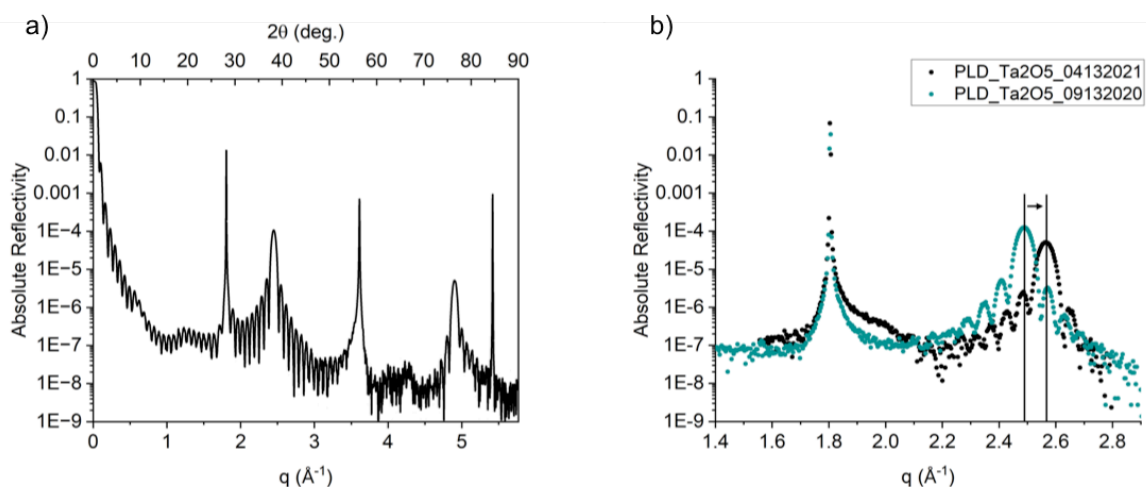


Figure 7.1: (a) HRXRD of epitaxial (101) $\text{Ta}_{0.8}\text{O}_2$ on (012) Al_2O_3 and (b) comparison of HRXRD of single crystal orthorhombic Ta_2O_5 and rutile $\text{Ta}_{0.8}\text{O}_2$.

HRXRD measurements were used to determine the orientation of the films (Figure 7.1). For the rutile film, the peak at $2\theta = 25.57^\circ$ ($q = 1.81 \text{ \AA}^{-1}$) corresponds to the Al_2O_3 (012) substrate, while the peak at $2\theta = 35.52^\circ$ ($q = 2.49 \text{ \AA}^{-1}$) corresponds to the film. Although the film was deposited from a Ta_2O_5 target, Ta_2O_5 has no reflections at this position, with the closest being the (111) reflection at $2\theta = 36.64^\circ$ ($q = 2.56 \text{ \AA}^{-1}$). Although strain in the film could cause shifting of the peak from the expected position, such a large change in the lattice constant is unlikely. However, rutile $\text{Ta}_{0.8}\text{O}_2$ has its (101) peak at $2\theta = 35.26^\circ$ ($q = 2.47 \text{ \AA}^{-1}$), matching well to the observed film peak in the XRD.^{137,138} The rutile structure is commonly found in films grown on r-plane sapphire, as the rectangular surface cell of the r-plane is a good geometric match for the tetragonal rutile structure. Indeed, the surface cell of Al_2O_3 (012), a rectangular cell with dimensions of 4.76 \AA by 5.13 \AA , matches the well to the rutile (101) plane, with its 2D cell having dimensions of 4.72 \AA by 5.64 \AA . The crystal structure of (101) oriented rutile TaO_x on r-sapphire is shown in Figure 7.2. While rutile tantalum oxide has been reported as both the TaO_2

or $\text{Ta}_{0.8}\text{O}_2$ stoichiometry, the film deposition was completed using a Ta_2O_5 target (Ta in the 5+ oxidation state) while flowing O_2 , making it unlikely the tantalum could have been reduced during deposition, making the $\text{Ta}_{0.8}\text{O}_2$ compound a more likely candidate. Additionally, the $\text{Ta}_{0.8}\text{O}_2$ (101) peak at 35.26° is a better match for the observed film peak than the TaO_2 (101) peak at $2\theta = 34.90^\circ$ ($q = 2.45 \text{ \AA}^{-1}$). We therefore propose the film structure to be $\text{Ta}_{0.8}\text{O}_2$ (101) // Al_2O_3 (012) (Figure 7.2).

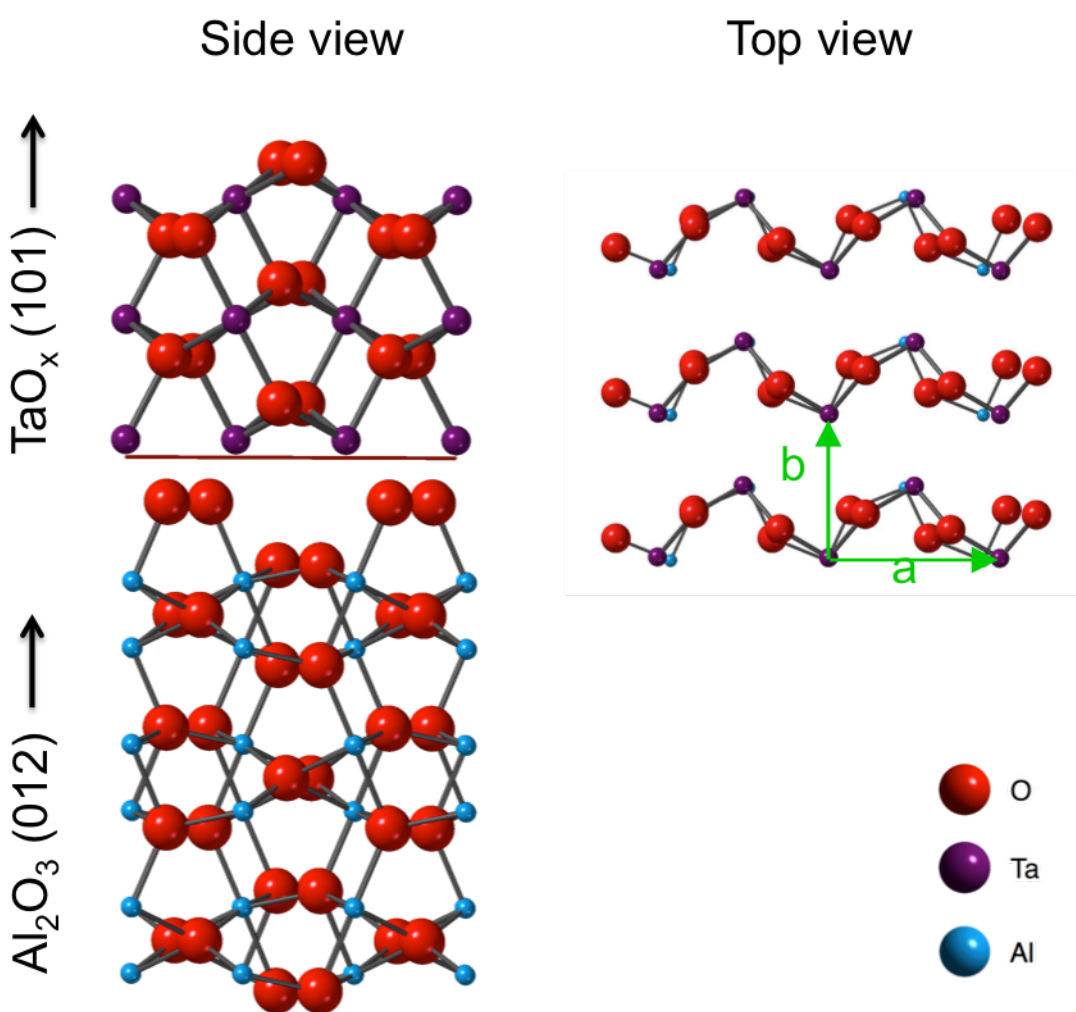


Figure 7.2: Crystal structure of (101) oriented rutile $\text{Ta}_{0.8}\text{O}_2$ on r-sapphire.

In order to confirm the proposed rutile structure of the film by identifying other expected reflections, in-plane and off-specular diffraction measurements were taken at the (040) and (121) Bragg conditions of the rutile $\text{Ta}_{0.8}\text{O}_2$. The (040) reflection was measured at $q = 5.34 \text{ \AA}^{-1}$ and the (121) reflection at $q = 3.60 \text{ \AA}^{-1}$. The presence of multiple reflections at the expected positions confirmed the rutile structure of the film and comparison of the $\text{Ta}_{0.8}\text{O}_2$ (040) peak to the Al_2O_3 (4-20) showed the in-plane epitaxial orientation to be $\text{Ta}_{0.8}\text{O}_2$ (010) // Al_2O_3 (2-10) (Figure 7.3e).

The films were further characterized by XRR to determine the film thickness, roughness, and electron density. XRR measurements showed the oxide films to be 109.2 \AA thick with a 5 \AA surface layer of slightly lower density. The electron density of the film was calculated to be 1.93 e/\AA^3 , very close to the expected bulk value for Ta_2O_5 of 1.95 e/\AA^3 (Figure 7.3c).

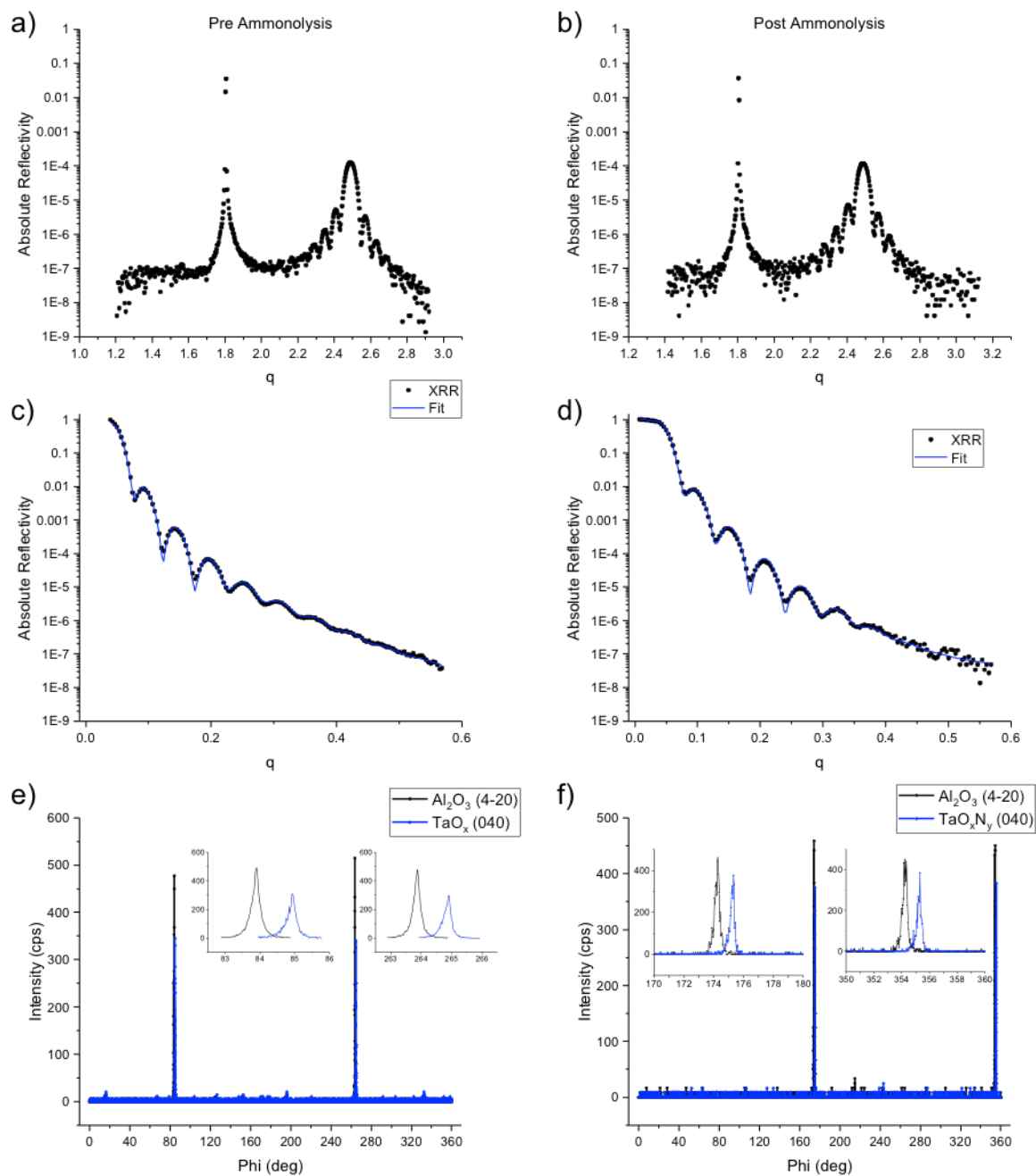


Figure 7.3: Pre-ammonolysis (a) specular XRD, (c) XRR, (e) in-plane diffraction, and post ammonolysis (a) specular XRD, (c) XRR, (e) in-plane diffraction indicates no change in crystal structure following the ammonolysis treatment.

XPS measurements were taken at the Ta 4f and O 1s binding energies to determine the chemical composition and oxidation states of the species (Figure 7.4). The Ta 4f consists of a $4f_{7/2}$ and $4f_{5/2}$ doublet, with the expected binding energy for the Ta $4f_{7/2}$ peak at 26.3-26.6 eV for Ta_2O_5 , 24.7-25.0 eV for Ta_3N_5 , and 25.0-26.0 eV for TaON.^{4,139-141} For the as-deposited oxide film, a single doublet was used to fit the Ta 4f region, with the $4f_{7/2}$ binding energy at 26.0 eV. This is within the range of expected binding energy values for Ta_2O_5 , confirming that tantalum remained in the 5+ oxidation state. The atomic ratios, calculated from the integrated XPS signal corrected for the relative sensitivity factors and inelastic mean free path of the photoelectrons, gave a composition of $Ta_{0.84}O_2$ for the oxide film.

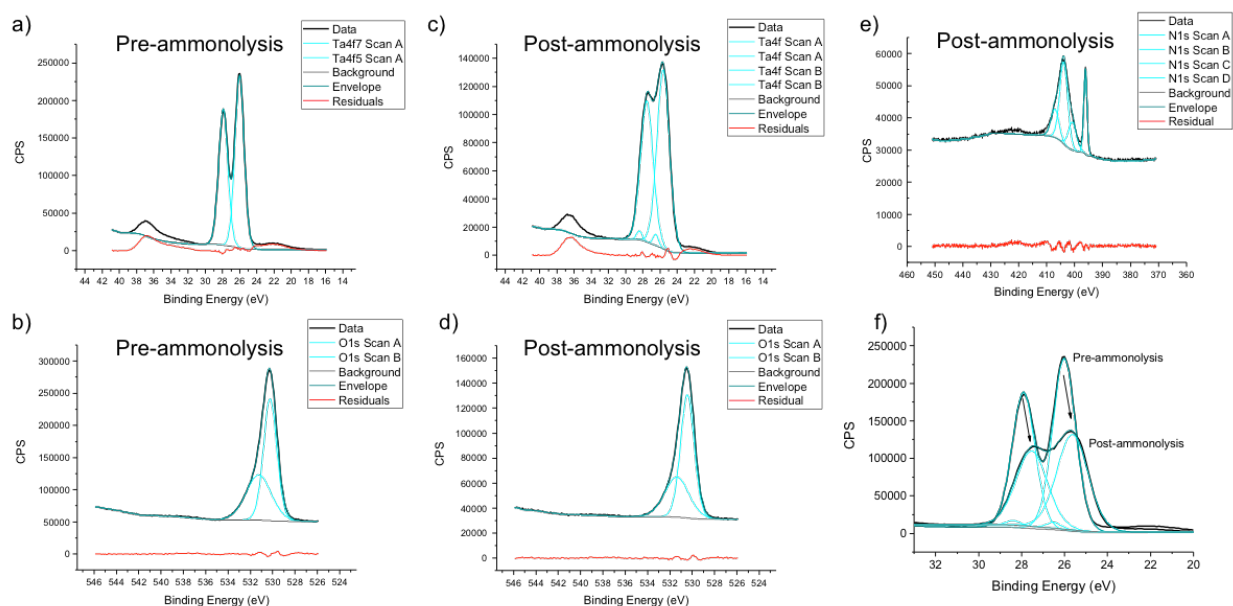


Figure 7.4: XPS of (a) the Ta4f and (b) the O1s spectra of the as deposited $Ta_{0.84}O_2$ film and (c) the Ta4f, (d) O1s, (e) N1s spectra of the film after ammonolysis. The N1s spectra overlaps with the Ta 4p and appears as the sharp peak to the right in the spectrum. A comparison of the Ta4f spectra pre- and post-ammonolysis is shown in (f).

A series of ammonolysis attempts were used to convert the $Ta_{0.84}O_2$ film to an oxynitride (Table 7.2). The powder synthesis discussed in Chapter 4 showed that the use of dry ammonia typically results in the synthesis of Ta_3N_5 instead of TaON and this was the case for the film as

well – following dry ammonolysis, the film turned red (Figure 7.5a) and XPS showed significant nitrogen incorporation into the film and XRD confirmed polycrystalline Ta_3N_5 . In order to incorporate N into the film without inducing a phase transition, wet ammonolysis was used to slow down the reaction. Ultimately, a flow of 50 sccm NH_3 and 20 sccm Ar through a room temperature bubbler with an annealing time of 35 hours at $850^\circ C$ was found to successfully incorporate nitrogen while maintaining the rutile single crystal structure of the oxide film. Following this treatment, the film turned yellow, the color of TaON (Figure 7.5b).

Table 7.2: Ammonolysis recipes and corresponding results for the nitridation of TaO_x single crystal films deposited by PLD.

Heating Conditions	Hold Time	Gas Flow	Result
RT \rightarrow $850^\circ C$ @ $5^\circ C/min$	5 hrs	20 sccm NH_3 50 sccm Ar/ H_2O	Single crystal No nitrogen incorporation
RT \rightarrow $850^\circ C$ @ $5^\circ C/min$	35 hrs	20 sccm NH_3 50 sccm Ar/ H_2O	Single crystal No nitrogen incorporation
RT \rightarrow $850^\circ C$ @ $5^\circ C/min$	35 hrs	50 sccm NH_3	Polycrystalline Ta_3N_5 Has nitrogen incorporation
RT \rightarrow $850^\circ C$ @ $5^\circ C/min$	35 hrs	50 sccm NH_3 20 sccm Ar/ H_2O	Single crystal Has nitrogen incorporation

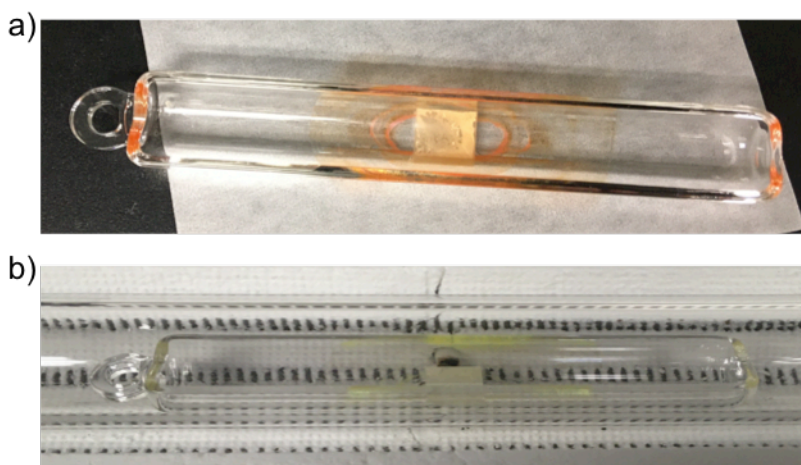


Figure 7.5: (a) After dry ammonolysis using a flow of 50 sccm anhydrous NH₃ the Ta_{0.8}O₂ film turned red, a color indicative of Ta₃N₅, (b) after wet ammonolysis using a flow of 50 sccm NH₃ and 20 sccm Ar/H₂O the Ta_{0.8}O₂ film turned yellow, a color indicative of TaON.

Following ammonolysis treatment, XPS showed the appearance of a strong N 1s peak (Figure 7.4e). Furthermore, the Ta 4f region for the oxynitride showed two doublets, a primary doublet with the Ta 4f_{7/2} peak at 25.6 eV and a minor set with the Ta 4f_{7/2} peak at 26.5 eV (Figure 7.4c). Based on the binding energy of the peaks, the strong doublet can be assigned to an oxynitride (reference binding energy of 25.0-26.0 eV) and the minor doublet to the binding energy of Ta₂O₅ (reference binding energy 26.3-26.6 eV), likely due to a small amount of unreacted or surface oxide. A clear shift in the Ta 4f binding energies from the oxide positions to lower binding energy can be seen following ammonolysis, as shown in Figure 7.4f. After removing the contributions from the surface oxide, the atomic ratios of the oxynitride film were found to be 31.5% Ta, 50.9% O, 17.6% N, corresponding to a composition of roughly Ta₂O₃N.

HRXRD measurements showed no change in the film peak with the position remaining at $2\theta = 35.51^\circ$ ($q = 2.49 \text{ \AA}^{-1}$) (Figure 7.3b). Owing to their similar scattering factors, distinguishing nitrogen and oxygen by x-ray diffraction is difficult, so if the structure of the film remained the same except for the substitution of oxygen for nitrogen, it is not expected that any changes would

be seen in the diffraction pattern. The width of the peak indicated a vertical crystalline domain size commensurate with the thickness of the film as measured by XRR. XRR also showed that the film retained similar thickness to before the ammonolysis treatment, with loss of the surface layer and reduction of the roughness consistent with high temperature annealing (Figure 7.3d). The electron density of the film decreased from $1.93 \text{ e}/\text{\AA}^3$ to $1.83 \text{ e}/\text{\AA}^3$, a change consistent with replacing oxygen in the structure with nitrogen, an atom with one fewer electron. As with the HRXRD, in-plane measurements of the film post ammonolysis showed the same in-plane epitaxial relation as the oxide film (Figure 7.3f). Presence of these reflections at the expected positions confirms that the film retained the rutile structure following ammonolysis and the incorporation of nitrogen into the film.

While this technique showed potential for producing the rutile TaON phase, due to the difficulties discussed above in reproducibly growing the rutile tantalum oxide film, no further films could be produced to continue this approach of producing tantalum oxynitride films. With no more samples to study, it was not possible to continue tailoring the ammonolysis conditions to incorporate more nitrogen into the films or produce more samples for further property measurements; however, the results shown here are a promising initial step towards the realization of the rutile TaON phase. Should future development or upgrades to the PLD instrument allow for higher temperature growths, this is an encouraging avenue for further study and a potentially useful method for the growth of metastable oxynitride materials that are difficult to achieve by other synthesis methods.

7.1.2 Growth method 2: N-plasma assisted PLD of TaON

In 2022, the PLD facility acquired and installed a RF plasma source capable of producing atomic nitrogen. Several reports exist for the use of activated nitrogen for growing nitride and oxynitride films.^{135,136,142,143} This technique differs from that of growing oxide films and using ammonolysis to convert them to oxynitrides because it allows the incorporation of nitrogen into the films during growth. This means that oxynitride phases that do not have direct oxide analogs can be targeted. For example, Suzuki et al. were able to grow anatase δ -TaON, a phase difficult to produce by bulk synthesis, by nitrogen plasma assisted PLD.^{135,136} While a high temperature anatase variant of Ta₂O₅ does exist,¹⁴⁴ targeting the δ - and other phases by direct growth with nitrogen incorporation still expands the space of achievable phases and allows exploration of another growth pathway. By selecting substrates with surface cells that match those of the oxynitride phases of interest, specific phases can be preferentially grown by lattice matching and epitaxial strain stabilization of the oxynitride films.

This method was explored as another route to grow the rutile TaON phase. In this method, the RF atom source is used to split N₂ gas into atoms, a highly active source of nitrogen, inside the PLD chamber. The atomic N in the chamber reacts with the depositing film during growth to directly nitride the material as it is produced. The plasma source was installed on the nanoPLD chamber and, beginning with the parameters identified for successful growth of the tantalum oxide films, a series of depositions were done to determine the optimal conditions for growth using the N source (Table 7.3). Parameters to control both the N content and the crystalline quality of the films were explored, including the forward power of the source, the flow of gas supplied to the source, the use of neutral or ionized plasma, the background pressure of other gases in the chamber, the substrate temperature, and the timing of plasma application

during deposition and cooling. Representative GIXRD and XPS data are shown for one of the films produced during this series (Figure 7.6). All of the films were rough and polycrystalline and the highest nitrogen content achieved was < 20 atomic %. The low chamber pressure needed to allow a sufficiently high mean free path for the N to reach the substrate during deposition caused increased roughness and decreased quality of the resultant films, but increasing the oxygen supplied during deposition greatly reduced the N content of the films. No deposition parameters could be found to achieve single crystal films with high nitrogen content.

Table 7.3: PLD growth parameters for attempted growth of TaON films by N-plasma assisted PLD. A Ta₂O₅ target, r-sapphire substrates, and target-substrate separation of 100mm were used for all depositions.

Date	Temperature Set Point (°C)	Laser Power (mJ)	Frequency (Hz)	Atom source power (W)	N pressure (mTorr)	Shutter open during cooling	Ion filter on
08052022	1100	200	5	300	3 E -4	N	N
08112022	1080	200	5	300	3 E -4	Y	N
0812022	1050	200	5	300	3 E -4	Y	Y
08172022	1050	200	5	300	3 E -4	N	Y
09142022	1200	200	1	300	3 E -4	Y	N
09212022	1200	130 + 7 attenuator plates	5	300	3 E -4	Y	N
10192022	900	200	5	300	3 E -4	Y	N
10212022	1000	200	5	300	3 E -4	Y	N
11292022	1130	200	5	400	3 E -4	Y	N
12012022	1130	200	5	300	3 E -4 + 2 mTorr O ₂	Y	N

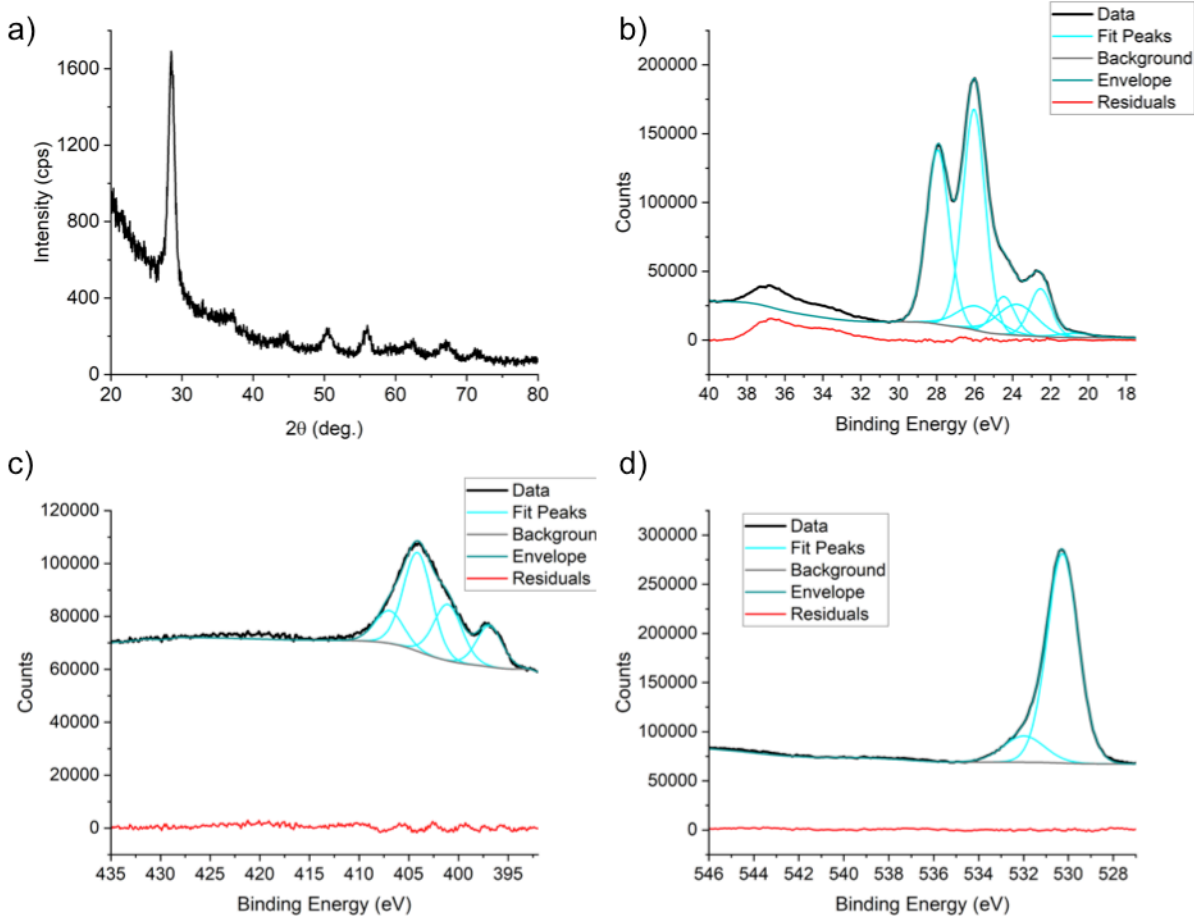


Figure 7.6: (a) GIXRD and XPS of the (b) Ta4f, (c) N1s (overlapping with Ta4p), and (d) O1s from a polycrystalline film produced by N-plasma assisted PLD of Ta₂O₅.

Separately, the use of the plasma source incorporate nitrogen into an oxide film directly after growth without removing the film from the deposition chamber was explored. The film was deposited using the standard parameters for growth of a tantalum oxide film, and following the deposition the oxygen was pumped from the chamber and atomic N was introduced. The film was left at a temperature of 1150°C (set point) overnight (~17 hours) with the atomic N

continuously supplied. Despite the length of time allowed for nitrogen incorporation, only a negligible amount of N was detected when the composition was measured by XPS.

Due to the difficulties in achieving both high quality films and high nitrogen incorporation simultaneously, the use of N-plasma assisted PLD to grow oxynitride films was deemed a challenging method for the growth of TaON and was not pursued further in this work.

7.1.3 Growth method 3: Reactive sputtering of TaON

Reactive sputtering was explored as another method to incorporate nitrogen in the films directly during growth. In this method cation atoms are sputtered from a metal target and anion atoms are supplied from a gas stream at the substrate that is activated by the plasma from the target. For the purpose of growing tantalum oxynitride, a Ta target was used with Ar as the sputtering gas and oxygen and nitrogen supplied at the substrate. This method produced a much higher N content in the film than N-plasma assisted PLD (Figure 7.7a-c); however, owing to heating limitations in the chamber, only a maximum substrate temperature of 600°C could be achieved, and this temperature was insufficient for the growth of crystalline films. XPS showing a film composition of 30.6% Ta, 43.5% N, and 25.9% O and XRD showing the TaON film produced by sputtering to be amorphous are presented in Figure 7.7d.

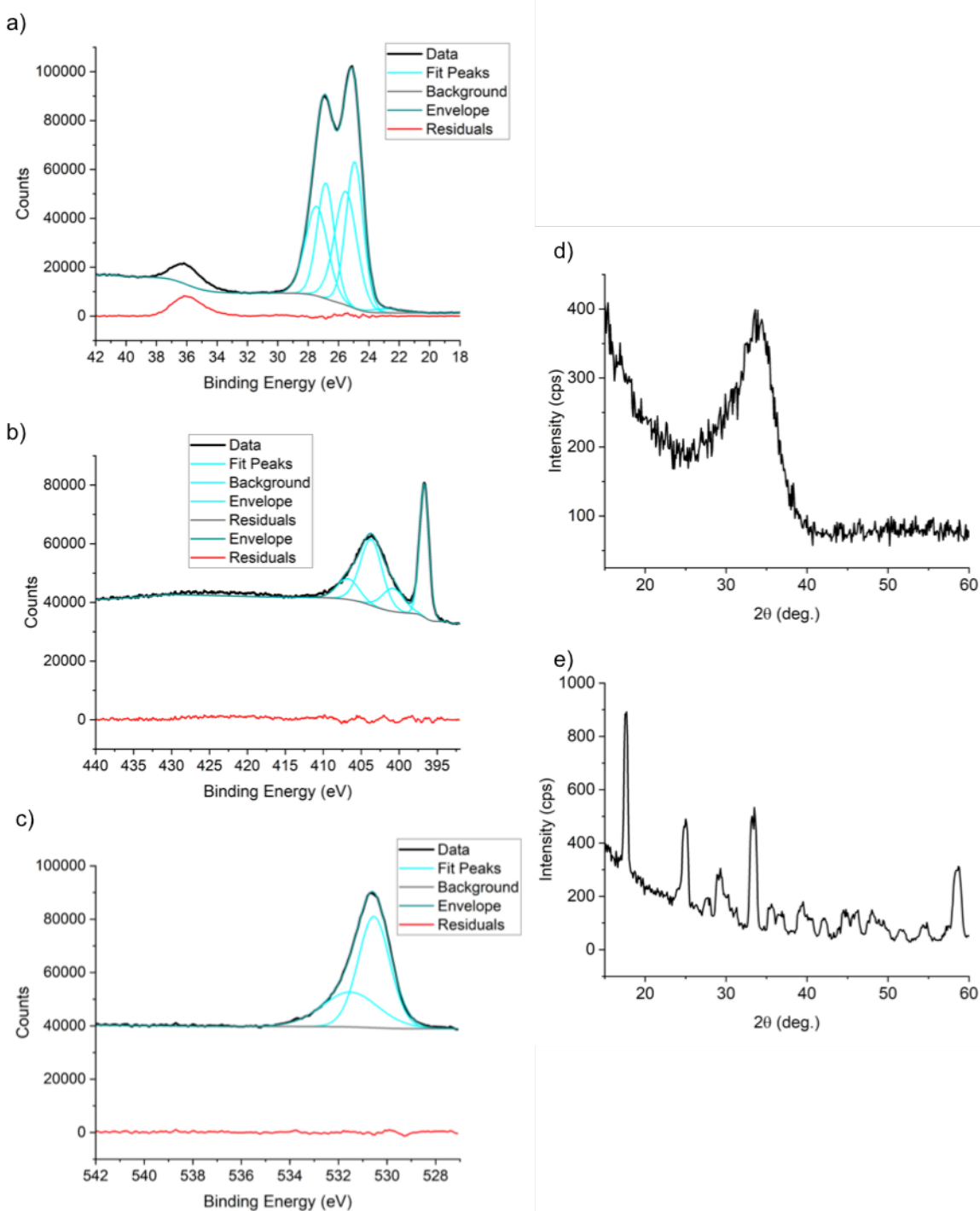


Figure 7.7: XPS of the (a) Ta4f, (b) N1s (overlapping with the Ta4p), and (c) O1s spectra for the TaON film produced by reactive sputtering. GIXRD of (d) the as deposited film shows the film to be amorphous and (e) after annealing at 1200°C the film became polycrystalline.

Post-deposition annealing was attempted in order to crystallize the amorphous film deposited by reactive sputtering. The film was heated to 1200°C under 500 sccm of N₂ at a rate of 10°C/min, held at 1200°C for 3 hours, and monitored by in situ XRD for crystallization. This treatment resulted in formation of polycrystalline Ta₂O₅ at 800°C, followed by a phase transition to another unidentified polycrystalline phase above 1000°C which persisted through the hold at 1200°C and cooling to room temperature (Figure 7.7e). A single crystal film was not achieved by post-deposition annealing.

7.2 Growth of monoclinic molybdenum oxynitride

Monoclinic MoON is a phase of interest as it is predicted to have a Peierls metal-insulator transition (MIT) at ~627°C when transforming from an ordered low temperature α -phase to a disordered high temperature β -phase.⁵² The α -phase is the ground state phase and has a TcO₂ structure type (the symmetry is reduced by anion ordering from the homoanionic TcO₂ space group of P4₂/mnm to Pc in the heteroanionic compound) composed of Mo-Mo dimers with alternating short and long Mo-Mo bond distances and Mo atoms displaced perpendicular to the anion chains. The anions are order about the Mo atoms with three nitrogen and three oxygen atoms coordinating each Mo atom. The β -phase has a MoO₂ structure type (similar to the TcO₂ structure, the symmetry is reduced by anion ordering from the homoanionic space group of P2₁/c to Pc in the heteroanionic compound) with all Mo-Mo bond distances equal and the alternating Mo displacements seen in the low temperature phase absent. The Mo atoms are instead uniformly displaced parallel to the anion chains toward the nitride side creating the disorder in the structure. Like the α -phase, the β -phase has ordered anions with three oxygen and nitrogen atoms coordinating each Mo atom. The structural conformation of these phases is key, as in

order to display the MIT the Mo must have a d^1 electronic configuration. For Mo to have this electronic configuration, it must be in the +5 oxidation state; practically, this means the material must have the exact 1:1:1 MoON stoichiometry and the ordered anion coordination of the Mo atoms in order to display the MIT.

While there are no reports of synthesis or growth of either bulk or thin film MoON with the above described structure types, films of MoO_2 , Mo_2N , and MoN have been grown by sputtering,¹⁴⁵⁻¹⁴⁷ atomic layer deposition,^{148,149} PLD,¹⁵⁰⁻¹⁵⁸ and chemical vapor deposition.^{159,160} $\gamma\text{-Mo}_2\text{N}$ and MoN can be selectively grown by epitaxial stabilization on MgO or SrTiO_3 and c-cut sapphire, respectively.^{161,162} MoO_2 can also be grown epitaxially on c-cut sapphire in a distorted rutile structure (sg. $\text{P}2_1/\text{c}$).¹⁶³ Additionally, due to the wide range of non-stoichiometry in molybdenum nitride phases, MoN_x films can be grown with compositions ranging from $0.5 \leq x \leq 1$.¹⁶⁴

Since single crystal thin films of MoO_2 in the $\text{P}2_1/\text{c}$ space group - the structure type for the high temperature MoON phase (Figure 7.8) - can be grown, in this work several methods for the incorporation of N into these films without changing the crystal structure were explored as a means to realizing the MoON phase.

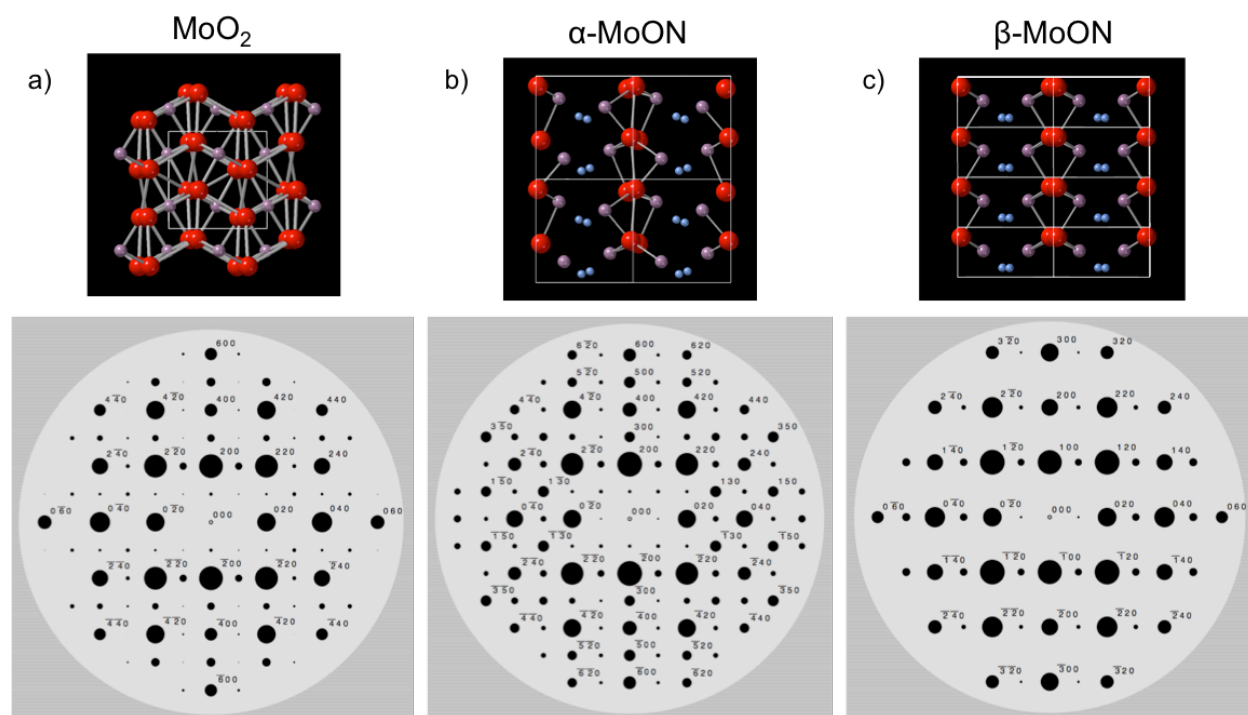


Figure 7.8: Crystal structures and single crystal diffraction patterns oriented with the (200) direction up of (a) MoO_2 , (b) $\alpha\text{-MoON}$, and (c) $\beta\text{-MoON}$. The $\beta\text{-MoON}$ phase has the same structure as MoO_2 with half the oxygen atoms replaced with nitrogen.

7.2.1 Growth method 1: Molybdenum oxide PLD with post-deposition ammonolysis

Methods

Films of molybdenum oxide were grown on $\alpha\text{-Al}_2\text{O}_3$ (001) (c-plane sapphire) substrates by PLD. Substrates were annealed for two hours at 1000°C in air and cleaned with isopropanol before deposition. Deposition was performed in a PVD Products nanoPLD 1000 chamber with a 248 nm KrF excimer laser with a 25 ns pulse duration. A target of dense hot-pressed MoO_3 purchased from Kurt J. Lesker Company was used. The deposition was performed at a pressure of 10 mTorr O_2 and set point temperature of 550°C , corresponding to a substrate temperature of

400°C. The film was deposited with 500 pulses at 5 Hz and laser energy of 150 mJ with a target-substrate separation of 80 mm.

Discussion

Single crystal MoO₂ was grown by PLD on α -Al₂O₃ (001) (c-plane sapphire) from a MoO₃ target. HRXRD showed the films to be monoclinic MoO₂ with out-of-plane orientation of (200). In-plane diffraction measurements confirmed the epitaxial orientation of the films to be MoO₂ (200) // Al₂O₃ (001) and MoO₂ (020) // Al₂O₃ (-210) (Figure 7.9). The crystal structure of the (200) oriented film on the c-sapphire substrate is shown in Figure 7.10.

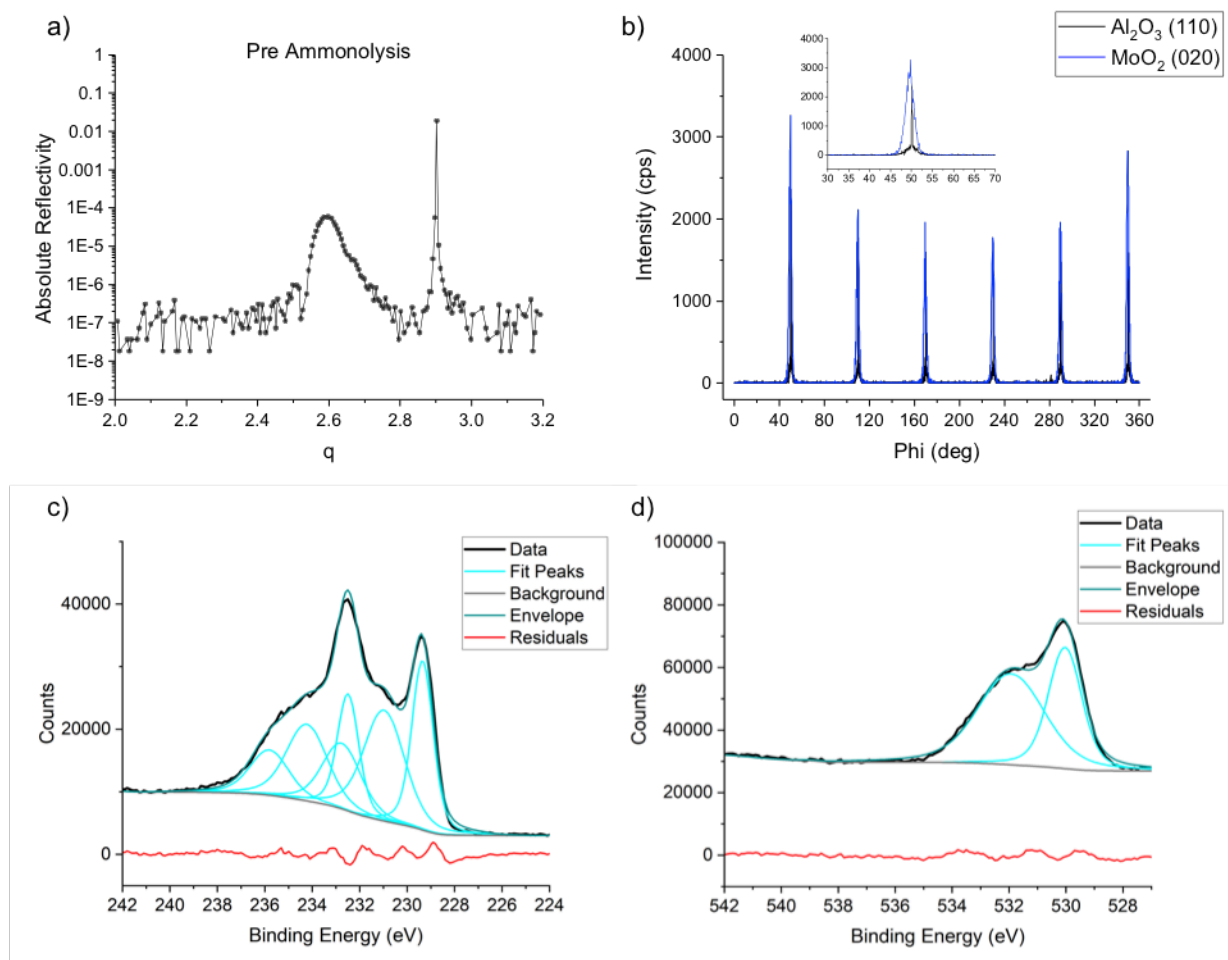


Figure 7.9: (a) Specular XRD, (b) in-plane XRD, (c) Mo3d XPS spectrum, and (d) O1s spectrum for the as deposited MoO_2 film.

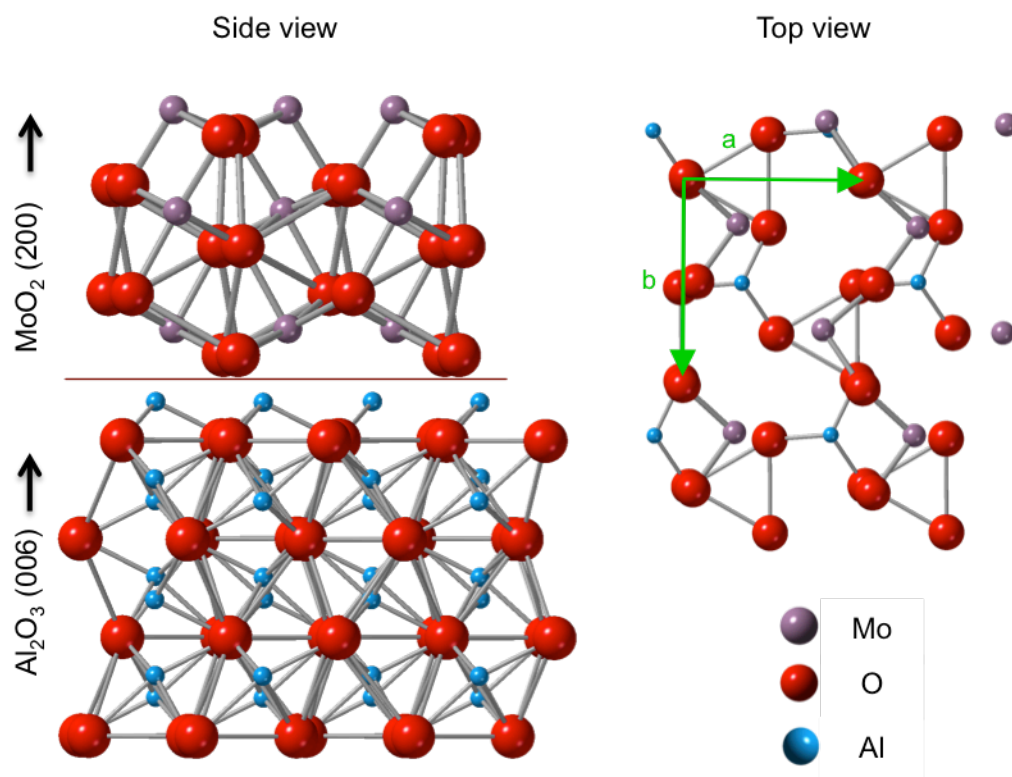


Figure 7.10: Crystal structure of (200) oriented MoO₂ on c-sapphire.

XPS measurements taken at the Mo 3d showed three doublets with binding energies of 229.1 eV, 230.2 eV, and 232.1 eV (Figure 7.9c). The Mo 3d consists of a 3d_{5/2} and 3d_{3/2} doublet, with the expected binding energy for the Mo 3d_{5/2} peak at 233.1 eV for MoO₃, 229.5 eV for MoO₂, and 228.8 eV for Mo metal (Avantage KnowledgeView). The binding energies used to fit the XPS of the film corresponded to the binding energies of MoO₂ and a slightly higher, or more oxidized, binding energy. Multiple doublets are typically needed to fit the MoO₂ spectra and the measured profile matched to that of a bulk MoO₂ standard.

Numerous ammonolysis recipes, including varying the reaction temperature, time, flow rate, and gas composition, were explored for the incorporation of nitrogen into the MoO₂ films (Table 7.4). The composition of the resulting films was measured by XPS and the structure and

crystallinity were evaluated by XRR and XRD. High temperature ammonolysis (700°C) resulted in polycrystalline films, even at short reaction times, while a reaction temperature of 400°C was found to be too low to induce nitrogen incorporation in the film. Even at a reaction temperature of 500°C, dry ammonolysis resulted in polycrystalline films. The use of wet ammonolysis, however, allowed retention of the single crystal nature of the films, likely because it slowed down the reaction enough to allow nitrogen incorporation without a change in the crystal structure. A nearly equal anion ratio and the closest composition to the desired MoON stoichiometry was achieved using a flow rate of 100 sccm NH₃ and 35 sccm Ar through a room temperature bubbler with an annealing time of 16 hours at 500°C. This produced a film of composition 40% Mo, 31% O, and 29% N (Figure 7.11). Although the O:N ratio was close to the desired 1:1 ratio, the anion to cation ratio was low, with the sample being overall deficient in anions. XRD of the film before and after the ammonolysis procedure is identical, indicating retention of the MoO₂ structure after ammonolysis (Figure 7.12).

Table 7.4: Ammonolysis recipes and corresponding results for the nitridation of MoO₂ single crystal films deposited by PLD.

Temperature	Time	Gas	Result
700°C	3 hrs	100 sccm NH ₃	Polycrystalline 44% Mo/6% O/50% N
700°C	30 min	100 sccm NH ₃	Polycrystalline 38% Mo/23% O/39% N
700°C	1.5 hrs	100 sccm NH ₃	Polycrystalline 38% Mo/22% O/40% N
700°C	3 hrs	100 sccm Ar	Polycrystalline
400°C	8 hrs	100 sccm NH ₃	No nitrogen incorporation
500°C	10 hrs	100 sccm NH ₃	Polycrystalline
500°C	16 hrs	100 sccm NH ₃ 50 sccm Ar/H ₂ O	Single crystal 37% Mo/21% O/29% N/12% Al
500°C	16 hrs	100 sccm NH ₃ 20 sccm Ar/H ₂ O	Single crystal 38% Mo/33.5% O/28.5% N
500°C	16 hrs	100 sccm NH ₃ 35 sccm Ar/H ₂ O	Single crystal 40% Mo/31% O/29% N

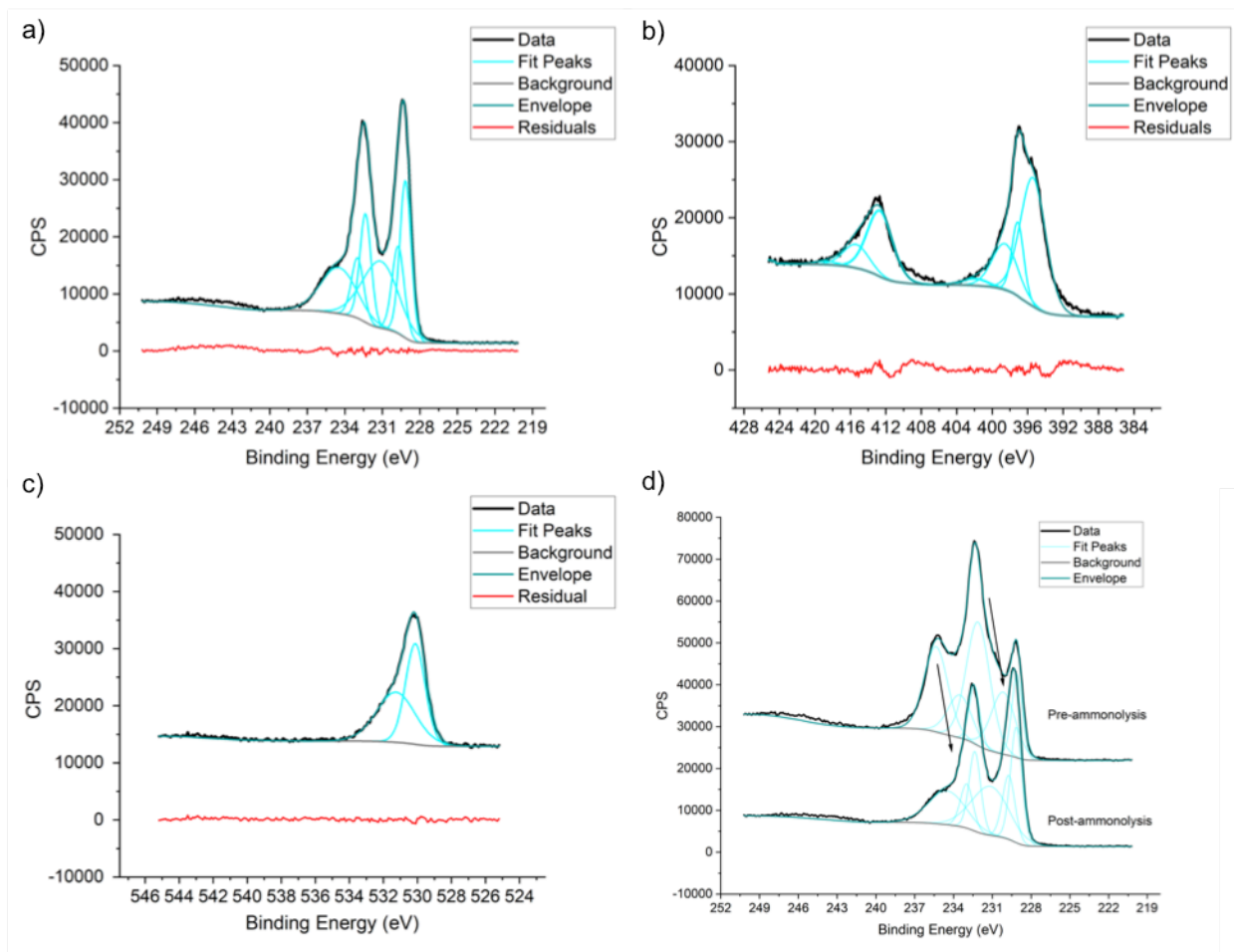


Figure 7.11: XPS of the MoON film produced by ammonolysis of MoO₂ using a flow rate of 100 sccm NH₃ and 35 sccm Ar/H₂O at a temperature of 500°C for 16 hours: (a) Mo3d, (b) N1s (overlapping with Mo3p), (c) O1s, and (d) comparison of Mo3d spectra pre- and post-ammonolysis.

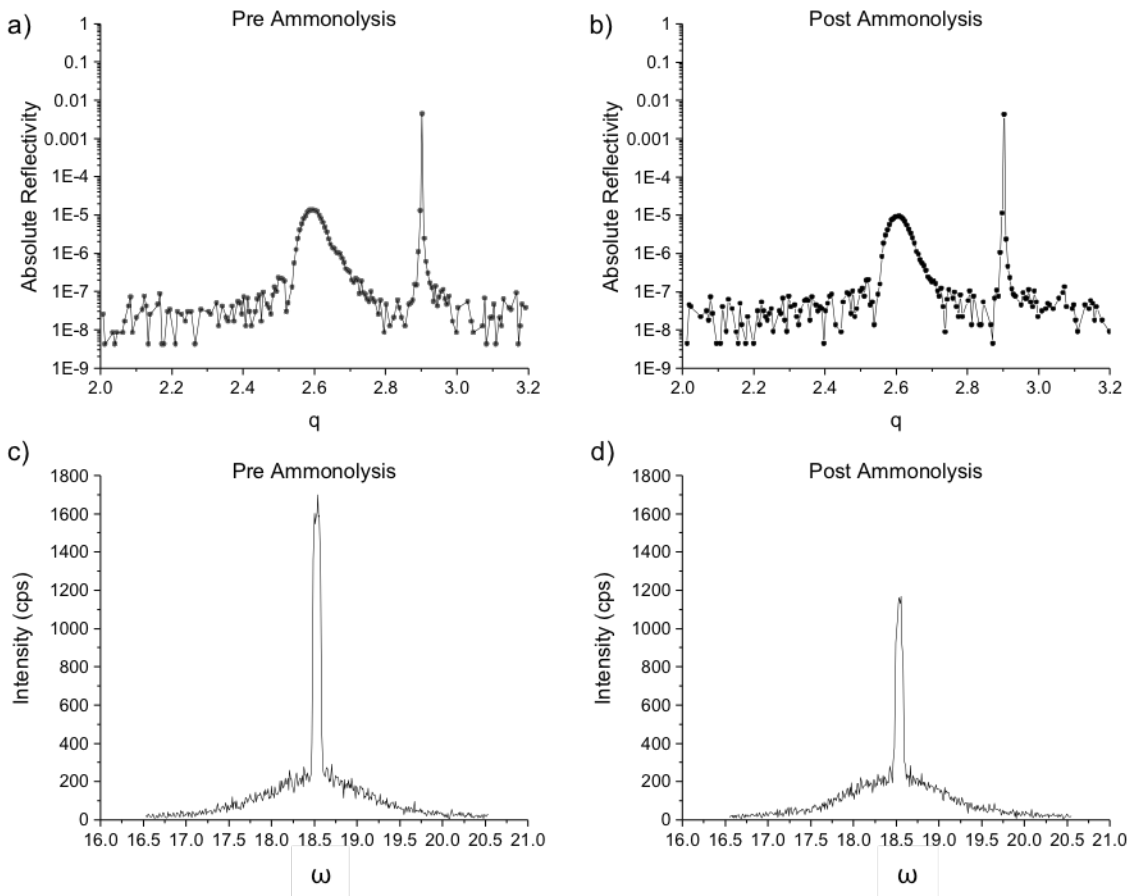


Figure 7.12: Specular XRD (a), (b) and rocking curves (c), (d) of the MoO_2 film pre- and post-ammonolysis.

Of additional concern in these syntheses is the fact that previous studies of bulk molybdenum oxynitride produced by ammonolysis have shown significant H incorporation.^{47,92} Hydrogen incorporation into the MoON films would preclude the formation of the MoON with the necessary +5 oxidation state to have the d^1 electronic configuration required to display the MIT. In order to determine if there was H content in the MoON films produced by ammonolysis RBS/FReS measurements were performed on the post-ammonolysis films at the Characterization Facility at the University of Minnesota. Figure 7.13 shows the FReS signal for the MoON film

compared to the signal from a mica reference sample containing 9.5% H. The hydrogen signal from the film indicates a H content of $\sim 1\text{-}2\%$, a sufficient H content to preclude the formation of MoON with the necessary +5 oxidation state to display the MIT. While increasing the ammonolysis temperature can reduce hydrogen incorporation, high temperature ammonolysis was incompatible with retaining the single crystal nature of the films (Table 7.4). Based on this information, ammonolysis of MoO₂ films was deemed an unsuitable method for the synthesis of MoON due to the hydrogen incorporation occurring along with the nitrogen incorporation.

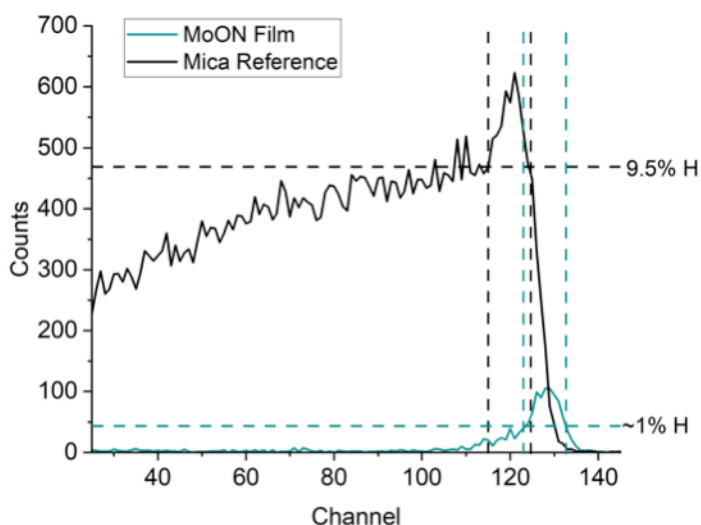


Figure 7.13: FReS measurement of the MoON film produced by ammonolysis of PLD grown MoO₂ in comparison to a mica reference sample containing 9.5% H shows the film to contain $\sim 1\%$ H after the ammonolysis procedure.

7.2.2 Growth method 2: N-plasma assisted PLD of MoON films

Using the PLD recipe for MoO₂ growth as the starting point, N-plasma assisted PLD was studied as an option for growing MoON films without hydrogen. The parameters explored for

the depositions are listed in Table 7.5. In all cases in which N plasma was used during the deposition, the resulting films were poorly crystallized with large polycrystalline contributions to the diffraction patterns. Representative diffraction data is shown in Figure 7.14a. Additionally, negligible or no nitrogen was detected in any of the films by XPS (Figure 7.14d). As such, N-plasma assisted PLD of MoON was not pursued further in this work.

Table 7.5: PLD growth parameters for attempted growth of MoON films by N-plasma assisted PLD. A MoO₃ target and c-sapphire substrates were used for all depositions.

Date	Temperature Set Point (°C)	N pressure (mTorr)	Power (mJ)	Frequency (Hz)	Target-substrate separation (mm)
12212021a	550	2.5 E -4	200	5	100
12212021b	550	2.5 E -4	200	1	100
12232021a	650	2.5 E -4	200	5	100
12232021b	550	2.5 E -4	250	5	100
01122022	550	1.3 E -3	200	5	100
01212022a	550	10 mTorr O ₂ during, 2.5 E -4 N for 1hr post deposition	200	5	100
01212022b	550	2.5 E -4	200	5	80

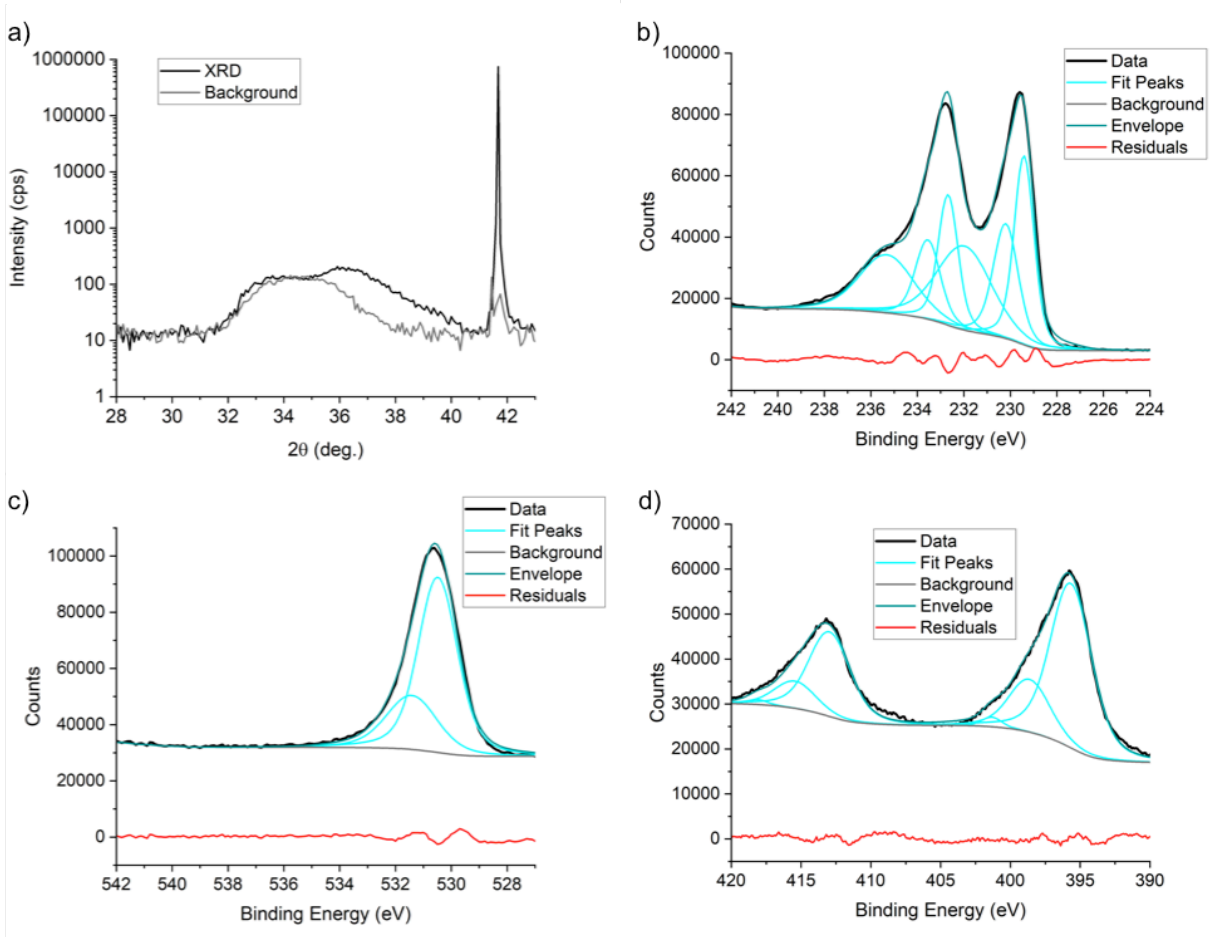


Figure 7.14: (a) Specular XRD of a representative film grown by N-plasma assisted PLD of an MoO_3 target shows a poorly crystallized film with large polycrystalline contribution. XPS of the (b) $\text{Mo}3d$, (c) $\text{O}1s$, and (d) $\text{N}1s$ (overlapping with $\text{Mo}3p$) spectra. No $\text{N}1s$ signal is seen in the $\text{N}1s/\text{Mo}3p$ range.

7.2.3 Growth method 3: Reactive sputtering of MoON films

Because of the low nitrogen incorporation by N-plasma assisted PLD, reactive sputtering was studied as another potential method for growth of MoON films. The sputter grown films were characterized by XRR and XRD for structure and film quality and by XPS for composition. The attempted deposition parameters and resulting film characteristics are listed in Table 7.6.

Ultimately, smooth single crystal films with a composition of 39% Mo, 33% O, 28%

N were the closest to the MoON stoichiometry achieved. Figure 7.15 displays the XRD, XRR, and XPS measurements for this film, showing the composition and smooth, single crystal nature of the film.

Table 7.6: Deposition parameters for attempted growth of MoON films by reactive sputtering. A Mo target, c-sapphire substrates, substrate temperature of 400°C, and 20 minute equilibration and pump down time upon reaching the target temperature were used for all depositions. All films were cooled in base pressure unless otherwise noted.

Date	Ar Flow (sccm)	N ₂ Flow (sccm)	O ₂ Flow (sccm)	Pressure (mTorr)	Power (W)	Deposition Time (s)	Composition
03082022	16	4	0	2	150	480	41.1% Mo, 26.5% O, 32.4% N
03102022	14	5	1	5	150	480	41.4% Mo, 56.1% O, 2.5% N
03162022	14	5	1	2	150	480	38.6% Mo, 45.7% O, 15.6% N
03172022	14.5	5	0.5	2	150	480	40.8% Mo, 32.5% O, 26.7% N
03232022	13	6.5	0.5	2	150	480	39.1% Mo, 33.3% O, 27.6% N
03242022	13	6.5	0.5	1	150	480	40.3% Mo, 28.3% O, 31.4% N
03292022	13	6.5	0.5	2	100	640	37.7% Mo, 38.2% O, 24.1% N
03312022	13	6.5	0.5	1	100	1280	39.3% Mo, 32.6% O, 28.1% N
04212022	13	6.5	0.5	2	100	1280	39.2% Mo, 34.2% O, 26.6% N *cooled in N ₂

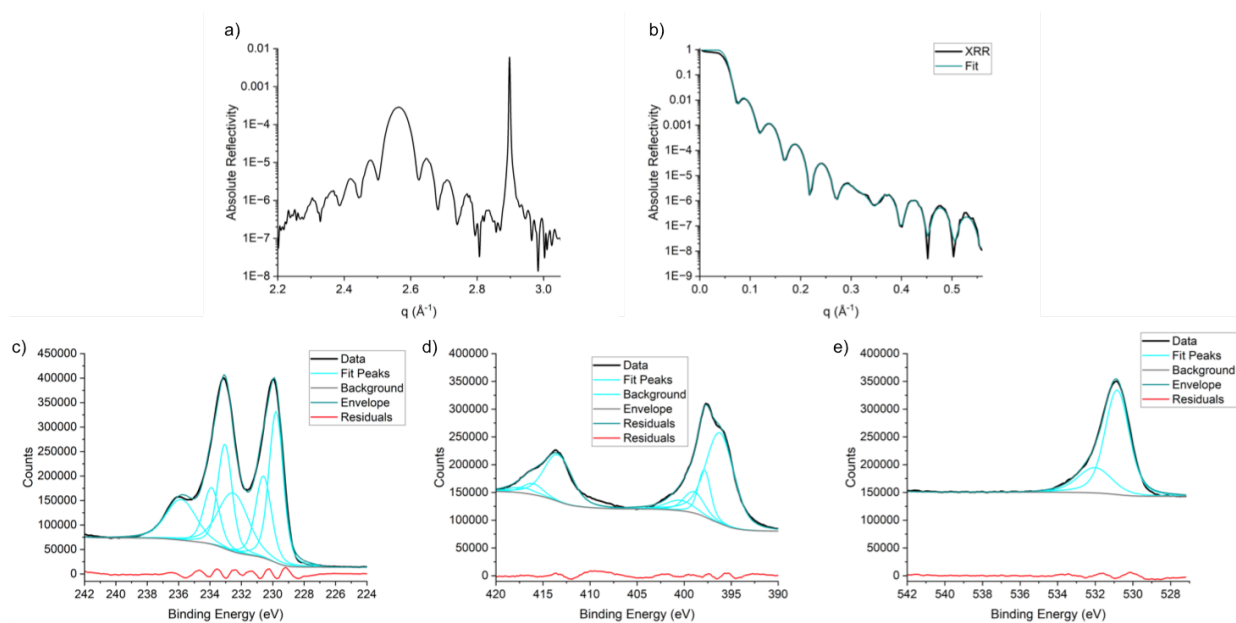


Figure 7.15: (a) Specular XRD, (b) XRR showing a 11 nm film with 1 nm surface layer, XPS of (c) the Mo3d, (d) N1s (overlapping with Mo3p), and (e) O1s spectra for the MoON film grown by reactive sputtering.

The sputter grown films were a shiny black and had a room temperature conductance of 1.25×10^3 S, showing them not be the insulating MoON phase, as would be expected at room temperature. Since the films were already conductive at room temperature, the low temperature conductivity was measured to see if the phase transition to the low temperature phase could be induced at temperatures below 25°C (Figure 7.16). The conductivity declined gradually with decreasing temperature, but no sharp change as would indicate a transition to an insulating phase was observed. Deviation from the exact 1:1:1 stoichiometry or a lack of anion ordering in the MoON film could be the reason the MIT was not observed, so future work in this direction could include further tuning of the deposition parameters to bring the stoichiometry closer to the desired composition and measurements to determine the degree, or lack, of anion ordering in the films.

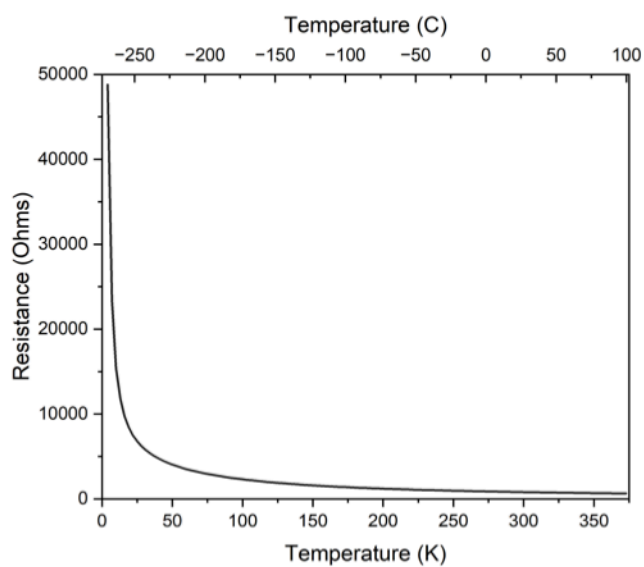


Figure 7.16: Low temperature conductivity of MoON film grown by reactive sputtering.

Chapter 8: Outlook and Summary

This thesis studied the science of synthesis of oxynitride materials. This was achieved by examining the synthesis of two model oxynitride materials – MoON and TaON. The reaction mechanism for the synthesis of these materials by ammonolysis was investigated via in situ XRD. The understanding of the reaction garnered from the in situ studies was then used to guide the synthesis of oxynitride materials with targeted properties. Methods for the thin film growth of oxynitride materials were also explored and recipes for the growth of new phases of MoON and TaON were developed. This work establishes methodologies for understanding, controlling, and advancing the synthesis of oxynitride materials and serves as a foundation to enabling synthesis-on-demand of oxynitride materials with targeted properties through the understanding and control of the synthesis reactions.

Recommendations for future work building off this thesis fall into three categories: (1) Use of the synthesis characterization methods developed in this work to explore other oxynitride materials with technologically relevant properties, (2) use of the enhanced synthesis control to produce the oxynitride materials with desirable properties and then study them for their intended applications, and (3) development of advanced characterization methods for better measuring the structural and chemical nature of oxynitride materials. In more detail:

- (1) Other oxynitride materials beyond those examined in this thesis display promising catalytic activity, and the same methods deployed in this work to study MoON and TaON could be applied to those materials. For example, cobalt molybdenum oxynitride and titanium oxynitride show encouraging activity for NH_3 synthesis, HER, and ORR.^{165–170} The synthesis of these, or other, oxynitride materials could be

studied using the methods and instrumentation developed to enable the work done in this thesis.

- (2) The driving purpose for studying oxynitride materials is for their use in catalytic applications. As such, a natural continuation of the synthesis studies performed in this work is the use of these materials for the catalytic applications they are intended for. Preliminary studies in this regard are already underway in the group. The photoactive capabilities of different TaON phases were explored by studying the photodegradation of methylene blue in the presence of TaON under visible light illumination. The use of molybdenum oxynitride for the isomerization of 1-butene and the relative activity of the different phases towards this reaction has also been explored. Additionally, the use of γ -MoO_xN_y as a cathode material in solid acid fuel cells for NH₃ synthesis is in progress.
- (3) While the use of combined TGA and combustion analysis has been demonstrated in this work as a method of determining the composition of oxynitride materials, the structural and chemical differentiation of anions in solids is a well-known challenge in the characterization of heteroanionic materials. The development of methods for further structural and chemical characterization of oxynitride materials is a space for continuing future development. Potential avenues include the use of neutron diffraction or NMR for the measurement of anion sites within oxynitride materials and x-ray standing wave (XSW) excited XPS for the observation of anion ordering.

Funding Acknowledgements

This work was supported by Northwestern University's MRSEC, funded by the National Science Foundation (DMR-1720139). This work made use of the Jerome B. Cohen X-Ray Diffraction Facility, the Reactor Engineering and Catalyst Testing Core (REACT), the Pulsed Laser Deposition Shared Facility, and the Keck-II Facility of Northwestern University's NUANCE Center, which have received support from the MRSEC program of the National Science Foundation (DMR-1720139) at the Materials Research Center of Northwestern University, the Soft and Hybrid Nanotechnology Experimental (SHyNE) Resource (NSF ECCS-2025633), and the IIN. Parts of this work were carried out in the Characterization Facility, University of Minnesota, which receives partial support from the NSF through the MRSEC (Award Number DMR-2011401) and the NNCI (Award Number ECCS-2025124) programs. Use of the Advanced Photon Source at Argonne National Laboratory was supported by the U.S. Department of Energy, Office of Science, Office of Basic Energy Sciences, under Contract no. DE-AC02-06CH11357.

Midwest Microlab is acknowledged for combustion analysis. Greg Haugstad is acknowledged for RBS and FReS measurements.

Commercial products are mentioned only to specify the procedure in sufficient detail. Their inclusion does not imply product endorsement, nor does it imply that the mentioned products are the best for such use.

Appendix: User Manual for In Situ XRD on the Smartlab 9kW Gen 3 at the J. B. Cohen X-ray Diffraction Facility

Hooking up gas tanks:

There are three gas lines. Each line is labeled with the gas that the MFC has been calibrated to (N_2 , H_2 , and NH_3). If you are using another gas on the line, the flow rate will need to be corrected using the tabulated correction factor (<https://www.mksinst.com/n/gas-correction-factors-for-thermal-based-mass-flow-controllers> has a good table, or similar will also work). For example the correction factor for He from N_2 is 1.444, so if you want to flow 100 sccm of He through the N_2 line, set the flow rate on the controller to $100/1.444 = 69.25$.



1. Put regulator on tank and connect tank to appropriate gas line.
 - a. If using an inert gas or other non-flammable, non-toxic gas: regulator can be attached directly to the appropriate gas line using either stainless steel or plastic flexible tubing.

- b. If using hydrogen or other flammable or hazardous gas: a N₂ tank will also need to be attached to the same line to allow purging of the line before and after use of the hazardous gas. A manifold with on/off valves should be set up to allow flow of either the purge or reaction gas on the same line as needed. A check valve should be used to prevent back flow of the reaction gas to the inert gas tank.
2. Once the tank is hooked up, open the tank and set the outgoing pressure to ~50 psi.
3. Open the black on/off valve before the MFC for the appropriate gas line.



4. Set the flow rate using the Rod4A controller. See section 10bv for instructions on how to program the flow rate.

Attaching gas lines to XRK900:

1. Mount furnace on diffractometer.
2. Plug in power and heater supply cables.
3. Hook up water lines. Make sure the correct water line for the furnace that is mounted is open and other line is closed – on/off valves for the water lines are on the floor behind the water circulator.
4. Connect inlet gas line to furnace. Make sure the inlet line is connected to the correct of the three gas lines coming from the gas tank farm. If multiple gases are to be used, a tee or cross

union should be used to connect the two supply lines to the single inlet line going to the furnace.

5. Connect primary exhaust line to base of sample holder.
6. Connect secondary exhaust line to pressure relief valve on furnace.

Note: The gas connections on the furnace and sample holder are 6mm and 3mm, respectively. All other gas lines are ¼ and 1/8 inch. 6mm to ¼ inch and 3mm to 1/8 inch converters have been installed on the furnace – these should not be removed.

Attaching gas or vacuum to HTK1200:

1. Mount furnace on diffractometer.
2. Plug in power and heater supply cables.
3. Hook up water lines. Make sure the correct water line for the furnace that is mounted is open and other line is closed – on/off valves for the water lines are on the floor behind the water circulator.
4. For use in air, leave vacuum port and gas inlet and outlet lines open.
5. For use with gas:
 - a. Close vacuum port
 - b. Connect inlet gas line to front of furnace using the flexible plastic tubing with the 3 mm brass connection on one end and 1/8 inch stainless steel connection on the other end. Make sure not to overtighten the connections as this can pinch closed the plastic tubing and stop gas flow.
 - c. Connect the exhaust line to the line coming from the rear of the furnace.
6. For use with vacuum:
 - a. Cap inlet and exhaust lines on furnace.
 - b. Attach turbo pump to the vacuum port on furnace
 - i. Attach pump to furnace and vacuum line to base of pump
 - ii. Plug in and screw on power supply to base of pump
 - iii. Plug in cable to turbo controller to side of pump
 - c. Once sample is placed in furnace and furnace is sealed, pump down with roughing pump for ~15 minutes until pressure reaches 10^{-1} Torr.
 - d. Turn on turbo pump. Should reach $\sim 10^{-4}$ Torr in ~15-30 minutes.
 - e. When experiment is finished, turn off turbo and allow it to cool for ~15 minutes (until you can't feel it spinning any more) before venting furnace to air with vent valve on right side of vacuum pump manifold.

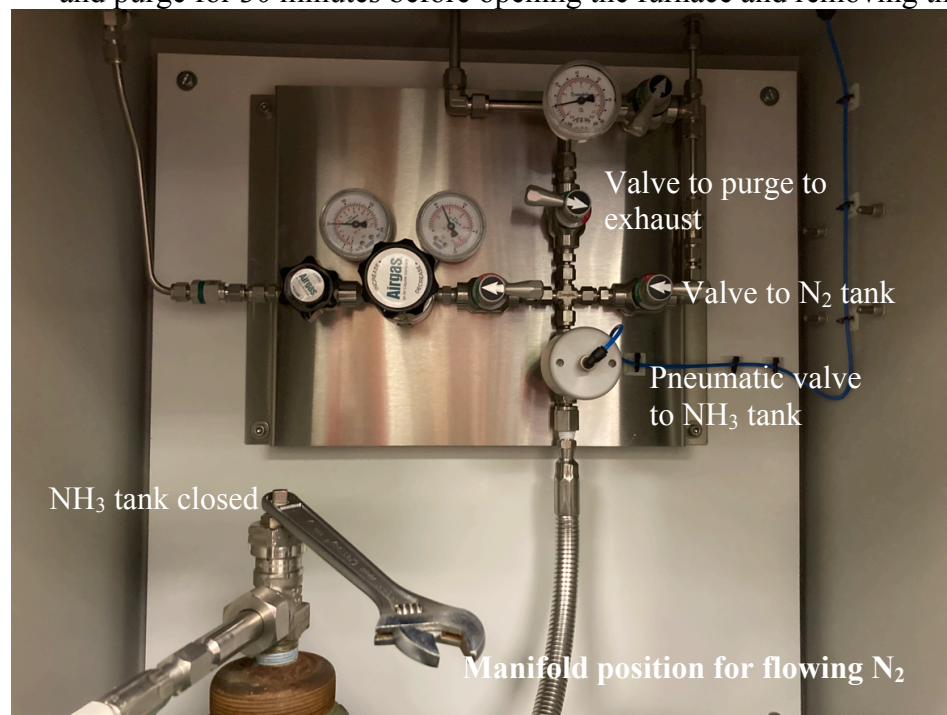
Using ammonia:

1. After putting in sample, with NH_3 tank closed turn on nitrogen flow and purge chamber for 30 minutes.
2. Switch to NH_3 by closing valve to N_2 tank, and the open/close knob after the regulator, venting the manifold to exhaust until the pressure in the regulator drops to zero, closing the vent to exhaust, and opening the NH_3 tank.

Note: The pneumatic valve to the NH_3 tank is kept open by pressurized air and controlled by the ammonia detector system. If the ammonia alarm goes off, it will automatically close the valve and stop the flow of ammonia and it will have to be cleared to reopen the valve. Also, if there is

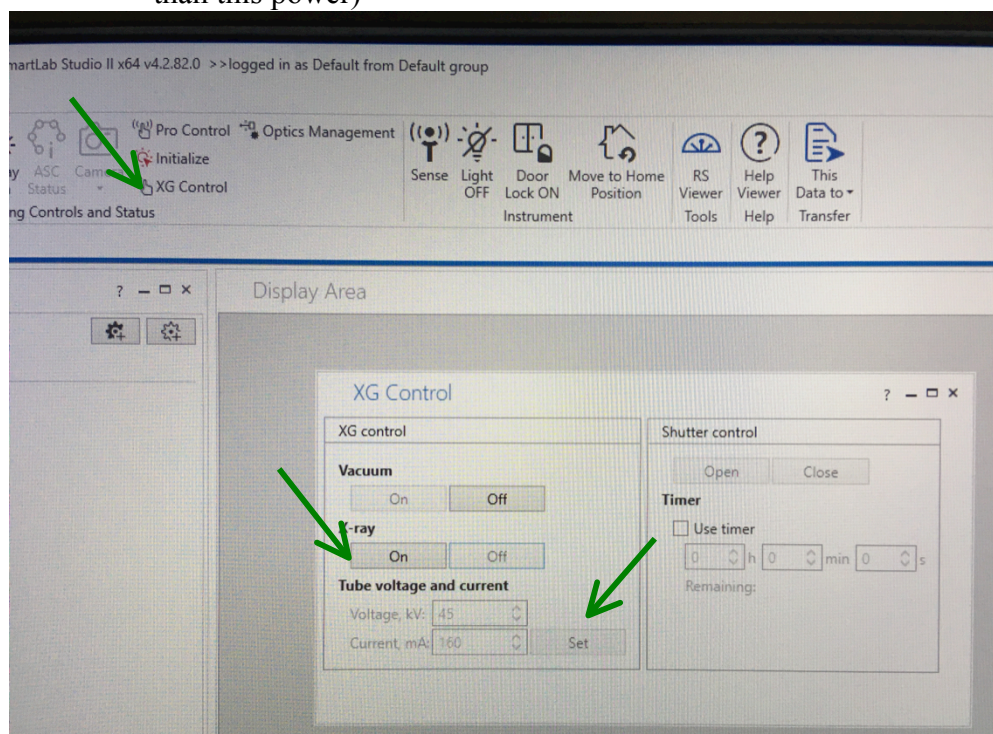
a loss of compressed air supply in the lab, the valve will close and the flow of ammonia will stop. If you are not getting ammonia flow when the tank is open, check first with Sumit to see if there is a problem with the supply of compressed air before changing to a new tank.

3. After the experiment, close the NH_3 tank and the open/close knob after the regulator, vent the ammonia in the manifold, then open the valve to the N_2 tank and the knob after the regulator and purge for 30 minutes before opening the furnace and removing the sample.



High temperature measurements:

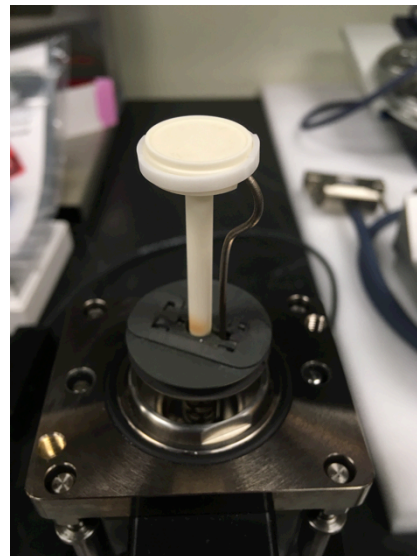
1. Log in to NuCore and begin reservation
2. Set correct optics
3. Check that correct furnace is mounted (XRK900 for reactive gases, HTK1200 for inert gases, air, or vacuum environments). If the furnace you need is not mounted, contact staff for assistance.
4. Turn on X-ray generator
 - a. Select “XG Control” from top menu bar
 - b. Press “X-ray On”
 - c. Set power to desired level (usual operating set point is 45kV and 160mA, lower power may be used if sample is sensitive to beam damage – do not set it to higher than this power)



5. Mount sample

HTK1200:

- a. For powder samples:
 - i. Select sample holder of appropriate depth for amount of sample (0.4mm, 0.8mm, 1.0mm sample holders available)
 - ii. Pack powder into sample holder, use glass slide to flatten
- b. For film samples:
 - i. Place film in center of sample holder, make sure top of film is above edge of sample holder
- c. Place sample holder on top of sample stage pedestal
- d. Use fixing ring to attach sample holder to stage
- e. Mount sample stage to furnace:
 - i. Lift sample stage from holder, taking care with wires
 - ii. Slide sample stage straight upward onto guiding rods into furnace. Indicator lights should be facing towards you
 - iii. Tighten the four screws to attach the stage to furnace – hand tight is sufficient
 - iv. Plug thermocouple into bottom of stage
 - v. Plug sample spinner wire into control box. Make sure to align tooth with gap on the plug, then screw tight



XRK900:

- f. For powder samples:
 - i. Select sample holder of appropriate material for your sample reactivity and maximum temperature (macor for up to 900C, stainless steel for up to 550C). Macor is typically installed - ask staff for help if you need a sample holder of a different material.
 - ii. Pack powder into sample holder, use glass slide to flatten
- g. For film samples:
 - i. Place film in center of sample holder, make sure top of film is above edge of sample holder
- h. Mount sample stage to furnace:
 - i. Lift sample stage from holder, taking care with wires
 - ii. Slide sample stage straight upward onto guiding rods into furnace. Indicator lights should be facing towards you
 - iii. Tighten the four screws to attach the stage to furnace – hand tight is sufficient
 - iv. Plug thermocouple into front of furnace
 - v. Attach white sample spinner cable. Make sure to align the three teeth, then click and turn to attach.
 - vi. Screw on exhaust line to bottom of sample holder.

6. Turn on water chiller. This is used to cool external parts of the furnace and the instrument should never be run without cooling water. Heating without cooling water can cause the furnace to overheat and the windows to melt.
7. Turn on Temperature Control Unit (TCU) and heater. There is one TCU for each furnace, labeled at the top left corner.



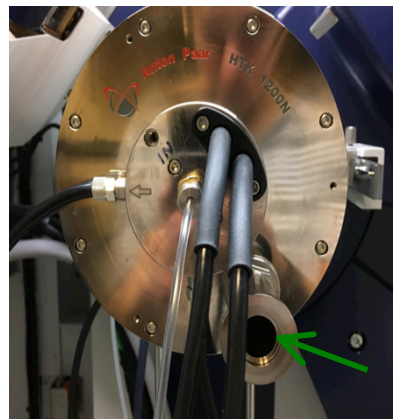
8. If using sample spinning, enable the rotations by pressing the enter key once to access “Params”, then press “Select” until you reach “rot.s”, and press the up arrow until the rotation speed reaches 10. Start sample spinning by pressing black switch in diffractometer enclosure. If using the HTK1200, you will be able to see the sample spinning. If using the XRK900, you cannot see the sample spinning but you can hear that the motor is on to check that you have successfully enabled the rotations.

9. Set up sample environment

HTK1200

a. For use in air:

- i. Make sure port of furnace is open
- ii. No further action necessary

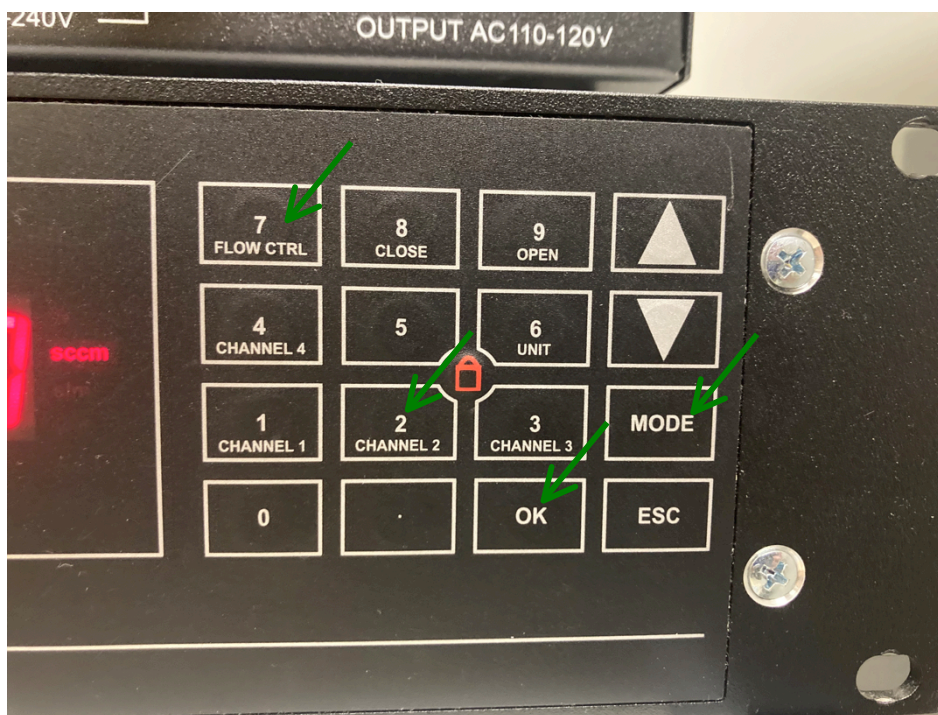


b. For use in inert gas:

- i. Make sure gas in/out lines are connected to furnace. If they are not connected please ask staff for assistance.
- ii. Make sure tank of desired gas is connected, if it is not please ask staff for assistance. If using anything other than N₂ or He check with staff to make sure this gas is compatible with furnace.
- iii. Open tank and set outgoing pressure to ~50 psi.
- iv. Make sure switch to the N₂ MFC is in the open position.

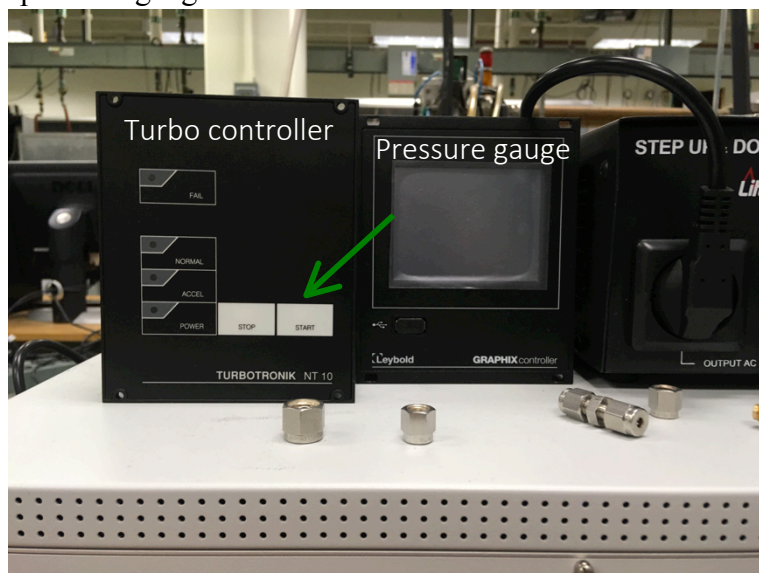


- v. Set flow rate using the controller to the left of the diffractometer. Select “Channel 2” for inert gas. Long press “Mode” and type in the desired flow rate – remember to use the appropriate conversion factor if using anything other than N₂. Press “Ok” to enter the new set point. Press “Flow Control” to start the flow of gas. After experiment is complete, press “Close” to stop the flow of gas.



c. For use in vacuum:

- i. Make sure vacuum pump is connected to furnace and all gas lines are closed. If it is not connected please ask staff for assistance.
- ii. Turn on pressure gauge and turbo controller. Both have switches on the back.



- iii. Turn on roughing pump. You will have to walk behind the diffractometer and press the white switch to turn on. Be careful of hanging wires. Allow roughing pump to pump down chamber for ~15 minutes.



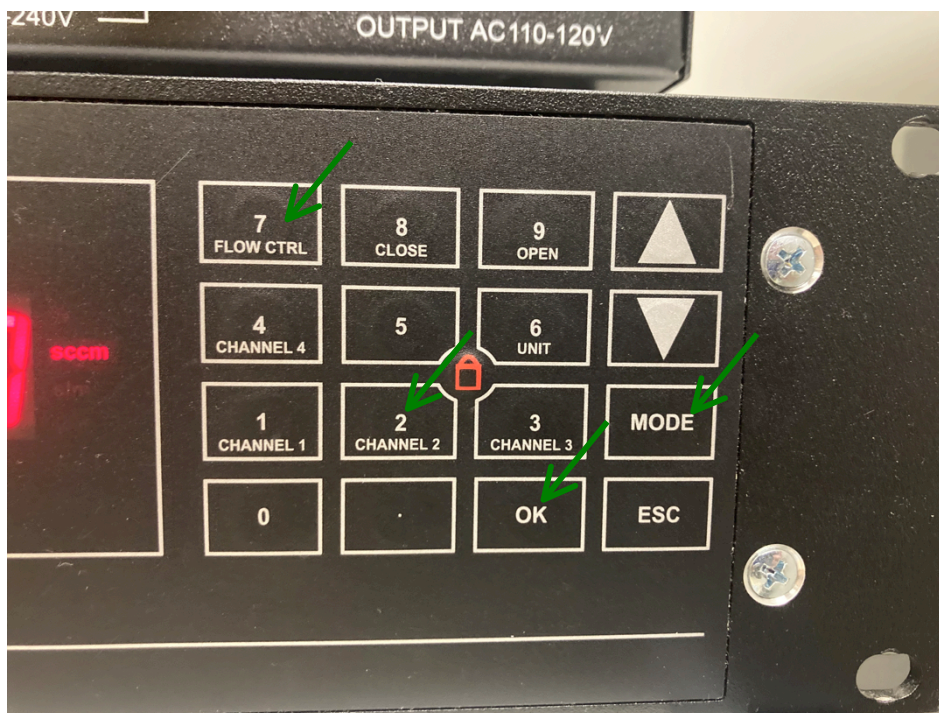
- iv. Turn on turbo pump and allow it to pump down. Should reach $\sim 1 \times 10^{-4}$ mbar.

XRK900

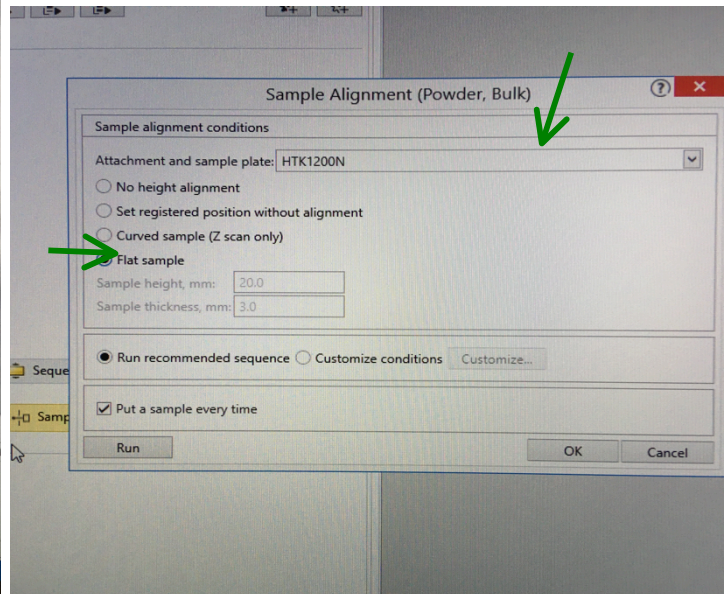
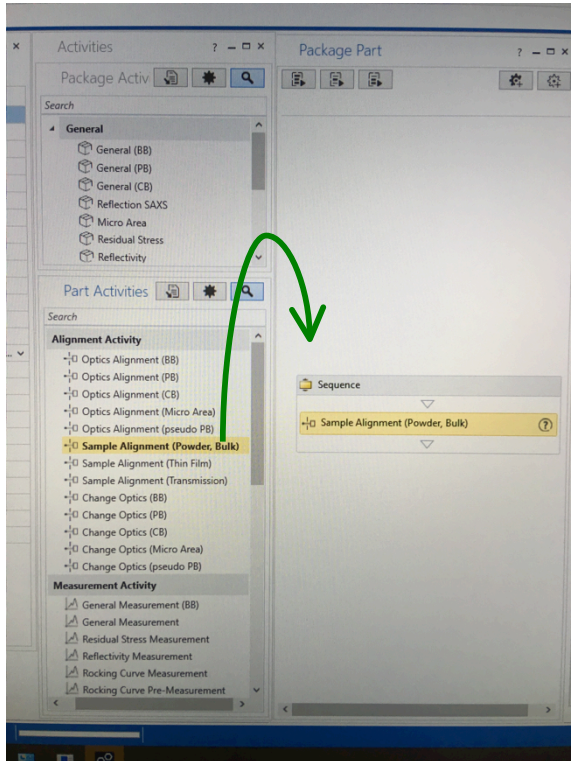
- a. For use with reactive gas:
 - v. Make sure gas in/out lines are connected to furnace. If they are not connected please ask staff for assistance.
 - vi. Make sure tank of reaction gas and purge gas are connected, if they are not please ask staff for assistance.
 - vii. Make sure switch to the MFC labeled H2 is in the open position.
 - viii. Open purge tank and set outgoing pressure to ~50 psi. Set flow rate as detailed in step x below. Purge for 30 minutes.
 - ix. Open reaction gas tank and set outgoing pressure to ~50 psi.



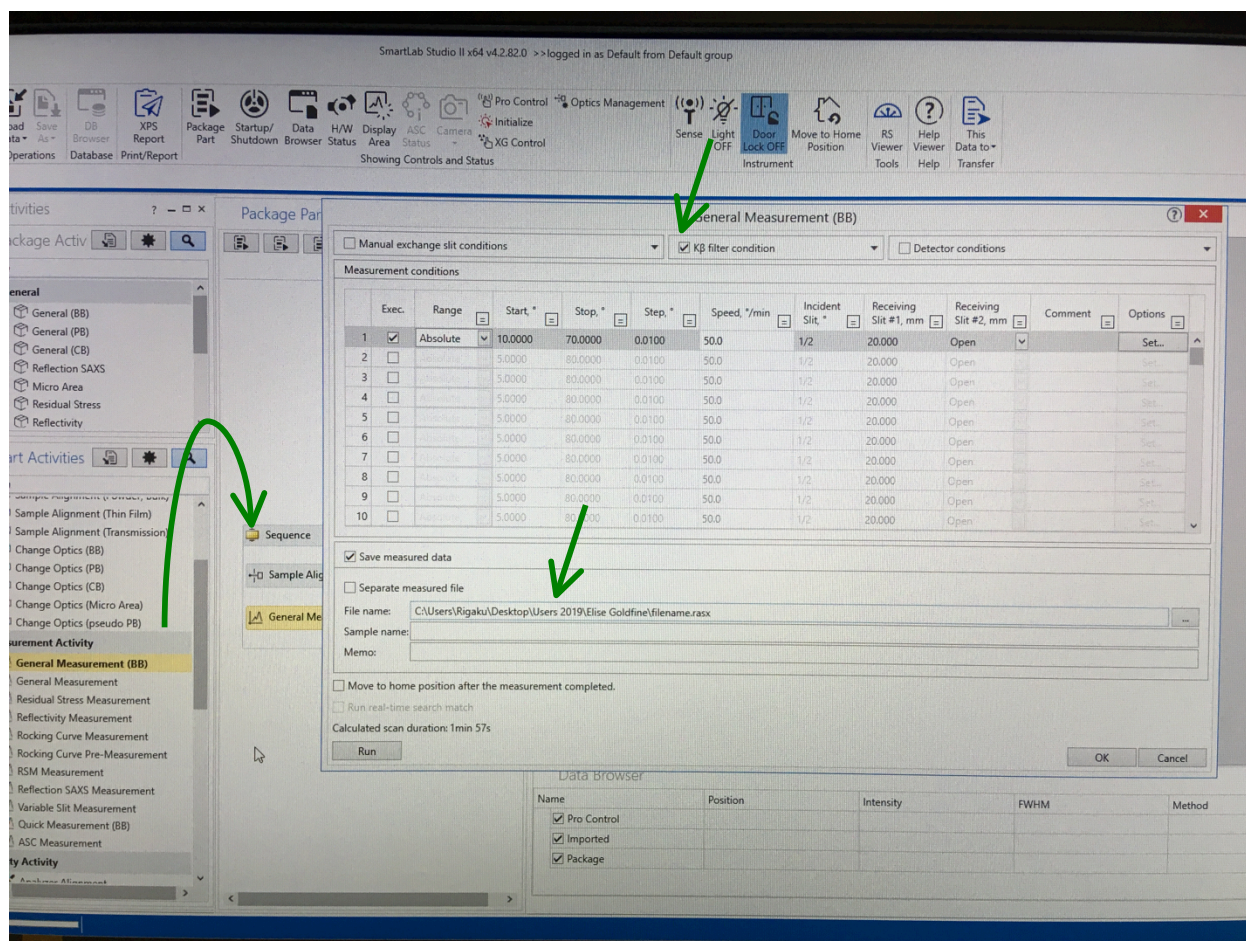
- x. Set flow rate using the controller to the left of the diffractometer. Select “Channel X” for the gas line that you are using. Long press “Mode” and type in the desired flow rate – remember to use the appropriate conversion factor if using anything other than the gas the line is labeled for. Press “Ok” to enter the new set point. Press “Flow Control” to start the flow of gas. After experiment is complete, press “Close” to stop the flow of gas.



10. Align sample. For both powders and films select “Sample Alignment (Powder/Bulk)” from Part Activities menu and drag to package work area. Double click to open the alignment options.
 - a. Select “HTK1200” or “Use current attachment” from dropdown menu
 - b. Press the “Flat Sample” radio button
 - c. Run the alignment



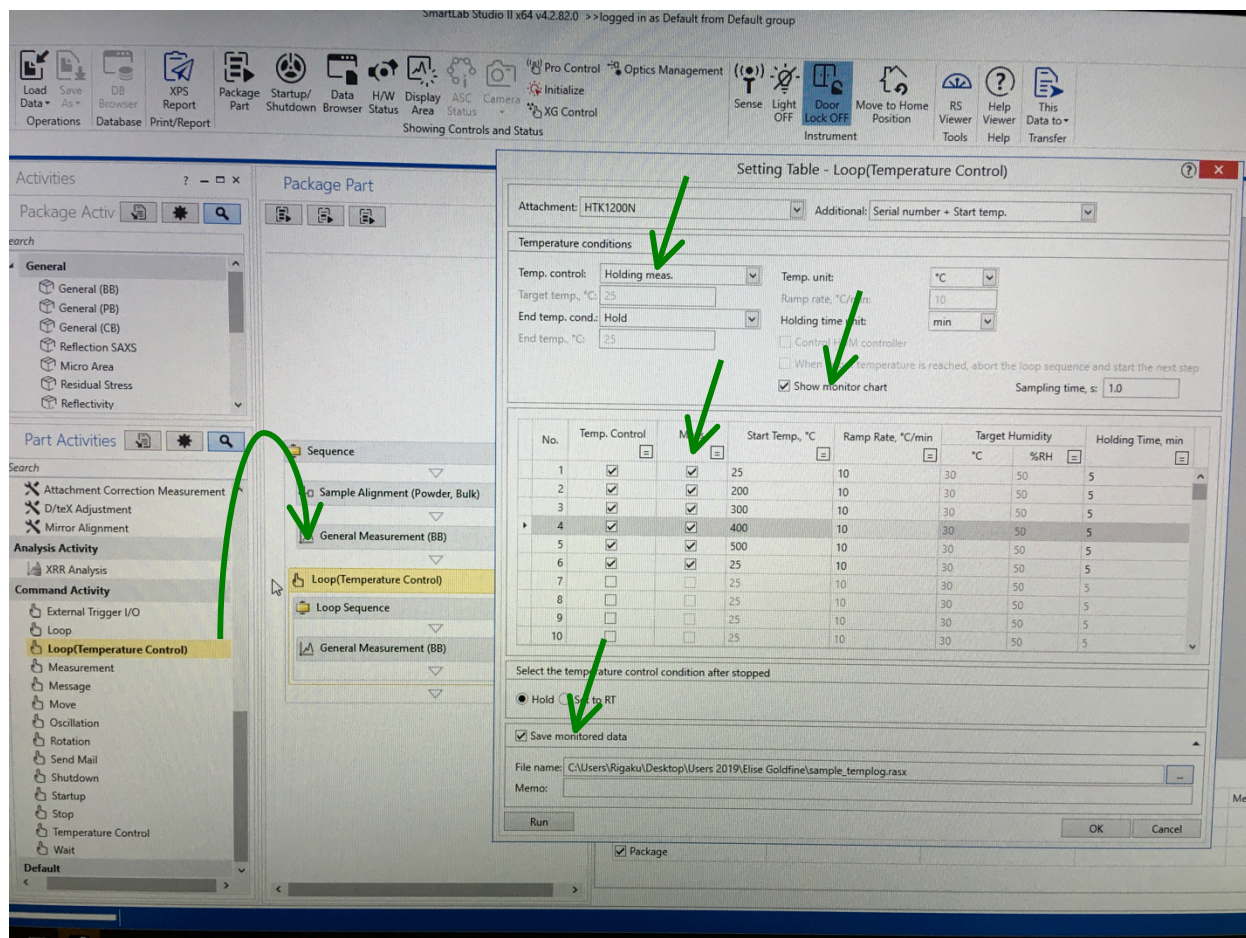
11. Do initial scan to determine optimal parameters. Drag “General Measurement (BB)” from Activity menu into work area. Double click to open the scan options.
 - a. Select the “ $k\beta$ Filter” option
 - b. Set start and end degrees, step size, and scan speed
 - c. Browse folder and give a file name to save data (if you do not give a valid name a red X will remain and when you close the window there will be a red exclamation point in the package)
 - d. Run scan
 - e. Repeat until satisfied with data quality



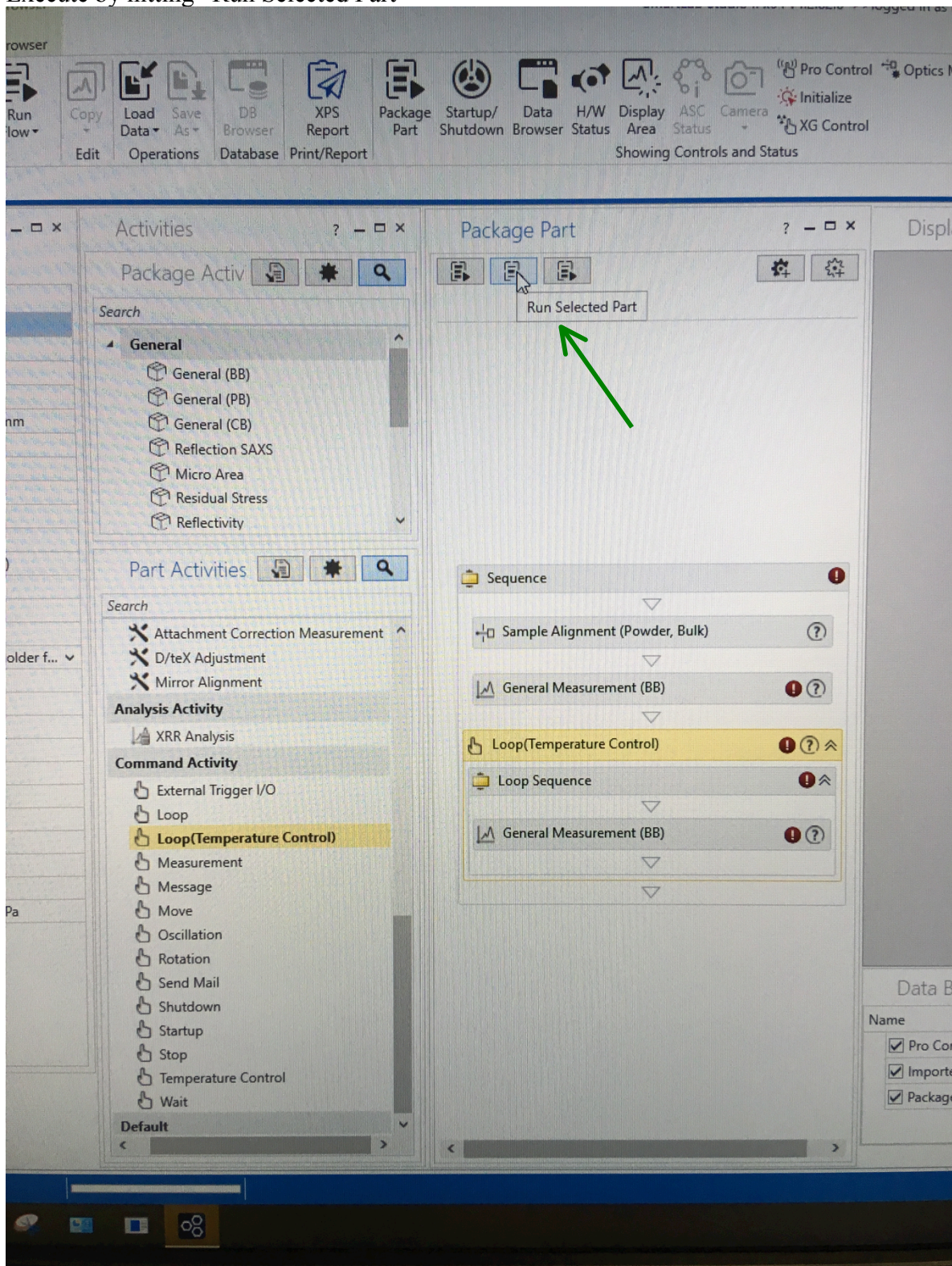
12. Program temperature loop

- a. Drag “Temperature Loop Control” into working window
- b. Copy your initial scan into the loop. This will copy in your set values determined above. Rename the scan file. When running the loop, a serial number and scan start temperature will be appended to this name. For example, the name “SampleX_date” will become “SampleX_date_001_200C” and then “SampleX_date_002_300C” etc. as each new scan is saved into a separate data file.
- c. Double click on “Temperature Loop Control” to open the temperature program window

- i. Select “HTK1200” or “XRK900” from dropdown menu
- ii. Select type of measurement
 1. Holding measurement will go to the set starting temperature and hold there while taking a measurement before moving to the next temperature (this is the recommended type of measurement)
 2. Constant up/down will execute scans at a constant time interval while the temperature changes according to the program
 3. Set temperature will go to a single temperature and scan there for the set amount of time
- iii. Program in your start temperatures, ramp rates, and hold times. The start temperature is the temperature at which the measurement will be taken. The ramp rate is the rate at which the furnace will heat to that temperature. The hold time is the time the program will dwell at that temperature before starting the measurement. Make sure to click the “Measure” radio button if you want a measurement to be taken at this temperature.
- iv. Select “Record data”, this will allow you to check “Save measured data” and enter a file name. This is where the temperature log will be saved. If you do not do this, no time vs. temperature data for the experiment will be logged or saved.
- v. Click “Ok” to exit the window



13. Execute by hitting “Run Selected Part”



14. After experiment is complete and furnace has returned to room temperature:
 - a. Turn of x-rays.
 - b. If using gas:
 - i. Purge for 30 minutes if using a non-inert gas
 - ii. Turn off gas by pressing “Close” on the gas controller
 - c. If using vacuum:
 - i. Turn off turbo and allow it to cool for ~15 minutes (until you can’t feel it spinning any more)
 - ii. Vent furnace to air with vent valve on right side of vacuum pump manifold
 - d. Turn off TCU and water circulator.
 - e. Remove sample stage from furnace. Remove sample from holder and clean the holder.
Move data to NetID folder on network drive and convert .rasx data files

References

1. Kageyama, H. *et al.* Expanding frontiers in materials chemistry and physics with multiple anions. *Nat. Commun.* **9**, (2018).
2. Charles, N., Saballos, R. J. & Rondinelli, J. M. Structural Diversity from Anion Order in Heteroanionic Materials. *Chem. Mater.* **30**, 3528–3537 (2018).
3. Fuertes, A. Metal oxynitrides as emerging materials with photocatalytic and electronic properties. *Mater. Horizons* **2**, 453–461 (2015).
4. Chun, W.-J. *et al.* Conduction and valence band positions of Ta₂O₅, TaON, and Ta₃N₅ by UPS and electrochemical methods. *J. Phys. Chem. B* **107**, 1798–1803 (2003).
5. Kreider, M. E. *et al.* Nitride or Oxynitride? Elucidating the Composition – Activity Relationships in Molybdenum Nitride Electrocatalysts for the Oxygen Reduction Reaction. *Chem. Mater.* (2020).
6. Stevens, M. B. *et al.* Identifying and Tuning the in Situ Oxygen-Rich Surface of Molybdenum Nitride Electrocatalysts for Oxygen Reduction. *ACS Appl. Energy Mater.* **3**, 12433–12446 (2020).
7. Oyama, S. T. Introduction to the chemistry of transition metal carbides and nitrides. in *The Chemistry of Transition Metal Carbides and Nitrides* 1–27 (1996). doi:10.1007/978-94-009-1565-7_1
8. Chen, X. Z., Dye, J. L., Eick, H. A., Elder, S. H. & Tsai, K. L. Synthesis of Transition-Metal Nitrides from Nanoscale Metal Particles Prepared by Homogeneous Reduction of Metal Halides with an Alkalide. *Chem. Mater.* **9**, 1172–1176 (1997).
9. Yao, Z. *et al.* A novel carbothermal reduction nitridation route to MoN nanoparticles on CNTs support. *J. Mater. Chem.* **21**, 6898–6902 (2011).
10. Yao, Z. W. Exploration on synthesis of activated carbon supported molybdenum carbide, nitride and phosphide via carbothermal reduction route. *J. Alloys Compd.* **475**, 38–41 (2009).
11. Shen, L. H. *et al.* A new method for preparation of nanocrystalline molybdenum nitride. *Chinese Phys. Lett.* **22**, 3192–3194 (2005).
12. Ma, J. & Du, Y. A convenient thermal reduction-nitridation route to nanocrystalline molybdenum nitride (Mo₂N). *J. Alloys Compd.* **463**, 196–199 (2008).
13. Sidana, H. K., Mir, R. A. & Pandey, O. P. Synthesis of molybdenum nitride (Mo₂N) nano flakes via in-situ reduction-nitridation. *J. Alloys Compd.* **736**, 255–265 (2018).
14. Chiu, H. T., Chuang, S. H., Lee, G. H. & Peng, S. M. Low-temperature solution route to molybdenum nitride. *Adv. Mater.* **10**, 1475–1479 (1998).
15. O’Loughlin, J. L., Wallace, C. H., Knox, M. S. & Kaner, R. B. Rapid solid-state synthesis of tantalum, chromium, and molybdenum nitrides. *Inorg. Chem.* **40**, 2240–2245 (2001).
16. Dezelah IV, C. L., El-Kadri, O. M., Heeg, M. J. & Winter, C. H. Preparation and characterization of molybdenum and tungsten nitride nanoparticles obtained by thermolysis of molecular precursors. *J. Mater. Chem.* **14**, 3167–3176 (2004).
17. Afanasiev, P. New single source route to the molybdenum nitride Mo₂N. *Inorg. Chem.* **41**, 5317–5319 (2002).
18. Ma, L., Ting, L. R. L., Molinari, V., Giordano, C. & Yeo, B. S. Efficient hydrogen evolution reaction catalyzed by molybdenum carbide and molybdenum nitride nanocatalysts synthesized via the urea glass route. *J. Mater. Chem. A* **3**, 8361–8368

- (2015).
19. Giordano, C., Erpen, C., Yao, W. & Antonietti, M. Synthesis of Mo and W carbide and nitride nanoparticles via a simple 'urea glass' route. *Nano Lett.* **8**, 4659–4663 (2008).
 20. Panda, R. N. & Kaskel, S. Synthesis and characterization of high surface area molybdenum nitride. *J. Mater. Sci.* **41**, 2465–2470 (2006).
 21. Zhang, Y., Xin, Q., Rodriguez-Ramos, I. & Guerrero-Ruiz, A. Temperature dependence of the pseudomorphic transformation of MoO₃ to γ -Mo₂N. *Materials Research Bulletin* **34**, 145–156 (1999).
 22. Choi, J., Curl, R. L. & Thompson, L. T. Molybdenum Nitride Catalysts I. Influence of the Synthesis Factors on Structural Properties. *J. Catal.* **146**, 218–227 (1994).
 23. Jagers, C. H., Michaels, J. N. & Stacy, A. M. Preparation of High-Surface-Area Transition-Metal Nitrides: Mo₂N and MoN. *Chem. Mater.* **2**, 150–157 (1990).
 24. Baek, S. H. *et al.* Characteristics of high surface area molybdenum nitride and its activity for the catalytic decomposition of ammonia. *Catalysts* **11**, 1–15 (2021).
 25. Volpe, L. & Boudart, M. Compounds of Molybdenum and Tungsten with High Specific Surface Area. *J. Solid State Chem.* **59**, 332–347 (1985).
 26. Morozan, A. *et al.* Synergy between molybdenum nitride and gold leading to platinum-like activity for hydrogen evolution. *Phys. Chem. Chem. Phys.* **17**, 4047–4053 (2015).
 27. Cárdenas-Lizana, F., Lamey, D., Kiwi-Minsker, L. & Keane, M. A. Molybdenum nitrides: a study of synthesis variables and catalytic performance in acetylene hydrogenation. *J. Mater. Sci.* **53**, 6707–6718 (2018).
 28. Choi, J. *et al.* Synthesis and Characterization of Molybdenum Nitride Hydrodenitrogenation Catalysts. *Catal. Today* **15**, 201–222 (1992).
 29. Jaf, Z. N., Altarawneh, M., Miran, H. A., Jiang, Z. T. & Dlugogorski, B. Z. Mechanisms governing selective hydrogenation of acetylene over γ -Mo₂N surfaces. *Catal. Sci. Technol.* **7**, 943–960 (2017).
 30. Cao, B., Neuefeind, J. C., Adzic, R. R. & Khalifah, P. G. Molybdenum nitrides as oxygen reduction reaction catalysts: Structural and electrochemical studies. *Inorg. Chem.* **54**, 2128–2136 (2015).
 31. Pan, X. *et al.* A facile route to graphite-tungsten nitride and graphite-molybdenum nitride nanocomposites and their ORR performances. *Ceram. Int.* **42**, 16017–16022 (2016).
 32. Lee, K. *et al.* Single-crystalline mesoporous Mo₂N nanobelts with an enhanced electrocatalytic activity for oxygen reduction reaction. *Mater. Lett.* **124**, 231–234 (2014).
 33. Kojima, R. & Aika, K. Molybdenum nitride and carbide catalysts for ammonia synthesis. *Appl. Catal. A Gen.* **219**, 141–147 (2001).
 34. Tagliazucca, V., Schlichte, K., Schüth, F. & Weidenthaler, C. Molybdenum-based catalysts for the decomposition of ammonia: In situ X-ray diffraction studies, microstructure, and catalytic properties. *J. Catal.* **305**, 277–289 (2013).
 35. Song, Y.-J. & Yuan, Z.-Y. One-pot Synthesis of Mo₂N_{1-x}NC Catalysts with Enhanced Electrocatalytic Activity for Hydrogen Evolution Reaction. *Electrochim. Acta* **246**, 536–543 (2017).
 36. Ojha, K., Saha, S., Banerjee, S. & Ganguli, A. K. Efficient Electrocatalytic Hydrogen Evolution from MoS₂-Functionalized Mo₂N Nanostructures. *ACS Appl. Mater. Interfaces* **9**, 19455–19461 (2017).
 37. Mtukula, A. C., Bo, X. & Guo, L. Highly active non-precious metal electrocatalyst for the

- hydrogen evolution reaction based on nitrogen-doped graphene supported MoO₂/WN/Mo₂N. *J. Alloys Compd.* **692**, 614–621 (2017).
38. Wang, C. *et al.* Molybdenum Nitride Electrocatalysts for Hydrogen Evolution More Efficient than Platinum/Carbon: Mo₂N/CeO₂@Nickel Foam. *ACS Appl. Mater. Interfaces* **12**, 29153–29161 (2020).
 39. Aika, K. ichi & Ozaki, A. Mechanism and isotope effect in ammonia synthesis over molybdenum nitride. *Journal of Catalysis* **14**, 311–321 (1969).
 40. Hargreaves, J. S. J. Nitrides as ammonia synthesis catalysts and as potential nitrogen transfer reagents. *Appl. Petrochemical Res.* **4**, 3–10 (2014).
 41. Mckay, D., Hargreaves, J. S. J., Rico, J. L., Rivera, J. L. & Sun, X. L. The influence of phase and morphology of molybdenum nitrides on ammonia synthesis activity and reduction characteristics. *Journal of Solid State Chemistry* **181**, 325–333 (2008).
 42. Volpe, L. & Boudart, M. Ammonia Synthesis on Molybdenum Nitride. *J. Phys. Chem.* **90**, 4874–4877 (1986).
 43. Wyvratt, B. M. *et al.* Reactivity of Hydrogen on and in Nanostructured Molybdenum Nitride: Crotonaldehyde Hydrogenation. *ACS Catal.* **6**, 5797–5806 (2016).
 44. Pandey, S. *et al.* Hydrogen-incorporated Cubic Molybdenum Oxynitrides. *Prep.*
 45. Balasubramanian, K., Huang, L. & Gall, D. Phase stability and mechanical properties of Mo_{1-x}N_x with $0 \leq x \leq 1$. *J. Appl. Phys.* (2017).
 46. Jehn, H. & Ettmayer, P. The Molybdenum-Nitrogen Phase Diagram. *J. Less-Common Met.* **58**, 85–98 (1978).
 47. Pandey, S. A. *et al.* Hidden Complexity in the Chemistry of Ammonolysis-Derived ‘ γ -Mo₂N’’: An Overlooked Oxynitride Hydride. *Chem. Mater.* **33**, 6671–6684 (2021).
 48. Hargreaves, J. S. J. Heterogeneous catalysis with metal nitrides. *Coord. Chem. Rev.* **257**, 2015–2031 (2013).
 49. Fuertes, A., Ciència, I. De, Barcelona, D. M. De & Uab, C. Progress in Solid State Chemistry Synthetic approaches in oxynitride chemistry. *Prog. Solid State Chem.* **51**, 63–70 (2018).
 50. Wise, R. S. & Markel, E. J. Synthesis of High Surface Area Molybdenum Nitride in Mixtures of Nitrogen and Hydrogen. *Journal of Catalysis* **145**, 344–355 (1994).
 51. Dewangan, K., Patil, S. S., Joag, D. S., More, M. A. & Gajbhiye, N. S. Topotactical Nitridation of α -MoO₃ Fibers to γ -Mo₂N Fibers and Its Field Emission Properties. *J. Phys. Chem. C* **114**, 14710–14715 (2010).
 52. Szymanski, N. J., Walters, L. N., Puggioni, D. & Rondinelli, J. M. Design of Heteroanionic MoON Exhibiting a Peierls Metal-Insulator Transition. **236402**, 1–6 (2019).
 53. Sivula, K. & van de Krol, R. Semiconducting materials for photoelectrochemical energy conversion. *Nat. Rev.* **1**, (2016).
 54. Xie, R. J. & Hintzen, H. T. Optical properties of (oxy)nitride materials: A review. *J. Am. Ceram. Soc.* **96**, 665–687 (2013).
 55. Takata, T., Pan, C. & Domen, K. Design and Development of Oxynitride Photocatalysts for Overall Water Splitting under Visible Light Irradiation. *ChemElectroChem* **3**, 31–37 (2016).
 56. Jafari, T. *et al.* Photocatalytic Water Splitting — The Untamed Dream: A Review of Recent Advances. *Molecules* **21**, (2016).

57. Higashi, M., Domen, K. & Abe, R. Fabrication of efficient TaON and Ta₃N₅ photoanodes for water splitting under visible light irradiation. *Energy Environ. Sci.* **4**, 4138 (2011).
58. Hitoki, G. *et al.* An oxynitride, TaON, as an efficient water oxidation photocatalyst under visible light irradiation ($\lambda \leq 500$ nm). *Chem. Commun.* **2**, 1698–1699 (2002).
59. Swisher, J. H. & Read, H. M. Thermodynamic Properties and Electrical Conductivity of Ta₃N₅ and TaON. *Metall. Trans.* **3**, (1972).
60. Takata, T. *et al.* Visible-light-driven photocatalytic behavior of tantalum-oxynitride and nitride. *Res. Chem. Intermed.* **33**, 13–25 (2007).
61. Tsang, M.-Y. *et al.* Enhanced Photocatalytic Hydrogen Generation Using Polymorphic Macroporous TaON. *Adv. Mater.* **24**, 3406–3409 (2012).
62. Ullah, H., Tahir, A. A., Bibi, S., Mallick, T. K. & Karazhanov, S. Z. Electronic properties of B-TaON and its surfaces for solar water splitting. *Appl. Catal. B Environ.* **229**, 24–31 (2018).
63. Xiao, M., Wang, S., Thaweesak, S., Luo, B. & Wang, L. Tantalum (Oxy)Nitride: Narrow Bandgap Photocatalysts for Solar Hydrogen Generation. *Green Chem. Eng.* **3**, 365–378 (2017).
64. Cui, Z. H. & Jiang, H. Theoretical Investigation of Ta₂O₅, TaON, and Ta₃N₅: Electronic Band Structures and Absolute Band Edges. *J. Phys. Chem. C* **121**, 3241–3251 (2017).
65. Brauer, G. & Weidlein, J. R. Synthesis and Properties of Tantalum Oxide Nitride, TaON. *Angew. Chemie Int. Ed.* **4**, 875–875 (1965).
66. Weishaupt, M. & Strähle, J. Darstellung der Oxidnitride VON, NbON und TaON. Die Kristallstruktur von NbON und TaON. *ZAAC - J. Inorg. Gen. Chem.* **429**, 261–269 (1977).
67. Schilling, H. *et al.* γ -TaON: A metastable polymorph of tantalum oxynitride. *Angew. Chemie - Int. Ed.* **46**, 2931–2934 (2007).
68. Wang, Z. *et al.* Hierarchical metastable γ -TaON hollow structures for efficient visible-light water splitting. *Energy Environ. Sci.* **6**, 2134–2144 (2013).
69. Lütke, T. *et al.* Synthesis and characterization of metastable transition metal oxides and oxide nitrides. *Zeitschrift für Krist. - Cryst. Mater.* **232**, 3–14 (2017).
70. Lütke, T. *et al.* Synthesis and crystal structure of δ -TaON, a metastable polymorph of tantalum oxide nitride. *Inorg. Chem.* **53**, 11691–11698 (2014).
71. Nakhal, S., Lumey, M. W., Bredow, T., Dronskowski, R. & Lerch, M. Synthesis and approximated crystal and electronic structure of a proposed new tantalum oxide nitride Ta₃O₆N. *Zeitschrift für Anorg. und Allg. Chemie* **636**, 1006–1012 (2010).
72. Lumey, M.-W. & Dronskowski, R. The Electronic Structure of Tantalum Oxynitride and the Falsification of α -TaON. *Zeitschrift für Anorg. und Allg. Chemie* **629**, 2173–2179 (2003).
73. Orhan, E., Tessier, F. & Marchand, R. Synthesis and energetics of yellow TaON. *Solid State Sci.* **4**, 1071–1076 (2002).
74. De Respinis, M. *et al.* Oxynitrogenography: Controlled Synthesis of Single-Phase Tantalum Oxynitride Photoabsorbers. *Chem. Mater.* **27**, 7091–7099 (2015).
75. Matizamhuka, W. R., Sigalas, I. & Herrmann, M. Synthesis, sintering and characterisation of TaON materials. *Ceram. Int.* **34**, 1481–1486 (2008).
76. Yoon, S. *et al.* The Influence of the Ammonolysis Temperature on the Photocatalytic

- Activity of b-TaON. *Int. J. Photoenergy* (2013).
77. Dabirian, A., Van't Spijker, H. & Van De Krol, R. Wet ammonia synthesis of semiconducting N:Ta₂O₅, Ta₃N₅ and β-TaON films for photoanode applications. *Energy Procedia* **22**, 15–22 (2012).
 78. Bredow, T. *et al.* Structure and stability of TaON polymorphs. *Zeitschrift fur Anorg. und Allg. Chemie* **632**, 1157–1162 (2006).
 79. Rasaki, S. A., Zhang, B., Anbalgam, K., Thomas, T. & Yang, M. Synthesis and application of nano-structured metal nitrides and carbides: A review. *Prog. Solid State Chem.* **50**, 1–15 (2018).
 80. Li, X. liang *et al.* Synthesis and characterization of uniform nanoparticles of γ-Mo₂N for supercapacitors. *Transactions of Nonferrous Metals Society of China (English Edition)* **19**, 620–625 (2009).
 81. Ruan, D. *et al.* High-Performance Porous Molybdenum Oxynitride Based Fiber Supercapacitors. *ACS Appl. Mater. Interfaces* **9**, 29699–29706 (2017).
 82. Wu, H. & Lian, K. The Development of Pseudocapacitive Molybdenum Oxynitride Electrodes for Supercapacitors. *ECS Trans.* **58**, 67–75 (2014).
 83. Kihlberg, L. Least squares refinement of the crystal structure of molybdenum trioxide. *Ark. Kemi* **21**, 357–364 (1963).
 84. Wang, L., Zhang, G. H. & Chou, K. C. Study on reduction reaction of MoO₂ powder with NH₃. *J. Am. Ceram. Soc.* **100**, 1368–1376 (2017).
 85. Li, Z., Chen, C., Zhan, E., Ta, N. & Shen, W. Mo₂N nanobelts for dehydrogenation of aromatic alcohols. *Catal. Commun.* **51**, 58–62 (2014).
 86. Bertrand, O. & Dufour, L. C. X-ray and electron microscopy investigation of the topotactic transformation of MoO₃ into MoO₂. *Phys. Status Solidi* **60**, 507–519 (1980).
 87. Wang, D., Su, D. S. & Schlögl, R. Electron beam induced transformation of MoO₃ to MoO₂ and a new phase MoO. *Zeitschrift fur Anorg. und Allg. Chemie* **630**, 1007–1014 (2004).
 88. Chen, J. & Wei, Q. Phase transformation of molybdenum trioxide to molybdenum dioxide: An in-situ transmission electron microscopy investigation. *Int. J. Appl. Ceram. Technol.* **14**, 1020–1025 (2017).
 89. McClain, R., Malliakas, C. D., Shen, J., Wolverton, C. & Kanatzidis, M. G. In Situ Mechanistic Studies of Two Divergent Synthesis Routes Forming the Heteroanionic BiOCuSe. *J. Am. Chem. Soc.* **143**, 12090–12099 (2021).
 90. Martinolich, A. J. & Neilson, J. R. Toward Reaction-by-Design: Achieving Kinetic Control of Solid State Chemistry with Metathesis. *Chem. Mater.* **29**, 479–489 (2017).
 91. Chen, H. *et al.* Antiferromagnetic Semiconductor BaFMn_{0.5}Te with Unique Mn Ordering and Red Photoluminescence. *J. Am. Chem. Soc.* **141**, 17421–17430 (2019).
 92. Pandey, S. A. Materials and Structures for the Electrodes of Solid-State Electrochemical Energy Devices. *ProQuest Dissertations and Theses* (Northwestern University PP - United States -- Illinois, 2021).
 93. Adams, S. CDW Superstructures in Hydrogen Molybdenum Bronzes H_xMoO₃. *J. Solid State Chem.* **149**, 75–87 (2000).
 94. Brandt, B. G. On the crystal structures of MoO₂ and MoO₃(H₂O)₂. An account of computer programming and structure refinement. *Chem. Commun. (Stockholm Univ.* 1–41 (1971).

95. Bull, C. L., Mcmillan, P. F., Soignard, A. E. & Leinenweber, K. Determination of the crystal structure of d-MoN by neutron diffraction. *J. Solid State Chem.* **177**, 1488–1492 (2004).
96. Toby, B. H. & Von Dreele, R. B. GSAS-II: The genesis of a modern open-source all purpose crystallography software package. *J. Appl. Crystallogr.* **46**, 544–549 (2013).
97. Braïda, B., Adams, S. & Canadell, E. Concerning the structure of hydrogen molybdenum bronze phase III. A combined theoretical-experimental study. *Chem. Mater.* **17**, 5957–5969 (2005).
98. Adams, S., Ehses, K. & Spilker, J. Proton Ordering in the Peierls-Distorted Hydrogen Molybdenum Bronze H_{0.33}MoO₃: Structure and Physical Properties. *Acta Chystallographica Sect. B* **B49**, 958–967 (1993).
99. Goldfine, E. A. *et al.* Molybdenum Oxide Precursors that Promote the Low-Temperature Formation of High-Surface-Area Cubic Molybdenum (Oxy)nitride. *Inorg. Chem.* **61**, 16760–16769 (2022).
100. Bursill, L. A. Crystallographic shear in molybdenum trioxide. *Proc. R. Soc. London. A. Math. Phys. Sci.* **311**, 267–290 (1969).
101. Allpress, J. G. & Sanders, J. V. The direct observation of the structure of real crystals by lattice imaging. *J. Appl. Crystallogr.* **6**, 165–190 (1973).
102. Harada, S., Tanaka, K. & Inui, H. Thermoelectric properties and crystallographic shear structures in titanium oxides of the Magnli phases. *J. Appl. Phys.* **108**, (2010).
103. Stoneham, A. M. & Durham, P. J. The Ordering of Crystallographic Shear Planes: Theory of Regular Arrays. *J. Phys. Chem. Solids* **34**, 2127–2135 (1973).
104. Kirklin, S. *et al.* The Open Quantum Materials Database (OQMD): Assessing the accuracy of DFT formation energies. *npj Comput. Mater.* (2015). doi:10.1038/npjcompumats.2015.10
105. Saal, J. E., Kirklin, S., Aykol, M., Meredig, B. & Wolverton, C. Materials design and discovery with high-throughput density functional theory: The open quantum materials database (OQMD). *JOM* **65**, 1501–1509 (2013).
106. Penn, R. L. & Banfield, J. F. Formation of rutile nuclei at anatase {112} twin interfaces and the phase transformation mechanism in nanocrystalline titania. *Am. Mineral.* **84**, 871–876 (1999).
107. Hanaor, D. A. H. & Sorrell, C. C. Review of the anatase to rutile phase transformation. *J. Mater. Sci.* **46**, 855–874 (2011).
108. Hyoungh, G. L. & Zuo, J. M. Growth and Phase Transformation of Nanometer-Sized Titanium Oxide Powders Produced by the Precipitation Method. *J. Am. Ceram. Soc.* **87**, 473–479 (2004).
109. Rao, C. N. R. Kinetics and Thermodynamics of the Crystal Structure Transformation of Spectroscopically Pure Anatase To Rutile. *Can. J. Chem.* **39**, 498–500 (1961).
110. Marchand, R., Gouin, X., Tessier, F. & Laurent, Y. New routes to molybdenum nitrides and oxynitrides: preparation and characterization of new phases. in *The Chemistry of Transition Metal Carbides and Nitrides* 252–273 (1996).
111. Glemser, V. O., Lutz, G. & Meyer, G. Über niedere Molybdanhydroxyde. *Zeitschrift für Anorg. und Allg. Chemie* **285**, (1956).
112. Glemser, V. O., Hauschild, U. & Lutz, G. Darstellung von Hydroxyden durch Anlagerung von atomarem Wasserstoff an Oxyde. *Zeitschrift für Anorg. und Allg. Chemie* **269**, (1952).

113. Glemser, V. O. & Lutz, G. Uber Molybdanblau. *Zeitschrift fur Anorg. und Allg. Chemie* **264**, (1951).
114. Dickens, P. G. & Birtill, J. J. Hydrogen Molybdenum Bronzes. *J. Electron. Mater.* **7**, 679–686 (1978).
115. Kurusu, Y. Thermal Behavior of a New Type Molybdenum Oxide Obtained by Oxidation of Molybdenum Powder or Molybdenum Trioxide with Hydrogen Peroxide. *Bulletin of the Chemical Society of Japan* **54**, 293–294 (1981).
116. Reid, J. W., Kaduk, J. A. & Matei, L. The crystal structure of $\text{MoO}_2(\text{O}_2)\text{H}_2\text{O}$. *Powder Diffraction* **33**, 49–54 (2018).
117. Dickens, P. G., Hibble, S. J. & James, G. S. The Preparation and Thermochemistry of the Ammonium Hydrogen Insertion Compound $(\text{NH}_4)_0.23\text{H}_0.08\text{MoO}_3$. *Solid State Ionics* **20**, 213–216 (1986).
118. Dittmann, M. & Schweda, E. Synthesis and Structure of Two Forms of Ammonium Monomolybdate $(\text{NH}_4)_2\text{MoO}_4$. *Z. Anorg. Allg. Chem.* **624**, 2033–2037 (1998).
119. Garin, J. L. The Structure of Ammonium Decamolybdate $(\text{NH}_4)_8\text{Mo}_{10}\text{O}_{34}$. *Acta Cryst.* **C44**, 779–782 (1988).
120. Dittmann, M. & Schweda, E. In situ Investigation of the Reaction of Ammonium Monomolybdate $(\text{NH}_4)_2\text{MoO}_4$ with Ammonia: The Structure of $(\text{NH}_4)_2[\text{Mo}_3\text{O}_{10}]$. *Zeitschrift fur Anorg. und Allg. Chemie* **626**, 569–573 (2000).
121. Benchrif, R., Leblanc, M. & De Pape, R. Synthesis and crystal structure of two polymorphs of $(\text{NH}_4)_2\text{Mo}_4\text{O}_{13}$, orthorhombic (o) and triclinic (t). *Eur. J. Solid State Inorg. Chem.* **26**, 593–601 (1989).
122. Wise, R. S. & Markel, E. J. Catalytic NH_3 Decomposition by Topotactic Molybdenum Oxides and Nitrides- Effect on Temperature Programmed $\gamma\text{-Mo}_2\text{N}$ Synthesis. *J. Catal.* **145**, 335–343 (1994).
123. Jette, E. R. & Foote, F. Precision determination of lattice constants. *J. Chem. Phys.* **3**, 605–616 (1935).
124. Zhou, E. *et al.* Facile synthesis of MoO_2 nanoparticles as high performance supercapacitor electrodes and photocatalysts. *Ceram. Int.* **42**, 2198–2203 (2016).
125. Pei, L., Xu, Z., Yan, S. & Zou, Z. Temperature-controlled evolution of microstructures that promote charge separation in a TaON photoanode for enhanced solar energy conversion. *J. Mater. Chem. A* **5**, 12848–12855 (2017).
126. Higashi, M., Domen, K. & Abe, R. Highly stable water splitting on oxynitride TaON photoanode system under visible light irradiation. *J. Am. Chem. Soc.* **134**, 6968–6971 (2012).
127. Hara, M. *et al.* TaON and Ta₃N₅ as new visible light driven photocatalysts. *Catal. Today* **78**, 555–560 (2003).
128. Merdrignac-Conanec, O. *et al.* TaON and Ta₃N₅ thin films: a new class of gas sensors. *Silic. Ind.* **69**, (2004).
129. Kerlau, M., Merdrignac-Conanec, O., Guilloux-Viry, M. & Perrin, A. Synthesis of crystallized TaON and Ta₃N₅ by nitridation of Ta₂O₅ thin films grown by pulsed laser deposition. *Solid State Sci.* **6**, 101–107 (2004).
130. Dabirian, A. High-Temperature Ammonolysis of Thin Film Ta₂O₅ Photoanodes: Evolution of Structural, Optical, and Photoelectrochemical Properties. *Chem. Mater.* **27**, 708–715 (2015).

131. Taviot-Gueho, C., Cellier, J., Bousquet, A. & Tomasella, E. Multiphase Structure of Tantalum Oxynitride TaOxNy Thin Films Deposited by Reactive Magnetron Sputtering. *J. Phys. Chem. C* **119**, 23559–23571 (2015).
132. Capek, J. *et al.* Effect of annealing on structure and properties of Ta – O – N films prepared by high power impulse magnetron sputtering. *Ceram. Int.* **45**, 9454–9461 (2018).
133. Salaman, K. *et al.* β -TaON thin films: production by reactive magnetron sputtering and the question of non-stoichiometry. *J. Phys. D. Appl. Phys.* **52**, 305304 (2019).
134. Tao, J. *et al.* Growth of single crystalline TaON on yttria-stabilized zirconia (YSZ). *J. Solid State Chem.* **204**, 27–31 (2013).
135. Suzuki, A. *et al.* Low temperature epitaxial growth of anatase TaON using anatase TiO₂ seed layer. *Jpn. J. Appl. Phys.* **54**, 3–6 (2015).
136. Suzuki, A. *et al.* High-mobility electron conduction in oxynitride: Anatase TaON. *Chem. Mater.* **26**, 976–981 (2014).
137. Syono, Y., Kikuchi, M., Goto, T. & Fukuoka, K. Formation of Rutile-Type Ta(IV)O₂ by Shock Reduction and Cation-Deficient Ta_{0.8}O₂ by Subsequent Oxidation. *J. Solid State Chem.* **50**, 133–137 (1983).
138. Zhu, L., Zhou, J., Guo, Z. & Sun, Z. Realization of a reversible switching in TaO₂ polymorphs via Peierls distortion for resistance random access memory. *Appl. Phys. Lett.* **106**, (2015).
139. Wang, Y. *et al.* Facile synthesis of TaOxNy photocatalysts with enhanced visible photocatalytic activity. *RSC Adv.* **6**, 1860–1864 (2016).
140. Hara, M. *et al.* Ta₃N₅ and TaON thin films on Ta foil: Surface composition and stability. *J. Phys. Chem. B* **107**, 13441–13445 (2003).
141. Yokoyama, D. *et al.* Ta₃N₅ photoanodes for water splitting prepared by sputtering. *Thin Solid Films* **519**, 2087–2092 (2011).
142. Oka, D., Hirose, Y., Fukumura, T. & Hasegawa, T. Heteroepitaxial Growth of Perovskite CaTaO₂N Thin Films by Nitrogen Plasma-Assisted Pulsed Laser Deposition. 2–5 (2014).
143. Sowinska, M. *et al.* Plasma-enhanced atomic layer deposition of titanium oxynitrides films: A comparative spectroscopic and electrical study. *J. Vac. Sci. Technol. A* (2016). doi:10.1116/1.4936227
144. Liu, X. Q., Han, X. D., Zhang, Z., Ji, L. F. & Jiang, Y. J. The crystal structure of high temperature phase Ta₂O₅. *Acta Mater.* **55**, 2385–2396 (2007).
145. Jauberteau, I. *et al.* Molybdenum nitride films: Crystal structures, synthesis, mechanical, electrical and some other properties. *Coatings* **5**, 656–687 (2015).
146. Liu, Y. *et al.* High electrochemical performance and phase evolution of magnetron sputtered MoO₂ thin films with hierarchical structure for Li-ion battery electrodes. *J. Mater. Chem. A* **2**, 4714–4721 (2014).
147. Anitha, V. P., Major, S., Chandrashekhar, D. & Bhatnagar, M. Deposition of molybdenum nitride thin films by r.f. reactive magnetron sputtering. *Surf. Coatings Technol.* **79**, 50–54 (1996).
148. Hiltunen, L. *et al.* Laboratory of Inorganic and Analytical Chemistry, Helsinki University of Technology, SF-02150 Espoo. *Thin Solid Films* **166**, 149–154 (1988).
149. Nandi, D. K., Sen, U. K., Choudhury, D., Mitra, S. & Sarkar, S. K. Atomic layer deposited molybdenum nitride thin film: A promising anode material for li ion batteries. *ACS Appl.*

- Mater. Interfaces* **6**, 6606–6615 (2014).
150. Cyril Robinson Azariah, J. *et al.* Pulsed Laser Deposited Molybdenum Oxides (MoO₃ & MoO₂) Thin Films for Nanoelectronics Device Application. *Proc. 4th Int. Conf. Devices, Circuits Syst. ICDCS 2018* **3**, 42–47 (2019).
 151. Camacho-Lopez, S. *et al.* Laser Fluence Dependence of the Electrical Properties of MoO₂ Formed by High Repetition Femtosecond Laser Pulses. *Phys. Status Solidi Appl. Mater. Sci.* **215**, 1–6 (2018).
 152. Camacho-López, M. A., Escobar-Alarcón, L. & Haro-Poniatowski, E. Structural transformations in MoO_x thin films grown by pulsed laser deposition. *Appl. Phys. A Mater. Sci. Process.* **78**, 59–65 (2004).
 153. Al-Kuhaili, M. F., Durrani, S. M. A. & Bakhtiari, I. A. Pulsed laser deposition of molybdenum oxide thin films. *Appl. Phys. A Mater. Sci. Process.* **98**, 609–615 (2010).
 154. Fenech, M., Lim, S., Cheung, J. & Sharma, N. Mechanistic insights into the phenomena of increasing capacity with cycle number: Using pulsed-laser deposited MoO₂ thin film electrodes. *Phys. Chem. Chem. Phys.* **21**, 25779–25787 (2019).
 155. Lee, W. *et al.* MoO₂ as a thermally stable oxide electrode for dynamic random-access memory capacitors. *J. Mater. Chem. C* **6**, 13250–13256 (2018).
 156. Bereznai, M. *et al.* Reactive pulsed laser deposition of thin molybdenum- and tungsten-nitride films. *Thin Solid Films* **473**, 16–23 (2005).
 157. Inumaru, K., Baba, K. & Yamanaka, S. Structural distortion and suppression of superconductivity in stoichiometric B 1-MoN epitaxial thin films. *Phys. Rev. B* **73**, (2006).
 158. Inumaru, K., Baba, K. & Yamanaka, S. Synthesis and Characterization of Superconducting B-Mo₂N Crystalline Phase on a Si Substrate: An Application of Pulsed Laser Deposition to Nitride Chemistry. *Chem. Mater.* **17**, 5935–5940 (2005).
 159. Lee, Y. J., Seo, Y. I., Kim, S. H., Kim, D. G. & Kim, Y. Do. Optical properties of molybdenum oxide thin films deposited by chemical vapor transport of MoO₃(OH)₂. *Appl. Phys. A Mater. Sci. Process.* **97**, 237–241 (2009).
 160. Irfan, So, F. & Gao, Y. Photoemission spectroscopy characterization of attempts to deposit MoO₂ thin film. *Int. J. Photoenergy* **2011**, (2011).
 161. Luo, H. *et al.* Controlling Crystal Structure and Oxidation State in Molybdenum Nitrides through Epitaxial Stabilization. *J. Phys. Chem. C* **115**, 17880–17883 (2011).
 162. Inumaru, K., Baba, K. & Yamanaka, S. Superconducting molybdenum nitride epitaxial thin films deposited on MgO and α -Al₂O₃ substrates by molecular beam epitaxy. *Appl. Surf. Sci.* **253**, 2863–2869 (2006).
 163. Ahn, E. *et al.* Epitaxial growth and metallicity of rutile MoO₂ thin film. *RSC Adv.* **6**, 60704–60708 (2016).
 164. Inumaru, K., Baba, K. & Yamanaka, S. Preparation of superconducting molybdenum nitride MoN_x (0.5 < x < 1) films with controlled composition. *Phys. B* **383**, 84–85 (2006).
 165. Kojima, R. & Aika, K. I. Cobalt molybdenum bimetallic nitride catalysts for ammonia synthesis: Part 2. Kinetic study. *Appl. Catal. A Gen.* **218**, 121–128 (2001).
 166. Cao, B. *et al.* Cobalt Molybdenum Oxynitrides: Synthesis, Structural Characterization, and Catalytic Activity for the Oxygen Reduction Reaction. *Angew. Chemie* **125**, 10953–10957 (2013).
 167. Sharma, K., Hui, D., Kim, N. H. & Lee, J. H. Facile synthesis of N-doped graphene

- supported porous cobalt molybdenum oxynitride nanodendrites for the oxygen reduction reaction. *Nanoscale* **11**, 1205–1216 (2019).
168. Martínez-Ferrero, E. *et al.* Nanostructured titanium oxynitride porous thin films as efficient visible-active photocatalysts. *Adv. Funct. Mater.* **17**, 3348–3354 (2007).
169. Mohamed, S. H. *et al.* Optical, water splitting and wettability of titanium nitride/titanium oxynitride bilayer films for hydrogen generation and solar cells applications. *Mater. Sci. Semicond. Process.* **105**, (2020).
170. Abd El-Rahman, A. M. & Mohamed, S. H. Preparation and characterization of nanostructured titanium oxynitride films for the application in self-cleaning and photoelectrochemical water splitting. *Thin Solid Films* **698**, (2020).